PERFORMANCE OF TAILORED JOINTS IN DISCONTINUOUS CERAMIC CORED SANDWICH STRUCTURES

by

Jonathan W. Stephens

A thesis submitted to the Faculty of the University of Delaware in partial fulfillment of the requirements for the degree of Master of Civil Engineering

Fall 2012

PERFORMANCE OF TAILORED JOINTS IN

DISCONTINUOUS CERAMIC CORED SANDWICH STRUCTURES

by

Jonathan W. Stephens

Approved: ____
John W. Gillespie Jr., Ph.D.
Professor in charge of thesis on behalf of the Advisory Committee

Approved: ____
Harry W. Shenton III, Ph.D.
Chair of the Department of Civil and Environmental Engineering

Approved: ____
Babatunde A. Ogunnaike, Ph.D.
Interim Dean of the College of Engineering

Approved: ____
Charles G. Riordan, Ph.D.
Vice Provost for Graduate and Professional Education

ACKNOWLEDGMENTS

My experience at the Center for Composite Materials at the University of Delaware has been extremely demanding and wearisome, yet at the same time, I can resoundingly state that it has also been very rewarding. I have discovered how to exceed the basic expectations of an undergraduate student, and developed the skills and motivation required of a graduate student in order to understand a complex research topic and withstand the frustration associated with research. For this extra emphatic push, I would like to thank my advisor, Dr. John W. Gillespie Jr. who provided me with guidance and immeasurable knowledge to help me succeed. If not for his assistance, this thesis would not have been possible.

I would also like to thank the research professionals and administrative staff at the Center for Composite Materials for the countless services they have provided over the past few years. Most notably, Nick Shevchenko, John Tierney, and Anis Gawandi have contributed their time and assistance to help me understand the intricacies of composite materials and how to perform research at a professional level.

Last but not least, I would like to thank my family and friends, who have been supportive since the beginning of this journey. While I may not have always been receptive of their advice and encouragement, they have nonetheless remained understanding and helped me maintain a positive outlook through every adversity I encountered.

TABLE OF CONTENTS

LIST OF TABLES vii
LIST OF FIGURES x
ABSTRACT xix

Chapter

1 INTRODUCTION 1

- 1.1 Background 1
- 1.2 Objectives 30

2 MATERIALS, FABRICATION AND MACHINING 33

- 2.1 Materials 33
- 2.2 Fabrication Process 38
- 2.3 Machining Process 53

3 TEST PROCEDURE 61

- 3.1 Compressive Stress Relaxation Test 63
- 3.2 Static Test 69
- 3.3 Fatigue Test 72
- 3.4 Test Fixtures 81
  - 3.4.1 Stress Relaxation Set-Up: Instron Machine 81
  - 3.4.2 Stress Relaxation Set-Up: Washer Load Cell 83
  - 3.4.3 Static/Fatigue Test Fixture 84

4 COMPRESSIVE STRESS RELAXATION IN DISCONTINUOUS CERAMIC CORED SANDWICH STRUCTURES 89

- 4.1 Determination of Baseline Torque 90
- 4.2 Relaxation Test Using Instron Machine 104
  - 4.2.1 Instron Testing on Single Face Sheet 105
  - 4.2.2 Instron Testing on DCCS Structure 109

4.3 Formulate Empirical Equation of Stress Relaxation in DCCS Structures (Generalized Maxwell Model) 112
4.4 Relaxation Test Using Washer Load Cell 126
4.5 Hoop Stresses in Ceramic Tile Due to Clamping Forces 129
4.6 Results from Washer Load Cell Relaxation Tests 154
4.7 Compare Results from Instron Machine and Washer Load Cell 157

5 STATIC TENSION/BEARING TEST IN DISCONTINUOUS CERAMIC CORED SANDWICH STRUCTURES 161

5.1 Static Testing Set-Up 162
5.2 Results/Comparison of Pinned and Clamped Joints 166
5.3 Clamped Joint Test with Varying Torque 180

5.3.1 Results (Torque = 10 ft-lbs) 181
5.3.2 Results (Torque = 30 ft-lbs) 183
5.3.3 Results (Torque = 50 ft-lbs) 185
5.3.4 Results (Torque = 70 ft-lbs) 187
5.3.5 Results (Torque = 110 ft-lbs) 189

5.4 Comparison of Various Torque Levels 191
5.5 Finite Element Analysis of Clamped Joints in DCCS Structures 198

6 FATIGUE TESTING ON DISCONTINUOUS CERAMIC CORED SANDWICH STRUCTURES 212

6.1 Fatigue Testing Set-Up 213
6.2 High Level Fatigue Residual Strength and Stiffness 220
6.3 Low Level Fatigue Residual Strength and Stiffness 248

7 CONCLUSIONS AND RECOMMENDATIONS 269

7.1 Compressive Stress Relaxation in Discontinuous Ceramic Cored Sandwich Structures 269
7.2 Bearing in Discontinuous Ceramic Cored Sandwich Structures 274
7.3 Fatigue on Discontinuous Ceramic Cored Sandwich Structures 287
7.4 Directions Toward Future Work 293

REFERENCES 296

Appendix

A DCCS STATIC COMPRESSION TEST GRAPHS 299
B FACE SHEET STRESS RELAXATION TEST GRAPHS 304
C DCCS STRUCTURE STRESS RELAXATION TEST GRAPHS 311
D STATIC/FATIGUE SPECIMEN GEOMETRIES 317
E DCCS STRUCTURE BEARING TEST GRAPHS 324
F DCCS STRUCTURE BASELINE FAILURE MODES 331
G DCCS STRUCTURE FATIGUE DAMAGE/FAILURE MODES 332
H DCCS STRUCTURE RESIDUAL STRENGTH TEST GRAPHS 337

LIST OF TABLES

Table 2.1: Face Sheet Material Properties 35

Table 2.2: Mechanical Properties of Ceramic Tile and Interlayer 37

Table 3.1: Terms Used Throughout Document 62

Table 3.2: Test Matrix for Compressive Stress Relaxation Tests of Face Sheet and DCCS Structure 66

Table 3.3: Test Matrix for Static Tests of DCCS Structure 71

Table 3.4: Loads and Bearing Stresses for Low-Level Fatigue Tests 74

Table 3.5: Loads and Bearing Stresses for High-Level Fatigue Tests 75

Table 4.1: Clamping Force Upper Limit (according to fastener strength) 97

Table 4.2: Static Compression Tests 101

Table 4.3: Clamping Force Upper Limit (according to constituents) 103

Table 4.4: Face Sheet Stress Relaxation with Equivalent Stresses 108

Table 4.5: DCCS Stress Relaxation with Equivalent Stresses 111

Table 4.6: Coefficients for Generalized Maxwell Model – Face Sheet 116

Table 4.7: Coefficients for Generalized Maxwell Model – DCCS Structure 120

Table 4.8: Coefficients for Generalized Maxwell Model – Interlayer 123

Table 4.9: Material Properties Used for FEA Modeling (Ceramic Tile, Adhesive Interlayer, Resin Gap, and Steel Bolt/Washer) 139

Table 4.10: Material Properties for FEA Modeling (Face Sheet Only) 140

Table 5.1: 17-4 pH Stainless Steel Pin vs. Grade 8 Bolt 164

Table 5.2: Strength and Displacement Comparisons (Pinned vs. Baseline Torque) 172

Table 5.3: Strength and Displacement Comparisons (Torque = 10 ft-lbs).......... 182

Table 5.4: Strength and Displacement Comparisons (Torque = 30 ft-lbs).......... 184

Table 5.5: Strength and Displacement Comparisons (Torque = 50 ft-lbs).......... 186

Table 5.6: Strength and Displacement Comparisons (Torque = 70 ft-lbs).......... 188

Table 5.7: Strength and Displacement Comparisons (Torque = 110 ft-lbs).......... 190

Table 5.8: Strength and Displacement Comparisons (All Clamped Tests - Averages).......... 192

Table 6.1: Loads and Bearing Stresses for Fatigue Tests.......... 215

Table 6.2: Summary of High Level Fatigue (Pinned and Clamped).......... 221

Table 6.3: Stiffness Loss according to Tangent Modulus (at zero load) and Secant Modulus (based on load range from 1024 lbs to 10240 lbs) for Stress Level 2 – Pinned.......... 231

Table 6.4: Stiffness Loss according to Tangent Modulus (at zero load) and Secant Modulus (based on load range from 1024 lbs to 10240 lbs) for Stress Level 2 – Clamped 232

Table 6.5: Strength and Displacement Comparisons (Stress Level 2 Residual Strength vs. Pinned/Baseline).......... 237

Table 6.6: Stiffness Loss according to Tangent Modulus (at zero load) and Secant Modulus (based on load range from 512 lbs to 5120 lbs) for Stress Level 1 – Pinned 240

Table 6.7: Stiffness Loss according to Tangent Modulus (at zero load) and Secant Modulus (based on load range from 512 lbs to 5120 lbs) for Stress Level 1 – Clamped.......... 242

Table 6.8: Strength and Displacement Comparisons (Stress Level 1 Residual Strength vs. Pinned/Baseline).......... 247

Table 6.9: Stiffness Loss according to Tangent Modulus (at zero load) and Secant Modulus (based on load range from 340 lbs to 3400 lbs) for Stress Level 5 – Clamped.......... 252

Table 6.10: Strength and Displacement Comparisons (Stress Level 5 Residual Strength vs. Baseline) ... 255

Table 6.11: Stiffness Loss according to Tangent Modulus (at zero load) and Secant Modulus (based on load range from 272 lbs to 2720 lbs) for Stress Level 4 – Clamped ... 258

Table 6.12: Strength and Displacement Comparisons (Stress Level 4 Residual Strength vs. Baseline) ... 261

Table 6.13: Strength and Displacement Comparisons (Stress Level 3 Residual Strength vs. Baseline) ... 264

Table 6.14: Stiffness Loss according to Secant Modulus (based on load range from 272 lbs to 2720 lbs) for all stress levels ... 268

Table 7.1: Fitting Parameters for Ramberg-Osgood Relationship ... 277

Table 7.2: Fatigue Design Table – Design Load (lbs) and Max/Min Fatigue Load (lbs) ... 292

Table D.1: Pinned vs. Baseline Torque Test Specimen Geometries ... 317

Table D.2: Variable Torque Test Specimen Geometries ... 318

Table D.3: High Level Fatigue Test Specimen Geometries (Clamped) ... 320

Table D.4: High Level Fatigue Test Specimen Geometries (Pinned) ... 322

Table D.5: Low Level Fatigue Test Specimen Geometries (Clamped) ... 323

LIST OF FIGURES

Figure 1.1: Discontinuous Ceramic Cored Sandwich Structure 4

Figure 1.2: Single Lap (Left) and Double Lap (Right) Test Configurations 10

Figure 1.3: Primary and Secondary Failure Modes due to In-Plane Tension (a) Net-Tension, (b) Shearout, (c) Bearing, (d) Cleavage, (e) Tearout... 11

Figure 1.4: Face Sheet and DCCS Structure Design Chart with varying w/D ratio and constant e/D = 4 (Weidner) 14

Figure 1.5: Face Sheet and DCCS Structure Design Chart with varying e/D ratio and constant w/D = 8 (Weidner) 14

Figure 1.6: Constitutive Viscoelastic Models: Maxwell Model 24

Figure 1.7: Constitutive Viscoelastic Models: Kelvin-Voigt Model 25

Figure 1.8: Constitutive Viscoelastic Models: Standard Linear Solid (SLS) Model... 26

Figure 1.9: Constitutive Viscoelastic Models: Generalized Maxwell (Weichert) Model 27

Figure 2.1: 3Tex 3Weave S-2 Glass 100 oz. ZZ Fabric weave fiber structure (3Tex Incorporated).. 34

Figure 2.2: Cutting Half-Tiles using Wet Tile Saw 45

Figure 2.3: Tile Array (red lines denote individual testing specimens)..................... 45

Figure 2.4: Ceramic Tiles with Spacers... 46

Figure 2.5: Mold Frame and Base Plate... 46

Figure 2.6: Placement of Distribution Media 47

Figure 2.7: Placement of Peel Ply.. 47

Figure 2.8: Placement of Wrap Ply and Second Fabric Ply.. 48

Figure 2.9: Placement of Surlyn Interlayer.. 48

Figure 2.10: Align Tiles According to Tile Array.. 49

Figure 2.11: Placement of Remaining Surlyn and Fabric Plies, Caul Plate and Infusion Connectors.. 49

Figure 2.12: Placement of Vacuum Bag over Mold.. 50

Figure 2.13: Remove Air from Vacuum Bag, Check for Leaks.. 50

Figure 2.14: Mix Resin and Allow to Transfer through Mold.. 51

Figure 2.15: Cure in Mold at Room-Temperature for 48 hours; De-Mold.. 51

Figure 2.16: Post-Cure in Oven at 300 degrees Fahrenheit for 8 hours.. 52

Figure 2.17: Cut Panels on Wet Saw with Diamond-Tipped Blade.. 58

Figure 2.18: Diamond-Tipped Core Drill Bit.. 58

Figure 2.19: Drill Holes with Water-Cooled Drill Press.. 59

Figure 2.20: Refine Specimen Ends with Milling Machine.. 59

Figure 2.21: Machined Edge of Specimen.. 60

Figure 2.22: Machined Bolt Hole of Specimen.. 60

Figure 3.1: Loading Methods for Stress Relaxation Test (ASTM E328-02).. 67

Figure 3.2: Sinusoidal output of one loading cycle at a frequency of 3 Hz (Stress Level 1 – High Level).. 76

Figure 3.3: Sinusoidal output of one loading cycle at a frequency of 2 Hz (Stress Level 3 – High Level).. 77

Figure 3.4: Sinusoidal output of one loading cycle at a frequency of 1 Hz (Stress Level 5 – High Level).. 78

Figure 3.5: Infrared Camera Image of Stress Level 5 (High Level) Fatigue Test.. 80

Figure 3.6: Stress Relaxation Test of DCCS Specimen using Instron Machine........ 82

Figure 3.7: Stress Relaxation Test of DCCS Specimen using Washer Load Cell 84

Figure 3.8: Test Fixture Parts........ 86

Figure 3.9: Test Fixture for Static Testing of DCCS Structure 87

Figure 3.10: Static Test Fixture Set-Up in Instron Grips........ 88

Figure 4.1: Types of Bolted Joints: Tensile (top) and Shear (bottom), (Bickford) 92

Figure 4.2: Interlayer Plasticization and Fiber-Buckling in the Face Sheet after Static Compression Test........ 100

Figure 4.3: Face Sheet Stress Relaxation with Variable Stresses........ 106

Figure 4.4: DCCS Stress Relaxation with Variable Stresses........ 109

Figure 4.5: Mechanics of DCCS Structure under Compressive Loading........ 112

Figure 4.6: Face Sheet Stress Relaxation Average vs. Generalized Maxwell Model (Regular Plot)........ 118

Figure 4.7: Face Sheet Stress Relaxation Average vs. Generalized Maxwell Model (Log Plot)........ 119

Figure 4.8: DCCS Stress Relaxation Average vs. Generalized Maxwell Model (Regular Plot) 121

Figure 4.9: DCCS Stress Relaxation Average vs. Generalized Maxwell Model (Log Plot) 122

Figure 4.10: Interlayer Calculated Stress Relaxation vs. Generalized Maxwell Model (Regular Plot)........ 124

Figure 4.11: Interlayer Calculated Stress Relaxation vs. Generalized Maxwell Model (Log Plot)........ 125

Figure 4.12: Calibration Chart of Torque Coefficient ‘k’........ 127

Figure 4.13: Stress Relaxation of DCCS Joint with 90 ft-lbs of Torque 128

Figure 4.14: Hairline Cracks in Ceramic Tile Due to Hoop Stresses caused by Torque 129

Figure 4.15: Geometric Parameters for DCCS Structure........ 131

Figure 4.16: Influence of Poisson Ratio and Transverse Strains on Hoop Stress in Ceramic Tile........ 132

Figure 4.17: Free Body Diagram of DCCS Structure under Clamp Load at the Joint 134

Figure 4.18: Mechanics of Un-bonded DCCS Structure Due to Uniform Compression (without Interlayer) 136

Figure 4.19: Mechanics of Bonded DCCS Structure Due to Uniform Compression (without Interlayer) 136

Figure 4.20: Mechanics of Bonded DCCS Structure with Friction Coefficient Due to Uniform Compression (without Interlayer)........ 137

Figure 4.21: Mechanics of Bonded DCCS Structure with Friction Coefficient Due to Uniform Compression (with Interlayer)........ 137

Figure 4.22: Effect of Friction Coefficient between Face Sheet and Washer on Hoop Stress in Ceramic Tile (Model without Interlayer)........ 143

Figure 4.23: Displacement of DCCS Structure with Friction Ratio of 0.5 (Model without Interlayer)........ 144

Figure 4.24: Effect of Friction Coefficient between Face Sheet and Washer on Hoop Stress in Ceramic Tile (Model with Interlayer)........ 146

Figure 4.25: Displacement of DCCS Structure with Friction Ratio of 0.5 (Model with Interlayer) 147

Figure 4.26: Effect of Interlayer on Hoop Stress in Ceramic Tile........ 149

Figure 4.27: Lines of Compressive Stress in Joint Members under a 100 kip Clamping Load (Bickford)........ 151

Figure 4.28: Lines of Compressive Stress in DCCS Joint using CATIA 152

Figure 4.29: Extent of Yielded Interlayer around DCCS Joint for Various Torque Levels........ 153

Figure 4.30: Stress Relaxation using Method of Re-Torque 155

Figure 4.31: Stress Relaxation of DCCS Joint with Various Methods to Reduce Stress Relaxation 156

Figure 5.1: Static Testing Set-Up (Pinned).. 163

Figure 5.2: Static Testing Set-Up (Clamped) 165

Figure 5.3: Typical DCCS Structure first failure mode (Net Tension).................... 167

Figure 5.4: Typical DCCS Structure second failure mode (Bending/Shear)........... 168

Figure 5.5: Typical DCCS Structure final failure mode (Delamination of Ceramic Tile, Interlayer and Face Sheet) 170

Figure 5.6: Load vs. Displacement Curve for Pinned and Baseline Torque Specimens (W4E2T0 and W4E2T90) 171

Figure 5.7: Net Tension Cracks in Tile prior to Ultimate Failure (horizontal views looking at left and right edges of specimen) 174

Figure 5.8: Bending/Shear Failure Mode Schematic – Pinned on left (Weidner); Clamped on right 176

Figure 5.9: Bending/Shear Crack in Tile and Delamination of Ceramic Tile, Interlayer and Face Sheet (vertical view looking down on top edge of specimen; pin loaded normal to current view)................................. 177

Figure 5.10: Bearing Failure in Face Sheet 178

Figure 5.11: Plastic Deformation of Grade 8 Bolt.. 179

Figure 5.12: Load vs. Displacement Curves for Baseline Torque and Torque = 10 ft-lbs (W4E2T90 and W4E2T10).. 181

Figure 5.13: Load vs. Displacement Curves for Baseline Torque and Torque = 30 ft-lbs (W4E2T90 and W4E2T30).. 183

Figure 5.14: Load vs. Displacement Curves for Baseline Torque and Torque = 50 ft-lbs (W4E2T90 and W4E2T50).. 185

Figure 5.15: Load vs. Displacement Curves for Baseline Torque and Torque = 70 ft-lbs (W4E2T90 and W4E2T70).. 187

Figure 5.16: Load vs. Displacement Curves for Baseline Torque and Torque = 110 ft-lbs (W4E2T90 and W4E2T110).. 189

Figure 5.17: Constraints used for Quarter-Symmetric Finite Element Model........... 200

Figure 5.18: Loading used for Finite Element Model of Clamped Case 201

Figure 5.18: Comparison of hole boundary x stresses between pinned and baseline torque for the Face Sheet in DCCS Structure Modeling (Applied 4250 lb far field load/2125 psi pressure)................................ 204

Figure 5.19: Comparison of hole boundary x stresses between pinned and baseline torque in the Ceramic Tile in DCCS Structure Modeling (Applied 4250 lb far field load/2125 psi pressure)................................ 205

Figure 5.20: Pinned Joint Finite Element Model, x Stresses 206

Figure 5.21: Clamped Joint Finite Element Model, x Stresses.................................. 206

Figure 5.22: Pinned Joint Finite Element Model, x Stresses (Tension only) 207

Figure 5.23: Clamped Joint Finite Element Model, x Stresses (Tension Only) 207

Figure 6.1: Load vs. Number of Cycles (Stress Level 2 – High Level) 217

Figure 6.2: Tangent and Secant Modulus (Instron) 219

Figure 6.3: Increased Net Tension Displacement at Stress Levels 4 and 5 222

Figure 6.4: Tile Protruding after Delamination and Ultimate Failure at Stress Levels 4 and 5.. 223

Figure 6.5: Failed Steel Pin/Grade 8 Bolt at Stress Level 3 (and during select cases at Stress Level 2)... 225

Figure 6.6: Normalized Fatigue Stiffness vs. Number of Cycles (Stress Level 2) based on Secant Modulus (defined from 1024 lbs to 10240 lbs)...... 226

Figure 6.7: Periodic Hysteresis Curves for Stress Level 2 – Pinned Case 228

Figure 6.8: Periodic Hysteresis Curves for Stress Level 2 – Clamped Case 230

Figure 6.9: Fatigued vs. Non-Fatigued Specimens at Stress Level 2 – Pinned Case 233

Figure 6.10: Fatigued vs. Non-Fatigued Specimens at Stress Level 2 – Clamped Case 235

Figure 6.11: Normalized Fatigue Stiffness vs. Number of Cycles (Stress Level 1) based on Secant Modulus (defined from 512 lbs to 5120 lbs).......... 238

Figure 6.12: Periodic Hysteresis Curves for Stress Level 1 – Pinned Case 239

Figure 6.13: Periodic Hysteresis Curves for Stress Level 1 – Clamped Case 241

Figure 6.14: Fatigued vs. Non-Fatigued Specimens at Stress Level 1 – Pinned Case 243

Figure 6.15: Fatigued vs. Non-Fatigued Specimens at Stress Level 1 – Clamped Case 245

Figure 6.16: Normalized Fatigue Stiffness vs. Number of Cycles (Stress Level 5) based on Secant Modulus (defined from 340 lbs to 3400 lbs).......... 250

Figure 6.17: Periodic Hysteresis Curves for Stress Level 5 – Clamped Case 251

Figure 6.18: Fatigued vs. Non-Fatigued Specimens at Stress Level 5 253

Figure 6.19: Normalized Fatigue Stiffness vs. Number of Cycles (Stress Level 4) based on Secant Modulus (defined from 272 lbs to 2720 lbs).......... 256

Figure 6.20: Periodic Hysteresis Curves for Stress Level 4 – Clamped Case 257

Figure 6.21: Fatigued vs. Non-Fatigued Specimens at Stress Level 4 259

Figure 6.22: Underwater C-Scan Images of Fatigued Specimens at Stress Level 5 (left) and Stress Level 4 (right) 262

Figure 6.23: Fatigued vs. Non-Fatigued Specimens at Stress Level 3 263

Figure 7.1: Ramberg-Osgood Relationship (Pinned).......... 278

Figure 7.2: Ramberg-Osgood Relationship (Clamped) 279

Figure 7.3: Torque Design Chart – Net Tension Failure Mode.......... 284

Figure 7.4: Torque Design Chart – Bending/Shear Failure Mode.......... 285

Figure 7.5: Torque Design Chart – Ultimate/Delamination Failure Mode.......... 286

Figure 7.6: DCCS Joint Failure vs. Bolt Failure 289
Figure 7.7: Fatigue Load Design Chart 291
Figure 7.8: Test Fixture for Transverse Loading of DCCS Joint 294
Figure 7.9: Metallic Insert in DCCS Joint 295
Figure A.1: Compressive Stress vs. Displacement (DCCS-SC-1) 299
Figure A.2: Compressive Stress vs. Displacement (DCCS-SC-2) 300
Figure A.3: Compressive Stress vs. Displacement (DCCS-SC-3) 301
Figure A.4: Compressive Stress vs. Displacement (DCCS-SC-4) 302
Figure A.5: Compressive Stress vs. Displacement (DCCS-SC-5) 303
Figure B.1: Normalized Stress vs. Time (FS-SRT90-1) 304
Figure B.2: Normalized Stress vs. Time (FS-SRT90-2) 305
Figure B.3: Normalized Stress vs. Time (FS-SRT90-3) 306
Figure B.4: Normalized Stress vs. Time (FS-SRT90-4) 307
Figure B.5: Normalized Stress vs. Time (FS-SRT90-5) 308
Figure B.6: Normalized Stress vs. Time (FS-SRT90-6) 309
Figure B.7: Normalized Stress vs. Time (FS-SRT90-7) 310
Figure C.1: Normalized Stress vs. Time (DCCS-SRT90-1) 311
Figure C.2: Normalized Stress vs. Time (DCCS-SRT90-2) 312
Figure C.3: Normalized Stress vs. Time (DCCS-SRT90-3) 313
Figure C.4: Normalized Stress vs. Time (DCCS-SRT90-4) 314
Figure C.5: Normalized Stress vs. Time (DCCS-SRT90-5) 315
Figure C.6: Normalized Stress vs. Time (DCCS-SRT90-6) 316
Figure E.1: Load vs. Displacement (W4E2T0) 324

Figure E.2: Load vs. Displacement (W4E2T10) 325

Figure E.3: Load vs. Displacement (W4E2T30) 326

Figure E.4: Load vs. Displacement (W4E2T50) 327

Figure E.5: Load vs. Displacement (W4E2T70) 328

Figure E.6: Load vs. Displacement (W4E2T90) 329

Figure E.7: Load vs. Displacement (W4E2T110) 330

Figure F.1: Baseline Failure of DCCS Structure with Torque = 90 ft-lbs 331

Figure G.1: Stress Level 1 High Level (5120 lbs/512 lbs) after 1 Million Cycles 332

Figure G.2: Stress Level 2 High Level (10240 lbs/1024 lbs) after 1 Million Cycles 333

Figure G.3: Stress Level 3 High Level (15360 lbs/1536 lbs) after Bolt Failure 334

Figure G.4: Stress Level 4 High Level (20480 lbs/2048 lbs) after DCCS Structure Failure 335

Figure G.5: Stress Level 5 High Level (25600 lbs/2560 lbs) after DCCS Structure Failure 336

Figure H.1: Load vs. Displacement at Stress Level 2 – High Level (Pinned) 337

Figure H.2: Load vs. Displacement at Stress Level 2 – High Level (Clamped) 338

Figure H.3: Load vs. Displacement at Stress Level 1 – High Level (Pinned) 339

Figure H.4: Load vs. Displacement at Stress Level 1 – High Level (Clamped) 340

Figure H.5: Load vs. Displacement at Stress Level 5 – Low Level 341

Figure H.6: Load vs. Displacement at Stress Level 4 – Low Level 342

Figure H.7: Load vs. Displacement at Stress Level 3 – Low Level 343

ABSTRACT

Composite sandwich structures with discontinuous ceramic tile cores offer a unique combination of structural and penetration resistance at minimum weight. Panels of these materials are often bolted to vehicles to provide soldier protection. Design guidelines and durability of bolted attachments in static and fatigue loadings are not well understood. In this study, Discontinuous Ceramic Cored Sandwich Structures, comprised of S2-Glass/epoxy composite face sheets bonded to a ceramic tile core are fabricated and tested to understand the complexities of stress distribution and load transfer between materials and the stress concentrations and failure modes in the bolted connections. Static testing of the composite structure with and without bolted joints provides insight into failure modes and joint capacity. Fatigue testing provides insight into long term durability as measured by stiffness loss, residual strength and change in failure modes. Previous testing has been performed to study the in-plane stresses and failure modes due to tensile loading with pinned joints. This study examines the effect of bolt torque through static loading and quantifying the changes in failure progression and load capacity. Data provided from these tests allow for fatigue parameters to be established in order to examine stiffness loss and joint sensitivity to fatigue loading. Stress relaxation testing is performed on each of the DCCS constituents to estimate the magnitude of clamp load loss due to mechanical

features in the joint and viscoelastic properties of the DCCS Structure. The information gathered from these experiments is used as an integral part of the design process to create a more structurally efficient, durable bolted joint for this composite structure.

Chapter 1

INTRODUCTION

1.1 Background

In broad terms, a composite material is a combination of two or more distinctly different constituents that when combined during processing creates a new material with superior properties. This combination of materials typically enhances the individual benefits of the constituents and offers an alternative to bulk materials, such as metals or plastics. In many cases, composites are a light-weight option for structural designs, yet they do not necessarily sacrifice strength or stiffness of the fabricated part. In fact, constituents can be selected and fabricated in such a way that the composite can be designed to meet the anticipated needs and desired properties of the application. This versatility allows for designs with improved strength, stiffness, weight, fatigue-resistance, corrosion, thermal wear, electrical, and other important properties (Gillespie).

Composites are comprised of two primary constituents: a fibrous reinforcement (e.g. glass, carbon and Kevlar tows), or fabrics (e.g. 2-D and 3-D woven tows) and a matrix that binds the reinforcement together to create a structural material (e.g. epoxy, vinyl ester and phenolic polymers). Gillespie explains the importance of each of the constituents, and their respective roles in the function of a composite material. The fibrous reinforcement functions as the primary source of strength and stiffness for the composite. Different types of commercial fibers include carbon/graphite, S- and E-glass, Spectra and Kevlar. Depending on their intended use, fibers can have various aspect ratios (e.g. continuous, short or particles). In this study, our interest is in the highest performance fibers that are continuous. Fibers are typically combined into tows that are woven into 2-D or 3-D fabric architectures. The polymer matrix allows for load to transfer between fibers, in addition to other functions, including protecting the fibers, preserving the correct fiber orientation and prevent fiber damage from propagating to adjacent fibers. Where the fibers generate the strength and stiffness, the matrix provides interlaminar shear strength, toughness, moisture resistance and temperature-dependant properties. The type of polymer matrix controls the fabrication and curing process, along with some critical properties of the composite material. A thermoset matrix is normally stiff, but brittle, with low resin viscosity and creep resistance. A thermoplastic matrix is more ductile and damage resistant, but has a tendency to creep and has poor melt flow. An elastomer, or rubber matrix, has very low strength and stiffness properties and when cured, provides high levels of ductility and energy absorption.

Manufacturing any combination of fiber and matrix requires a specific fiber-to-matrix ratio (i.e. fiber volume fraction), along with a strict fabrication process that includes a method of matrix infusion, heat or pressure during the curing process, and a prescribed duration of time for the composite to completely cure. The physical and chemical properties of a composite are a function of how the composite was manufactured, along with the properties of the individual constituents. Micromechanics and macromechanics provide a method to quantify average properties for a specific combination of fiber and matrix, and structural properties for multiple plies of given orientations. Basic testing methods, such as tensile, flexure, compression and shear testing, can be performed to supplement micro and macromechanics of the constituents and composite. Such testing can provide insight on the performance of composite laminates and failure modes in the composite structure under typical loading conditions.

Hybrid composites are a unique subdivision of the composite family. They incorporate two or more reinforcements into a single structural element. This may include multiple combinations of fibers and polymers, or the inclusion of homogeneous and isotropic elements, such as steel and ceramics. These designs are often more cost-effective and structurally efficient, but they can introduce issues with incompatible coefficients of thermal expansion (CTE), bonding between dissimilar materials, and interlaminar stresses that can induce delamination.

A prevailing hybrid structure used in the application of armored vehicles is the Discontinuous Ceramic Cored Sandwich (DCCS) Structure. The material studied in this thesis is comprised of two external face sheets made of S2-glass fabric reinforcements and infused with an epoxy resin matrix, a discontinuous ceramic tile core, and a compliant and high elongation adhesive interlayer to bond the face sheet with the ceramic tiles. Figure 1.1 demonstrates the symmetry and uniformity of the DCCS Structure (figure not to scale). This particular configuration was chosen for its' additional energy-absorption, penetration resistance and compressive strength properties contributed by the ceramic core, and the tensile strength and stiffness properties provided by the composite face sheet. In conjunction with the compliant interlayer, this structure provides a unique blend of strength, impact resistance and durability when subjected to high impact forces.

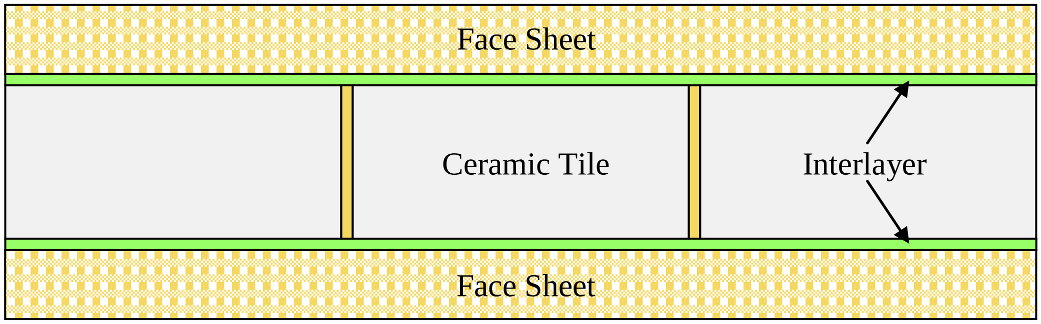

Figure 1.1: Discontinuous Ceramic Cored Sandwich Structure

Due to the configuration of the DCCS Structure, a Vacuum Assisted Resin Transfer Molding (VARTM) process serves as the most cost-effective infusion process. The VARTM process is an adaptation of the more common Resin Transfer Molding (RTM) process. A generic procedure is followed for all composites fabricated using the VARTM process. Five primary steps comprise the process: (1) mold preparation and fabric lay-up, (2) sealing the mold and creating a vacuum, (3) resin preparation and degassing, (4) resin impregnation, and (5) cure of fabricated panels (Bolick 1 – 7). Preparation and lay-up are important to ensure that fabric plies are correctly oriented and the panel can be de-molded with ease. Plies oriented only slightly off axis can significantly affect the structural properties of the composite. Creating a perfect vacuum without leaks will reduce the risk for air voids in the finished panel and generate the maximum force to pull the resin through the entire preform. The resin infused in a mold is a precise mixture of commercial resin and hardener, with the ratio of the two governing the necessary cure time of the composite panel. Once the resin and hardener have been thoroughly mixed, the resin must be placed in a de-gassing chamber to remove any air bubbles from the mixture that may potentially enter the infusion line and the part. The actual impregnation of resin in the panel may take several hours, depending on the thickness of the panel and the viscosity of the chosen resin. The vacuum should remain on during this process to ensure the panel is entirely soaked in resin. The resin takes several days to fully cure at room temperature prior to de-molding. In the case of hybrid composites, such as the DCCS Structure, an additional post-cure at elevated temperatures is needed to secure the bond between materials. This five-step process remains consistent between all VARTM fabrications, while internal details are adjusted to meet necessary conditions of composite panel. Details on each material are given in Chapter 2.

The manufacturing process is an important step in establishing the structural integrity of a composite. Mahdi et al examined the effect of different manufacturing processes and the quality at which manufacturing was performed on the overall structural performance of Composite Integral Armor (CIA). The CIA Structures similar to the DCCS Structure used in this research was originally developed for the United States Army to satisfy specific structural criteria, including stiffness, strength, penetration resistance, damage tolerance, fatigue and environmental durability. Optimizing the manufacturing process was a major task to ensure these criteria were met on a consistent basis. Mahdi et al determined that the VARTM process was not only more efficient than the labor-intensive, multi-step process previously required to fabricate composite panels, but the one-step VARTM process also enhanced the interfacial properties of the panel, improving the aforementioned structural properties.

Understanding the effect manufacturing can have on the structural integrity of a composite material and optimizing this process is one method to enhance the production and reproducibility of composite structures. Another method to improve a composite is to understand the mechanics of a particular configuration and optimize the structure by choosing the most appropriate constituents to achieve the desired properties and attaining the perfect geometrical relationship between the constituents. Huang et al was one of the first to analyze the specific characteristics of Discontinuous Ceramic Core Sandwich Structures. Using the same general model as Figure 1.1, Huang et al examined the load transfer between constituents, and the effects of different interlayer properties and tile lengths. A variational analysis approach was used to model the response of the constituents under tension and in-plane shear loading conditions, which allowed Huang et al to establish a preliminary understanding of the stress transfer throughout the structure. Because the stiffness of the adhesive resin is much less than that of the ceramic tiles, very little stress is transferred in the gap region between adjacent tiles; subsequently the axial stress distribution shifts to the face sheet at these particular regions. Stress transfer in the through-thickness direction of the structure was found to be highly dependent on the properties and thickness of the interlayer and the size of the stress transfer region between the two constituents. A stiffer, thinner interlayer allows for a higher rate of stress transfer between the face sheet and ceramic core. Increasing the tile length provides a larger region for stress to transfer from the face sheet to the ceramic core. Reducing stress transfer by way of a thicker, more compliant interlayer or shorter tile length causes the effective stiffness of the DCCS Structure to approach the stiffness of the face sheet. This concept is reasonable, considering that the majority of the load and stresses are carried exclusively by the face sheet. With a higher rate of stress transfer between the face sheet and the tiles, the effective stiffness of the DCCS

Structure increases due to a greater amount of stress carried by the stiffer ceramic core. Huang et al quantified that increasing the tile length to 4 inches (101.6 mm) raised the effective stiffness of the DCCS Structure to nearly twice as much as the face sheet stiffness. Gawandi et al questioned whether maximizing stress transfer was beneficial using the methods proposed by Huang et al. Gawandi et al used the same DCCS Structure to observe the influence of thermal and interlaminar stresses on the structural capacity of the composite structure. Using two different face sheet materials, Gawandi et al examined the influence of varying the difference in coefficients of thermal expansion between the face sheet and ceramic core. He found that a greater mismatch in CTE's increased the interlaminar stresses when exposed to temperature change, often leading to premature delamination between the face sheet and tiles. This phenomenon can occur during cool down from post-cure temperature (i.e. process induced residual stress), reduction in environmental service temperatures, or during cyclic fatigue where defects nucleate and grow typically at the interfaces in DCCS Structure. Much like the effective stiffness of the DCCS Structure, Gawandi et al determined that the effective CTE of the DCCS Structure increased with a stiffer, thinner adhesive interlayer, as well as longer tiles. Whereas geometrical and physical attributes that reduce the amount of stress transfer cause the effective CTE of the DCCS Structure to converge to that of the face sheet. Incorporating the conclusions from Huang et al, Gawandi et al found that increasing the stress transfer ultimately led to an increase in interlaminar stresses, creating a structural weakness in the adhesive interlayer. If the stresses exceeded those capable of being carried by the interlayer, the structure could fail due to debonding at the face-sheet to ceramic tile interface. Thus, the final structural design had to balance the need for stress transfer from the face sheet into the ceramic core without causing excessive interlaminar stresses that could lead to reduced fatigue life and structural failure.

Armored panels, such as the DCCS Structure, are mounted on vehicles to serve as a means of ballistic and blast protection. Composite joints are the most common, efficient method of attaching composite panels to other structural components. However, they are also a prime location for local and catastrophic damage in the composite structure due to an increase in stress concentrations at the joint, caused by machined hole in the panel and the direct bearing of the bolt on interior joint walls of the composite. Failure is no longer determined by the composites' basic structural properties of the face sheet, but is instead determined by the strength of the hybrid composite joint where the ceramic tile plays a major role.

Extensive research has been conducted and compiled to understand and predict the performance of joints made solely of composites, and identify methods to improve the structural efficiency of the joint. Thoppul et al presented a comprehensive review based on multiple literary articles on joint design methodologies in composite structures. Some of the topics he discussed included: particular ASTM Standards for mechanical testing; design consideration to optimize joint strength; common failure modes of composite joints and methods to predict when and where these failures occur; issues due to clamping forces, primarily stress relaxation; a comparison between pin and bolted joints, and the respective effects of environmental conditions on each; and evaluation techniques to monitor and assess the performance of the composite joint. A majority of the work presented by Thoppul et al in this review focuses on thin laminates. While thin laminates are not as structurally complex as the DCCS Structure in this study, Thoppul et al provides the foundation for an appropriate design methodology to supplement the research necessary to gain a thorough understanding of composite joints in the DCCS Structure.

Gaining an understanding of the performance of bolted composite joints begins with determining an appropriate test method to quantify and identify the joints strengths and weaknesses. Thoppul et al suggests ASTM Standard D5961 as a guideline for testing composite laminates in tension to examine the bearing response at the joint. Single- and double-lap joints are widely considered the best joint testing configurations, as evident by the abundant number of studies on composite laminates that have utilized these two configurations. Both configurations can be seen in Figure 1.2. According to the figure, the single-lap test fixture consists of a single plate aligned next to the composite laminate, whereas the double-lap test fixture consists of two plates that are symmetric about the composite laminate in between. The primary issue with the single-lap configuration is that the distribution of load across the joint is asymmetric. This eccentricity increases with thicker laminates and causes more complex failure modes due to bending. Despite this, the single-lap configuration is more prevalent due to better representing the joint in many applications. The double lap configuration offers an even load distribution across the joint, and eliminates the eccentricities when testing thicker composite structures. However, there is potential for bolt bending in the double-lap configuration, which could lead to the bolt bearing on the edges of the composite joint. Typically, the DCCS Structure is within the range of 0.90 inches (22.86 mm) to 0.94 inches (23.88 mm) thick. To accommodate the thicker DCCS Structure, a double-lap configuration provides the best scenario and eliminates the concern of eccentric loading.

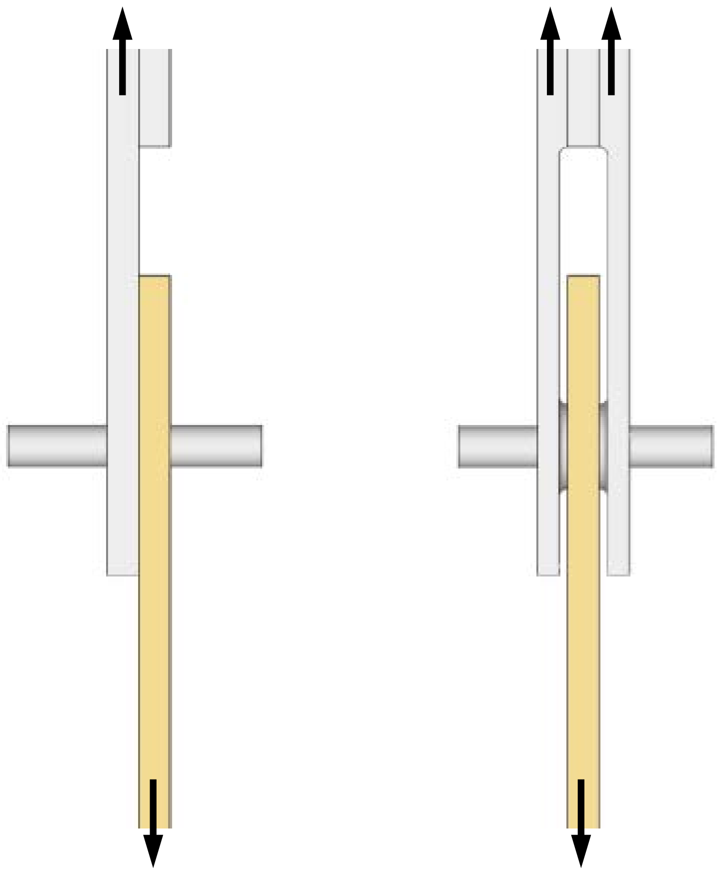

Figure 1.2: Single Lap (Left) and Double Lap (Right) Test Configurations

Each of the aforementioned configurations can be used for a variety of joint arrangements, including a single bolt, multiple bolts on a single row, or multiple rows of bolts. Introducing more joints causes a more complex sequence of failure. For the purpose of gaining an initial understanding of the effect of joints in the DCCS Structure, a single-bolt arrangement is best suited for this study.

Before predicting the failure modes of the joint in the DCCS Structure, it is beneficial to understand the behavior of joints in thin laminates, their respective failure modes, and what attributes to those failures. There are five failure modes of composite laminates under in-plane tension: three primary failure modes – net tension, shearout, and bearing; and two secondary failure modes – cleavage and tearout. All five failure modes are shown in Figure 1.3. In addition to joint configuration, several other parameters can influence the failure mode of thin laminates. Joint geometry (specimen width, edge distance, and hole diameter), loading under in-plane tension (static and fatigue), and fastening conditions (joint type, joint size, bolt/hole clearance, washer size, tightening torque/clamping force, and protruding/countersunk head bolt) all contribute to the performance of composite joints. Understanding the effect of these respective parameters on joint performance will provide an appropriate baseline for the DCCS Structure.

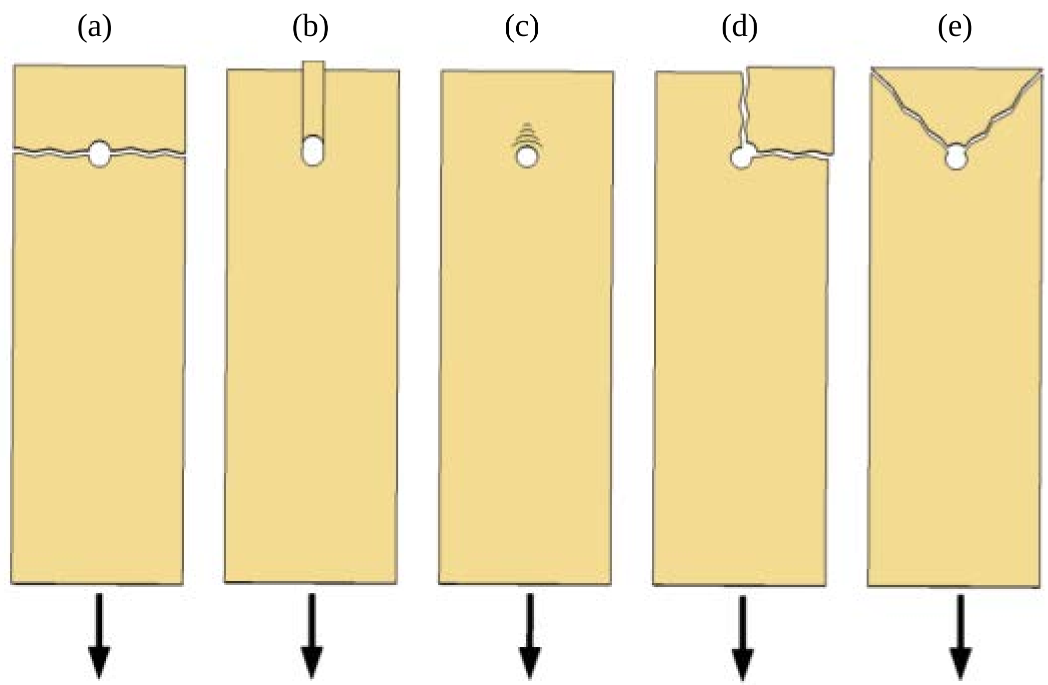

Figure 1.3: Primary and Secondary Failure Modes due to In-Plane Tension (a) Net-Tension, (b) Shearout, (c) Bearing, (d) Cleavage, (e) Tearout

Several studies have been performed regarding the affect of joint geometry on the failure modes of laminate composites. ASTM Standard D5961 provides a brief insight on these different geometries and indicates that they can have a significant influence on the performance of composite joints. The primary geometrical ratios of concern include the ratio of specimen width to the hole diameter (w/D), the ratio of the distance between the specimen edge and the center of the hole to the hole diameter (e/D), and the ratio of the specimen thickness to the hole diameter (h/D). Sen et al examined the two former geometrical ratios in glass/epoxy composite laminates, a composition not too different than the face sheet of the DCCS Structure. An extensive test matrix was derived, utilizing five different e/D ratios and four different w/D ratios, and testing each conceivable combination. This allowed for concise and definite conclusions to be made about the geometrical parameters. He determined that specimens with w/D ratios lower than e/D ratios, typically failed due to net-tension and cleavage. Increasing the w/D ratios or decreasing the e/D ratios of these specimens resulted in a transition to shearout failure. Specimens with w/D and e/D ratios above a threshold level failed almost exclusively in bearing. This geometry also revealed the greatest joint bearing strength compared to the other geometrical arrangements. Increasing thickness can also increase joint bearing strength, and additionally reduces the risk of delamination and fiber-buckling in the composite (Hou et al 1921 – 1938). As a result, the joint deviates from bearing failure to more catastrophic failure modes such as net-tension and cleavage. With a more catastrophic failure, the composite joint displays more brittle properties, lower displacements to failure and less energy absorption prior to failure. For a given composite material and laminate stacking sequence, geometric ratios have the most deliberate impact on joint failure and can be modified and optimized to control the failure mode and bearing strength of the joint.

The DCCS Structure is much more complex than the carbon/epoxy composite laminate studied by Sen et al. Given the unique structure presented in the case of armored hybrid composites, Weidner et al performed geometric ratio tests on the DCCS Structure to gain a clear understanding of the failure modes associated with various ratios and established appropriate design charts (Figures 1.4 and 1.5) for variable w/D and e/D ratios. Initially testing the face sheet material, Weidner et al confirmed many of the statements made by Sen et al. He quantified the transition from net tension to bearing failure in face sheet specimens with increasing w/D ratios to be slightly greater than 2.0 (with a constant e/D ratio of 4.0). Conversely, Weidner et al also determined that an e/D ratio of 3.5 resulted in the transition from shear out to bearing failure in the face sheet (with a constant w/D ratio of 8.0). Identifying these transition ratios are an important part of optimizing the strength of the joint. Incorporating a w/D > 2.5 and an e/D > 3.5 into the design will provide slow bearing failure to occur in the face sheet, which not only increases the bearing strength of the joint, but also reduces the potential for catastrophic failures, such as net tension or shear out.

Testing the DCCS Structure as a whole introduces several new modes of failure, primarily failure of the ceramic tile in net tension and bearing/shear, and delamination between the various constituents, causing ultimate failure of the ceramic tile. Once delamination and ultimate failure of the tile occurs, the load is transferred entirely through the face sheet, reiterating the importance of having a gradual failure in the face sheet rather than catastrophic failure (Weidner et al). The DCCS failure modes can be seen in the shaded regions of Figures 1.4 and 1.5.

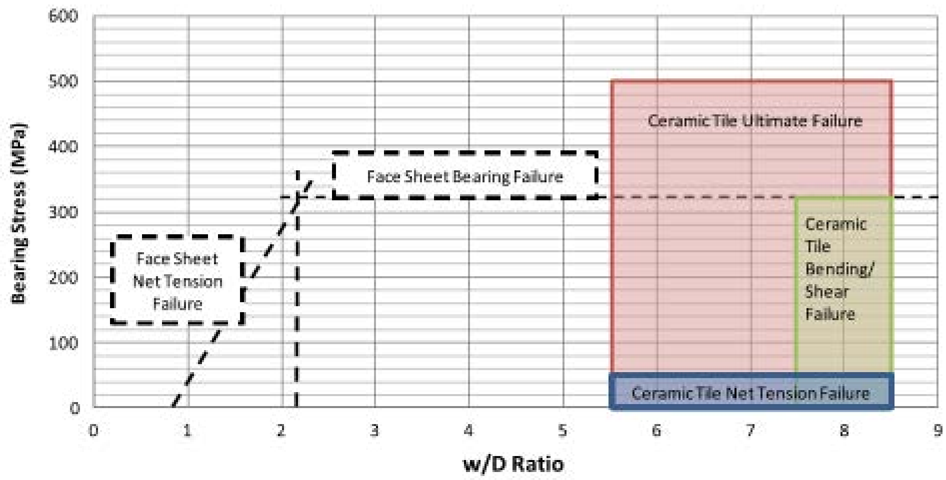

Figure 1.4: Face Sheet and DCCS Structure Design Chart with varying w/D ratio and constant e/D = 4 (Weidner)

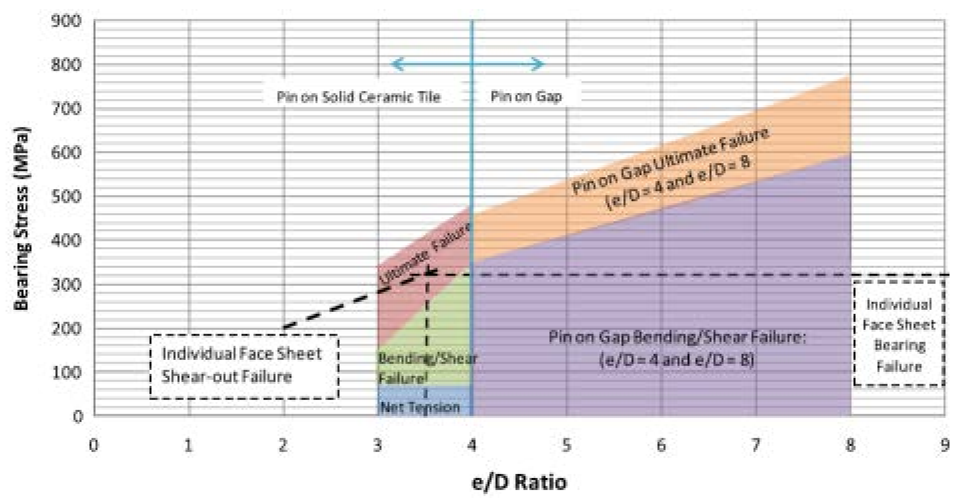

Figure 1.5: Face Sheet and DCCS Structure Design Chart with varying e/D ratio and constant w/D = 8 (Weidner)

To identify the performance and strength of any composite material, specimens are subjected to a variety of loading patterns using different test methods. This particular study will focus on in-plane tension loading of the bolted joint, under both static and fatigue loading conditions. Both loading conditions introduce unique issues that must be addressed, as well as damage evaluation requirements depending on the extent of damage in the specimens. Static testing is useful in determining composite strength and stiffness properties, as well as optimizing joint configurations and fastening conditions. The most important factors in static tests are determining a suitable loading rate and finding a reliable instrument to quantify displacement. A slow loading rate, relative to the compliance of the composite, is recommended (ASTM Standard D 5961/D 5981-M-05). Choosing a slow loading rate negates the affect of rate-dependent properties in the composite, eliminates the dynamic response factor of faster loading rates, and allows for better damage evaluation during the test. The majority of testing equipment have built-in displacement capabilities; however, an external method of measuring displacement, such as the use of LVDT's, may reduce the amount of machine compliance and yield more accurate data. Fatigue testing is important in understanding a composites resistance to cyclic loading, typical in environmental and application-specific conditions. To produce a consistent sinusoidal loading pattern that simulates the expected fatigue, maximum and minimum stresses are chosen and classified by their R ratio, which is the ratio of minimum stress to maximum stress (ASTM Standard D6873-03). Depending on the R ratio chosen, fatigue testing can be performed under compression-compression (R = 10.0 typ.), tension-tension (R = 0.1 typ.), or tension-compression (R = -1.0 typ.) loading patterns. Since the maximum loads in a fatigue test are typically considerably less than the ultimate strength of a given composite under static loading conditions, fatigue failure must be quantified differently. In terms of bolted composite joints, which will be the main focus of this study, the definition of fatigue failure is when the bolt hole exceeds 4% of the original diameter due to bearing damage (ASTM Standard D6873-03), whereas for non-failed fatigue specimens one can measure hole elongation, joint stiffness loss, and the residual strength of the composite joint (Whitworth 25 – 31). Non-destructive evaluation techniques are another alternative to gain a better understanding of the progressive damage at the joint, considering that the joint is the most sensitive region to damage due to the presence of the stress concentrations. These techniques include: visual examination with the aid of colored dyes, which, when applied to a composite structure, can highlight locations of fiber buckling and fracture, and delamination; electrical resistance change, which is sensitive to fractures in the fiber, delamination in the composite structure, or bearing failure of the joint, when the path of an electrical current changes direction away from the natural flow through the composite; acoustic emission testing, which converts the wave energy released from progressive damage in the micro-structure into electrical signals using piezoelectric transducers to quantify the amount of energy released and magnitude of the damage; using a bolt-gauge that utilizes a strain gage within a fastener to measure the clamping load, which can decrease with stress relaxation, or increase due to bearing or delamination failure; vibration techniques, which pertains to any method of subjecting a composite to a particular frequency of vibration and characterizing the vibrations using accelerometers, strain sensors and other devices; and sonic infrared imaging, which measures the temperature differential of local friction and heating within a composite when exposed to vibration techniques (Thoppul et al 301 – 329).

Several of these non-destructive evaluation methods were utilized through the course of this research. Visual examination was the best method of evaluating damage during the testing sequence and immediately after a specimen was removed from the test fixture. Specimens were then placed in an underwater ultrasonic C-scan, which measures the reflected echo of ultrasonic waves emitted by transducers to map the internal damage of a composite structure. The quality of these scans is directly correlated to the frequency of the transducer and the scanning rate, with a higher frequency transducer and slower scanning rate resulting in a higher resolution image of the damaged specimen (Steiner et al 193 – 198). During fatigue testing, an infrared camera was used to monitor the temperature at the joint to ensure energy was not lost to heating and friction. Experiencing a temperature gradient could also result in the changing of material properties, resulting in potentially variable results.

When it comes to optimizing a composite joint, the type of joint, the components that comprise the joint, and the fastening conditions can have a significant influence on the overall performance of the joint, primarily its' strength and stiffness. Three types of joints have been researched and used extensively for composite materials: mechanically fastened, adhesively bonded, and hybrid mechanically fastened/adhesively bonded joint (Thoppul et al 301 – 329). Each type of joint possesses unique benefits, but they also have their detriments. For example, mechanically fastened joints are typically easier to install since they do not require the surface preparation that adhesively bonded joints require, and are not sensitive to environmental effects such as temperature and humidity (Thoppul et al 301 – 329). They also have the luxury of being easily replaceable without damaging the composite. Adhesively bonded joints provide a range of benefits, both economically and functionally. Not only are bonded joints structurally lighter in weight and reduce fabrication costs, but more importantly, they maintain a high level of structural integrity at the joint, whereas this is reduced when a hole is manufactured for mechanical joints (Banea et al 1 – 18). However, the quality of the bonded joint is highly variable making the joint strength difficult to predict. The introduction of hybrid joints has solved some of the main issues with mechanically fastened and adhesively bonded joints. Conventional hybrid joints are comprised of the atypical mechanical joint with a machined hole and an adhesively bonded interface between the attached constituents. In this scenario, the adhesive interface carries the initial load, until the load exceeds the bond line strength, wherein the load is then transferred to the mechanical bolted joint (Sun et al 1 – 20). This arrangement allows the adhesive joint to withstand minor static and fatigue loads, without damaging the ultra-sensitive bolt hole, until the joint is exposed to larger loads. Other variations of hybrid joints include incorporating angular attachments and L-shaped attachments, which have been shown to increase the joint strength by 75% and 115%, respectively (Sun et al 1 – 20). This improvement conceptually offsets the additional weight of the attachments.

Mechanically fastened joints will be the focus of this study; however there are several factors that make up mechanically fastened joints that can have a drastic effect of their performance, primarily joint size, bolt-hole clearance, and washer size. Hou et al examined different sizing effects and thickness constraints in composite joint, including the effect of joint size. He found that increasing the joint size while scaling the specimens appropriately in order to maintain constant e/D, w/D and h/D ratios, resulted in lower joint strengths and progressively changing failure modes, from bearing to catastrophic net-tension failure. This can be explained by the concept that thicker composites tend to display more brittle properties, smaller displacements to failure, and smaller energy absorption during the failure process, hence catastrophic net-tension failure. Hou et al uses Weibull's strength and scaling theories, which state that "the larger the size of a material, the larger the size of defect in the material, and the lower the strength of the material," to support his experimental findings. McCarthy et al performed extensive research on the effects of variable bolt-hole clearances in composite bolted joints. He suggested that allowable tolerances were necessary in composite joints, as interference fits could potentially cause local damage, reducing strength and stiffness. However, larger tolerances led to smaller contact areas on the interior of the bolt hole, resulting in more concentrated loads and higher stresses at lower strengths. This also changed the location and direction of peak circumferential stresses. To obtain the maximum strength of a joint, the bolt-hole clearance should be minimized without causing an interference fit. Under the circumstance when a washer is used on the exterior of the composite joint, the selection of the washer size can be very important. By decreasing the washer size, the contact pressure between the washer and composite increases due to a decrease in contact area. However, assuming a constant clamping force, if the contact area becomes too small, the contact pressure may exceed the compressive strength of the composite, causing local damage in the composite micro-structure and premature failure of the joint. Studies performed by Yan et al and confirmed by Khashaba et al concluded that for varying tightening torque, an optimal outer diameter-to-inner diameter washer ratio of 3.0 should be utilized. Prior studies involving joints in the DCCS Structure were solely pinned joints, without the use of washers. By introducing a clamping force, washers will be added to protect the exterior face sheet from the bolt head and help distribute the clamping pressure over the surface of the face sheet surrounding the bolt hole. An appropriate washer size will be chosen based on the aforementioned outer diameter-to-inner diameter ratio, as recommended by Yan et al and Khashaba et al.

The main fastening conditions can be simplified to the decision between a protruding or countersunk head bolt and the amount of clamping force desired in the joint. The majority of the time, protruding and countersunk head bolts are chosen for aesthetic reasons or space limitations. Quantitatively, protruding head bolts have been found to be much more efficient and effective. Protruding head bolts are more resistant than countersunk head bolts; hence they experience less displacement at the joint prior to failure. They also exhibit higher stiffness and strength, although the evolution of damage tends to progression more quickly (Riccio et al 2071 – 2090 and McCarthy et al 1415 – 1431). Several studies have examined the impact of clamping force of bolted joints. In all cases, the addition of a clamping force has improved the strength and stiffness of the joint. This is attributed to the suppression of delamination and fiber-matrix splitting conducive in joint failure (Yan et al 1215 – 1229). Given the knowledge that clamped joints are an improvement over pinned joints, the question arises on how much clamping force is optimal. Khashaba et al determined that bearing strength and stiffness increased with increasing torque; however, the strength and stiffness tended to plateau and some level of torque, unique to every composite laminate depending on its' properties. This plateau is generally caused by the clamping force exceeding the compressive strength of the composite. Other factors to consider in determining the optimal torque include the composite structure, bolt strength, short- and long-term relaxation, fatigue resistance, and expected load directions (Bickford). These factors, and others, will need to be examined more closely before a final determination is made on the torque used in this study.

One of the major concerns of structural joints, as previously mentioned, is the tendency to relax, or lose clamp load, over time. If the clamp load is reduced below a given service limit, the mechanical joint could potentially loosen and lose all effectiveness. This relaxation can be caused by a number of things, most notably conditions within the mechanical joint, types of external loads, and the properties of the structural components comprising the joint. Relaxation within the mechanical joint is mainly caused by thread slipping from fatigue loading over time, though relaxation has also been found to result from other factors, including imperfect mechanical parts, which can reduce surface interaction between parts and cause poor thread engagement; under- or over-sized holes, resulting in less-than-ideal surface contact area between the fastener and structure; thread engagement length, basically meaning that the more thread that is engaged, the higher the thread surface friction against loosening; and the rate of tightening speed (Bickford). Nevertheless, if a joint is tightened to an appropriate level of torque, the relaxation in the mechanical joint is typically negligible. In many static loading cases, the clamping load felt at the joint can increase. Under bending loads, the structural components will tend to pull out on the joints, increasing the axial load felt by the fastener. In-plane axial loads that cause bearing failure can also exert additional axial forces on the fastener that increase the clamp load. In the case of fatigue loading, the cyclic nature of the loading pattern is believed to progressively damage the thread surfaces, slowly losing friction over time, and consequently causing thread slippage (Bickford). It is commonly suggested that slightly over-torquing a joint will counter the eventual loss of clamp load over time. One other feature of the structural joint that allows for relaxation is the composition of the structural component. Composite structures, such as the DCCS Structure, possess inherent viscoelastic properties due to its constituents. This characteristic allows a material to lose stress when a constant strain is imposed, as would be the case in a structural joint. It is vital to this research to understand viscoelastic materials and their responses under particular loading conditions, and apply this knowledge in order to quantify and accurately predict the amount of clamp load that will be lost due to stress relaxation of the DCCS Structure.

A viscoelastic material comprises properties of both elastic and viscous materials. Among the ways to identify a viscoelastic material include a decrease in stress when subjected to a constant strain (stress relaxation); an increase in strain when subjected to a constant stress (creep); and a definitive phase lag under cyclic loading, representing dissipation of mechanical energy (hysteresis). A distinctive property of these materials is the limit between linear and non-linear viscoelastic regime of the material. Linear viscoelasticity is much easier to model and predict, and occurs under small strains. Non-linear viscoelasticity occurs when strains are excessive or if the material properties change due to considerable deformations, most commonly due to elastic yielding or internal damage. Ideally, the strain induced by the fastener will not result in damage or excessive deformations, and the stress relaxation and creep can be modeled by linear viscoelastic constitutive models.

In recent studies, viscoelastic materials have been represented by increasingly complex models comprised of springs (simulating elastic response) and dashpots (simulating viscous response). However, some material responses can be modeled according to basic constitutive relationships, primarily the Maxwell Model, the Kelvin-Voigt Model, the Standard Linear Solid (SLS) Model and the Generalized Maxwell (Weichert) Model, each of which has a particular configuration of springs and dashpots, represented in Figures 1.4 through 1.8 (Roylance 1 – 29). The Maxwell Model is a single spring and dashpot in series; in a stress relaxation diagram, the stress would reduce to zero over time, and whereas, in a diagram modeling creep, the strain would increase linearly with time. This model is a sufficient representation of a viscoelastic fluid. The Kelvin-Voigt Model consists of a single spring and dashpot in parallel; a stress relaxation plot of this model would indicate an instantaneous drop in stress then remaining constant over time, while a creep plot would lack any initial strain due to an applied stress. The SLS Model uses a Maxwell Model in parallel with a single spring, which provides an accurate representation for both stress relaxation and creep; however, the numerical connotation is inaccurate as these associated values are based on a single relaxation time. The Generalized Maxwell Model is similar to the SLS Model, with the exception that multiple Maxwell Models are used in parallel with a single spring. This model offers similar visual accounts in terms of the stress relaxation and creep plots, but with the use of multiple relaxation times, the numerical data is more reliable. Conclusively, the Generalized Maxwell Model is the most suitable constitutive relationship to model the stress relaxation in the DCCS Structure. A study examining the compressibility and relaxation of fibrous composites also determined the Generalized Maxwell Model to best model to characterize stress relaxation (Echaabi et al 851 – 854).

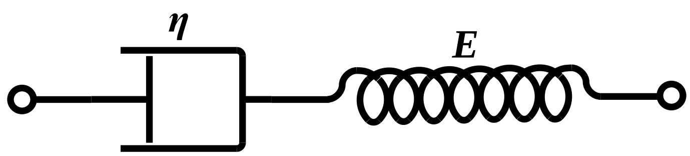

Schematic Representation

$$\sigma(t) = E\epsilon_0 e^{-\frac{E}{\eta}t}$$

Derived Equation for Stress Relaxation

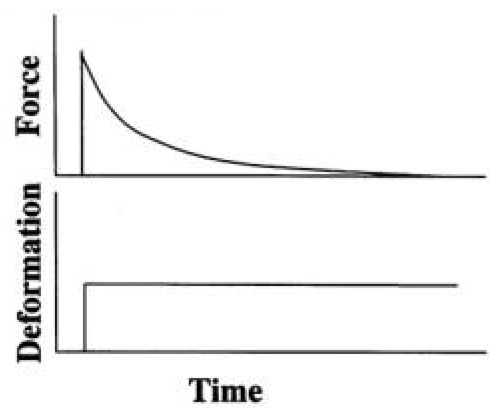

Force and Deformation Response of Maxwell Model

Figure 1.6: Constitutive Viscoelastic Models: Maxwell Model

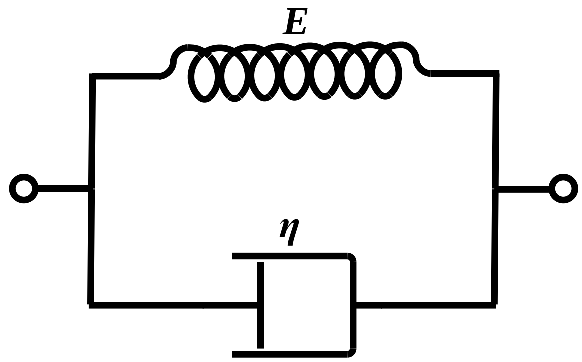

Schematic Representation

$$\sigma(t) = E\epsilon_0 + \eta\epsilon_0\delta(t)$$

Derived Equation for Stress Relaxation

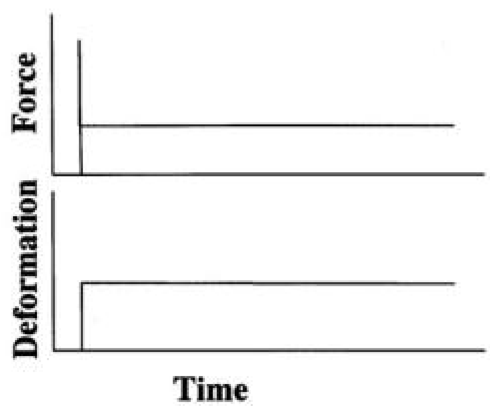

Force and Deformation Response of Kelvin-Voigt Model

Figure 1.7: Constitutive Viscoelastic Models: Kelvin-Voigt Model

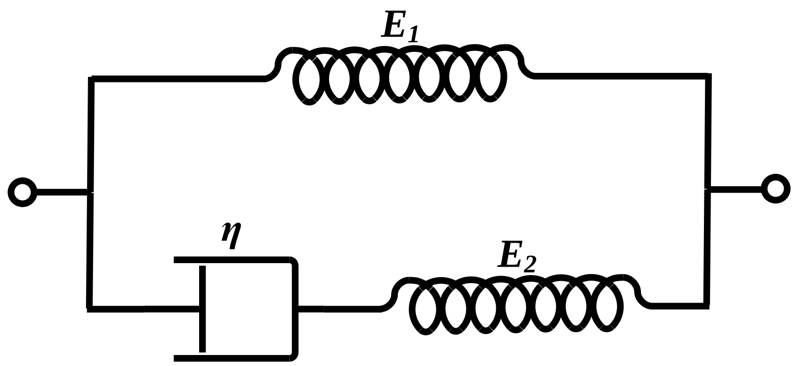

Schematic Representation

$$\sigma(t) = E_1\epsilon_0 + E_2\epsilon_0 e^{-\frac{E_2}{\eta}t}$$

Derived Equation for Stress Relaxation

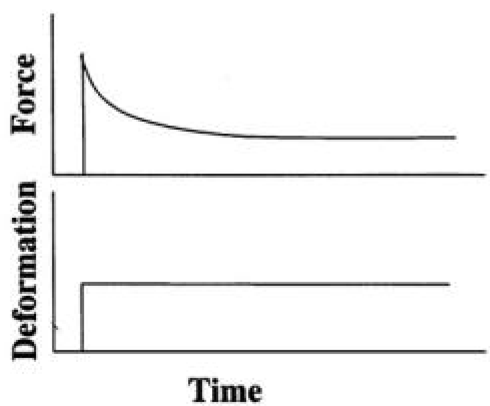

Force and Deformation Response of SLS Model

Figure 1.8: Constitutive Viscoelastic Models: Standard Linear Solid (SLS) Model

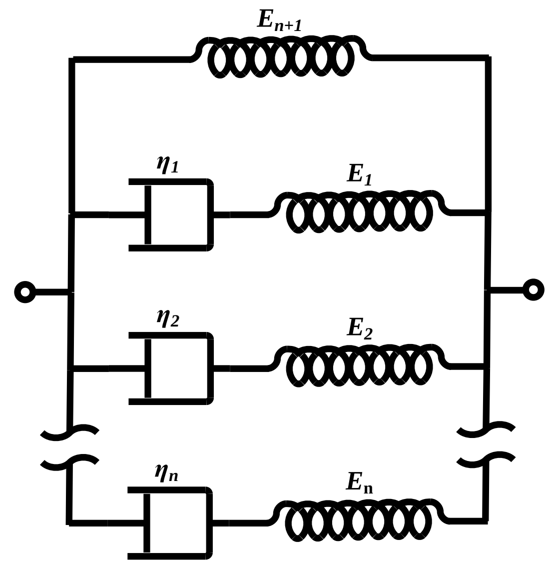

Schematic Representation

$$\sigma(t) = E_{n+1}\epsilon_0 + \sum_{j=1}^{n} E_j \epsilon_0 e^{-\frac{E_j}{\eta_j}t}$$

Derived Equation for Stress Relaxation

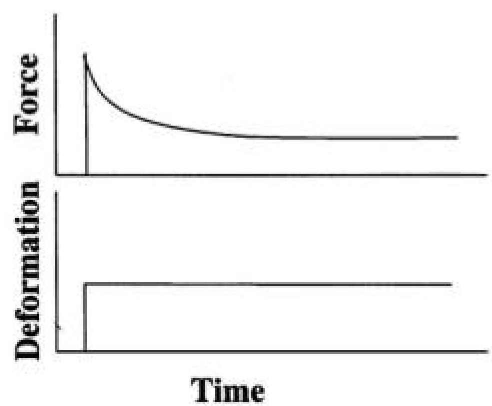

Force and Deformation Response of Generalized Maxwell Model

Figure 1.9: Constitutive Viscoelastic Models: Generalized Maxwell (Weichert) Model

The prototypical composite laminate is viscoelastic because it retains the elastic properties of the fiber reinforcing and the highly viscous properties of the matrix resin. The DCCS Structure is a bit more complicated, since it has several constituents working in series when compressed. The ceramic tile is assumed to be elastic and rigid, since it is the stiffest and strongest of the three main constituents and will have the least deformation. The composite face sheet and interlayer both have viscoelastic characteristics that contribute to stress relaxation, and need to be evaluated to determine the magnitude of each. It is important to first conduct a preliminary test to estimate the preload loss due to relaxation of the mechanical joint due to thread slip and bolt creep. A secondary test should incorporate the composite into the structural joint; since the relaxation of the mechanical joint has already been documented, the preload loss due to the viscoelastic nature of the composite is easily discernible. Thoppul et al performed the aforementioned testing procedure on a carbon/epoxy laminate, and concluded that approximately 3% of the initial preload was lost due to relaxation of the mechanical joint, a number that should remain consistent among mechanical joints. Several properties of a composite laminate factor into the amount of stress relaxation it may experience, including fiber-type, matrix-type, fiber volume fraction, void content, etc.; consequently, the relaxation of a carbon/epoxy laminate cannot be directly related to the DCCS Structure. Provided that the material properties are understood and quantified, ABAQUS finite element modeling can be used to predict the preload relaxation of composite joints given the assumption that the fibers are linear elastic, the matrix is linear viscoelastic, the laminate is specially orthotropic and transversely isotropic and the material does not change properties over time (Thoppul et al 1709 – 1729).

Other modeling techniques, including the aforementioned ABAQUS, can be implemented to predict and design bolted joints in composite laminates. Camanho et al successfully modeled composite joints to the extent of determining the elastic limit, the load at initial damage, the ultimate failure load, and the mode of failure. He utilized basic composite ply properties and a combination of the theory of elasticity and the Yamada-Sun failure criterion to simulate various joint configurations. His analytical calculations were found to be within 10% of the experimental results. Weidner et al used the Bolted Joint Stress Field Model (BJSFM) and ABAQUS to model the stress distribution around bolted joints in the DCCS Structure. This model will be updated in this study to include a clamping force to determine the change in stress distribution around the joint hole.

Much of the existing literature presented thus far has been applied to thin laminates. Due to the extreme complexity of the DCCS Structure, it is uncertain to what extent these reviews will directly apply to the current research. However, there are several issues that have been addressed and will provide beneficial throughout this study. Fabrication of the composite structure and machining of the individual specimens will be vital in ensuring that the structural integrity is maintained and accurate and reliable results are obtained. Research performed by Weidner et al will provide a baseline for this research including a joint geometry of e/D = 4.0 and w/D = 8.0 (using a 0.5 inch diameter bolt). Other properties of the joint, including washer size and the magnitude of torque will be established through testing and further research. Extensive testing will be performed to fully understand the viscoelastic nature of the DCCS Structure and its' constituents. The results obtained from this testing will ultimately influence the initial magnitude of torque. Static and fatigue testing will be implemented, along with appropriate damage evaluation techniques, to accurately determine the benefits and detriments of instituting a clamping force in bolted joints of the DCCS Structure.

1.2 Objectives

Discontinuous Ceramic Cored Sandwich (DCCS) Structures present a significant advancement in light-weight, armored protection for ground vehicles. Preliminary testing has revealed excellent strength and stiffness properties when subjected to transverse and in-plane loading conditions. This research will extend upon the existing research and focus on incorporating a joint within the DCCS Structure. Due to the complexity of the DCCS Structure and the arrangement of its constituents, the progression of failure and damage location is difficult to predict based on current literature. The majority of work to date focuses on understanding properties of composite laminates, and design methodologies for mechanical joints in composites. Designing a hybrid composite that introduces a discontinuous ceramic core, while important for mitigating damage and absorbing impact energy, causes structural concerns at the joint, concerns which have not yet been addressed in this prevailing field of composites. It is the objective of the current research to gain a better understanding of the performance of the joint in DCCS Structures when exposed to in-plane loading conditions. Testing will be done to examine the interaction of the DCCS Structure and the mechanical joint when fastened together. The viscoelastic nature of the face sheet and interlayer will cause inherent stress relaxation of the joint, a troubling factor affecting the longevity of the joint. Static testing will provide insight on the exact bearing response of the joint through its ultimate failure. Fatigue testing will replicate potential cyclic conditions caused by environmental phenomena. This analysis is an important aspect in the design of the joint, as fatigue often leads to reduced clamping forces in the joint, as well as progressive damage and diminished stiffness of the DCCS Structure.

This thesis will expand upon the all aspects of the aforementioned research topics. Chapter 2 will entail details concerning the materials comprising the DCCS Structure, including physical and directional properties of the constituents, the fabrication of the DCCS Structure using a Vacuum Assisted Resin Transfer Molding (VARTM) infusion process, and the different machining operations used to obtain appropriate specimen dimensions for testing. Test procedures for stress relaxation, static, and fatigue testing will be covered in Chapter 3. Multiple experimental set-ups are described in this Chapter for stress relaxation tests, and a test fixture inherited from research performed by Weidner et al will be utilized for static and fatigue testing. The addition of a clamp load at the joint is one of the significant variables within this research. Chapter 4 quantifies clamp load loss due to stress relaxation of the mechanical joint and viscoelastic constituents of the DCCS Structures. This Chapter will also include viscoelastic models of the face sheet, adhesive interlayer, and DCCS Structure to better predict load loss over time, and alternative methods to reduce the amount of load loss. Conducting different phases of static testing on the DCCS Structure will allow for disparities between test results to be easily attributed to the specific change in variable of the tests. These disparities will be discussed in detail in the Chapter 5, with a focus on the difference in pinned and clamped joints and the effect of varying torque levels on failure progression in the joint. Results from Chapter 5 will provide a baseline test matrix for fatigue testing explained in Chapter 6.

Fatigue testing will be performed to assess the sensitivity of the DCCS Structure to cyclic loads. Low level fatigue stresses are established based on the minimum load to cause first damage. They are tested to gauge the potential for damage or stiffness loss in the joint during fatigue and residual strength loss when exposed to higher loads after fatigue exposure. High level fatigue stresses are examined at loads exceeding first damage, to gain a better understanding of alternative failure modes due to fatigue. A collective analysis of the results will be documented in Chapter 7. This Chapter will also include recommendations for future work on the DCCS Structure, including dynamic impact loading and incorporating metallic inserts in the joint.

Chapter 2

MATERIALS, FABRICATION AND MACHINING

2.1 Materials

Discontinuous Ceramic Cored Sandwich (DCCS) Structures integrate composite materials with ceramic armor to create an effective, light-weight alternative to metallic armor. Each material comprised in the DCCS Structure serves a primary function, ultimately increasing the overall efficiency of the structure. The three main constituents of the DCCS Structure are the face sheet, adhesive interlayer, and discontinuous ceramic core. The structure is symmetric in the thru-thickness direction (having equivalent face sheet thicknesses). This simplifies the experimental process by allowing for definitive conclusions from experimental testing of the bolted joint. Once the materials are correctly oriented in the molding form, the part is infused with FCS-2 epoxy resin using a Vacuum Assisted Resin Transfer Molding (VARTM) process. After proper curing, the panels are carefully machined to the proper size for experimental testing.

The face sheet consists of multiple layers of fabric stacked in a prescribed orientation. The fabric is a 3Weave S-2 Glass 100 oz. ZZ fabric supplied by 3Tex Incorporated. This fabric features fibers interwoven in the x, y, and z direction. See Figure 2.1 for the 3Weave fiber structure. The addition of the fibers woven in the z direction provides additional “impact damage tolerance by suppressing delamination.” (3Tex Incorporated) Each layer of the 3-Weave fabric measures 0.12 inches (3.05

mm) thick, providing a face sheet consisting of two layers of fabric, a total thickness of 0.24 inches (6.10 mm).

Each of the two face sheet fabrics are infused with CCMFCS-2 resin, which is a mixture of SC-15 and SC-79 epoxy resins, both provided by Applied Poleramics, Inc. This particular blend, developed at the Center for Composite Materials, University of Delaware, combines the excellent toughness and strength properties of the SC-15 resin with the low-viscosity, long-processing properties of the SC-79 resin. Additionally, it increases the low glass-transition temperature (T_g) of the SC-15 to a suitable T_g for its' desired applications, while still being capable of VARTM process. (Wang et al 1 – 26) Extensive mechanical characterization has been performed on the 3Weave face sheet and the properties are listed in Table 2.1. (Gillespie et al 1 – 123)

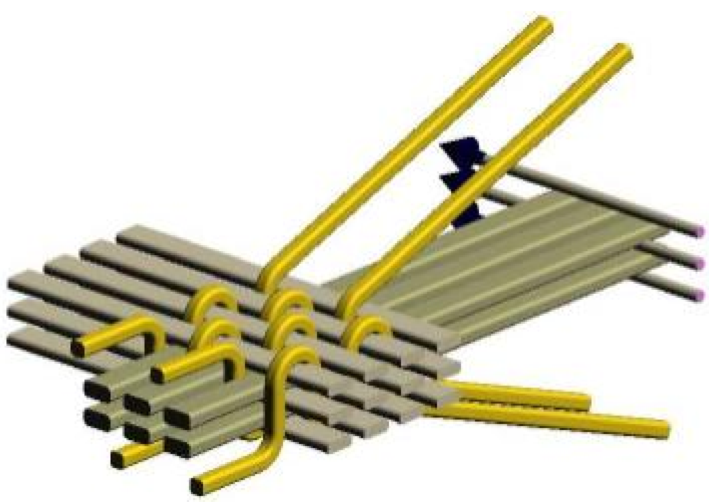

Figure 2.1: 3Tex 3Weave S-2 Glass 100 oz. ZZ Fabric weave fiber structure (3Tex Incorporated)

Table 2.1: Face Sheet Material Properties

Inplane		**Interlaminar**	
Tension		Tension	
E_1^T (Msi)	3.25	E_3^T (Msi)	1.70
E_2^T (Msi)	3.34	S_3^T (Ksi)	1.21
υ_{12}^T	0.11	ε_3^T (%)	0.07
υ_{21}^T	0.10	υ_{31}^T	0.13
X_1^T (Ksi)	69.6	υ_{32}^T	0.18
X_2^T (Ksi)	87.2		
ε_1^T (%)	2.56		
ε_2^T (%)	2.84		
Compression		Compression	
E_1^C (Msi)	3.66	E_3^C (Msi)	1.79
E_2^C (Msi)	4.19	S_3^C (ksi)	43.5
X_1^C (Ksi)	39.2	ε_3^C (%)	2.44
X_2^C (Ksi)	30.8	υ_{31}^C	0.19
ε_1^C (%)	1.02	υ_{32}^C	0.21
ε_2^C (%)	0.74		
Shear (1-2) (2 Rail)		V-Notch (1-3)	
G_{12} (Msi)	0.42	G_{13} (Msi)	0.43
S_{12} (Ksi)	5.47	S_{13} (Ksi)	5.03
γ_{12} (%)	4.89	γ_{13} (%)	>5.0
		V-Notch (2-3)	
		G_{23} (Msi)	0.44
		S_{23} (Ksi)	5.16
		γ_{23} (%)	4.58

1: Roll direction
2: Transverse to roll direction
3: Through thickness direction

The discontinuous tile core is made up of CoorsTek FG-995 Fine-Grain Alumina. The alumina material is part of a line of CeraShield Ceramic Armor Materials produced by CoorsTek. These materials are designed to have improved hardness and strength in ballistic performance, while maintaining a low weight-to-volume ratio. (CoorsTek Inc.) Incorporating these properties in the DCCS Structure proves beneficial in terms of dissipating energy upon dynamic impact. A single panel is comprised of thirty full-tiles measuring 4 inch by 4 inch by 0.4 inch thick (101.6 mm by 101.6 mm by 10.16 mm thick), and twelve half-tiles measuring 4 inch by 2 inch by 0.4 inch thick (101.6 mm by 50.8 mm by 10.16 mm thick).

An adhesive interlayer is used in bonding the face sheet and discontinuous ceramic core. Each interlayer is comprised of two 0.01 inch (0.254 mm) sheets of grade 8150 Surlyn thermoplastic resin supplied by DuPont, Inc. The stiffness and thickness of the surlyn controls the redistribution of loads between the face sheet and ceramic tiles; a stiffer, thinner interlayer allows greater load transfer while a less stiff, thicker interlayer prevents the load from being redistributed between the face sheet and tiles. Mechanical properties of the alumina tiles and adhesive interlayer are documented in Table 2.2.

Table 2.2: Mechanical Properties of Ceramic Tile and Interlayer

Property Description	Units	Ceramic Tile	Interlayer
Elastic Modulus	US	51.0 Msi	71.0 Ksi
	Metric	350 GPa	489 MPa
Tensile Strength, Ultimate	US	36.0 Ksi	4.50 Ksi
	Metric	248 MPa	31.0 MPa
Tensile Strain, Ultimate	US	N/A	320%
	Metric	N/A	320%
Tensile Yield Strength	US	N/A	2.70 Ksi
	Metric	N/A	18.6 MPa
Compressive Strength, Ultimate	US	363 Ksi	N/A
	Metric	2500 MPa	N/A
Poisson's Ratio	US	0.22	0.35
	Metric	0.22	0.35

Compositely, the three constituents each contribute particular material properties to collectively resist high impact forces. At the application of a dynamic load, the discontinuous tile core utilizes high energy absorption properties to dissipate the energy supplied from the impact. While the tiles may have strong compressive properties, they are extremely weak in tension and susceptible to cracking when loaded as a structure in static and fatigue. Alone, the tiles would experience catastrophic cracking and damage from a dynamic impact; however, in conjunction with the other constituents, the cracking is not as severe. The face sheet holds the ceramic tiles securely in place and the discontinuity of the tiles prevents the propagation of cracks to adjacent tiles. Additionally, the face sheet performs comparably in both tension and compression, and provides the sandwich structure with increased load capacity in both inplane and transverse loading. The adhesive layer, which bonds the ceramic core to the face sheet, is sufficiently compliant and tough to allow a marginal amount of the load to transfer to the tiles to prevent excessive damage in the core. Individually, the face sheet, ceramic core and adhesive interlayer have structural deficiencies, but together, they form an efficient and light-weight composite with extraordinary impact performance.

2.2 Fabrication Process

Fabricating composites is a science that takes time and precision to maintain consistency in production. The fabrication process is even more important for Discontinuous Ceramic Cored Sandwich (DCCS) Structures due to their unusually thick section. The thick section can lead to issues in the Vacuum Assisted Resin Transfer Molding (VARTM) process, particularly creating an air-tight vacuum with no leaks and excessive air void content in the final product. To maintain consistent panel fabrication and excellent quality, a strict and detailed process is outlined in traveler documentation. Use of a traveler to document fabrication is a method practiced on a regular basis at the Center for Composite Materials – University of Delaware. Each panel manufactured has its' own individual traveler, complete with a material/equipment list, dimensions and weights of materials, and step-by-step directions of the VARTM process. As the panel is prepared, the manufacturer initials the traveler, acknowledging each step was completed as stipulated. Every panel made thereafter will follow the same procedure, reducing variability between panels, and ideally creating panels with equivalent material properties.

Prior to beginning the fabrication and VARTM process, it is important that all materials and tools are prepared and ready for immediate use. This begins by cutting the necessary amount of material stated in the traveler, from any material rolls. For the face sheet, three plies of the 3Weave S-2 Glass 100 oz. ZZ fabric shall be cut at 24.25 inches by 24.25 inches (616.0 mm by 616.0 mm), and one wrap ply (bottom layer in the mold) shall be cut at 26 inches by 26 inches (660.4 mm by 660.4 mm), with 0.9 inch (22.86 mm) square notches cut in each corner. The excess fabric from this bottom wrap ply will be folded up around the edges of the panel to hold all the material layers together. Four pieces of 0.01 inch (0.254 mm) DuPont Grade 1601-2 Surlyn shall be cut with the dimensions of 24.25 inches by 24.25 inches (616.0 mm by 616.0 mm). Six tiles will be cut in half using a wet tile saw (seen in Figure 2.2), to produce twelve 4 inch by 2 inch by 0.4 inch thick tiles (101.6 mm by 50.8 mm by 10.16 mm thick). These will be used in conjunction with thirty full tiles, sized at 4 inch by 4 inch by 0.4 inch thick (101.6 mm by 101.6 mm by 10.16 mm thick), to produce the tile array seen in Figure 2.3. This particular array was chosen to maximize the number of individual testing specimens. (Specimens cut from the panel are aimed to avoid panel edges along the specimen length; panel edges consist of frayed fabric edges, meaning inconsistent and weaker properties of the composite structure as a whole.) After the thirty full tiles and twelve half tiles are accounted for, each tile is cleaned in an acetone bath to remove all residue and debris from the surface of the tile. They are then coated in glycidoxypropyltri-methoxysilane (a silane-based solution, known by the acronym GPS), a common coupling agent for ceramic surfaces. The tiles are air-dried and cured in the oven at 212 degrees Fahrenheit (100 degrees Celsius) for an hour. To guarantee a solid chemical bond between the tiles and adhesive interlayer, the panel must be laid-up and vacuum-bagged within 24 hours of GPS application, otherwise they must be re-coated. After cooling for several hours, spacers are applied to the edges of the tiles. The spacers, approximately 0.02 inches (0.508 mm) thick, serve the purpose of maintaining a consistent gap between tiles in the array. These gaps will be filled with resin during the VARTM process. Figure 2.4 shows a batch of tiles in their prepared state with the spacers applied.

In addition to the primary materials of the Discontinuous Ceramic Core Sandwich Structure, several other materials need to be prepared for the fabrication. A piece of distribution media, used to guide the resin throughout the mold during transfer, shall be cut at 24.4 inches by 60 inches (619.8 mm by 1524.0 mm). Each side of the distribution media shall be covered with two inch wide Flashbreaker I tape. The tape will keep the resin within the confines of the distribution media and prevent "running" along the mold edges. A piece of peel ply, also cut at 24.4 inches by 60 inches (619.8 mm by 1524.0 mm), is used as a barrier between the constituents of the panel and the remaining materials and mold, allowing for easier de-molding after cure. Other materials include: two pieces of 0.5 inch (12.7 mm) spiral tubing, 5 inches (127.0 mm) in length; one piece of breather strip, 2 inches by 5 inches (50.8 mm by 127.0 mm); two pieces of 0.5 inch (12.7 mm) tubing, approximately 6 feet (1.829 m) and 4 feet (1.219 m) long, respectively.

Before the materials are stacked sequentially in the mold, the mold frame and base plate shall be wiped down with acetone and applied with three coats of Freeman wax. The wax will prevent the resin from creating a strong adhesive bond with the mold and allow for easier separation between the mold and panel following the curing process. The waxed mold frame and base plate can be seen in Figure 2.5. After the wax is dry, the materials can be carefully stacked in the mold.

The actual fabrication process is crucial in obtaining quality panels that generate valuable results during testing. Routinely following the directions specified in the traveler will ideally prevent inconsistency in panels. Additionally, the stacking sequence and precision placement of the materials is important in assuring that the VARTM process is executed properly. First, the distribution media is placed at the bottom of the mold, with one end butted against the side rail, demonstrated in Figure 2.6. Next, the peel play is placed on top of the distribution media, with one end having two to three inches of overlap on the same end that the distribution media is butted against the side. The orientation of the peel ply is shown in Figure 2.7. Lay wrap ply over the peel ply such that the ply is centered in the mold. The sides of the ply should fold up along the side rails of the mold, with each side approximately the same height. This ensures the wrap ply is centered and the sides will hold the other layers centered and in place. A flat-edge scraper is used to work the corners of the wrap ply until they are completely square; this will allow the remaining materials to fit evenly inside the wrap ply. A second ply is placed over the wrap ply in the same fiber orientation (see Figure 2.8) and two sheets of the surlyn interlayer are stacked on top of the plies (see Figure 2.9). The tiles should be inserted in the mold according to the tile array and handled with latex gloves. Bare hands could leave oil or residue on the surface of the tiles, compromising the GPS solution and preventing a secure bond to the interlayer. The tile array in the mold frame is seen in Figure 2.10. The remaining two sheets of surlyn interlayer and two fabric plies are stacked on the ceramic tile core. The excess peel ply is folded back over the top layer of fabric, and the distribution media is done likewise. The extra distribution media is trimmed flush with the side rail and placed along the opposing side rail, on top of the existing distribution media. The caul plate is placed on top of the distribution media, providing a smooth surface for the top of the panel. On one side of the panel, there should be approximately two to three inches of excess peel ply; this will be folded over the top of the caul plate and serve as the vacuum side. On the opposite side of the panel, there should be the same amount of excess distribution media; this also should be folded on top of the caul plate and serve as the infusion side. This arrangement is shown in Figure 2.11, along with the breather strip and spiral tubing on the vacuum side, and the sole spiral tubing on the infusion side. The spiral tube has been stretched and taped in place to allow the resin to flow in-between the spiral openings in the tube. A resin infusion connector is centrally-placed over each of the spiral tubes, with the opening in the connector directly over a spiral opening. If the connector is not placed appropriately, the resin flow may be restricted, leading to incomplete infusion of the panel.

Using a large piece of vacuum bagging and tacky tape, a continuous bond is made between the edges of the vacuum bag and the base plate. Any air voids between the tacky tape, vacuum bag and base plate will compromise the VARTM process, preventing the strong vacuum force needed for the resin to pull through the mold. Once the entire vacuum bag has been securely attached to the base plate, as seen in Figure 2.12, a small hole is made slightly off-center in the vacuum bag, favoring the side of the vacuum. Using one piece of the regular tubing, feed one end of the tube through the hole in the vacuum bag and into the resin infusion connector, sealing the hole with tacky tape, and feed the other end into a vacuum bucket attached to a vacuum pump. As the air is being removed from the vacuum bag, the bag shall be adjusted and fitted to prevent bridging in female radii. Before the bag becomes too tight, a second hole is made near the infusion connector on the infusion side. The other piece of regular tubing is used in the same method as the first, with one end being fed through the hole in the bag into the infusion connector and sealed with tacky tape; however, the other end will be temporarily clamped off until the bag is leaked checked and ready to be infused. Clamping the end of the tube creates a closed vacuum, and the remaining air in the mold can be withdrawn. The vacuum pump is connected to a machine capable of measuring the leak rate of the system. After approximately five minutes, the leak rate may be checked to see if there are any significant leaks. Leak rates less than -0.02 Hg/min are negligible, and should not have an effect on the VARTM process. Any leak rates exceeding this value indicate potentially problematic leaks that must be corrected and sealed before the mold is infused. Figure 2.13 exhibits a successful bag without leaks.

A batch of CCMFCS-2 epoxy resin will be infused in the panel molding. This epoxy resin is a combination of SC-15 and SC-79 resins supplied by Applied Poleramics, Inc. (combined to form Part A), thoroughly mixed with a hardener (Part B) in a 100:37.5 resin-to-hardener (R:H) ratio by weight. Once the vacuum bag has stabilized and stopped pulling air from the mold, the clamped tubing can be placed in the resin bucket and unclamped, as seen in Figure 2.14. It is important that the end of the tube remain fully submerged in the resin while unclamping, otherwise air could enter the infusion line and fill the bag. After unclamping the infusion line, the vacuum will gradually pull the resin through the mold, guided by the distribution media, until it eventually reaches the vacuum line on the opposite side of the panel. At this time, the vacuum line may be partially clamped to prevent resin from entering the vacuum bucket.

The panel is required to cure in the mold at room temperature for 24-48 hours. Once the necessary cure time has elapsed, the vacuum and infusion lines are cut, vacuum bag removed, and the panel may be separated from the mold frame. After the distribution media and peel ply have been stripped from the panel (Figure 2.15), the panel shall be place in the oven for post-cure (Figure 2.16). The recipe for the post-cure cycle consists of a ramp time of one hour from room temperature to 300 degrees Fahrenheit (149 degrees Celsius); hold for eight hours at 300 degrees Fahrenheit (149 degrees Celsius); and a ramp time of one hour from 300 degrees Fahrenheit (149 degrees Celsius) to room temperature. The average panel dimensions attained have been center thicknesses of approximately 0.92 inches (23.37 mm) and width-to-length dimensions of 24.4 inches by 24.4 inches (619.8 mm by 619.8 mm).

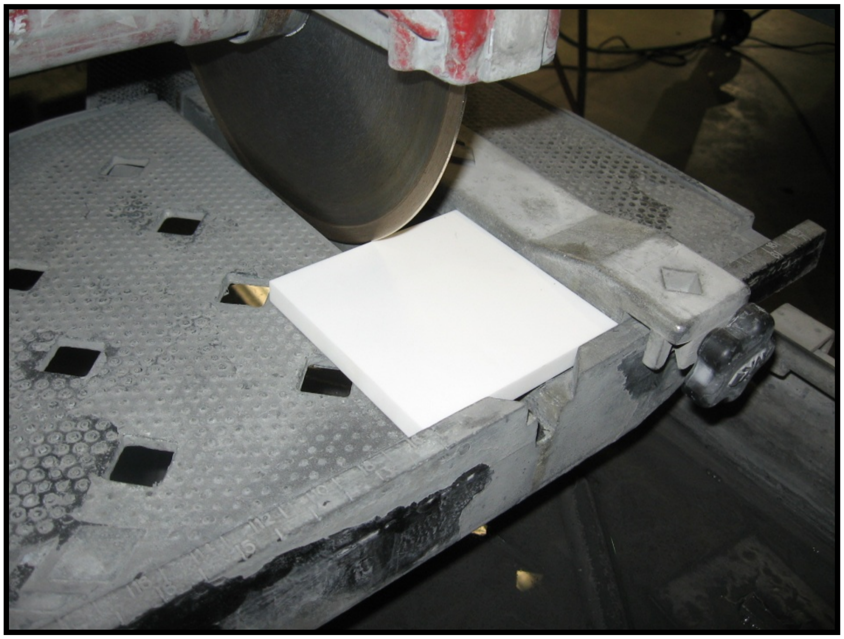

Figure 2.2: Cutting Half-Tiles using Wet Tile Saw

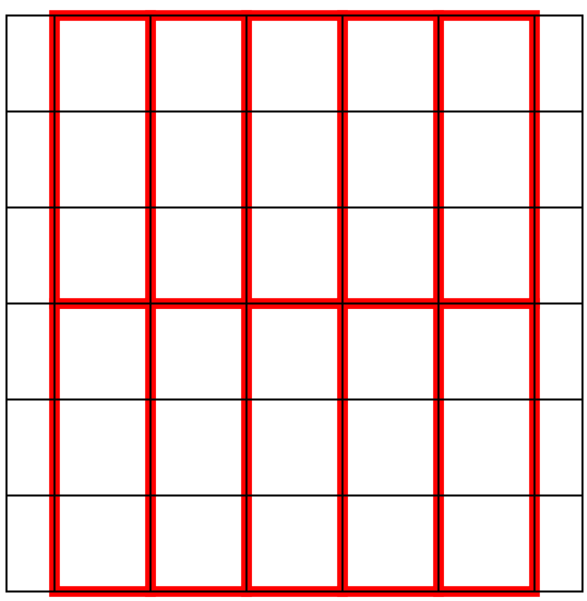

Figure 2.3: Tile Array (red lines denote individual testing specimens)

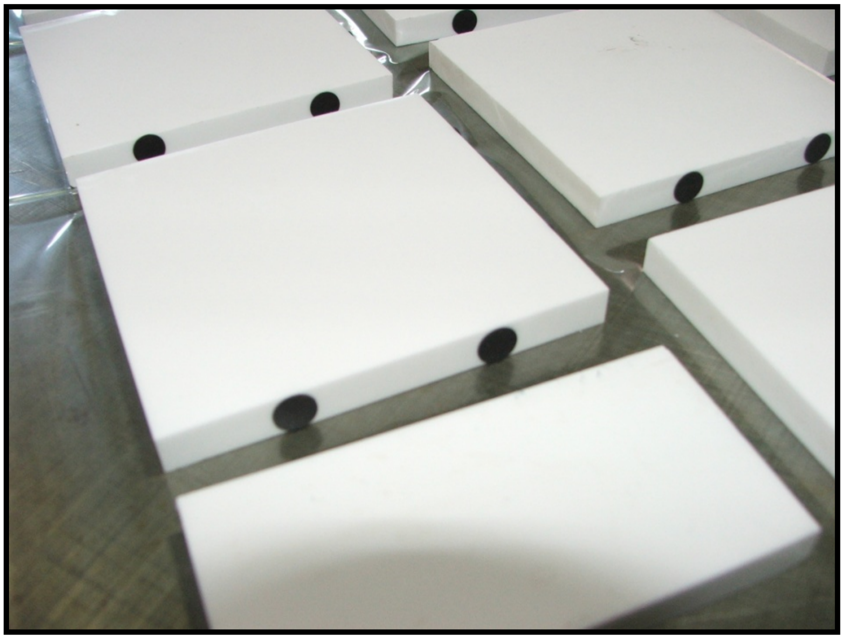

Figure 2.4: Ceramic Tiles with Spacers

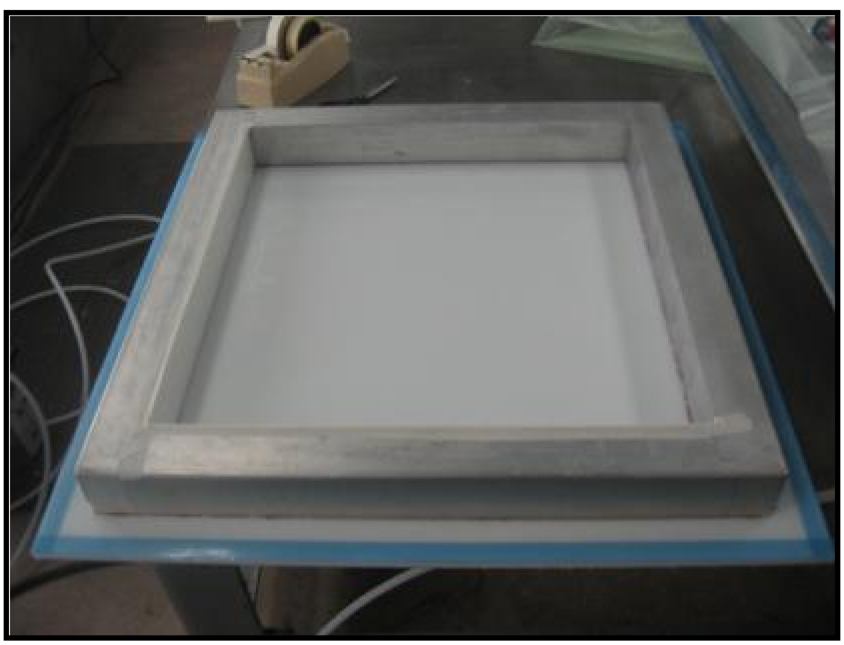

Figure 2.5: Mold Frame and Base Plate

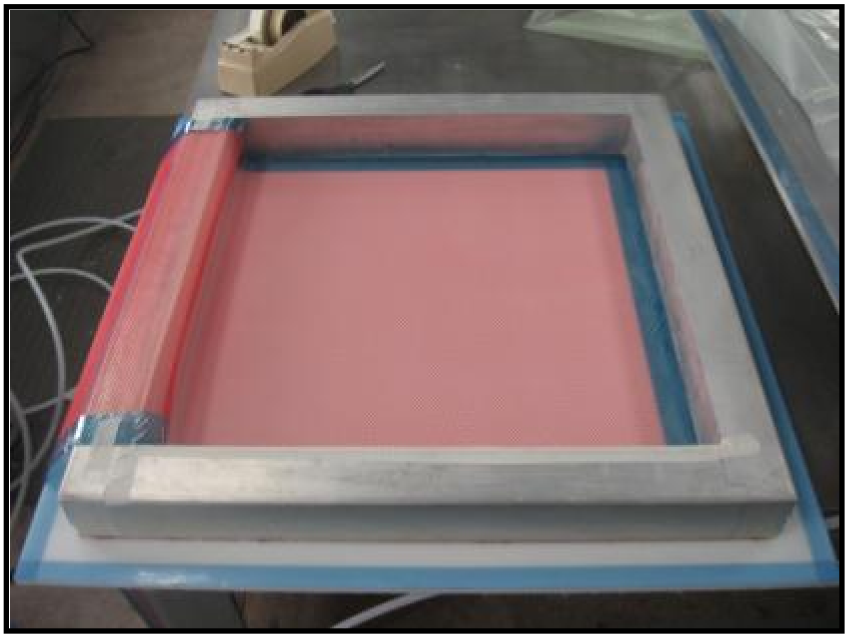

Figure 2.6: Placement of Distribution Media

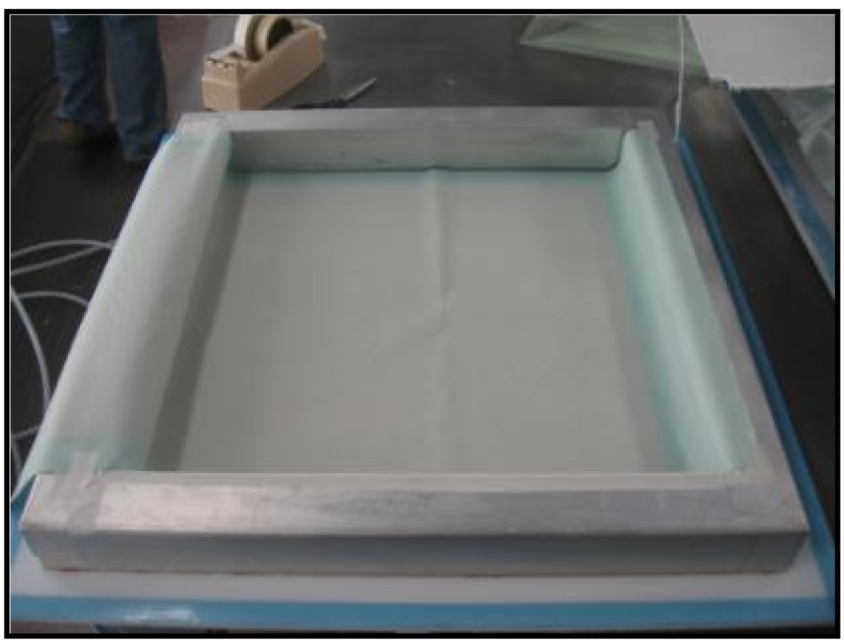

Figure 2.7: Placement of Peel Ply

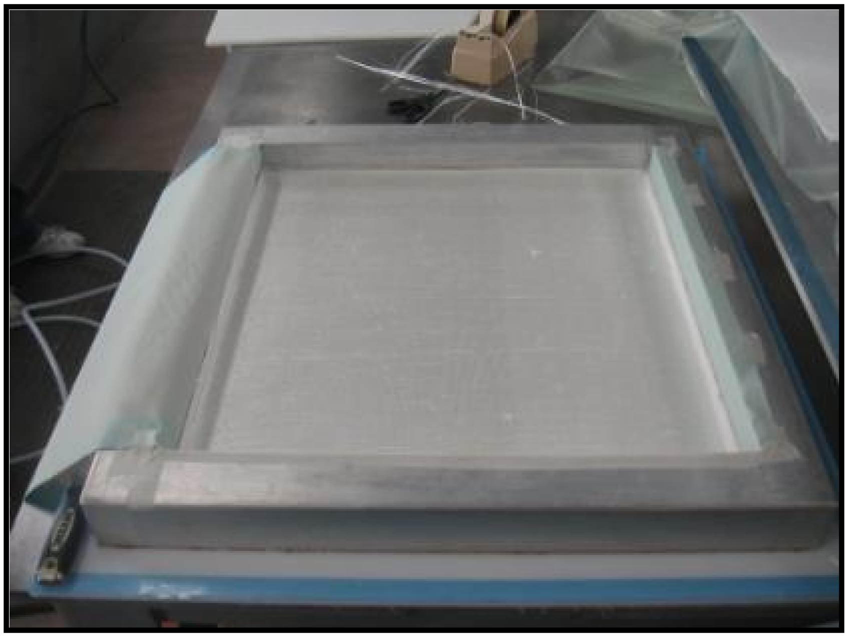

Figure 2.8: Placement of Wrap Ply and Second Fabric Ply

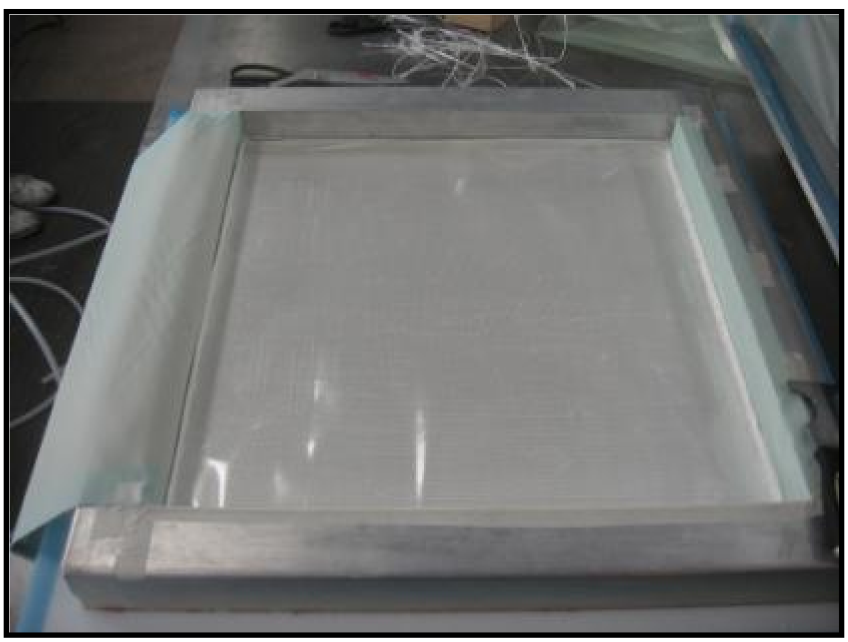

Figure 2.9: Placement of Surlyn Interlayer

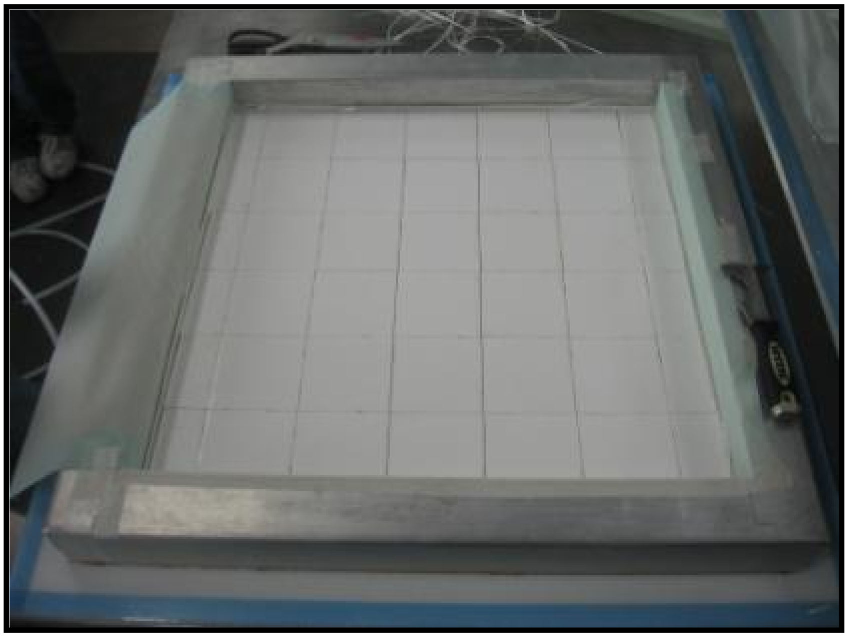

Figure 2.10: Align Tiles According to Tile Array

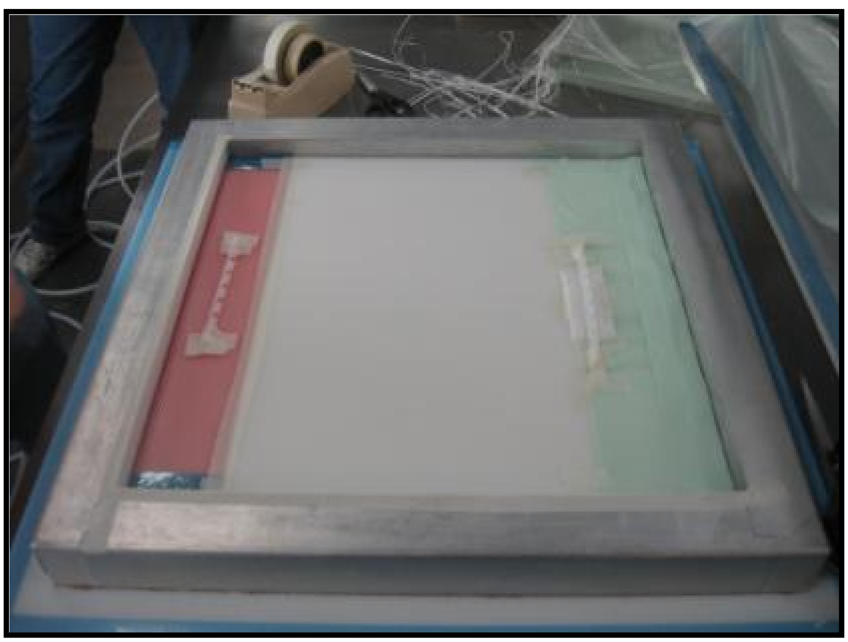

Figure 2.11: Placement of Remaining Surlyn and Fabric Plies, Caul Plate and Infusion Connectors

Figure 2.12: Placement of Vacuum Bag over Mold

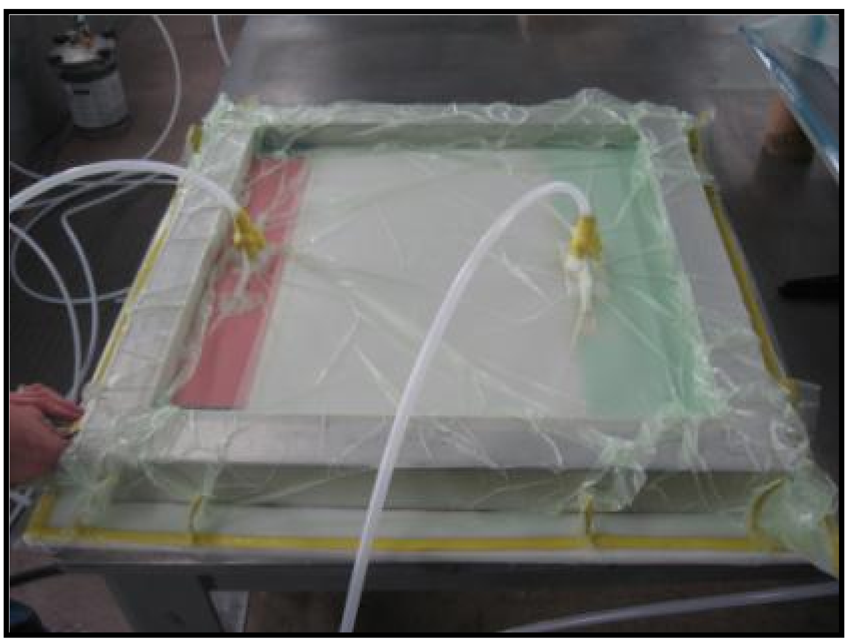

Figure 2.13: Remove Air from Vacuum Bag, Check for Leaks

Figure 2.14: Mix Resin and Allow to Transfer through Mold

Figure 2.15: Cure in Mold at Room-Temperature for 48 hours; De-Mold

Figure 2.16: Post-Cure in Oven at 300 degrees Fahrenheit for 8 hours

2.3 Machining Process

Machining composites is an arduous task that requires precision and patience. Careful consideration must be made to machining techniques in order to ensure pristine samples for testing. Improper machining can result in rough and frayed edges, cracked tiles, and delamination of the composite layers. These results can have a negative impact on experimental testing and produce misleading data. Thus, each step in the machining process is vital to maintaining consistent and flawless test specimens.

Machining materials to meet certain specification, such as composite glass face sheets and alumina ceramic tiles, can be difficult. To do so when the materials are joined compositely, as in the case of the DCCS Structure, is an even more challenging task. A speed-controlled, water-cooled table saw, equipped with a diamond-tipped circular blade, is used for cutting the panel into individual test specimens with nominal dimension of 12 inches by 4 inches (304.8 mm by 101.6 mm). (Figure 2.3 demonstrates the optimal cutting sequence of each panel to maximize the number of test specimens.) The blade should be examined prior to each cut to evaluate the condition of the diamond-encrusted edge. Poor blade quality can lead to increased cut time and potentially unsmooth cutting edges. The panel is placed on the table, where a laser projects the approximate cutting line of the saw. Once the panel is adjusted such that the laser correctly projects over the anticipated cutting surface, hydraulic clamps are engaged to hold the panel in place during the cut. The saw spindle should be vertically adjusted such that the blade cuts through the entire depth of the panel. When entering the cut, the carriage speed should be kept at a minimum. If the blade goes into the cut too fast, there is an increased chance that the specimen delaminates or the tiles crack near the saw entry. Through the duration of the cut, the blade amperage reading should be monitored and never display a reading greater than 5.0 amps. This would indicate that the blade is working too hard to cut through the DCCS Structure, and there is a greater likelihood that internal damage is occurring. Some forms of internal damage include overheating and burning of the constituents, tile cracking, and delamination. The solution to this problem is reducing the carriage speed until the amperage reading is at an acceptable level. (Figure 2.17 exhibits a cut in progress.)

After a test specimen has been machine-cut using the table saw, the hole must be drilled. For this, a water-cooled drill press with diamond-tipped core drill bit is used. The drill bit, as seen in Figure 2.18, specializes in drilling through hard, brittle materials like the ceramic tile. Like the saw blade used to cut the panel, the drill bit is diamond encrusted to provide a clean and precise cut through the DCCS Structure. The bit should be inspected periodically to verify that it is not damaged or mis-shaped in any form. Since the joint is the basis for this research, the hole must be perfectly circular with the smallest tolerance available. A damaged bit could cause for a slightly larger or oval-shaped hole, greatly affecting the experimental test. Also, it is important to avoid using dulled drill bits, as they generate more heat when drilling, which could cause burning of the materials or potentially delamination. Before drilling, the specimen should be correctly aligned to meet the anticipated e/D and w/D ratios, and clamped securely onto the drilling stand. Typically, a backing plate is placed under the specimen to prevent fraying near the edge of the hole when the bit emerges through the bottom face sheet. As the drill bit first penetrates the surface of the face sheet, very little pressure is required; only slow, gentle strokes are needed.

Applying too much pressure as the drill goes through the face sheet can cause overheating, which can be detrimental to the adhesive interlayer if not corrected. The adhesive interlayer is very sensitive to heat and is prone to burn and discolor if drilled incorrectly. This could ultimately lead to premature yielding or delamination of the adhesive interlayer. After cutting through the interlayer, there is a distinguishable sound once the drill bit contacts the ceramic core and the resistance increases significantly. At this time, the drill bit is dressed using an aluminum oxide stick to remove any residue left from the face sheet and adhesive interlayer. Drilling through the ceramic core is time-consuming and a little more pressure may be applied to expedite the process. As the drill approaches the second interlayer and face sheet, the pressure is reduced and the strokes become less frequent, in order to prevent burning through the interlayer. After the drill is complete, the interior of the hole should be examined for any discoloration or roughness. Either of these could be an indication of a damaged drill bit or an incorrectly drilled hole. The average surface diameter of the drilled hole is 0.504 inches (12.80 mm) with a tolerance of ±0.005 inches (0.127 mm). Holes with a substantially larger surface diameter may be a result of a dull drill bit. If the hole is within the given tolerance and shows no signs of discoloration or damage, then the hole was drilled correctly and the tools were functional. (Figure 2.19 demonstrates the use of a water-cooled drill press to machine holes in a specimen.)

For the specimen to be compatible with the experimental set-up, one end of the specimen must be machined to a width less than 0.84 inches (21.33 mm). This dimension is based on a grip clearance of 0.85 inches (21.59 mm). While one end of the specimen will be situated in the hydraulic grip, the other end will be attached at the pinned joint using a custom designed double-lap test fixture. Both the hydraulic grip and the test fixture will be attached to an Instron machine to conduct experiments. With the existing thickness of the specimen approximately 0.92 inches (23.37 mm), a milling machine is used to remove the necessary amount from each side to meet the width requirements. A surface mill blade was used to remove 0.005 inches (0.127 mm) of the face sheet at a time; each layer was tapered from the previous layer to prevent stress concentrations from forming due to immediate changes in thickness. An equal amount of face sheet was removed from the top and bottom to provide stability within the grip. (Figure 2.20 shows the end of a specimen being milled to meet thickness requirements.)

It is important to keep in mind that specimen with consistent dimensions and properties are easily comparable for experimental purposes. However, due to limitations within the machining process, the dimensions are expected to have a certain amount of variability. As previously discussed, the anticipated hole diameter was 0.5 inches (12.70 mm). Post-machined holes generated an actual average diameter of 0.504 inches (12.8 mm) with minimum and maximum diameters of 0.501 inches (12.72 mm) and 0.507 inches (12.88 mm), respectively. Two properties of the utmost concern are the e/D and w/D ratios. These ratios have a definitive impact on the ultimate capacity and failure modes of the individual specimens. For this reason, it is imperative that these ratios are consistently within a comparable range. The average edge distance was 2.001 inches (50.82 mm), only marginally greater than expected edge distance of 2.000 inches (50.80 mm). However, there was a larger discrepancy between the minimum and maximum edge distance than was truly desired. The minimum edge distance was measured at 1.932 inches (49.07 mm), while the maximum edge distance was measured at 2.063 inches (52.39 mm). The average specimen width was 3.937 inches (99.99 mm), considerably less than the anticipated 4.000 inches (101.6 mm). This difference can be attributed to the saw blade thickness of the water-cooled table saw during machining. Due to the imprecise nature of the laser-projected cutting line on the table saw, the minimum and maximum widths have some variability. The minimum specimen width was measured at 3.897 inches (98.97 inches) and the maximum specimen width was measured at 4.021 inches (102.1 mm). The last property of significant importance is centering of the machine-drilled hole. Although the hole was initially measured to be precisely on-center within each specimen, accurately lining the drill bit and the anticipated hole introduced the element of human error by visual confirmation. Consequently, the most accurate hole was 0.001 inches (0.025 mm) off-center, whereas the most in-accurate hole was 0.043 inches (1.092 mm) off-center. Figures 2.21 and 2.22 show the final machined specimen edge and hole diameter, respectively.

Fabricating and machining consistent samples are the first step in obtaining reliable and accurate results. Both processes adhere to strict guidelines that must be replicated in order to create samples with consistent properties and dimensions. However, to assure dependable data, this rigorous mentality must be continued through experimental testing. Like the fabrication and machining processes, certain procedures must be followed while testing to validate that the results are accurate.

Figure 2.17: Cut Panels on Wet Saw with Diamond-Tipped Blade

Figure 2.18: Diamond-Tipped Core Drill Bit

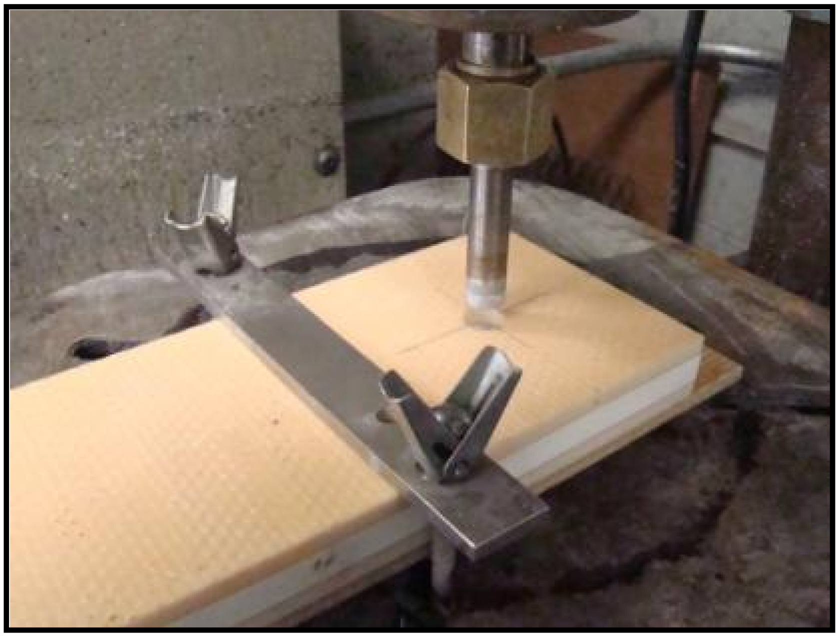

Figure 2.19: Drill Holes with Water-Cooled Drill Press

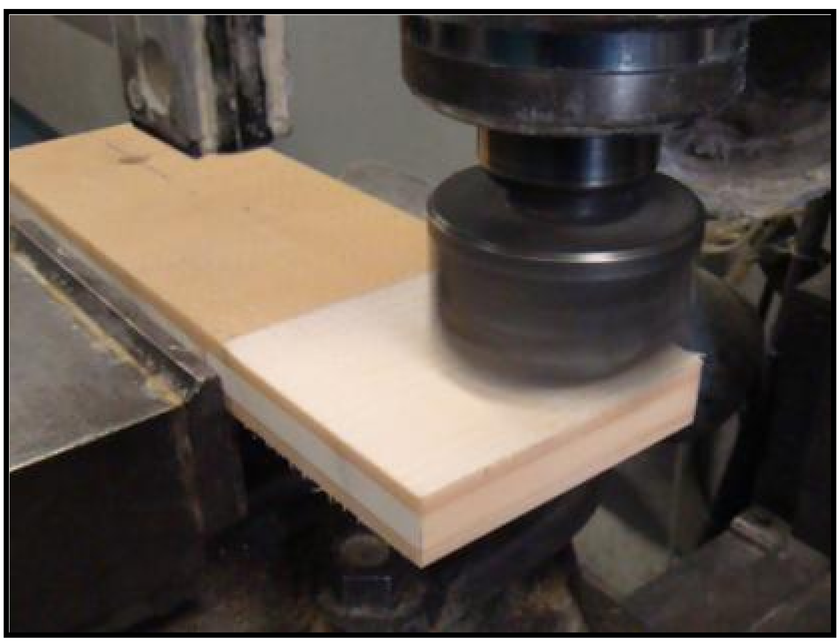

Figure 2.20: Refine Specimen Ends with Milling Machine

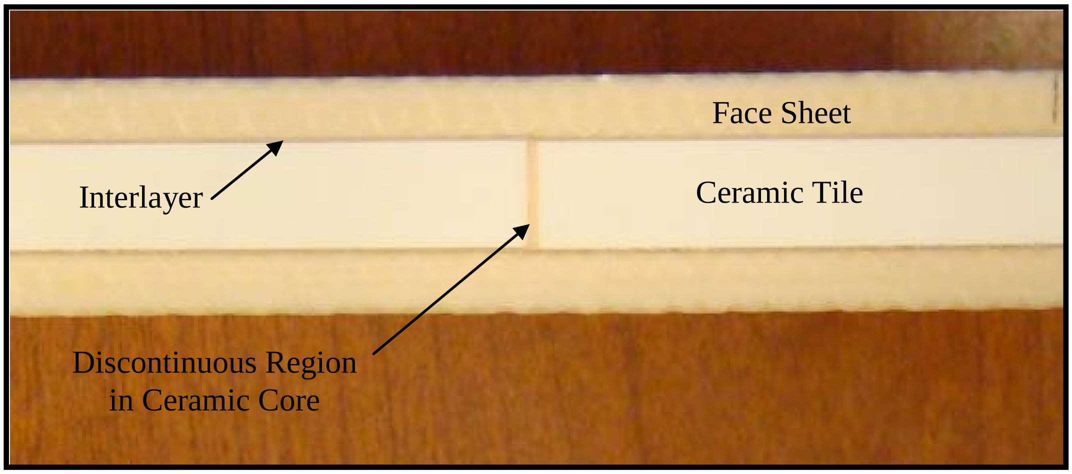

Figure 2.21: Machined Edge of Specimen

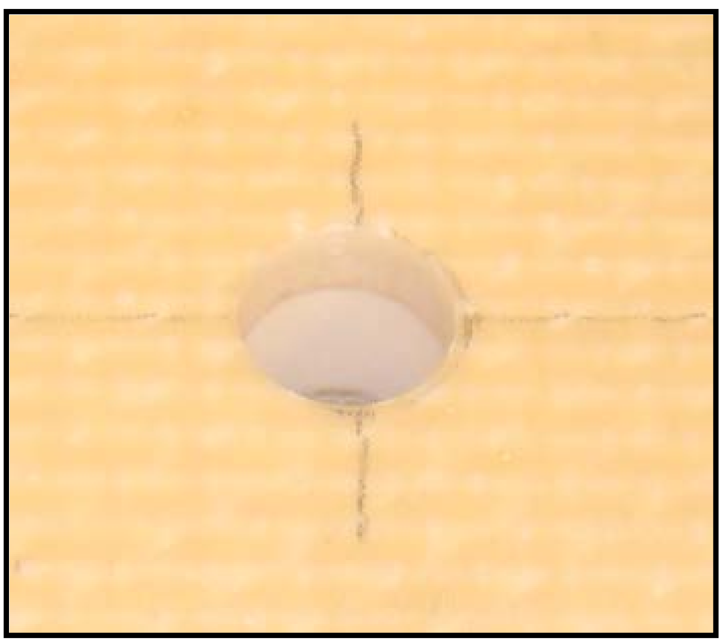

Figure 2.22: Machined Bolt Hole of Specimen

Chapter 3

TEST PROCEDURE

Several factors can affect the reproducibility and overall accuracy of experimental data. The first factor is fabricating composite panels with consistent material properties. The second factor is machining test specimens to the prescribed physical dimensions without compromising the material properties by introducing external defects. The last factor is producing consistent experimental arrangements and following rigid test procedures. If done collectively with appropriate precision, experimental data can be effectively compared and contrasted. Three primary test procedures were derived and utilized to test the DCCS Structure. A stress relaxation test will be performed on the DCCS Structure and its' constituents to determine their viscoelastic response under compression. This test will provide a better illustration of the clamp load at the joint following initial torque. Circular core samples with an average diameter of 0.447 inches (11.35 mm) will be used to conduct this experiment. Static and fatigue tests will consistent of specimens of the same geometry. Specimens will have nominal dimensions of 12 inches long by 4 inches wide (304.8 mm by 101.6 mm), with a 0.5 inch (12.70 mm) diameter hole placed 2 inches (50.79 mm) from the specimen edge. A Grade 8 bolt will be used for both testing procedures, however, the bolt diameters have some variation, as do the drilled holes. Bolt-hole clearance can have a significant effect on the joint strength (Hou et al. 1921 – 1938). Hou et al found that an increase in the bolt-hole clearance led to a decrease in the contact area and subsequently, high bearing stress and decreased joint strength. To minimize this problem, all bolt and hole diameters should be measured before testing to assure a tolerance of no more than 0.005 inches (0.127 mm). On average, hole diameters were 0.504 inches (12.80 mm) and bolt diameters were 0.499 inches (12.67 mm), establishing the tolerance criteria. For static tests, the testing procedure will remain consistent, with the only variable being the level of torque applied to the joint. Likewise, all fatigue tests will follow the same procedure, only the magnitude of applied load will change. Several short-hand notations were developed in the compilation of this report. Table 3.1 is a comprehensive list of the symbols and corresponding terms used throughout this document.

Table 3.1: Terms Used Throughout Document

Symbol	Definition
w	Width of Specimen
e	Edge Distance of Specimen
L	Length of Specimen
h	Thickness of Specimen
D	Diameter of Bolt Hole
w/D	‘Width-to-Diameter of Bolt Hole’ Ratio of Specimen
e/D	‘Edge Distance-to-Diameter of Bolt Hole’ Ratio of Specimen
h/D	‘Thickness-to-Diameter of Bolt Hole’ Ratio of Specimen
LVDT	Linear Variable Differential Transformers
DCCS	Discontinuous Ceramic Cored Sandwich
FS	Face Sheet
IL	Interlayer
CT	Ceramic Tile
BL	Baseline
SC	Static Compression
F	Fatigue Test
RS	Residual Strength Test
SR	Stress Relaxation Test
T	Torque

3.1 <u>Compressive Stress Relaxation Test</u>

Understanding the viscoelastic response of the DCCS Structure is important to quantifying the clamp load loss of a mechanically fastened joint. A significant relaxation of the DCCS Structure could potentially result in little to no clamp load, creating concern that the joint may eventually disassemble. Conducting compressive stress relaxation tests to simulate the load and pressure exerted by a torqued joint on the DCCS Structure could go a long way in determining the optimal torque level required for fastening panels to their desired application. Establishing a common test procedure for all compressive stress relaxation tests required special attention to detail. Viscoelastic properties are time-dependent by nature, thus a constant loading rate was important to allow for direct comparison. Deflections encountered in this experiment are very small considering the thickness of the individual constituents and DCCS Structure; consequently, short-stroke linear variable differential transformers (LVDT) were used to measure displacements. Other than the specimen material, the only other variable during the testing process was the initial stress and strain applied to the specimen. Changing the initial stress and strain, then normalizing the acquired data, allowed for direct comparison between tests and provided the opportunity to separate linear and non-linear viscoelastic regions of the different materials. The remaining characteristics of the test procedure were held constant through each test, as minor variations could result in significant inaccuracies of the data.

For help establishing a set procedure for compression testing, ASTM Standard E328-02 “Standard Test Methods for Stress Relaxation for Materials and Structures” was used as a guideline. Performing a stress relaxation test requires very controlled settings. Viscoelastic materials have temperature-dependent properties, thus testing must be done in an environment with non-extreme, constant temperatures. The apparatus designated for testing must have a sturdy base and frame, and independent from its surroundings in order to prevent vibrations from impacting a test in progress. The bearing surfaces which compress the specimen must be parallel and smooth, to ensure an even distribution of stress through the specimen. Specimens should be machined to constant and consistent dimensions. The core specimens used in this research were extracted from the diamond-tipped drill bit used in machining holes for the static and fatigue test specimens. Despite the use of a 0.5 inch (12.70 mm) diameter drill bit, the core specimens were actually 0.447 inches (11.35 mm) in diameter. This discrepancy does not make a difference in the overall testing procedure; however, the applied loads must be calculated based on the expected initial stress and the surface area of the core specimen.

Calculating the applied load for the compression test is more than a single conversion or calculation. It consists of several conversions and assumptions that must be defined. The basic concept of these calculations is to determine the load that must be applied to a 0.447 inch (11.35 mm) diameter specimen, such that it receives the same stress as the DCCS Structure would experience at the joint due to an applied torque. Given a magnitude of torque, the equivalent clamp load must be determined. This is done by dividing the magnitude of torque by the product of the torque coefficient and the nominal diameter of the bolt (the torque coefficient is a function of thread geometry and the coefficient of friction between the bolt and fastener; it is taken as 0.2 for these purposes). The clamp load is the axial load acting through the length of the bolt, which is ultimately transferred through the bearing washers into the

DCCS Structure. The washers used for all experimental testing are typical galvanized steel washers, with an inner diameter of 0.5625 inches (14.28 mm) and an outer diameter of 1.375 inches (34.91 mm). Assuming that the washer remains rigid when the clamp load is applied, the pressure applied from the washer face to the DCCS Structure is simply the clamp load divided by the surface area of the washer. This value is the initial stress that the specimen will achieve for compression testing. The actual load that needs to be programmed into the testing apparatus is the initial stress or pressure just calculated, multiplied by the area of the test specimen, 0.1569 in^2 (101.2 mm^2). A complete test matrix for the compressive stress relaxation tests can be viewed in Table 3.2, which includes torque levels, clamp loads, and initial stresses. A particular specimen naming sequence was adopted to represent the characteristics of each individual test. The first label signifies the testing material, primarily FS for Face Sheet and DCCS for Discontinuous Ceramic Cored Sandwich. The second label signifies the type of test, SR for Stress Relaxation, and the level of torque, T90 for 90 ft-lbs (122.0 N-m) of torque.

Table 3.2: Test Matrix for Compressive Stress Relaxation Tests of Face Sheet and DCCS Structure

Sample #	Testing Material	Magnitude of Torque	Equivalent Clamp Load	Equivalent Stress on Specimen
FS-SRT36	Face Sheet	36 ft-lbs	4320 lbs	3495 psi
		48.8 N-m	19216 N	24.10 MPa
FS-SRT54	Face Sheet	54 ft-lbs	6480 lbs	5242 psi
		73.2 N-m	28824 N	36.14 MPa
FS-SRT72	Face Sheet	72 ft-lbs	8640 lbs	6989 psi
		97.6 N-m	38433 N	48.19 MPa
FS-SRT90	Face Sheet	90 ft-lbs	10800 lbs	8735 psi
		122.0 N-m	48041 N	60.23 MPa
DCCS-SRT36	DCCS Structure	36 ft-lbs	4320 lbs	3495 psi
		48.8 N-m	19216 N	24.10 MPa
DCCS-SRT54	DCCS Structure	54 ft-lbs	6480 lbs	5242 psi
		73.2 N-m	28824 N	36.14 MPa
DCCS-SRT72	DCCS Structure	72 ft-lbs	8640 lbs	6989 psi
		97.6 N-m	38433 N	48.19 MPa
DCCS-SRT90	DCCS Structure	90 ft-lbs	10800 lbs	8735 psi
		122.0 N-m	48041 N	60.23 MPa

When it comes to the actual test, ASTM E328-02 presents two different loading methods that can be performed to reach the initial stress. The first is applying a constant displacement, or strain rate, to the specimen. As seen in Figure 3.1, for a constant strain rate, the application of stress can tend to decrease at higher strains once a certain elastic strength has been exceeded. The second method loading is performed by applying a constant force, or stress, to the specimen. Figure 3.1 shows that in this application, the strain may rapidly increase if the aforementioned elastic strength is exceeded. This method could potentially be dangerous if the specimen were to unexpectedly fail or yield prior to the initial stress. Consequently, a constant strain-rate was selected as the appropriate loading procedure. It is important that a high strain rate is applied to simulate an instantaneous stress and strain; the viscoelastic constituents of the DCCS Structure begin to lose stress during the loading process, which cannot be quantified without extensive mechanical testing. By instituting an instantaneous strain, marginal stress is lost during the loading process. A loading rate of 1.0 inch/minute (25.4 mm/min) was chosen to meet these criteria. Once the initial stress level is achieved, the loading will immediately stop at the current strain and maintain that strain for the duration of the relaxation period.

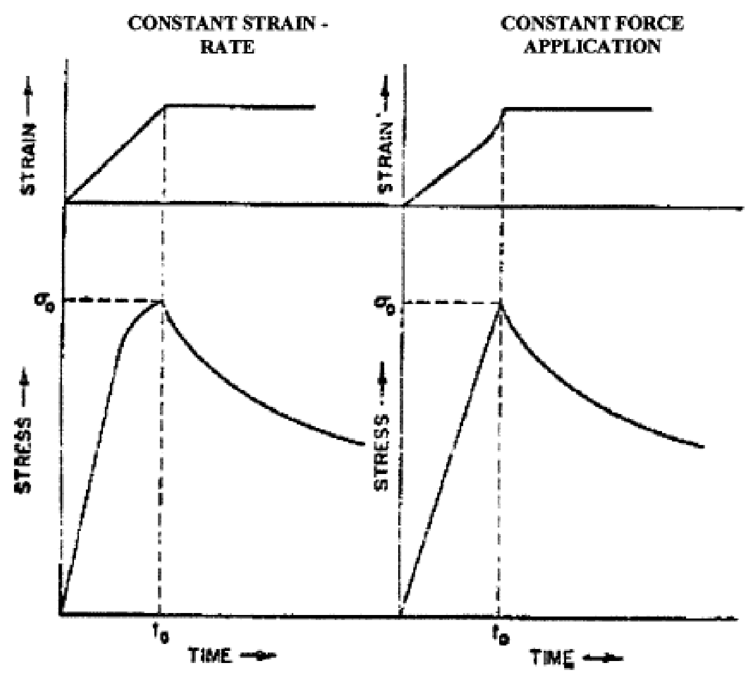

Figure 3.1: Loading Methods for Stress Relaxation Test (ASTM E328-02)

Special attention should be made during the loading process to assure no damage occurred to the specimen. Repeated damage at a given stress would give the indication that the equivalent torque level exceeds the compressive strength capacity of the DCCS Structure. Viewing a stress-strain plot of the loading process would provide assurance whether damage has occurred. The majority of stress loss occurs within seconds following the instantaneous strain. In order to attain this essential information, a data acquisition rate of 100 records per second is used to capture the stress loss in each specimen. After multiple initial stress levels have been tested, the results can be normalized and compared. If the relaxation curves are similar, this indicates the initial stress levels are within the linear viscoelastic region. Relaxation curves that significantly vary with higher stresses indicate a non-linear viscoelastic response. This property is crucial when modeling the relaxation behavior of the DCCS Structure.

A second stress relaxation experiment will incorporate the mechanical joint. Using the knowledge gained from the previous experiment, an educated guess can be fielded on the amount of stress loss in the joint. However, this experimental procedure is more complicated with slightly more uncertainty. A washer load cell from Futek Advanced Sensor Technology, Inc. will be used in conjunction with the mechanical joint to measure the clamp load. It is important that the sensors on either side of the load cell are positioned against rigid surfaces in order to obtain accurate readings. The joint will be loaded with a torque wrench, the actual method of tightening the joint. However, this approach prevents an instantaneous strain from being applied; instead, tightening the joint may take several seconds, in which some of the stress has begun to dissipate. While this unaccounted loss may be significant, it is assumed that the loss determined in the previous experiment will translate directly to this experiment. The primary purpose of this experiment is to investigate the losses in the mechanical joint due to thread slippage, embedment relaxation, creep, etc. To do this, the experiment is first conducted on an elastic material, such as steel, which does not exhibit viscous characteristics and experience relaxation. This will isolate the relaxation of the mechanical joint. Then, the experiment will be performed on the DCCS Structure. The two experiments can be compared to determine the contribution of relaxation of the mechanical joint and the viscoelastic properties of the DCCS Structure. Lastly, different techniques to eliminate the relaxation of the mechanical joint will be investigated. Reducing stress relaxation and optimizing the level of torque are important for ensuring the stability of the joint during static and fatigue loading.

3.2 <u>Static Test</u>

Static tests are useful in understanding the strength limits and stiffness properties of the joint in the Face Sheet and DCCS Structure. Weidner et al examined the effect of width-to-diameter and edge distance-to-diameter ratios of the DCCS Structure through static testing. Those findings will be applied to the current static testing and remain constant through all tests. In addition to specimen geometry, loading rates, bolt diameter and methods for measuring displacement remain constant for all static tests. This research will focus on the effect of different face sheet materials and varying levels of torque on the strength and stiffness of the joint.

For help establishing a set procedure for static testing, ASTM Standard D 5961/D 5981-M-05 “Standard Test Methods for Bearing Response of Polymer Matrix

Composite Laminates" was used as a guideline. The standard provides two different fixtures to test composites joints subjected to tension or bearing forces. A single-lap joint test fixture consists of a single fixture plate bolted to the test specimen and pulled in opposite directions. A double-lap joint test fixture consists of two fixture plates situated adjacently with the test specimen bolted between the plates. The latter was the chosen as the most effective fixture design for this study. A custom-designed double-lap fixture was fabricated to meet the geometric requirements of the Face Sheet and DCCS Structure. The test fixture is designed to meet thickness dimensions of 0.24 inches (6.09 mm) for the composite face sheet and 0.92 inches (23.37 mm) for the DCCS Structure. Also, the test fixture should accommodate test specimens with nominal dimensions of 12 inches long by 4 inches wide (304.8 mm by 101.6 mm), with a 0.5 inch (12.70 mm) diameter hole placed 2 inches (50.79 mm) from the specimen edge. In addition to the primary test fixture, LVDT's are independently attached to the test specimen at the joint to gain isolated data on the extension of the joint during loading. A complete test matrix for the static tests can be viewed in Table 3.3, which includes specimen geometries and torque levels. A naming sequence, similar to the one used for stress relaxation testing, was adopted to represent the characteristics of each individual test. The first label signifies the testing material, primarily FS for Face Sheet and DCCS for Discontinuous Ceramic Cored Sandwich. The second label signifies the geometric properties of the test, W4 for a specimen width of 4 inches (101.6 mm) and E2 for an edge distance of 2 inches (50.79 mm), and the level of torque, T90 for 90 ft-lbs (122.0 N-m) of torque.

Table 3.3: Test Matrix for Static Tests of DCCS Structure

Sample #	Testing Material	Width	Edge Distance	Magnitude of Torque
DCCS-W4E2T0	DCCS Structure	4 inches	2 inches	0 ft-lbs
		101.6 mm	50.79 mm	0 N-m
DCCS-W4E2T10	DCCS Structure	4 inches	2 inches	10 ft-lbs
		101.6 mm	50.79 mm	13.6 N-m
DCCS-W4E2T30	DCCS Structure	4 inches	2 inches	30 ft-lbs
		101.6 mm	50.79 mm	40.7 N-m
DCCS-W4E2T50	DCCS Structure	4 inches	2 inches	50 ft-lbs
		101.6 mm	50.79 mm	67.8 N-m
DCCS-W4E2T70	DCCS Structure	4 inches	2 inches	70 ft-lbs
		101.6 mm	50.79 mm	94.9 N-m
DCCS-W4E2T90	DCCS Structure	4 inches	2 inches	90 ft-lbs
		101.6 mm	50.79 mm	122.0 N-m
DCCS-W4E2T110	DCCS Structure	4 inches	2 inches	110 ft-lbs
		101.6 mm	50.79 mm	149.1 N-m

All static tests were conducted at a loading rate of 0.01 inch/min (0.254 mm/min). This particular rate was chosen for several reasons. First, it is known that the loading rate can affect the response of viscoelastic materials; reducing the loading rate negates the effects of the rate-dependent material properties. Second, increasing the duration of the test allows for ample time to inspect and document the progression of failure of the specimen. Lastly, due to the brittle nature of the ceramic tile, small deformations are expected before failure of the ceramic occurs. By maintaining a low rate of loading and extending the period of failure, this failure can be characterized much easier. During the test, a blue dye was applied to the specimen to identify cracks within the tile and at the tile gaps. Visible damage and acoustic emissions were recorded in a certified lab notebook, which documented the progression of failure, the loads at which failures occurred, and their location on the specimen. By performing consistent experimental tests, this information can be directly compared from one test to another. Understanding the progression of failure in a baseline test is the foundation to being able to predict the outcome of static failures with varying torque levels and face sheet materials.

3.3 <u>Fatigue Test</u>

In any environmental surrounding, there is potential for fatigue loading. In the case of the DCCS Structure, the mismatch of coefficient of thermal expansion between constituents could result in fatigue loading. Other potential sources of fatigue include vehicle vibrations, travel on uneven terrain, or intense weather conditions. It is important to understand the influence of fatigue, as it most commonly results in a loss of stiffness and strength. This becomes even more significant in areas of high stress, including joints. This research will include low- and high-level fatigue testing and examine their influence on the residual strength of the DCCS Structure.

For help establishing a set procedure for fatigue testing, ASTM Standard D 6873-03 “Standard Practice for Bearing Fatigue Response of Polymer Matrix Composite Laminates” was used as a guideline. Research performed by Weidner et al preceded the current research, thus Weidner’s documented experimental testing procedures were taken into consideration. The double lap test fixture used for static testing will be utilized for all fatigue testing. All specimen geometries maintain a width-to-diameter ratio of 8.0 and an edge distance-to-diameter ratio of 4.0, with nominal dimensions of 12 inches long by 4 inches wide (304.8 mm by 101.6 mm). The standard offers three possible methods of fatiguing a specimen: compression-compression, tension-tension, or tension-compression. This research examines tension-tension fatigue only; this corresponds with prior static testing that was performed only in the tensile direction to identify bearing response and tensile failure.

Fatigue stress levels were derived from strength limits determined in static testing. Low-level fatigue testing consisted of maximum loads prior to first damage. The highest stress level, Stress Level 5, was relative to the first net tension crack observed in the ceramic tile. The average load that caused first crack was 4252 lbs (18910 N), with a standard deviation of 740 lbs (3290 N). The minimum load to cause cracking occurred at approximately 3750 lbs (16680 N). Stress Level 5 was taken as 90% of the minimum first damage, and was verified to be at least one standard deviation outside the mean. The remaining stress levels were established based on a given percentage of Stress Level 5. The loads and bearing stresses for each low-level fatigue stress are listed in Table 3.4.

Table 3.4: Loads and Bearing Stresses for Low-Level Fatigue Tests

	Maximum Load		Minimum Load		Percent of 3400 lbs
Stress Level 1	680 lbs	1478 psi	68 lbs	148 psi	20
	3024 N	10.19 MPa	302.4 N	1.019 MPa	
Stress Level 2	1360 lbs	2956 psi	136 lbs	296 psi	40
	6050 N	20.38 MPa	605.0 N	2.038 MPa	
Stress Level 3	2040 lbs	4435 psi	204 lbs	444 psi	60
	9074 N	30.58 MPa	907.4 N	3.058 MPa	
Stress Level 4	2720 lbs	5913 psi	272 lbs	591 psi	80
	12099 N	40.77 MPa	1209.9 N	4.077 MPa	
Stress Level 5	3400 lbs	7391 psi	340 lbs	739 psi	100
	15123 N	50.96 MPa	1512.3 N	5.096 MPa	

High-level fatigue testing was performed to examine the influence of cyclic loading at loads exceeding the initial cracking stages. The stress levels were determined in a similar manner to those of low-level fatigue testing. Stress Level 5 was based on the ultimate static capacity of the specimen. This failure mode was typically a combination of delamination between the face sheet and tile, and bending/ shear/tearout fracture of the ceramic core. Failure occurred at an average load of 32281 lbs (143590 N), with a standard deviation of 1010 lbs (4490 N). The minimum load to cause failure occurred at approximately 28330 lbs (126020 N). Stress Level 5 was taken as 90% of the minimum load to cause failure, and was verified to be at least one standard deviation outside the mean. Stress Levels 1 through 4 were determined as incrementally proportionate to Stress Level 5. The loads and bearing stresses for each high-level fatigue stress are listed in Table 3.5.

Table 3.5: Loads and Bearing Stresses for High-Level Fatigue Tests

	Maximum Load		Minimum Load		Percent of 25600 lbs
Stress Level 1	5120 lbs	11130 psi	512 lbs	1113 psi	20
	22775 N	76.74 MPa	2277.5 N	7.674 MPa	
Stress Level 2	10240 lbs	22261 psi	1024 lbs	2226 psi	40
	45550 N	153.5 MPa	4555.0 N	15.35 MPa	
Stress Level 3	15360 lbs	33391 psi	1536 lbs	3339 psi	60
	68325 N	230.2 MPa	6832.5 N	23.02 MPa	
Stress Level 4	20480 lbs	44522 psi	2048 lbs	4452 psi	80
	91100 N	307.0 MPa	9110.0 N	30.70 MPa	
Stress Level 5	25600 lbs	55652 psi	2560 lbs	5565 psi	100
	113874 N	383.7 MPa	11387.4 N	38.37 MPa	

To maintain consistency with research conducted by Weidner et al, an R value (ratio of minimum load to maximum load) of 0.1 was used. Table 3.4 and Table 3.5 show the minimum and maximum values for each stress level meet the R value criterion. Prior to each test, the specimen was loaded to the maximum load at a minimal loading rate. Initial stiffness data was recorded from this first loading cycle and blue dye was used to highlight any initial damage to the specimen. It is important to document what damage occurs during the static loading, in order to distinguish further damage caused by fatigue cycling. For low-level fatigue testing, where damage is not typically visible, tests are paused periodically to perform load-unload sequences for a better indication of the stiffness properties of the specimen. During actual fatigue testing, tracking data should be captured intermittently to verify a proper sinusoidal wave is produced during cyclic loading. Figures 3.2, 3.3 and 3.4 demonstrate accurate and smooth cyclic outputs for frequencies of three, two and one Hertz, respectively. The selection of these particular frequencies will be discussed in further detail later in the Chapter.

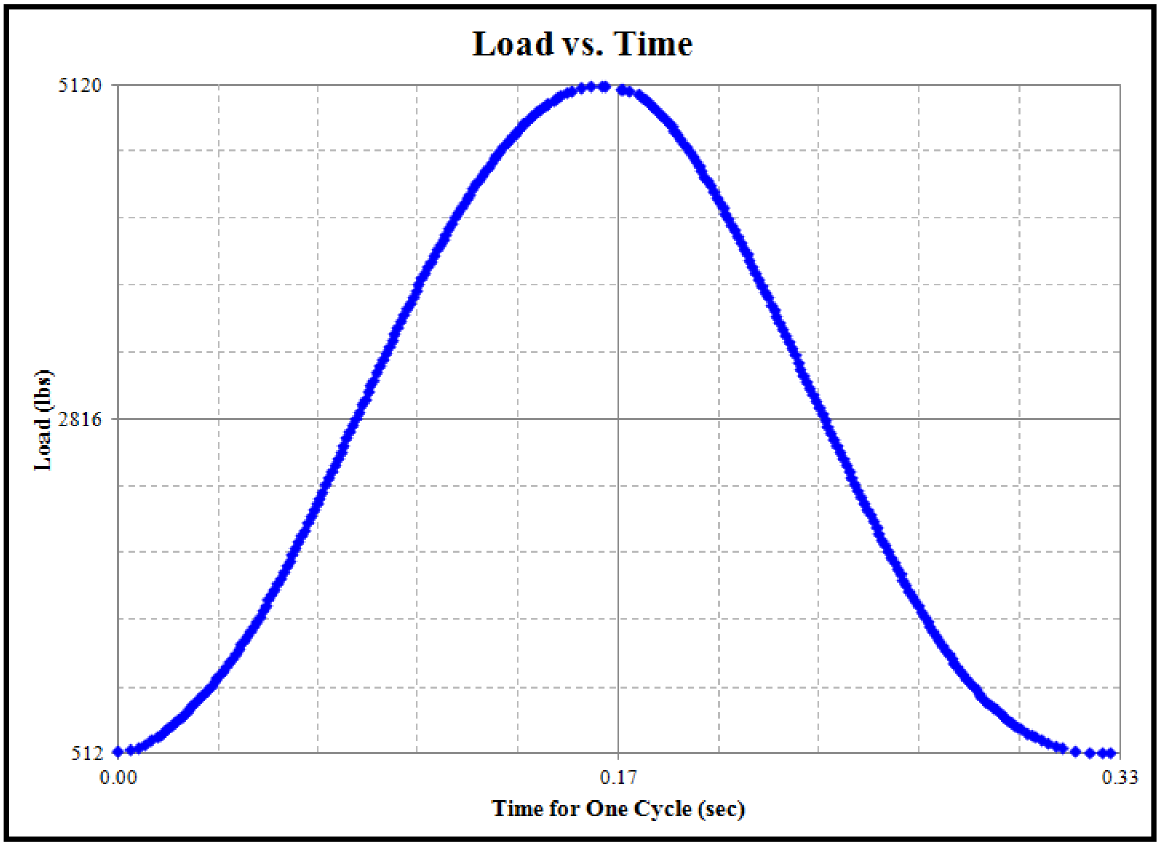

Figure 3.2: Sinusoidal output of one loading cycle at a frequency of 3 Hz (Stress Level 1 – High Level)

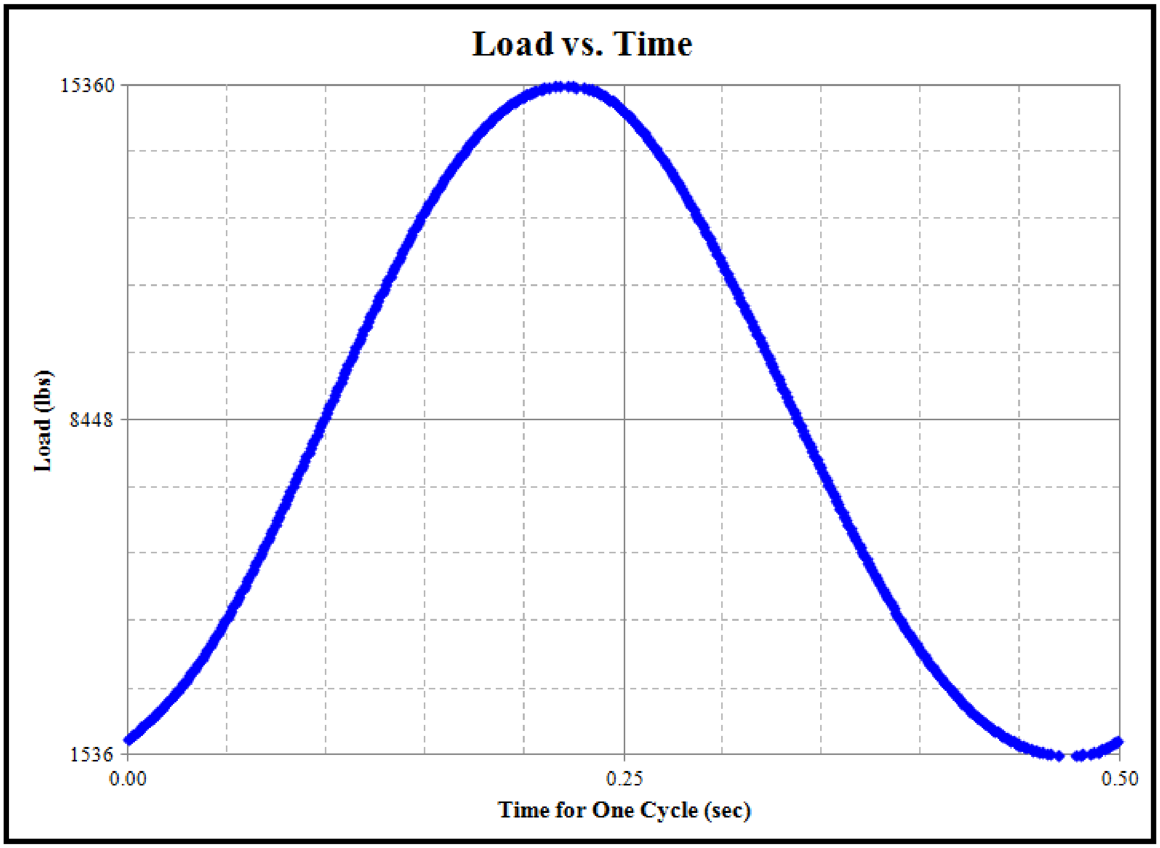

Figure 3.3: Sinusoidal output of one loading cycle at a frequency of 2 Hz (Stress Level 3 – High Level)

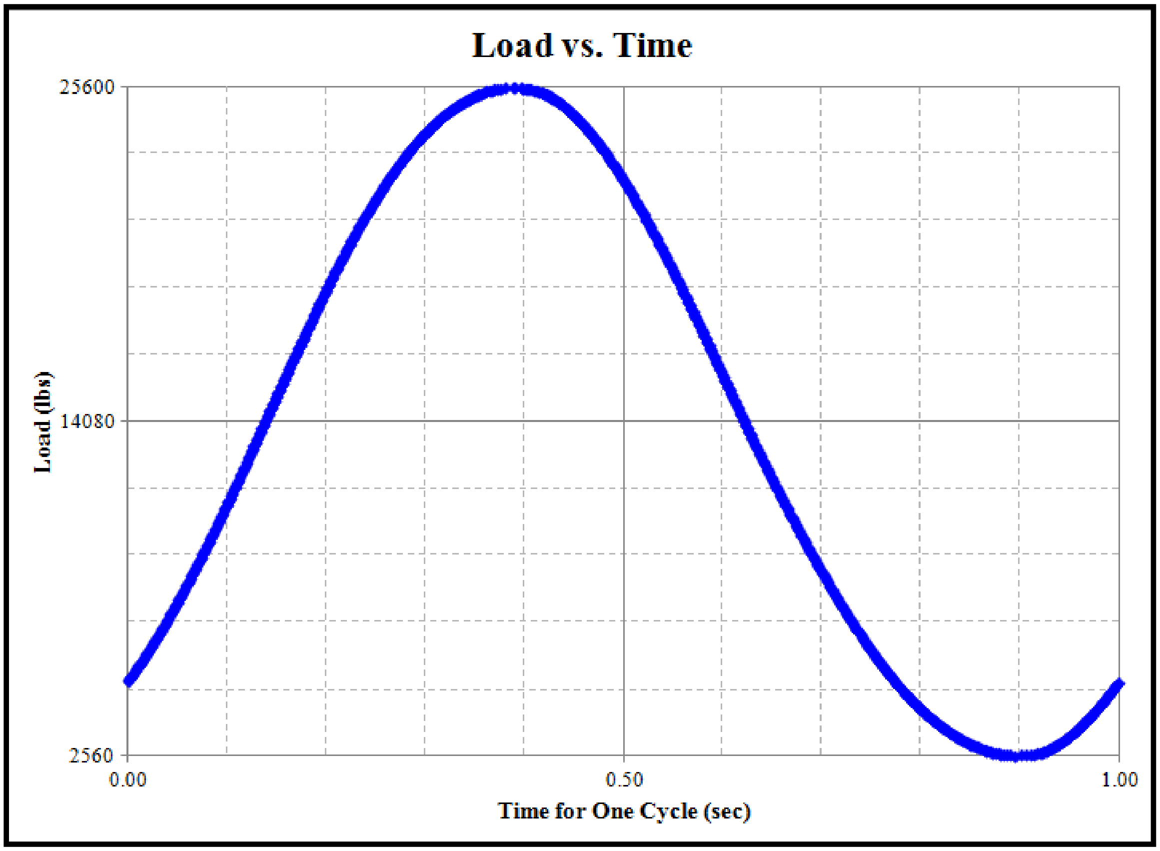

Figure 3.4: Sinusoidal output of one loading cycle at a frequency of 1 Hz (Stress Level 5 – High Level)

One of the primary concerns during fatigue testing was optimizing the frequency at which the test ran. A higher frequency is more time-efficient, reducing the overall duration of a single test; however, this could lead to overheating of the joint and energy loss. Changes in temperature inherently cause material properties to change, a variable that is assumed constant during this testing. Using a lower frequency results in longer tests, yet it eliminates all concerns of joint overheating.

Weidner et al ran fatigue tests with maximum loads ranging from 560 lbs (2490 N) to 2800 lbs (12450 N), at a frequency of 3 Hertz, and it was proven that overheating did not exist. The low-level fatigue ranges in this study are comparable to those studied by Weidner, thus a frequency of 3 Hertz was used for all low-level testing. For high-level fatigue testing, a frequency of 1 Hertz was used for Stress Levels 4 and 5, a frequency of 2 Hertz was used for Stress Levels 2 and 3, and a frequency of 3 Hertz was used for Stress Level 1. An infrared camera and a thermocouple attached to the bolt monitored the change in temperature at the joint during each of the high-level fatigue tests. Figure 3.5 is an infrared image taken just prior to catastrophic failure at Stress Level 5. Based on the infrared imaging of the area surrounding the experiment, the ambient temperature appears to be in the range of 74 and 76 degrees Fahrenheit. The side lap plates of the test fixture, made of 17-4PH stainless steel, are a few degrees cooler than the ambient temperature (seen as a darker shade of purple), while the joint and test specimen demonstrate temperatures approximately the same as the ambient temperature. Given that Grade 8 carbon steel (joint fastener) and stainless steel (test fixture) have significantly greater thermal conductivities than glass composites, if overheating of the joint was present, there would be a temperature gradient between the joint and the test specimen. Figure 3.5 shows no such gradient in the infrared image.

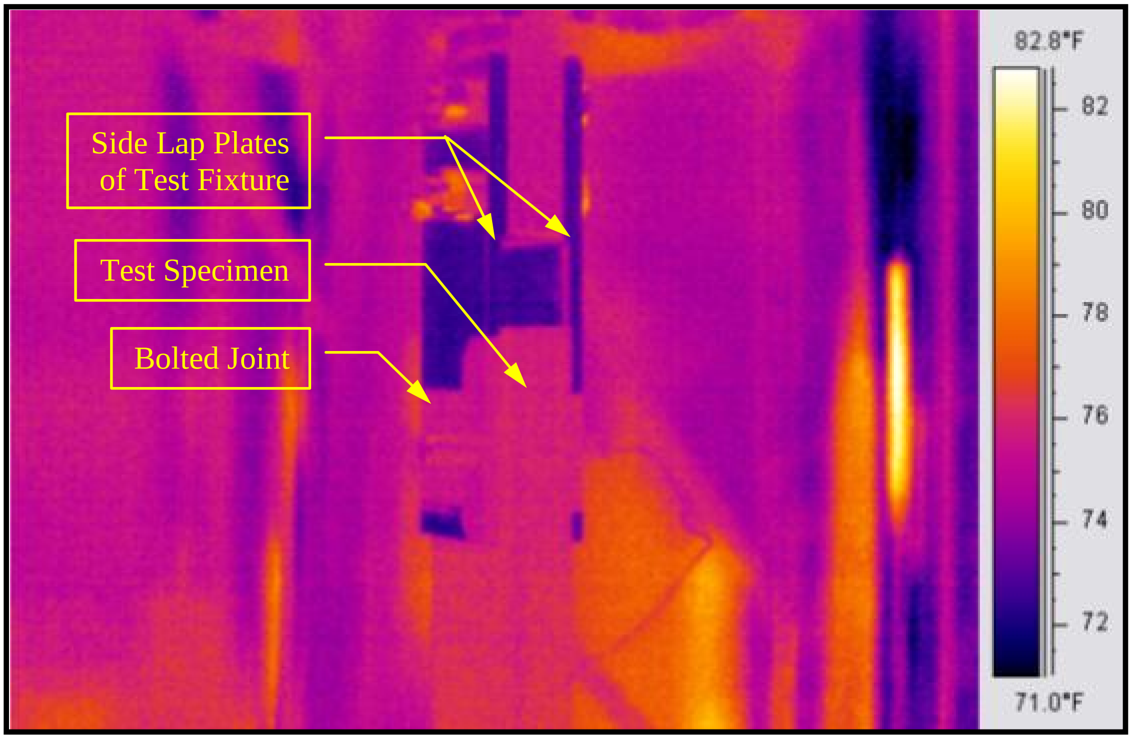

Figure 3.5: Infrared Camera Image of Stress Level 5 (High Level) Fatigue Test

Each specimen was subjected to one million cycles, unless catastrophic failure occurred prior to this benchmark. Blue dye was applied through the duration of each test, as well as at the conclusion of the test within the joint. Underwater C-scans were performed after testing to locate any internal damage as well as confirm damage identified by visual inspection. The C-scan images provided insight on internal cracking and debonding, which could be used to explain variations in stiffness from the experimental data. Several tests were conducted at each stress level to substantiate all conclusions, and residual strength tests were performed according to the static testing procedure prescribed in Section 3.2.

3.4 <u>Test Fixtures</u>

Several test fixtures and experimental configurations were used in this study. ASTM Standards suggest particular fixtures to be used for certain testing procedures, including stress relaxation and bearing response experiments. However, due to the complexity of the DCCS Structure and its' unusually high thickness for a composite, fixtures were adapted to suit the geometrical properties of the test specimens. Two different arrangements were used to study the stress relaxation of the DCCS Structure and its' constituents, and a single test fixture was designed and fabricated to conduct static and fatigue testing.

3.4.1 Stress Relaxation Set-Up: Instron Machine

The set-up for the Instron Stress Relaxation Test was derived from suggestions in ASTM E328-02 "Standard Test Methods for Stress Relaxation for Materials and Structures," the same ASTM Standard used for formulating a proper testing procedure. The test utilizes a screw-driven Instron Machine 4484 as the primary loading apparatus. Top and bottom plates are screwed into the cross-frame and Instron base using thread-to-thread adapters to provide a rigid connection. Both plates are inspected for surface nicks and undulations prior to testing. Once both plates are attached securely, measurements should be taken to assure that the plates are parallel to one another. LVDT's are placed below the top and bottom plate to measure the vertical displacement of the plates during the test. Using LVDT's as the method of measuring displacement is beneficial for several reasons. They offer an accurate alternative to the displacement readings of the Instron machine, while eliminating machine compliance factors. Using multiple LVDT's on each plate provides a way to check if the plates are rigid, or if they are rotating due to moments created by an off-center test specimen. Once the specimen is placed on the bottom plate, the cross-frame and top plate should be lowered until it is "resting" on the specimen, without exerting any stress on the specimen. This will prevent a sudden impact force from being applied to the specimen during loading. A schematic of the stress relaxation test using an Instron machine can be seen in Figure 3.6.

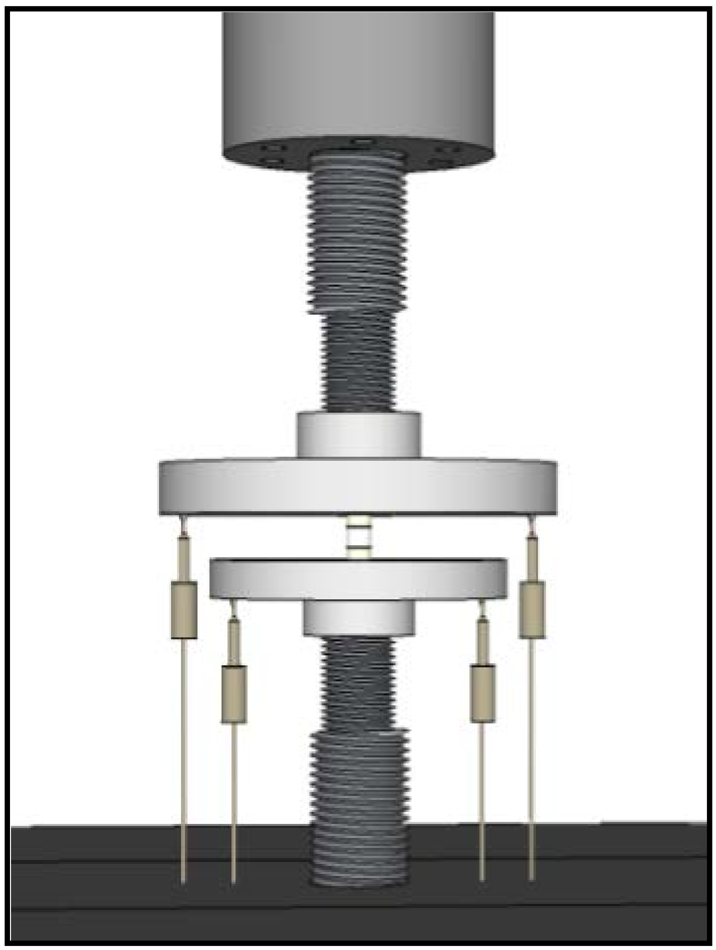

Figure 3.6: Stress Relaxation Test of DCCS Specimen using Instron Machine

3.4.2 Stress Relaxation Set-Up: Washer Load Cell

With the help of ASTM E328-02, a proper testing procedure was assigned for the Washer Load Cell Stress Relaxation Test. However, the standard did not provide a suitable method for measuring the stress relaxation of a joint using a washer load cell. The set-up for the Washer Load Cell Test was derived based on the concept of replicating the joint to simulate the actual loading and environmental conditions. A sturdy base, preferably of hardened tool steel, or equivalent, is clamped to a given testing location. The base should have a centrally-located 0.5 inch (12.70 mm) hole, such that a Grade 8 bolt can be inserted through the bottom. The underside of the base has an elongated hole for the bolt head to rest and to prevent the bolt from rotating while being tightened. Once the base is secure with the Grade 8 bolt protruding through the top, the following are placed over the bolt sequentially: a 0.5 inch (12.70mm) washer load cell with a capacity of 15,000 lbs (66723 N), a black luster-coated steel washer (as specified in ASTM Standards), 4 inch by 4 inch (101.6 mm by 101.6 mm) DCCS specimen with a centrally located 0.5 inch (12.70 mm) hole, a second black luster-coated steel washer, and the tightening nut. The transducer cable from the washer load cell is plugged into a computer switch board, so data from the load cell is monitored and recorded using StrainSmart software developed by Vishay Measurements Group. A schematic of the stress relaxation test using a washer load cell can be seen in Figure 3.7.

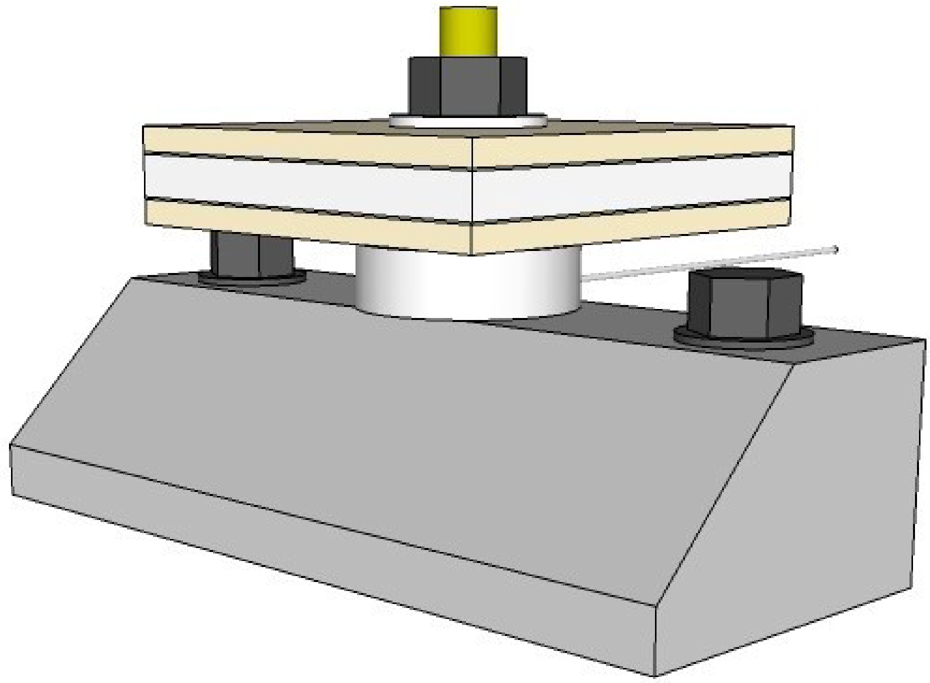

Figure 3.7: Stress Relaxation Test of DCCS Specimen using Washer Load Cell

3.4.3 Static/Fatigue Test Fixture

The test fixture used for static and fatigue testing was inherited as part of ongoing research involving the bearing response of the DCCS Structure, originally begun by Weidner et al. The design was influenced by the suggested test fixture in ASTM D 5961/D 5981-M-05 “Standard Test Method of Bearing Response for Polymer Matrix Composite Laminates,” though minor modifications were made to accommodate the test specimens. The fixture was made entirely from 17-4PH stainless steel, which is known for its’ high yield strength and durability under fatigue

(Weidner et al. 1 – 11). The components of the fixture include two spacer plates (one for testing the face sheet, one for testing the DCCS Structure), and two side lap plates, along with an efficient number of bolts to fasten the fixture together. The individual fixture parts are displayed in Figure 3.8. In addition to the primary parts of the double-lap test fixture, other attachments were used in conjunction with the fixture to help measure joint displacement. A pair of semi-circular blade clamps was situated in line with the specimen joint. LVDT's mounted on blade clamps were attached below the semi-circular clamps to measure the elongation of the joint during testing. These attachments were only required during static testing, where the displacement of the joint was one of the conditions being monitored. During testing, the side lap plates had a tendency to bow outward due to increased outward forces from the protruding face sheet during bearing failure and the natural bending of the bolt with increased loads. Lateral restraints were added around the side lap plates during high-level fatigue testing and static testing, to prevent excessive and detrimental bending of the plates. Originally, 0.5 inch (12.70 mm) diameter holes were fabricated in the making of the side lap plates. After increased concern over possible elongation of the holes during testing, inserts were substituted to provide increased joint stability and the ability to be replaced if damaged. A schematic of the final test fixture is shown in Figure 3.9, and an actual image of the fixture in the Instron grips is shown in Figure 3.10.

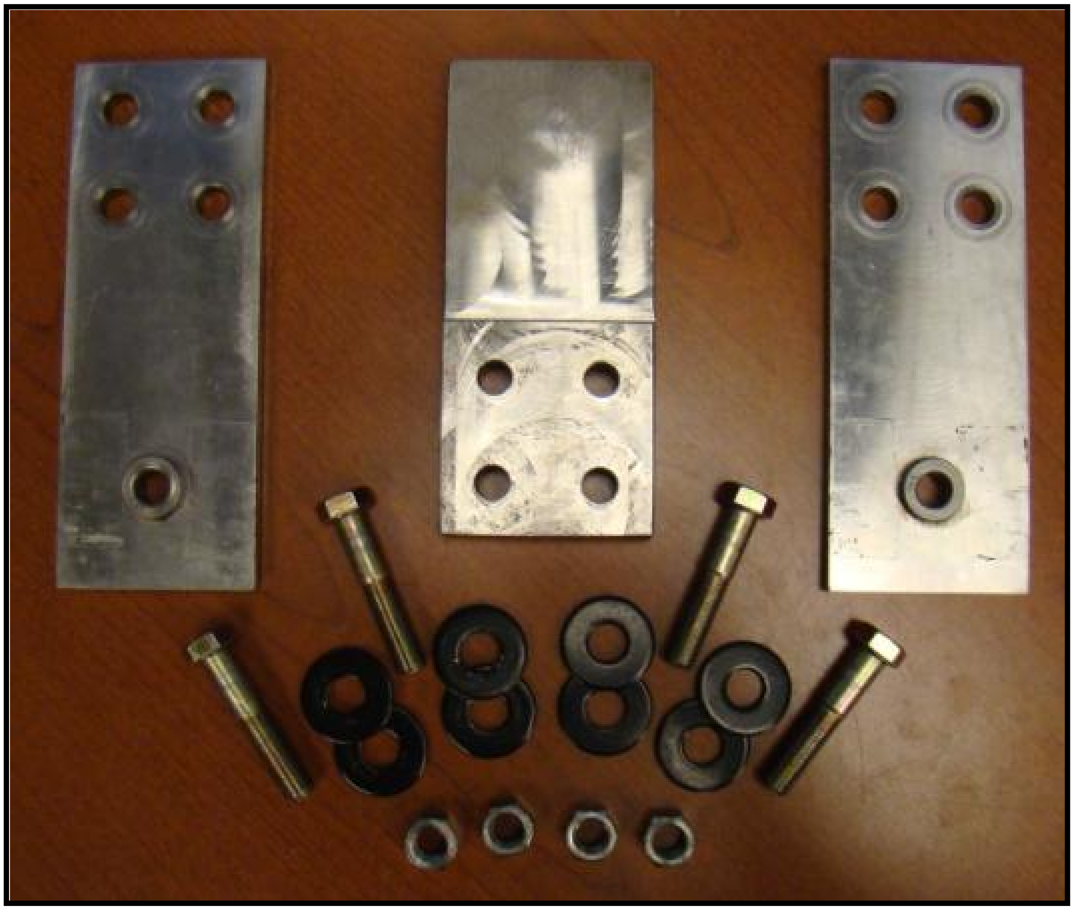

Figure 3.8: Test Fixture Parts

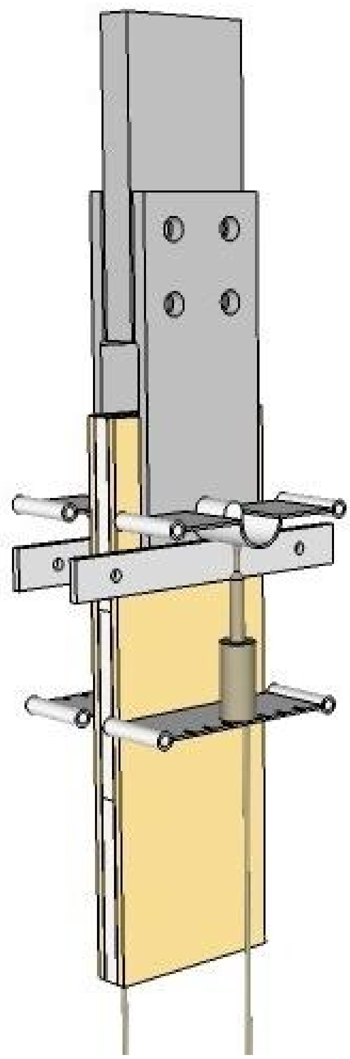

Figure 3.9: Test Fixture for Static Testing of DCCS Structure

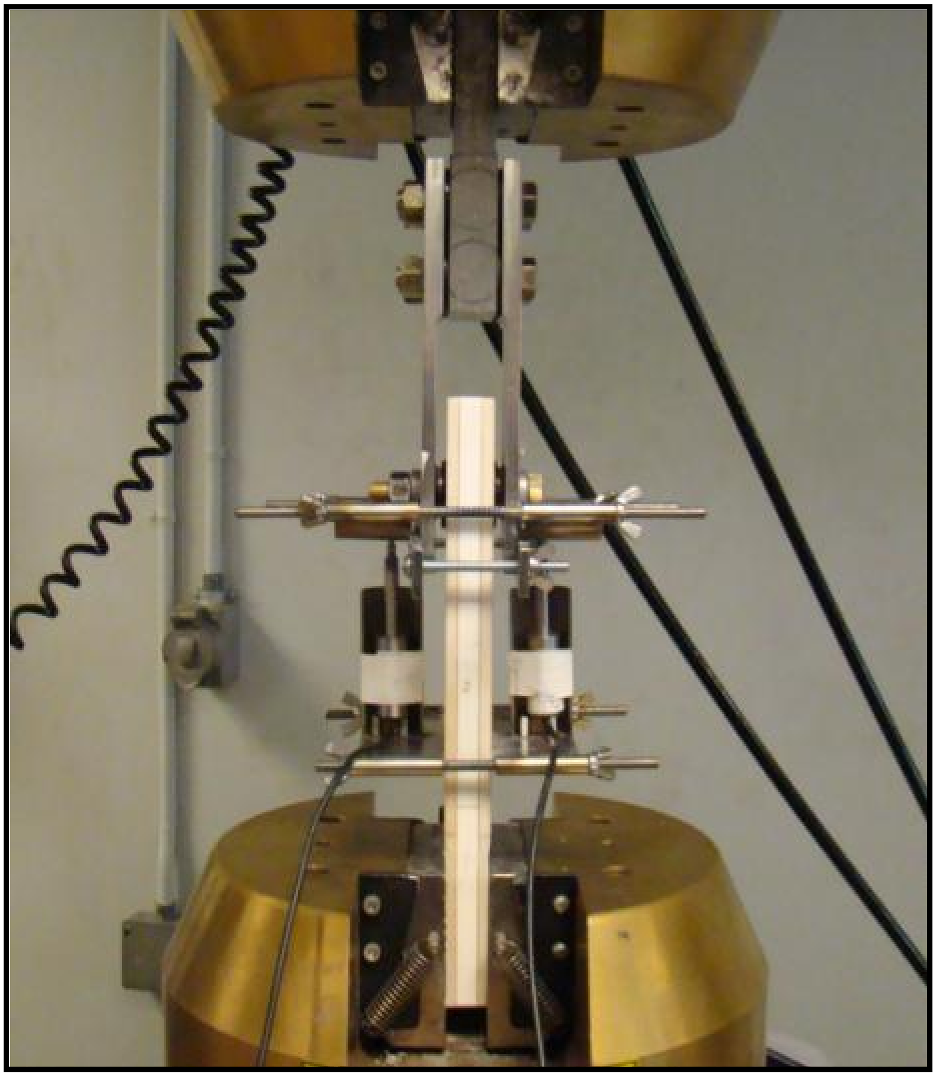

Figure 3.10: Static Test Fixture Set-Up in Instron Grips

Chapter 4

COMPRESSIVE STRESS RELAXATION IN DISCONTINUOUS CERAMIC CORED SANDWICH STRUCTURES

Several factors contribute to the overall strength of a joint. Many of these factors, including joint configuration and geometry, load definitions, and fastening conditions, were discussed at length in Chapter 1. One of the most important distinguishing features of a mechanical joint is determining the clamping force that provides the most benefit. Prior studies have examined the DCCS Structure with pinned joints. The evolution to clamped joints requires changes to the original fastening conditions. A baseline condition must be developed based on existing knowledge and research of composite joints and joint design. Once this baseline condition is established, testing will be performed to understand the durability and strength of the joint. One of the major contributing factors to joint life is the amount of stress relaxation that occurs in the joint over time. Stress relaxation can be a source of basic mechanisms in the mechanical joint (embedment between thread surfaces of the bolt and nut, and surfaces of the structural components making up the joint; poor thread engagement due to an undersized bolt or oversized nut or too short of an engagement length, reducing the thread contact area; creep of fastener components; undersized or oversized holes affecting the distribution of clamping pressure), secondary factors as a result of joint properties (bolt length – longer bolts with smaller diameters relax more than shorter bolts with large diameters; the number of joint members – more members allow for more embedment and greater relaxation; torque tightening speed – slower tightening speeds allow for relaxation to occur during the tightening process and reduces the amount of relaxation afterward), as well as the viscoelastic response of the layers within the composite material. To quantify the magnitude of stress relaxation experienced by a joint in the DCCS Structure, compressive relaxation testing of the individual constituents and the structure as a whole is paramount. This information will allow for empirical models to be formulated predicting long-term relaxation of the DCCS Structure in compression. Testing will be repeated using the actual joint, as compressive stresses in the mechanical joint are more complex than straight-forward through-thickness compression. Several alternative methods of applying torque will be tested to determine the method resulting in the least amount of stress relaxation.

4.1 <u>Determination of Baseline Torque</u>

Joint design is a highly complex subject, requiring many factors to be considered. Bickford's "Introduction to the Design and Behavior of Bolted Joints" is an instrumental resource in providing a step-by-step process to the design of bolted joints. A comprehensive book such as this one highlights and details all the factors that go into the design of a single bolted joint. Within the design process, Bickford documents a specific guideline to select the appropriate tightening torque for a given joint under various conditions. In order to define a baseline torque for this study, several parameters first needed to be examined, beginning by defining the type of joint in question, determining an upper limit for the torque based on the strength of the fastener components (tensile strength in the bolt shank, shear strength of bolt threads, torsional resistance in the bolt due to torque) and the strength of the joint members (ceramic tile, interlayer, and face sheet of DCCS Structure), and determining a lower limit based on the tendency for bolts to self-loosen (vibration, fatigue, stress relaxation). Identifying the upper and lower torque limits ultimately provides a range of suitable torque for the joint. The remainder of this section will detail this process, along with the selection of the baseline torque for this study.

The first objective in selecting a tightening torque for a joint is identifying the type of joint, according to the direction of the external loads exerted on the fastener (not including the load associated with the torquing effect). This is resolved into two primary types of joints: a tensile joint, where the external forces are parallel to the bolt shank, and a shear joint, where the external forces act perpendicular to the bolt shank. The two types of joints are diagrammed in Figure 4.1. It is not uncommon for a bolt to experience a combination of tensile and shear loads, typically resulting in bending of the bolt, but a joint is classified according to the dominant force acting on the bolt, either tension and shear. The primary purpose of a tensile joint is to clamp two or more joint members together to prevent them from pulling apart, whereas the purpose of a shear joint is to keep joint members from slipping (establishing a clamping load adds frictional resistance to slip) or pulling out (the bolt simulates a shear pin, creating bearing pressure on the members at the joint). Both joints require clamping force to enhance their efficiency, but because the in-service behaviors of the two types of joints vary significantly, the initial tightening torque is selected differently for each. For example, a tensile joint exposed to high service loads should not be preloaded with a high clamping force; this can ultimately cause premature tensile failure of the bolt. As for a shear joint, service loads (bearing of the joint members) on the bolt do not detract or enhance the preload from the initial clamping force, thus a higher initial tightening torque is permissible.

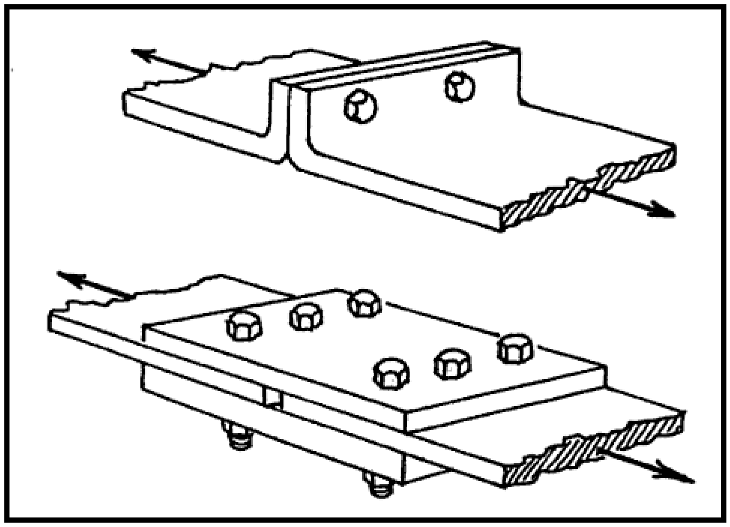

Figure 4.1: Types of Bolted Joints: Tensile (top) and Shear (bottom), (Bickford)

Shear joints are typical in structural applications, as external shear loads from bearing tend to have a minimal effect on the tensile forces in the bolt. For this particular study, the bolted joint in the DCCS Structure can be classified as a shear joint. This does not necessarily exclude the possibility of external tensile forces acting on the bolt; however, bearing of the DCCS joint on the bolt is the dominant external force. There are several factors that can induce a change in the clamping force, or tensile preload, in the bolt. Temperature change, vibrations or shock, corrosion, cyclic loading or fatigue, and self-loosening are all potential ways that a joint can lose clamping force. Of these factors, all except for self-loosening are a result of environmental surroundings and exposure. Self-loosening is a function of the magnitude of torque, friction in the mechanical joint, surface roughness of the joint members, hole interference, and relaxation of the joint members. To combat self-loosening, the baseline level of torque that achieves the highest residual clamping force without damaging the DCCS Structure or failing the fastener components should be chosen. For this reason, it is important to analyze each potential failure mechanism of the bolted joint and fastener components, followed by an investigation on the response of the materials comprising the DCCS Structure under compressive loading. These two analyses will provide enough information to select an upper torque limit, which upon exceeding, would result in damage to the joint. This will be ensued by selecting a lower torque limit, based upon which the potential for self-loosening is eliminated, or reduced to a small probability.

The first step in determining the upper torque limit is defining the bolt that will be used experimentally, and calculating the maximum allowable torque based on the bolt strength specifications and the types of loads expected during the clamping process. The process of torquing a joint ultimately induces tension in the bolt shank, shearing in the bolt and nut threads, and torsion along the length of the bolt; all three will be examined to determine which governs as the upper torque limit, in terms of the fastener. To replace the steel pin used in prior studies of the DCCS Structure, a ½”-13 Grade 8 bolt (0.5 inch nominal diameter, 13 threads per inch) was chosen as the most comparable. Grade 8 bolts are rated to have minimum tensile strength of 150000 psi, and shear strength of 91000 psi.

When torque is applied to a bolt, there is an inherent axial load, or tensile force, through the length of the bolt as the bolt is being stretched. The axial load is constant through the length; however, due to a variance in cross-sectional areas of the bolt shank and threads, the peak tensile stress occurs in the threads (the portion of the bolt with the smaller cross-sectional area). The tensile stress in the threads is calculated using the effective tensile stress area of the bolt, which in itself, is calculated according to Equation (1):

$$A_S = 0.785(D - \frac{0.9743}{n})^2 \tag{1}$$

Where, D = nominal diameter and n = number of threads per inch. The resulting tensile stress area, A_s is equal to 0.1418 in^2. Assuming the minimum tensile strength of 150000 psi, this provides an equivalent tensile load of 21270 lbs. Since it was determined that the structural joint was a shear joint (because the DCCS joint reciprocated shear stress in the bolt shank as a result of the bearing stress the shank placed on the DCCS joint), the primary anticipated loading in the shank direction is the axial load resulting from the initial torque. Thus the equivalent load of 21270 lbs can be converted to a corresponding torque according to Equation (2):

$$T = kDF \tag{2}$$

Where, k = torque coefficient or nut factor (typically 0.2 for as-received steel), D = nominal diameter and F = desired axial load. To achieve the minimum tensile load of 21270 lbs, 177 ft-lbs of torque is required on the joint. Consequently, a torque of this magnitude would cause the bolt to fail in tension at the threads. To provide a more conservative torque level for structural applications, several other milestone strengths are examined, including the yield strength and proof strength of the bolt, both of which are a function of the minimum tensile strength. The yield strength of a Grade 8 bolt, which is prescribed as having a strength of 130000 psi (equivalent tensile load of 18434 lbs; equivalent torque of 154 ft-lbs), is described as the transition between elastic and plastic deformation. Thus any torque above 154 ft-lbs would result in yielding and plastic deformation of the bolt. The proof strength of a Grade 8 bolt, which is prescribed as having a strength of 120000 psi (equivalent tensile load of 17016 lbs; equivalent torque of 142 ft-lbs), is described as an offset of the yield strength when there is uncertainty with the exact point of yield. Furthermore, bolts are provided with a recommended clamp strength, which is 75 percent of the proof strength. This is generally considered a “safety factor” that prevents over-tensioning of the bolt and reducing the risk of premature bolt failure. Using this recommended safety factor, the bolt clamp strength for Grade 8 bolts is 90000 psi (equivalent tensile load of 12762 lbs; equivalent torque of 106 ft-lbs). This is the most common upper limit when it comes to establishing a clamping force; however, shearing of the bolt and nut threads and torsion in the bolt shank should still be considered before declaring an upper limit based on fastener strengths.

When it comes to the shear strength of the threaded region of a bolt, reducing the risk of thread plasticization is extremely important because stripping bolt threads can make it extremely difficult to unfasten the joint and also reduces the clamping force on the joint. Assuming the thread length is fully engaged, the thread-stripping strength can be calculated according to Equation (3):

$$F = S_U A_{TS} \tag{3}$$

Where, S_U = ultimate shear strength and A_{TS} = cross-sectional area of the threads through which the shear occurs. A_{TS} is a function of the comparative strength of the bolt threads and nut threads. It is most common that the proof strength of the nut is greater than the proof strength of the bolt, and given this assumption, Bickford provides a table of the cross-sectional area, or stripping area, for various bolts. The stripping area for ½”-13 bolts is 0.390 in^2. Using Equation (3), the thread-stripping strength for the bolt in use is 35490 lbs. Because this shear force acts perpendicular to the threads and in line with the bolt, this load can be seen as an axial load acting through the length of the bolt and Equation (2) can be used to calculate the equivalent torque required to achieve this strength, which comes out to be 296 ft-lbs. This torque is far greater than the suggested torque according to the minimum tensile strength (determined previously to be 177 ft-lbs), such that if the same approach was used to calculate a conservative torque limit (by reducing the shear strength to yield strength, yield strength to proof strength, and reducing the proof strength by a safety factor), then the final torque limit for shearing of the threads would still be greater than the bolt clamp strength for tensile loading.

The last feature to consider is the torsional stress factor. When a bolt is subjected to torque by turning the nut or head, it is exposed to both torsional stresses from the twisting and tensile stresses from the bolt elongation. The combination of the two stresses results in an equivalent stress greater than anticipated tensile stress. As a result, the common safety factor used to compensate for this torsion is reducing the bolt proof strength (120000 psi) by 10 percent of the minimum tensile strength (150000 psi) of the bolt. This provides a torsional stress factor strength of 105000 psi (equivalent tensile load of 14889 lbs; equivalent torque of 124 ft-lbs). However, the torsional stress factor is generally accounted for in the safety factor applied to the recommended clamp strength, thus the torsional stress factor strength does not require the same reduction that the clamp strength received.

As a baseline upper-limit clamping force, Bickford recommends a stress of 62 percent of the minimum tensile strength, which equates to 93000 psi (equivalent tensile load of 13187 lbs; equivalent torque of 110 ft-lbs). This is also worth consideration, if only for comparison purposes to validate the calculated upper limit based on the fastener strength properties. Table 4.1 details all of the upper limit considerations, which is ultimately governed by the bolt clamp strength, equating to a maximum torque of 106 ft-lbs.

Table 4.1: Clamping Force Upper Limit (according to fastener strength)

Factors to Consider	Strength in Stress	Equivalent Load	Equivalent Torque
Bolt Minimum Tensile Strength	150,000 psi	21270 lbs	177 ft-lbs
	1034 MPa	94614 N	240 N-m
Bolt Yield Strength	130,000 psi	18434 lbs	154 ft-lbs
	896 MPa	81999 N	209 N-m
Bolt Proof Strength	120,000 psi	17016 lbs	142 ft-lbs
	827 MPa	75691 N	193 N-m
Bolt Clamp Strength	90,000 psi	12762 lbs	106 ft-lbs
	621 MPa	56768 N	144 N-m
Thread Stripping Strength	91,000 psi	35490 lbs	296 ft-lbs
	627 MPa	157867 N	401 N-m
Torsional Stress Factor Strength	105,000 psi	14889 lbs	124 ft-lbs
	724 MPa	66230 N	168 N-m
Suggested Upper Limit Strength	93,000 psi	13187 lbs	110 ft-lbs
	641 MPa	58659 N	149 N-m

The next consideration for the maximum clamping force is the compressive strength of each constituent comprising the DCCS Structure. In order to gain a better idea of the compressive stresses exhibited in the DCCS Structure, a suitable washer must be selected, keeping in mind that a smaller washer area concentrates the compressive stresses and a larger washer area distributes the stresses further from the joint. Previous studies performed by Yan et al and Khashaba et al concluded the use of an outer diameter-to-inner diameter washer ratio of 3.0 to optimize the performance of clamped joints. This would suggest the use of a washer with an outer diameter of approximately 1.5 inches (assuming an inner diameter of 0.5 inches). Consulting ASME standards, an appropriate washer size for a 0.5 inch bolt consists of an outer diameter of 1.375 inches (34.93 mm) and an inner diameter of 0.5625 inches (14.29 mm). Using an inner diameter slightly larger than the bolt diameter prevents an interference fit, and allows the full clamping force to act through the washer onto the surface area surrounding the DCCS joint. These dimensions equate to an OD-to-ID ratio of 2.44, and while slightly lower than the ratio recommended by Yan et al and Khashaba et al, are within a reasonable range. If crushing of the DCCS Structure becomes a concern, the washer can be exchanged for a larger size to better distribute the clamping pressure, or the torque can be revised to reduce compressive stresses.

To simplify the analysis in determining the allowable compressive limits for each constituent, uniform compressive stress is assumed. The compressive strength in the thru-thickness direction of the face sheet can be found in Table 2.1, and is listed as 43.5 ksi. The compressive strength of the ceramic tile and yield strength of the surlyn interlayer can be found in Table 2.2, and are listed as 363 ksi and 2.70 ksi, respectively. The yield strength is taken into account for the interlayer, as opposed to the ultimate strength, because the interlayer governs the stress transfer between the face sheet and ceramic tile, and if the interlayer is yielded, it will inhibit the stress transfer. Using these strengths and the assumption that the clamp load is evenly distributed through the full surface area of the washer (1.236 in^2), the compressive clamping loads that cause failure for each constituent are: 53760 lbs for the face sheet, which comes out to an equivalent torque of 448 ft-lbs (calculated using Equation (2)); 448600 lbs for the ceramic tile, with an equivalent torque of 3738 ft-lbs; and 3340 lbs for the interlayer, with an equivalent torque of 27.8 ft-lbs. To gain a better understanding of the response of the DCCS Structure under uniform compression, static, through-thickness compression tests were performed on the DCCS Structure to find the compressive strength which exhibited failure of any type within the constituents. The experimental set-up for this test is shown in Figure 3.6. Each specimen of the DCCS Structure was core-drilled using a 0.5 inch diamond-tipped core drill bit, resulting in specimens with nominal diameters of 0.447 inches and a surface area of 0.1569 in^2. During the testing process, specimens were monitored for interlayer yielding (or "squishing" of the interlayer causing it to protrude from the specimen), ceramic cracking, or fiber-buckling in the face sheet.

A total of five static compression tests were performed on the DCCS specimens (see Appendix A for plot of each individual test). As the specimens were loaded, the interlayer's showed evidence of yielding as they displayed the most compressive displacement with respect to constituent thickness, and was also seen to protrude around the perimeter of the specimen. However, the plots show no discernible load or stress to which yielding began in the interlayer. Despite yielding of the interlayer, specimens continued to withstand loading at a near-linear slope, until the onset of damage in the face sheet. The damage appeared to be a result of fiber-buckling in the z-direction, seen in Figure 4.2. Testing was stopped immediately after this mode of failure was seen in the face sheet, which occurred at an average compressive strength of 15604 lbs (an equivalent compressive stress of 99452 psi given cross-sectional specimen areas of 0.1569 in^2), with a standard deviation of 1485 lbs (9465 psi). Table 4.2 provides individual results from the five static compression tests.

Figure 4.2: Interlayer Plasticization and Fiber-Buckling in the Face Sheet after Static Compression Test

Table 4.2: Static Compression Tests

Sample #	Specimen Area	Compressive Load	Compressive Stress	Displacement
DCCS-SC-1	0.1569 in^2	17120 lbs	109080 psi	0.0769 in
	101.2 mm^2	76150 N	752 MPa	1.953 mm
DCCS-SC-2	0.1569 in^2	15950 lbs	101660 psi	0.0752 in
	101.2 mm^2	70950 N	701 MPa	1.910 mm
DCCS-SC-3	0.1569 in^2	13530 lbs	86190 psi	0.0553 in
	101.2 mm^2	60180 N	594 MPa	1.405 mm
DCCS-SC-4	0.1569 in^2	16730 lbs	106590 psi	0.0726 in
	101.2 mm^2	74420 N	735 MPa	1.844 mm
DCCS-SC-5	0.1569 in^2	14690 lbs	93590 psi	0.0613 in
	101.2 mm^2	65340 N	645 MPa	1.557 mm

The thru-thickness compressive strength of the face sheet according to Gillespie et al. was documented to be 43.5 ksi, which is much lower than the face sheet strength found from the static compression tests of 99.5 ksi. This strength was determined using the block compression test method in compliance with ASTM Standards. Loading was applied in the 3-direction (thru-thickness) of a 0.75 inch block of the face sheet material, which had four strain gages mounted on each side in order to take the average strain through the duration of the test. According to the results provided by Gillespie et al, failure was reported at an average strength of 43.5 ksi; however, specimens continued to achieve higher strengths without demonstrating any drop in load, despite a displacement-controlled loading pattern and progressive failure of the face sheet block. Not until approximately 90 – 95 ksi did the loading experience a significant drop, similar to that seen in the static compression test of the

DCCS Structure. This would indicate a second mode of failure in the face sheet, whereas the first mode of failure was detected only by the use of strain gages in the block compression test, and went undetected under human observation in the static compression test of the DCCS Structure. The first mode of failure in the face sheet could be attributed to matrix cracking, whereas the second mode of failure is a result of fiber-buckling. Not knowing the affect that any type of face sheet damage could have on the DCCS joint, the original thru-thickness strength of 43.5 ksi will be used to calculate the allowable clamp strength according to the face sheet. Furthermore, the resulting torque from the acclaimed thru-thickness strength is a conservative approach compared to the actual compressive stress seen at the same torque. Manzella et al explains that composites exposed to punch-shear tests experience a compression-shear interaction along a specific fracture plane due to the confinement of the composite outside the punch perimeter (conceptually, the way a clamp load is applied to a joint resembles penetration of a punch on a composite specimen, only with a centralized hole in the composite located at the center of the punch). Theoretically, thin laminates with large punches are expected to simulate uniform compression, whereas thick laminates with small punches demonstrate shear stresses around the punch perimeter. Introducing the compression-shear interaction reduces the amount of thru-thickness compression experienced for a given torque level. Thus, it can be assumed that even though the calculated torque of 448 ft-lbs will cause compressive failure through the thickness of the face sheet under uniform compression, in reality, the compression-shear interaction will reduce the true amount of thru-thickness compressive stresses in the face sheet. Table 4.3 summarizes the allowable clamping limits for each of the constituents of the DCCS Structure.

Table 4.3: Clamping Force Upper Limit (according to constituents)

Constituents	Strength in Stress	Equivalent Load	Equivalent Torque
Face Sheet	43,500 psi	53760 lbs	448 ft-lbs
	300 MPa	239100 N	607 N-m
Ceramic Tile	363,000 psi	448600 lbs	3738 ft-lbs
	2500 MPa	1995000 N	5068 N-m
Interlayer	2,700 psi	3340 lbs	27.8 ft-lbs
	18.6 MPa	14860 N	37.7 N-m

The final consideration for the torque range is the lower limit, to prevent the potential for self-loosening of the joint. This limit cannot be quantified easily, given the variability in environmental exposure and magnitude of fatigue loads; however, Bickford suggests a baseline lower-limit clamping force of 48 percent of the minimum tensile strength, which should provide enough clamping force to eliminate concern in regards to self-loosening, slippage, fatigue, etc. This equates to a lower limit strength of 72000 psi (an equivalent load of 10210 lbs; equivalent torque of 85 ft-lbs). This is notably higher than the governing upper limit clamping force provided by the interlayer in the DCCS Structure. Given the necessity to maintain clamping force for the lifetime of the joint, the interlayer strength around the joint must be sacrificed and allowed to yield. In doing so, the governing upper limit becomes 106 ft-lbs, provided by the bolt clamp strength (under tensile loading).

While the nature of this study highlights in-plane tension loading of the DCCS Structure, deducing the bolted joint as strictly a shear joint, other potential loading patterns, including bending and transverse loading could result in the joint experiencing tensile and shear joint properties. For this reason, the selected baseline clamping force will be on the lower end of the aforementioned range (85 – 106 ft-lbs), at 90 ft-lbs. With a baseline clamping force/torque selected, predicting the amount of torque loss over time becomes paramount, beginning with estimating the stress relaxation in the joint.

4.2 **Relaxation Test Using Instron Machine**

Of the potential sources for torque loss, the effective stress relaxation of the viscoelastic materials in the DCCS Structure is highly unknown and unpredictable to this point. To understand the response of the constituents under an initial clamping force, relaxation testing will prove essential. This will be done using two different methods, the first using an Instron machine (fixed displacement) to perform through-thickness compressive relaxation tests on the face sheet and DCCS Structure. The testing set-up requires core specimens situated between two smooth plates, one attached to the Instron base, the other attached to the moving crosshead. LVDT's are mounted to measure the displacement of the plates, to determine the strain experienced by the specimens (Figure 3.6). The load cell attached to the Instron measures the loading throughout the duration of the relaxation test. Of the three constituents, the face sheet and adhesive interlayer have viscoelastic properties, hence may have the tendency to relax over time. However, because the interlayer is significantly thinner in the through-thickness direction, the relaxation properties will have to be calculated based on the differences between the results of the face sheet and DCCS specimen (face sheet, interlayer and ceramic). This is possible because the ceramic tile is assumed to be completely rigid.

4.2.1 Instron Testing on Single Face Sheet

Viscoelasticity can be broken down into two parts: linear viscoelasticity and non-linear viscoelasticity. Linear viscoelasticity can be predicted using general viscoelastic relationships and models, and usually occurs under small strains. Non-linear viscoelasticity is much more difficult to predict, requiring complex relationships to model. This stage of viscoelasticity typically occurs at higher strains, which induce changes within the material properties due to plastic yielding or internal damage. (Recall from the previous section, the thru-thickness stresses created by the baseline torque of 90 ft-lbs is expected to cause the interlayer to yield and plasticize; potentially creating a scenario where the face sheet in linear viscoelastic and the interlayer is non-linear viscoelastic). One method to check whether a material is in the linear or non-linear viscoelastic regime is by performing stress relaxation tests with varying initial strains/stresses. If the normalized relaxation is consistent among the varying levels, then the stress/strain levels are within the linear viscoelastic region.

Core samples used for stress relaxation testing had average diameters of 0.447 inches (cross sectional area of 0.1569 in^2). Under normal joint conditions of the DCCS Structure, 10800 lbs (90 ft-lbs) of clamping force are applied over a washer area of 1.236 in^2 (based on a washer with an inner diameter of 0.5625 inches and an outer diameter of 1.375 inches) resulting in a clamping pressure of 8735 psi. To simulate the same pressure on the core samples, an applied compressive force 1371 lbs is required. Three other pressures were tested on the core samples to determine its viscoelastic nature (linear vs. non-linear); all were determined as a percentage of the baseline torque. The stress levels were 80 percent of the baseline torque (clamping pressure of 6988 psi; torque of 72 ft-lbs; compressive force of 1096 lbs), 60 percent of the baseline torque (5241 psi; 54 ft-lbs; 822 lbs) and 40 percent of the baseline torque (3494 psi; 36 ft-lbs; 548 lbs). The normalized stress relaxation of the face sheet from the four stress levels are plotted in Figure 4.3. Stress relaxation varied between 14 and 16 percent over a time period of 30 minutes, with almost 10 percent of the stress loss occurring in the first minute of the test. The relaxation curves and stress losses had no major discrepancies between the four tests and there was no indication of non-linear viscoelasticity in the face sheet at the applied stresses. With stresses in the linear viscoelastic range, modeling and predicting stress relaxation will be a much easier task.

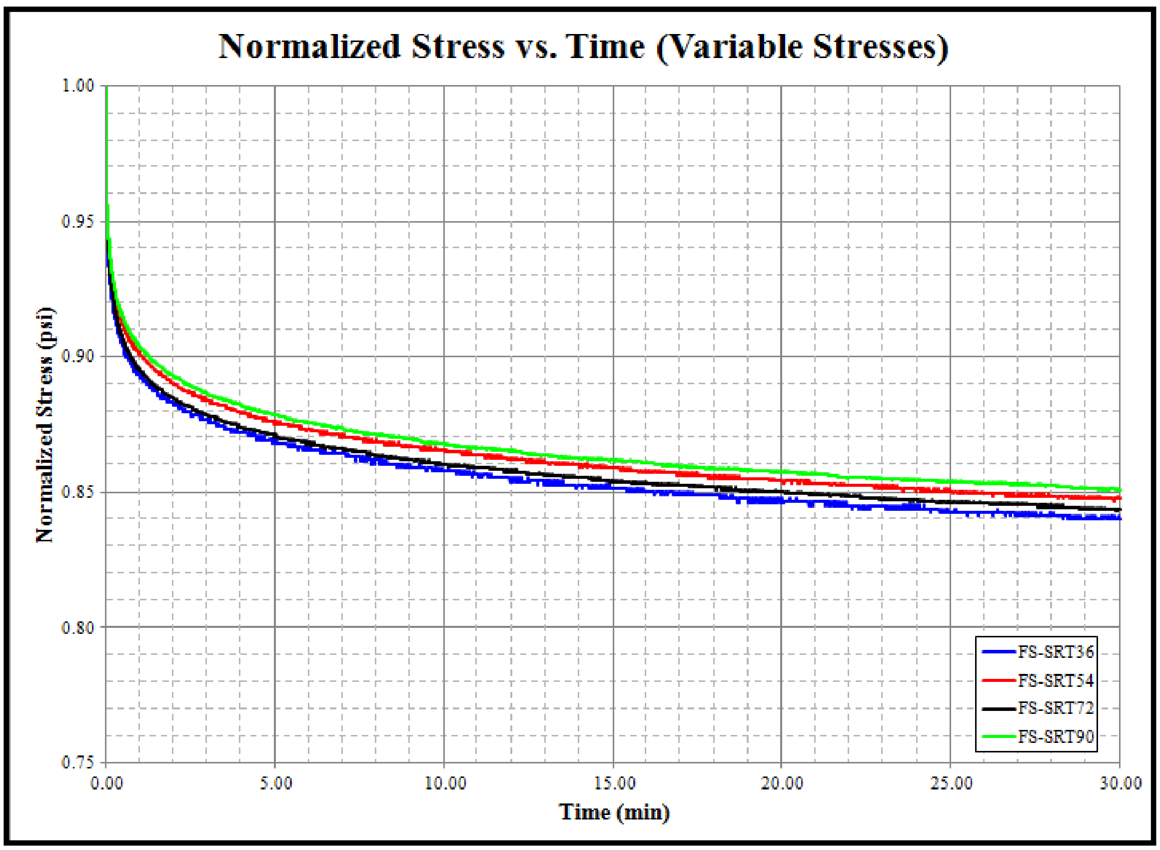

Figure 4.3: Face Sheet Stress Relaxation with Variable Stresses

Additionally, several relaxation tests were performed on the face sheet using the equivalent stress and compressive load required to simulate the baseline torque of 90 ft-lbs. The results and progressive stress loss of these tests are documented in Table 4.4 (plots of each individual test at an initial compressive stress of 8735 psi can be found in Appendix B). Several tests were run with high data acquisition rates and short time lengths to gain a better understanding of the stress loss in the first minute after the application of stress. These results will be utilized in the following section to formulate an empirical equation that models the short-term stress relaxation in the face sheet material.

Table 4.4: Face Sheet Stress Relaxation with Equivalent Stresses

Sample #	Time Elapsed	Progressive Stress		Percent Loss
FS-SRT90-1	0 sec	8735 psi	60.23 MPa	0.00%
	1 sec	8328 psi	57.42 MPa	4.66%
	10 sec	7989 psi	55.08 MPa	8.54%
	60 sec	7773 psi	53.59 MPa	11.02%
FS-SRT90-2	0 sec	8735 psi	60.23 MPa	0.00%
	1 sec	8306 psi	57.27 MPa	4.91%
	10 sec	7952 psi	54.83 MPa	8.96%
	60 sec	7743 psi	53.39 MPa	11.35%
FS-SRT90-3	0 sec	8735 psi	60.23 MPa	0.00%
	1 sec	8301 psi	57.23 MPa	4.97%
	10 sec	7952 psi	54.83 MPa	8.96%
	60 sec	7711 psi	53.17 MPa	11.72%
FS-SRT90-4	0 sec	8735 psi	60.23 MPa	0.00%
	1 sec	8317 psi	57.34 MPa	4.78%
	10 sec	7979 psi	55.01 MPa	8.66%
	60 sec	7759 psi	53.50 MPa	11.18%
FS-SRT90-5	0 sec	8735 psi	60.23 MPa	0.00%
	1 sec	8312 psi	57.31 MPa	4.85%
	10 sec	7974 psi	54.98 MPa	8.71%
	60 sec	7745 psi	53.40 MPa	11.34%
FS-SRT90-6	0 min	8735 psi	60.23 MPa	0.00%
	1 min	7841 psi	54.06 MPa	10.24%
	5 min	7641 psi	52.68 MPa	12.53%
	10 min	7547 psi	52.03 MPa	13.60%
FS-SRT90-7	0 min	8735 psi	60.23 MPa	0.00%
	10 min	7448 psi	51.35 MPa	14.27%
	50 min	7268 psi	50.11 MPa	16.79%
	100 min	7167 psi	49.41 MPa	17.95%

4.2.2 Instron Testing on DCCS Structure

The same sequence of tests that were performed on the face sheet material were repeated on the DCCS Structure. Testing specimens were of the same core size as the face sheet samples, with an average diameter of 0.447 inches and cross-sectional area of 0.1569 in^2. Four different initial stresses were tested, beginning with the equivalent to 90 ft-lbs (8735 psi), followed by 72 ft-lbs (6988 psi), 54 ft-lbs (5241 psi), and 36 ft-lbs (3494 psi), to assess its viscoelastic nature. If the DCCS Structure as a whole is found to be non-linear, this can be isolated to the interlayer because the face sheet has already been proven to be linear viscoelastic as the applied stresses.

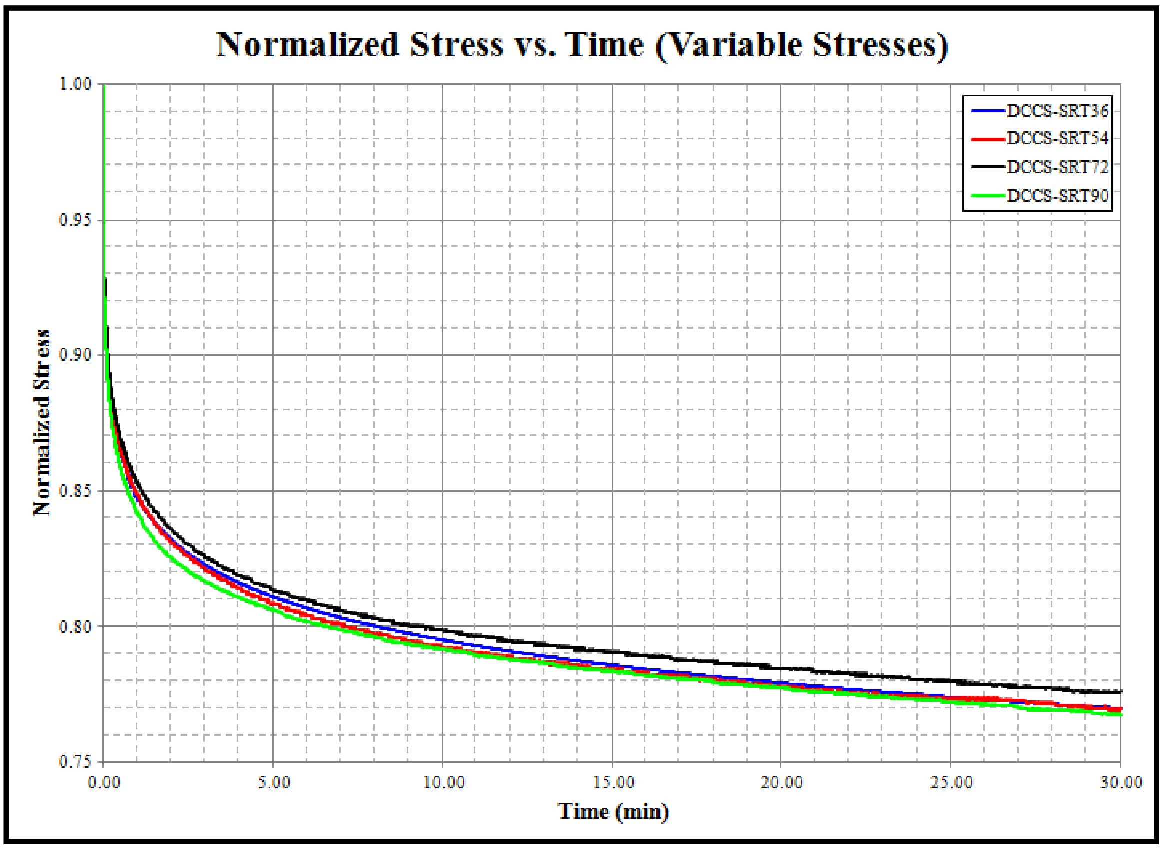

Figure 4.4: DCCS Stress Relaxation with Variable Stresses

Figure 4.4 is a plot of the normalized stress from the four varying stresses over a period of 30 minutes after the initial stress is applied. Stress relaxation ranges from 22 to 24 percent, with almost 15 percent of the overall stress loss coming within the first minute. Each of the relaxation curves and stress losses are very similar, and do not suggest that the DCCS Structure, or in particular, the adhesive interlayer, shows any properties or characteristics that resembles non-linear viscoelastic behavior. This confirms that all individual constituents and the DCCS Structure are capable of being modeled with basic viscoelastic relationships.

Relaxation tests were repeated on the DCCS Structure using the equivalent stress and compressive load required to simulate the baseline torque of 90 ft-lbs. The results and progressive stress loss of these tests are documented in Table 4.5. Like the face sheet, several tests were run with high data acquisition rates and to gain a better understanding of the stress loss in the first minute. From these results alone, it is evident that the interlayer has a significant role in stress relaxation of the DCCS Structure. Despite comprising less than 5 percent of the total thickness in the DCCS Structure, the addition of the interlayer causes the stress relaxation to increase to approximately 25 percent after 100 minutes for the DCCS Structure, compared to nearly 18 percent after 100 minutes for the face sheet. This discrepancy indicates that the interlayer undergoes significantly more stress loss compared to the face sheet and the DCCS Structure as a whole. These results will go under further scrutiny in the next section, where empirical equations will be formulated to model the short-term stress relaxation in the face sheet and DCCS Structure, and basic solid mechanics will be used to create a relationship between the constituents such that stress relaxation in the interlayer can also be modeled.

Table 4.5: DCCS Stress Relaxation with Equivalent Stresses

Sample #	Time Elapsed	Progressive Stress		Percent Loss
DCCS-SRT90-1	0 sec	8735 psi	60.23 MPa	0.00%
	1 sec	8122 psi	56.00 MPa	7.01%
	10 sec	7578 psi	52.25 MPa	13.25%
	60 sec	7205 psi	49.68 MPa	17.52%
DCCS-SRT90-2	0 sec	8735 psi	60.23 MPa	0.00%
	1 sec	8107 psi	55.90 MPa	7.19%
	10 sec	7543 psi	52.01 MPa	13.64%
	60 sec	7138 psi	49.21 MPa	18.28%
DCCS-SRT90-3	0 sec	8735 psi	60.23 MPa	0.00%
	1 sec	8123 psi	56.01 MPa	7.01%
	10 sec	7554 psi	52.08 MPa	13.52%
	60 sec	7168 psi	49.42 MPa	17.94%
DCCS-SRT90-4	0 sec	8735 psi	60.23 MPa	0.00%
	1 sec	8106 psi	55.89 MPa	7.20%
	10 sec	7528 psi	51.90 MPa	13.82%
	60 sec	7134 psi	49.19 MPa	18.33%
DCCS-SRT90-5	0 min	8735 psi	60.23 MPa	0.00%
	1 min	7480 psi	51.57 MPa	14.37%
	5 min	7159 psi	49.36 MPa	18.04%
	10 min	7037 psi	48.52 MPa	19.44%
DCCS-SRT90-6	0 min	8735 psi	60.23 MPa	0.00%
	10 min	6997 psi	48.24 MPa	19.89%
	50 min	6652 psi	45.86 MPa	23.50%
	100 min	6535 psi	45.06 MPa	25.19%

4.3 <u>Formulate Empirical Equation of Stress Relaxation in DCCS Structures (Generalized Maxwell Model)</u>

Results from face sheet and DCCS relaxation testing from the previous section will be utilized to generate empirical equations that model stress relaxation of the constituents over time. Compressive stress relaxation testing of the adhesive interlayer proved difficult due to its high compliance and thinness. However, given that the face sheet and interlayer are the only viscoelastic materials comprising the DCCS Structure, the stress relaxation of the interlayer can be calculated from the results of the face sheet and DCCS Structure using basic mechanics of materials relationships. Figure 4.5 diagrams the basic mechanics of the DCCS Structure during a through-thickness compression test, and the principal stresses experienced within the various constituents.

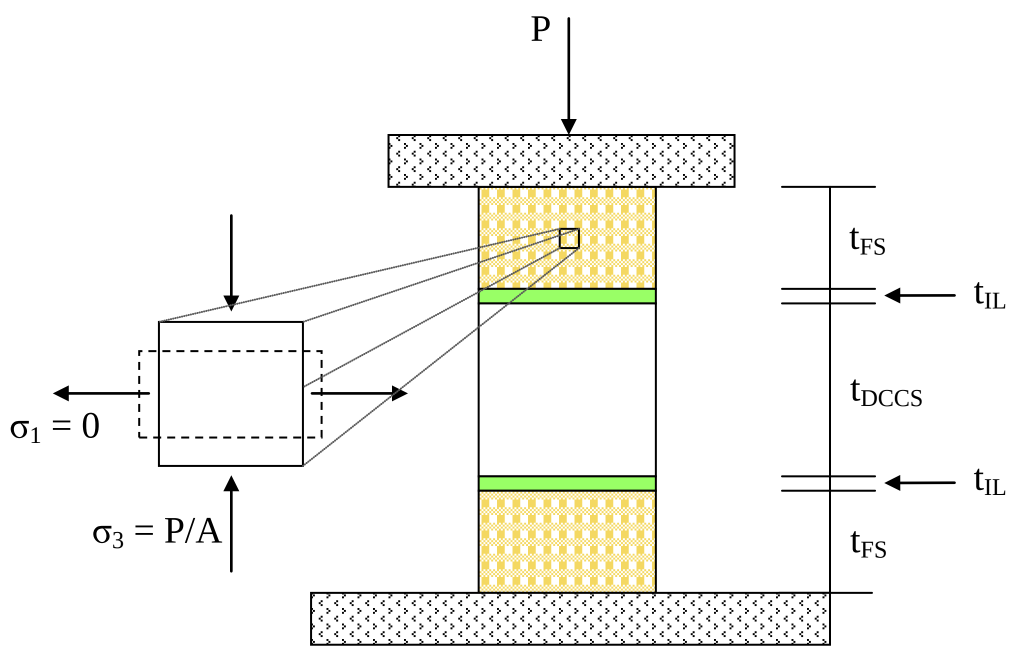

Figure 4.5: Mechanics of DCCS Structure under Compressive Loading

For a given compressive load, each constituent within the DCCS Structure experiences an equivalent compressive stress. If the constituents were isolated and tested individually with the same compressive force (and the same cross-sectional area), they would experience the same compressive stress as they would if the structure were a whole. Thus, the first relationship that can be made is the overall compressive displacement is equal to the sum of the compressive displacement of two face sheets, two sets of adhesive interlayer, and the ceramic core, demonstrated in Equation (4).

$$\Delta_{DCCS} = 2 * \Delta_{FS} + 2 * \Delta_{IL} + \Delta_{CT} \tag{4}$$

The strain of a material is equal the total elongation/displacement of a specimen divided by the specimens length. Rearranging this formula, the total displacement of each constituent is equal to the thickness of the constituent times the strain, changing Equation (4) to Equation (5).

$$\varepsilon_{DCCS} t_{DCCS} = 2 * \varepsilon_{FS} t_{FS} + 2 * \varepsilon_{IL} t_{IL} + \varepsilon_{CT} t_{CT} \tag{5}$$

Hooke's Law states that the stress in a material is equal to the strain times the modulus of elasticity. Applying this theorem to Equation (5), the strain of each constituent is replaced by the stress divided by the modulus, resulting in Equation (6).

$$\frac{\sigma_{DCCS} t_{DCCS}}{E_{DCCS}} = 2 * \frac{\sigma_{FS} t_{FS}}{E_{FS}} + 2 * \frac{\sigma_{IL} t_{IL}}{E_{IL}} + \frac{\sigma_{CT} t_{CT}}{E_{CT}} \tag{6}$$

It was stated earlier that the stress in the DCCS Structure is equivalent to the stress seen in each of the constituents, thus the stress variable can be dropped from Equation (6), leaving Equation (7) as the final relationship between the constituents.

$$\frac{t_{DCCS}}{E_{rel,DCCS}(t)} = 2 * \left(\frac{t_{FS}}{E_{rel,FS}(t)}\right) + 2 * \left(\frac{t_{IL}}{E_{rel,IL}(t)}\right) + \frac{t_{CT}}{E_{rel,CT}(t)} \tag{7}$$

The thickness of each constituent layer in Equation (7) is explicitly known, and it is assumed that the ceramic tile is purely elastic, consequently meaning that the relaxation modulus of the tile is equivalent to the compressive modulus (given according to manufacturer specifications, Table 2.2). This leaves the relaxation modulus of the DCCS Structure, face sheet and interlayer as the only unknowns in Equation (7). However, the former two moduli can be derived from experimental data in Section 4.2, thus allowing the relaxation modulus of the interlayer to be calculated according to the relationship provided in Equation (7).

Several different constitutive viscoelastic models were discussed in Chapter 1, including the strengths and weaknesses associated with each model. The best fit to describe the stress relaxation of the DCCS Structure and its' constituents was the Generalized Maxwell Model. This model consists of a single spring in parallel with several Maxwell Models (Figure 1.7). The relaxation stress in the Generalized Maxwell Model can be calculated according to Equation (8).

$$\sigma(t) = E_{n+1}\epsilon_0 + \sum_{j=1}^{n} E_j \epsilon_0 e^{-\frac{E_j}{\eta_j}t} \tag{8}$$

Where, $\sigma(t)$ = relaxation stress as a function of time, E_{n+1} = modulus of elasticity (or spring constant) of the single spring, ε_0 = initial strain of the material, E_j = modulus of elasticity (or spring constant) at each relaxation time, η_j = viscosity at each relaxation time, and t = time. The previous equation can be simplified by employing the ratio of viscosity to stiffness, $\tau_j = \eta_j/E_j$, which is a measure of the response time. Additionally, the initial strain can be divided throughout the equation to obtain the magnitude of relaxation in terms of elastic modulus. When normalized, the relaxation modulus and relaxation stress are of the same magnitude because the strain does not change during a stress relaxation test. Equation (9) shows the aforementioned changes. At this juncture, Equation (9) can easily be substituted into Equation (7) for the various constituents to ultimately determine the relaxation of the adhesive interlayer.

$$E_{rel}(t) = E_{n+1} + \sum_{j=1}^{n} E_j e^{-\frac{t}{\tau_j}} \tag{9}$$

A collocation matrix is used to determine the modulus of elasticity coefficient for the Generalized Maxwell Model. An example of one used for face sheet and DCCS Structure is shown in Equation (10).

$$\begin{bmatrix} e^{-\frac{t_1}{\tau_1}} & e^{-\frac{t_1}{\tau_2}} & e^{-\frac{t_1}{\tau_3}} & e^{-\frac{t_1}{\tau_4}} & e^{-\frac{t_1}{\tau_5}} & e^{-\frac{t_1}{\tau_6}} \\ e^{-\frac{t_2}{\tau_1}} & e^{-\frac{t_2}{\tau_2}} & e^{-\frac{t_2}{\tau_3}} & e^{-\frac{t_2}{\tau_4}} & e^{-\frac{t_2}{\tau_5}} & e^{-\frac{t_2}{\tau_6}} \\ e^{-\frac{t_3}{\tau_1}} & e^{-\frac{t_3}{\tau_2}} & e^{-\frac{t_3}{\tau_3}} & e^{-\frac{t_3}{\tau_4}} & e^{-\frac{t_3}{\tau_5}} & e^{-\frac{t_3}{\tau_6}} \\ e^{-\frac{t_4}{\tau_1}} & e^{-\frac{t_4}{\tau_2}} & e^{-\frac{t_4}{\tau_3}} & e^{-\frac{t_4}{\tau_4}} & e^{-\frac{t_4}{\tau_5}} & e^{-\frac{t_4}{\tau_6}} \\ e^{-\frac{t_5}{\tau_1}} & e^{-\frac{t_5}{\tau_2}} & e^{-\frac{t_5}{\tau_3}} & e^{-\frac{t_5}{\tau_4}} & e^{-\frac{t_5}{\tau_5}} & e^{-\frac{t_5}{\tau_6}} \\ e^{-\frac{t_6}{\tau_1}} & e^{-\frac{t_6}{\tau_2}} & e^{-\frac{t_6}{\tau_3}} & e^{-\frac{t_6}{\tau_4}} & e^{-\frac{t_6}{\tau_5}} & e^{-\frac{t_6}{\tau_6}} \end{bmatrix} \begin{bmatrix} E_1 \\ E_2 \\ E_3 \\ E_4 \\ E_5 \\ E_6 \end{bmatrix} = \begin{bmatrix} E_{rel}(t_1) - E_{n+1} \\ E_{rel}(t_2) - E_{n+1} \\ E_{rel}(t_3) - E_{n+1} \\ E_{rel}(t_4) - E_{n+1} \\ E_{rel}(t_5) - E_{n+1} \\ E_{rel}(t_6) - E_{n+1} \end{bmatrix} \tag{10}$$

In this matrix, the relaxation time *t*, and response time τ, have been predetermined. The relaxation at the given time increments, $E_{rel}(t_n)$, are experimental values that came from the relaxation tests performed in the previous section. A temporary value for the modulus of elasticity of the single spring is selected. This provides sufficient data to calculate each of the modulus of elasticity coefficients, E_1 through E_6. The coefficients for the Generalized Maxwell Model of the face sheet can be found in Table 4.6. Once the coefficients have been determined, the temporary value for the modulus of the single spring, E_{n+1}, can be back-calculated by using the goal seek function in Microsoft Excel such that the Normalized Stress of the Analytical Model at time zero is equal to 1.0.

Table 4.6: Coefficients for Generalized Maxwell Model – Face Sheet

t, min	j	τ_j, min	E_j, psi	Normalized Stress	
				Experimental	Analytical
0.000				1.0000	1.0000
0.001	1	0.001	0.008791	0.9919	0.9919
0.010	2	0.010	0.021221	0.9728	0.9728
0.100	3	0.100	0.048820	0.9358	0.9358
1.000	4	1.000	0.030432	0.8978	0.8978
10.00	5	10.00	0.039039	0.8621	0.8621
100.0	6	100.0	0.041597	0.8254	0.8254
Infinity*				0.8101	

Using the coefficients from Table 4.6, the Generalized Maxwell Model of the face sheet can predict the stress relaxation over the first 100 minutes after the initial stress and strain is applied to the face sheet. Figure 4.6 plots the normalized relaxation of the face sheet using experimental data and the calculated model. It is evident that the majority of relaxation occurs during this initial time period. Figure 4.7 uses a logarithmic plot of the same data to gain a better understanding of the progressive relaxation. This plot demonstrates that relaxation in the face sheet continues well beyond the 100 minute barrier, but at a much lower rate of stress loss per time.

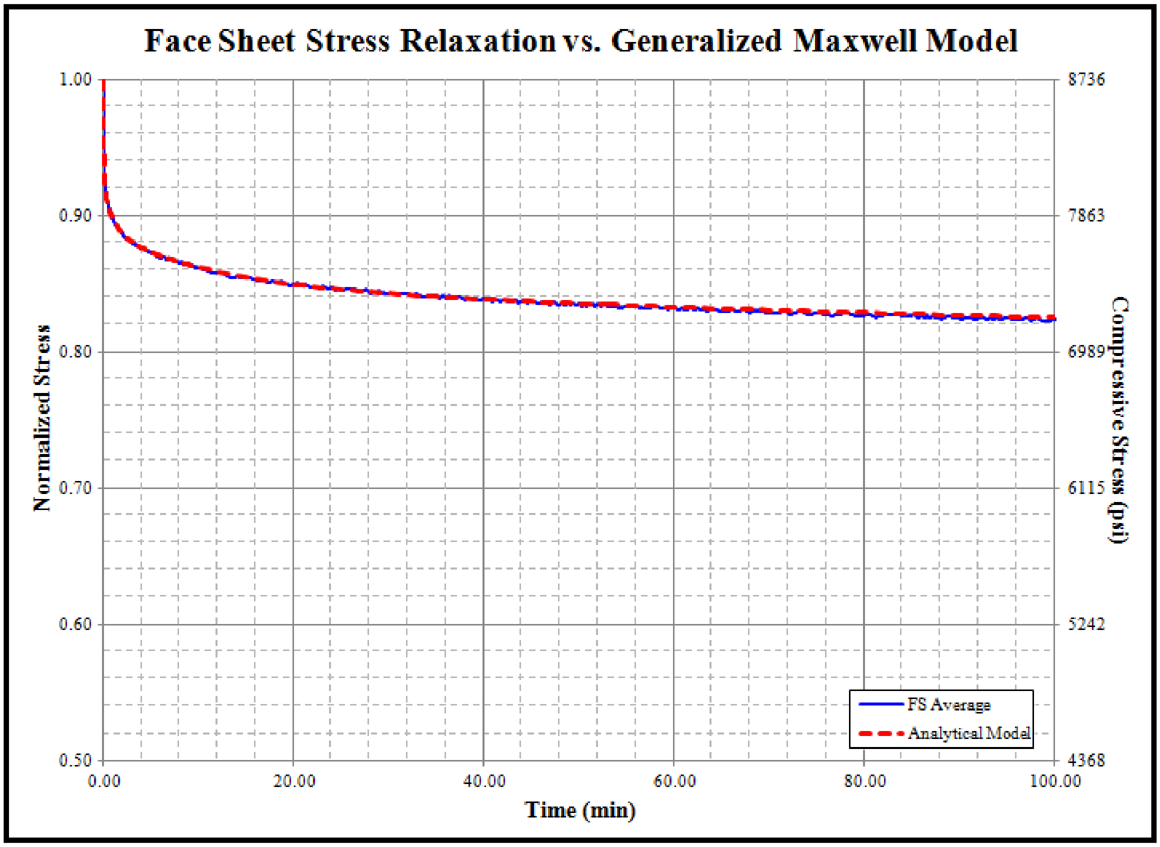

Figure 4.6: Face Sheet Stress Relaxation Average vs. Generalized Maxwell Model (Regular Plot)

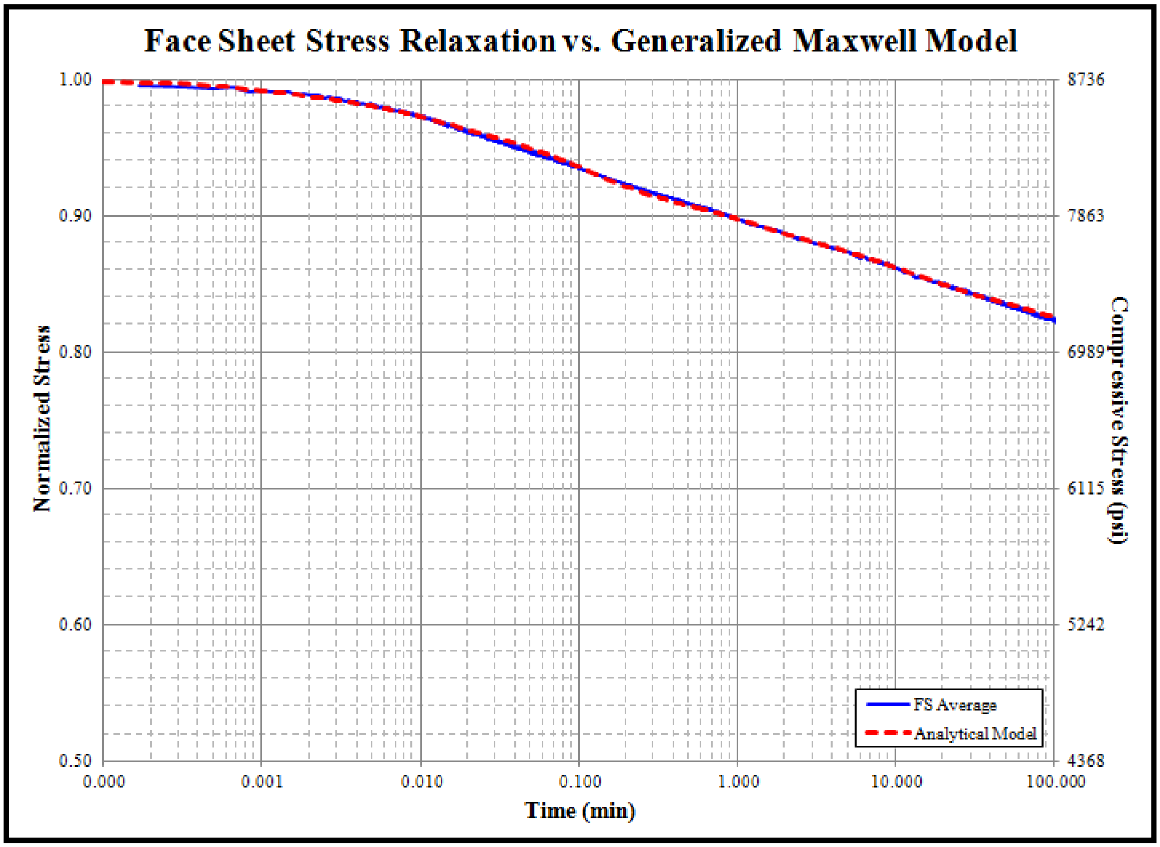

Figure 4.7: Face Sheet Stress Relaxation Average vs. Generalized Maxwell Model (Log Plot)

Table 4.7: Coefficients for Generalized Maxwell Model – DCCS Structure

t, min	j	τ_j, min	E_j, psi	Normalized Stress	
				Experimental	Analytical
0.000				1.0000	1.0000
0.001	1	0.001	0.008359	0.9902	0.9902
0.010	2	0.010	0.040408	0.9597	0.9597
0.100	3	0.100	0.061321	0.9071	0.9071
1.000	4	1.000	0.050160	0.8525	0.8525
10.00	5	10.00	0.054208	0.8003	0.8003
100.0	6	100.0	0.054482	0.7511	0.7511
Infinity*				0.7311	

The identical process used to formulate the Generalized Maxwell Model for the face sheet was used for the DCCS Structure. The collocation matrix used from Equation (10) utilized the same relaxation times (*t*) and response times (τ), and instituted results from the previous section for the relaxation values of the DCCS Structure. These values and the calculated coefficients are found in Table 4.7. Figure 4.8 plots the normalized relaxation of the DCCS Structure using experimental data and the calculated model. Like the face sheet, a majority of relaxation occurs immediately, with the rate of stress loss gradually decreasing over the first 100 minutes. Figure 4.9 uses a logarithmic plot of the same data to determine if the relaxation has reached, or begun to approach the rubbery plateau. The rubbery plateau, or the equilibrium moduli, is the time at which all relaxation has stopped. The plot confirms that, like the face sheet, relaxation is ongoing well beyond the 100 minute barrier, albeit at a much slower rate of relaxation.

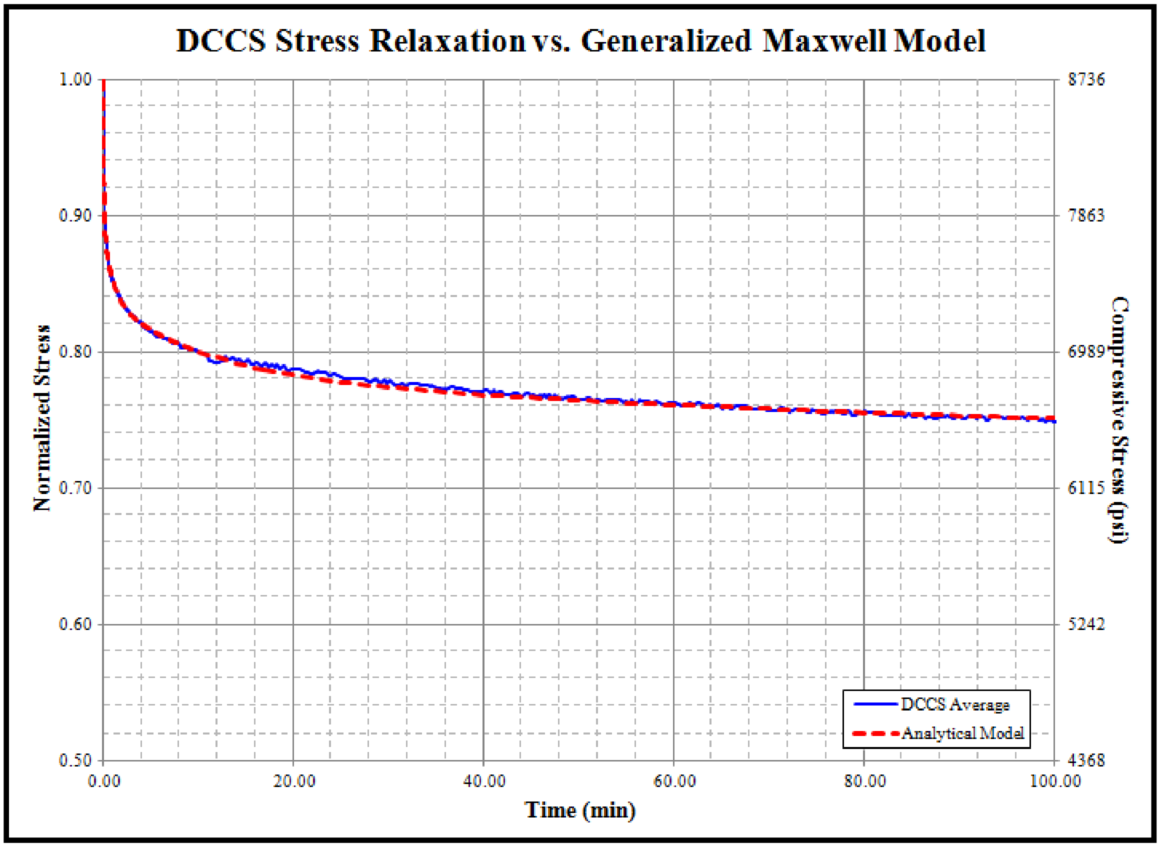

Figure 4.8: DCCS Stress Relaxation Average vs. Generalized Maxwell Model (Regular Plot)

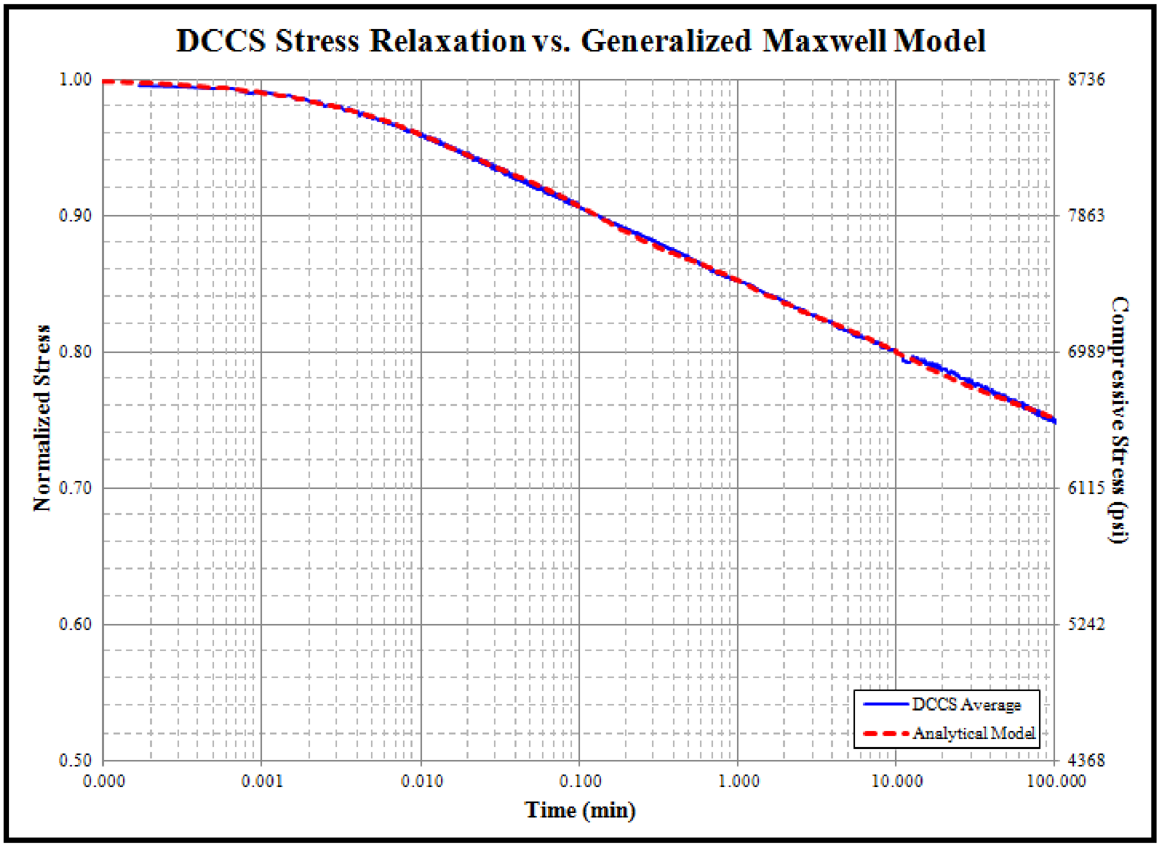

Figure 4.9: DCCS Stress Relaxation Average vs. Generalized Maxwell Model (Log Plot)

Table 4.8: Coefficients for Generalized Maxwell Model – Interlayer

t, min	j	τ_j, min	E_j, psi	Normalized Stress	
				Experimental	Analytical
0.000				1.0000	1.0000
0.001	1	0.001	0.117477	0.8858	0.8858
0.010	2	0.010	0.406999	0.6138	0.6138
0.100	3	0.100	0.104941	0.3952	0.3952
1.000	4	1.000	0.144203	0.2769	0.2769
10.00	5	10.00	0.019432	0.2076	0.2076
100.0	6	100.0	0.068252	0.1638	0.1638
Infinity*				0.1387	

To obtain the data for the Generalized Maxwell Model of the adhesive interlayer, the use of Equation (7) was required. The model could be calculated one of two ways; the first would use experimental data from the face sheet and DCCS Structure, in conjunction with Equation (7), to determine hypothetical experimental results of the interlayer; the second would be incorporating the models of the face sheet and DCCS Structure into Equation (7), creating a model for the interlayer that was a function of the other models. Ideally, the interlayer model should be independent of the other constituents, thus the former concept was used. Using the hypothetical data for the interlayer, the models constants and variable coefficients were calculated (Table 4.8). The results of the Generalized Maxwell Model and hypothetical data were plotted on a regular plot (Figure 4.10) and a logarithmic plot (Figure 4.11). Based on the plots, the interlayer was shown to have strong viscous characteristics, with total stress loss exceeding 84 percent over the course of the 100 minute test. Nearly 60 percent was lost instantaneously, along with an additional 20 percent in the 20 minutes following the initial stress/strain was applied. Based on the relaxation data from the face sheet and DCCS Structure, where the relaxation of the DCCS Structure exceeded the relaxation of the face sheet by approximately 7-8 percent, it was predetermined that the interlayer had a significant influence on the relaxation in the DCCS Structure. Given the interlayer properties, including its high compliance and strain-to-failure rate, the magnitude of relaxation was not unexpected. Stress relaxation testing will continue by incorporating the mechanical joint, as well as introducing various methods to reduce the amount of relaxation at the joint.

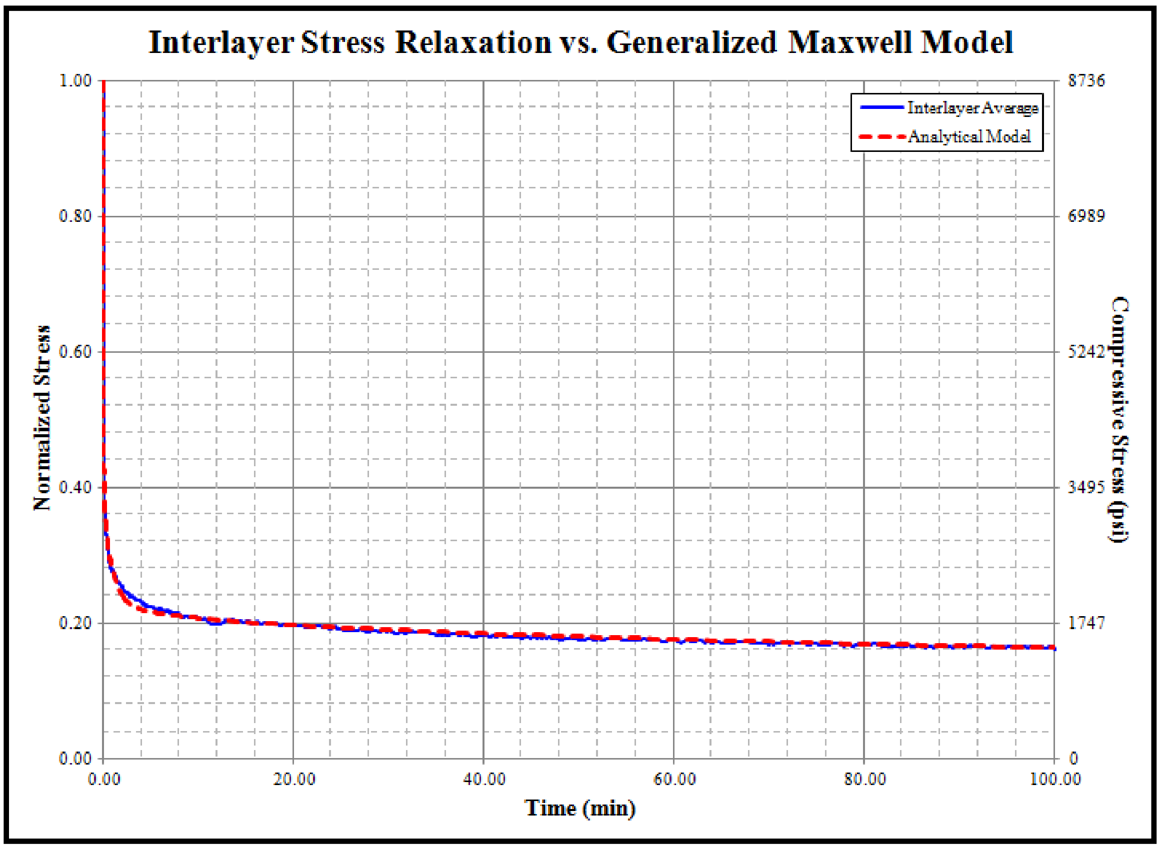

Figure 4.10: Interlayer Calculated Stress Relaxation vs. Generalized Maxwell Model (Regular Plot)

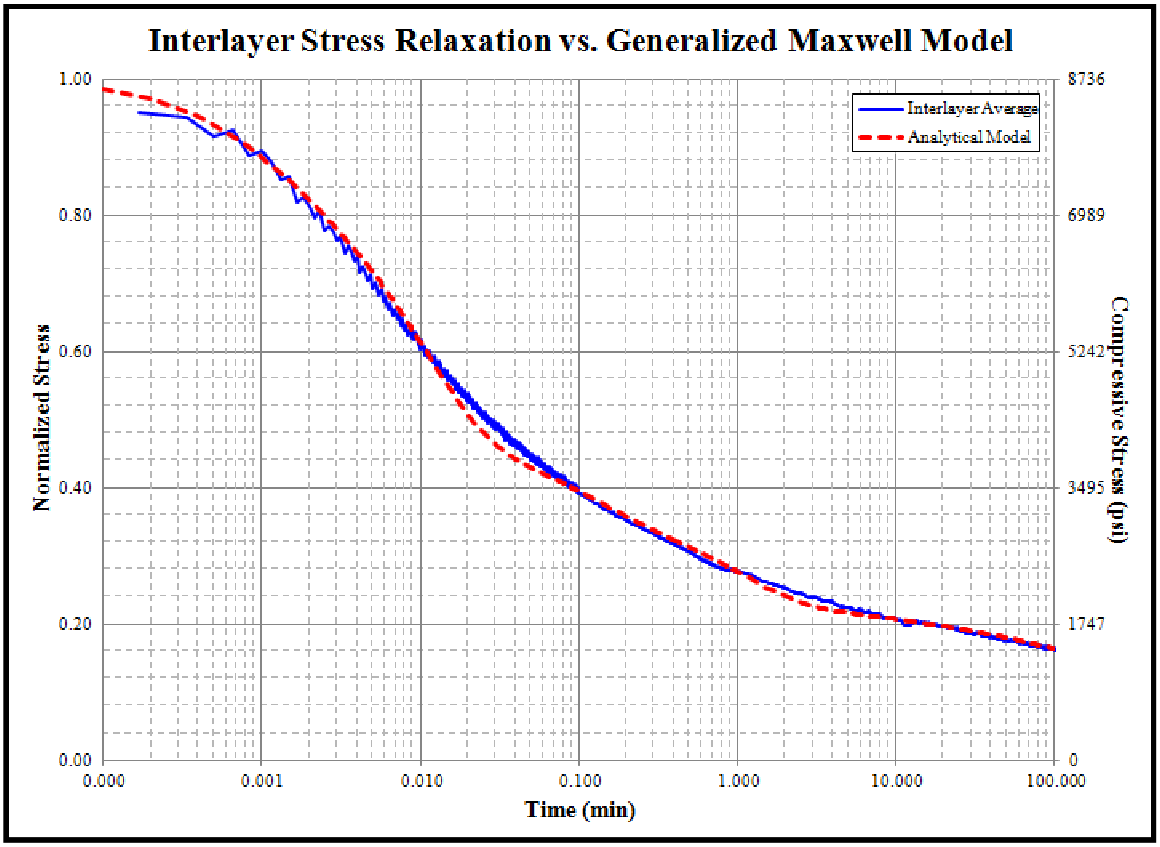

Figure 4.11: Interlayer Calculated Stress Relaxation vs. Generalized Maxwell Model (Log Plot)

4.4 Relaxation Test Using Washer Load Cell

Stress relaxation testing of the joint required a different testing set-up and method of obtaining data. Specimens were 4 inches by 4 inches, with a 0.5 inch hole core-drilled precisely in the center. This geometry was chosen to minimize specimen size, but allow a full tile to experience potential compressive stresses to the regions of discontinuity in the core, and maintain the baseline w/D and e/D ratios employed during static and fatigue testing. This test configuration is considered to most accurately replicate the actual joint loading in terms of loading and associated stress and deformation states related to the bolt hole. The test set-up used a sturdy base fixture used for transverse load testing of the DCCS Structure. This base employs a hole suitable for 0.5 inch bolts that restricts turning so torque can be applied. A washer load cell is placed through the bolt on top of the base, with the specimen positioned on top of the load cell (Figure 3.7). Torque is measured using a calibrated torque wrench, and the load cell reading should equate to the appropriate clamping load based on the torque. There was a small amount of variability between the expected clamp load and magnitude of torque; this discrepancy can be attributed to friction differences between each joint. The relationship between torque and clamping load is based on the torque coefficient *k* in Equation (2), which is a function of the materials frictional characteristics, including surface finish, coatings, thread quality, etc., all of which can vary from test to test. This torque coefficient typically ranges from 0.14 to 0.26 for steel fasteners, with a value of 0.2 widely assumed in engineering applications when a value is not explicitly known. To this point in the DCCS joint design, all calculations presumed a torque coefficient of 0.2. Using the washer load cell experimental set-up, it was possible to better-define a value for the torque coefficient. Applying various levels of torque with numerous repetitions provided sufficient data to conclude an actual torque coefficient of approximately 0.251. This is confirmed by the calibration chart in Figure 4.12. This revised torque coefficient will be utilized for all further calculations.

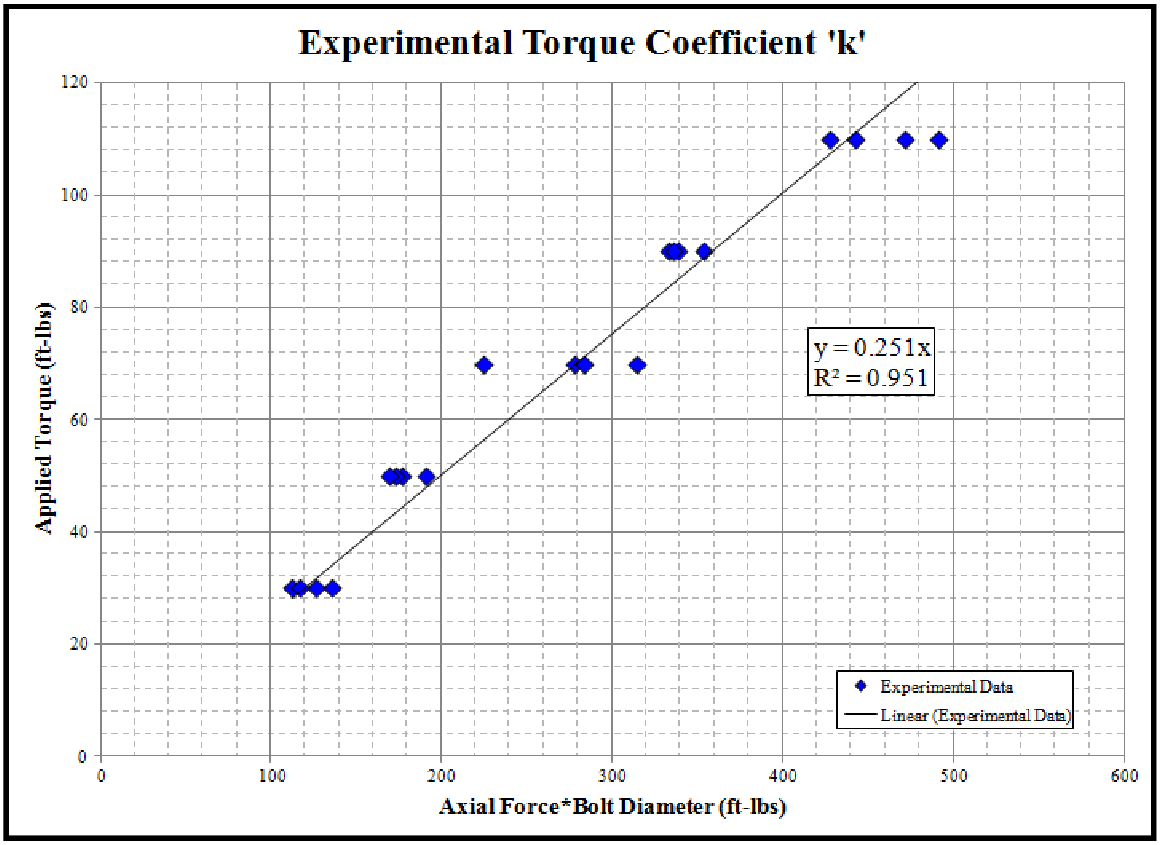

Figure 4.12: Calibration Chart of Torque Coefficient 'k'

A total of four relaxation tests were performed at the baseline torque of 90 ft-lbs (clamping force of approximately 8610 lbs). Of the four tests, three emitted high frequency acoustic emissions characteristic of tile cracks. One case occurred immediately after the baseline torque was achieved, while two others occurred within the first ten minutes of relaxation. These emissions were accompanied by instantaneous drops in clamp load, seen in Figure 4.13.

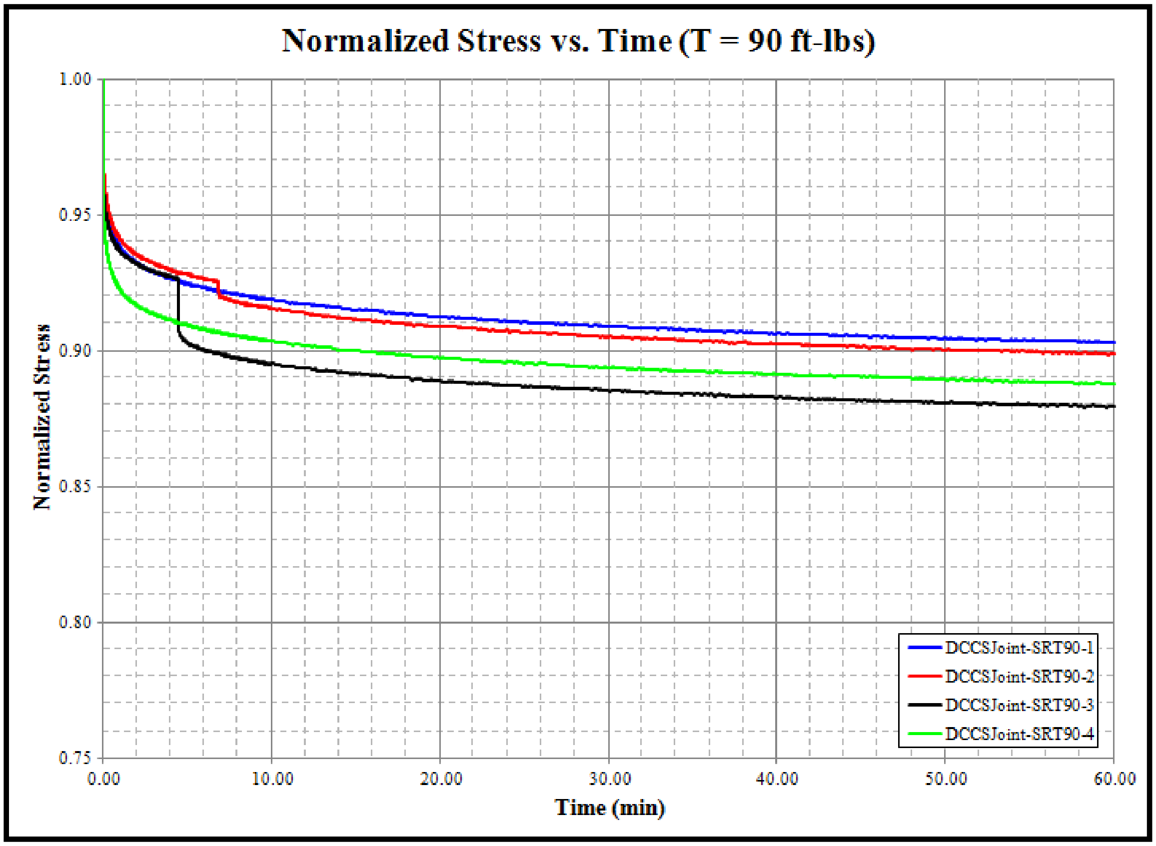

Figure 4.13: Stress Relaxation of DCCS Joint with 90 ft-lbs of Torque

After the tests were completed, specimens were removed and the joint was examined with blue dye. Figure 4.14 shows hairline cracks in the ceramic tile of a single specimen. The image on the far left was taken at 0/360 degrees, with each subsequent picture taken after rotating the specimen 90 degrees. This particular specimen demonstrated 3 cracks, each separated by roughly 120 degrees. According to material properties of the three constituents (see Table 2.1 and 2.2), the ceramic tile is the strongest in compression and very weak in tension, making the presence of cracks due to the compressive clamping force confounding. The only reasonable explanation for the cracks was that the tile was experiencing circumferential tensile stresses due to the application of the clamping force. Before proceeding with further relaxation testing, the cracks were investigated to better understand their origin and prevent future failure in this manner.

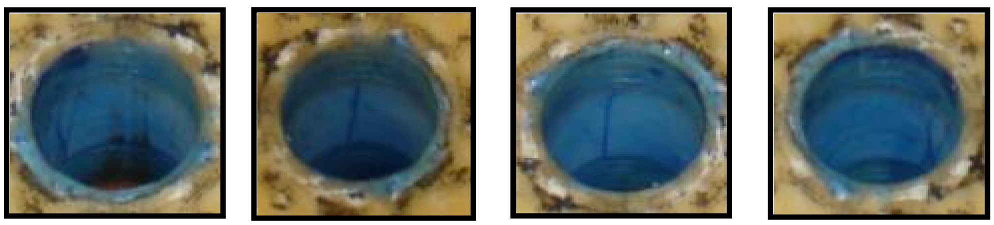

Figure 4.14: Hairline Cracks in Ceramic Tile Due to Hoop Stresses caused by Torque

4.5 <u>Hoop Stresses in Ceramic Tile Due to Clamping Forces</u>

In engineering applications, hoop stresses are routinely seen in thin-walled vessels with radial pressure on the inner wall forcing the diameter to increase, consequently leading to circumferential stresses, also called hoop stresses. Hoop stresses, in addition to radial stresses and axial stresses, make up the three primary directions in the cylindrical coordinate system. Under this premise, hoop stresses typically govern fracture of a material since it is routinely the largest principal stress when no other external loads are applied. However, in the case of the DCCS joint, the e/D ratio is 4.0, far exceeding the ID-to-OD conditions of a “thin-walled” vessel, and there exists an external force, thus potentially negating circumferential stresses as the largest principal stress. The effect of having “thick” walls, or in the case of the DCCS joint, a high e/D ratio, means that the joint is more confined and resistant to expansion. And while the greatest hoop stress occurs along the hole boundary, the stresses dissipate the further from the boundary, and in all likelihood, near zero along the tile edges (as a result of the e/D ratio). The clamping force is applied in the axial direction, causing compression of the joint’s length. Of the principal stresses, the axial stress is the largest, however, because the ceramic tile has such high compressive strength, this stress does not govern fracture of the ceramic tile. Instead, the circumferential stress causes fracture because of the weak tensile properties of the ceramic tile, and the fact that compression of the joint causes tensile hoop stresses. To gain a better understanding of the cause of tensile hoop stresses in the DCCS joint, a thorough and progressive analysis will be conducted. Several plots will be presented that are normalized according to the geometric parameters seen in Figure 4.15. The analysis will be begin by examining the effect of discrepancies in the Poisson ratio of each constituent and whether that discrepancy is the cause for significant hoop stresses in the ceramic tile. Basic mechanics will be used to explain Poisson ratio and transverse strains in a simplified version of the DCCS Structure, followed by the effect of bonding the constituents, incorporating friction between the washer and face sheet (in the joint arrangement), and the role of the adhesive interlayer located between the face sheet and ceramic tile. This mechanical analysis will be conducted under the assumption of uniform compression. However, because uniform compression does not depict the true nature of the joint, a finite element model will be used to address the complications that cannot be resolved in the mechanical analysis. The model should provide an accurate representation of the stress distribution around the joint. The model will also be utilized in selecting an appropriate friction coefficient between the face sheet and washer for future modeling endeavors.

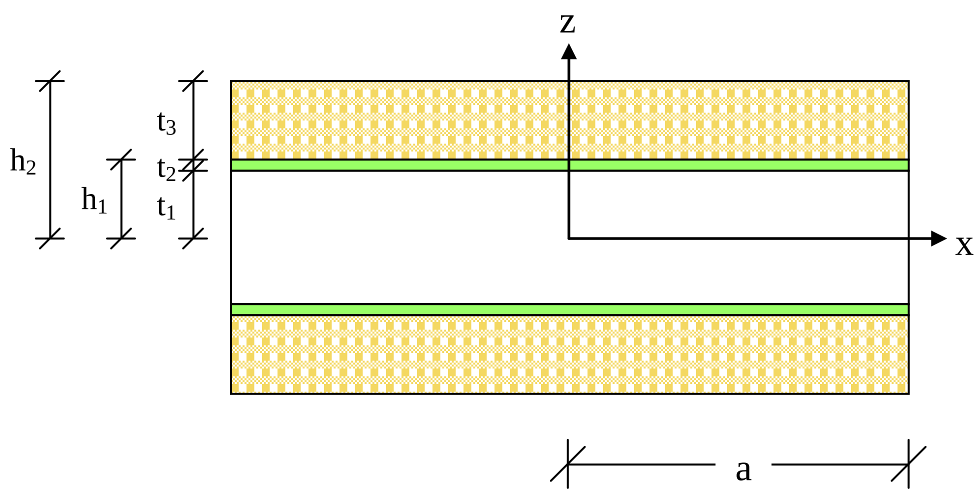

Figure 4.15: Geometric Parameters for DCCS Structure

A preliminary finite element model was created with the sole purpose of determining the effect of the Poisson ratio and transverse strains on hoop stress in the ceramic tile. The model was created without the presence of the interlayer; the interlayer stiffness is several orders of magnitude less than the ceramic tile and face sheet causing it to have very high compliance, for this reason, it was omitted in order to better visualize the transverse strains in the face sheet and ceramic tile. The first computation utilized the prescribed Poisson ratio for the face sheet and ceramic tile; the second computation assumed the Poisson ratio to be zero for each. Figure 4.16 compares the hoop stress from each analysis through the thickness of the ceramic tile ($z/t = 0$ is the center of the tile and $z/t = 1$ is the tile/face sheet interface) where the maximum stress occurs at the mid-tile thickness. It can also be seen that the computation performed with the presence of Poisson ratios exhibited much higher hoop stresses than the computation without Poisson ratios. This gives reason beyond a doubt that the existence of varying transverse strains between constituents is a major cause for hoop stresses in the ceramic tile. The next step is to look at the basic mechanics of the DCCS Structure under uniform compression to see the reactions of the constituents and provide supplemental assurance that hoop stresses are caused by the difference in Poisson strains.

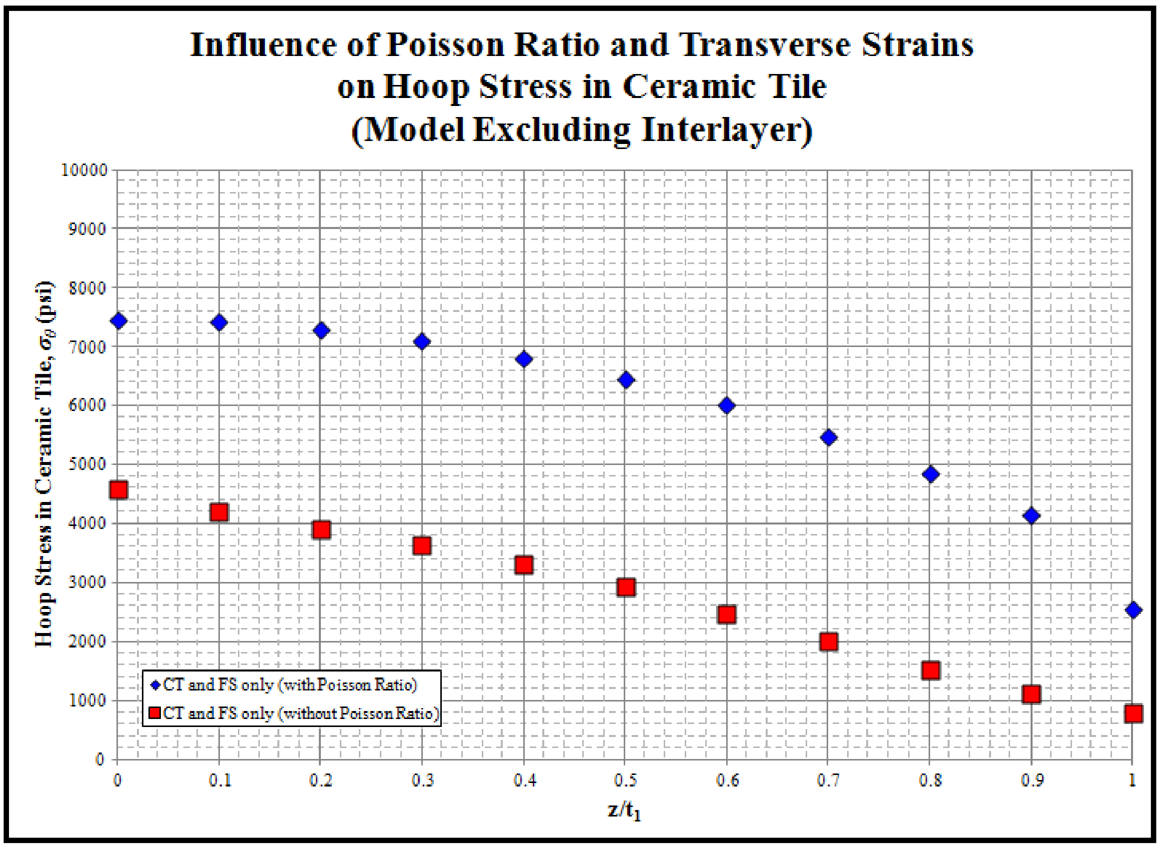

Figure 4.16: Influence of Poisson Ratio and Transverse Strains on Hoop Stress in Ceramic Tile

To gain a better understanding of the mechanics and interaction of the constituents under a clamp load, a free body diagram with principal stresses of the constituents was sketched (see Figure 4.17). The clamping force from the bolt head and nut is transferred through the washer into the face sheet. Assuming the bolt and washer to be rigid, pressure from the clamping force is spread throughout the full contact area between the washer and face sheet. Under compressive forces in the through-thickness direction of a composite, each layer undergoes compressive normal strain in the load direction. The amount of compressive strain in a layer will be dependent on the layer thickness and the through thickness modulus of the layer. Although the thickness of the ceramic is the large, the stiffness of the ceramic is approximately 30 and 700 times stiffer than the face sheet and adhesive layers, respectively. Consequently most of the deformation occurs in the compliant layers. In addition, each layer will undergo a positive inplane tensile strain due to Poisson ratio. The magnitude of this tensile strain will be proportional to the through thickness compressive strain of the layer. Note that the layers are bonded together and that the inplane tensile strain is restricted by a stiff ceramic layer. Consequently, this interaction subjects the ceramic to inplane tensile stress and the face sheet in inplane compressive stress. The adhesive is thin and compliant and is likely highly loaded in shear due to this interaction. (The interlayer has been omitted from Figure 4.17 to simplify the mechanical representation and focus solely on the compressive strain in the DCCS Structure. The presence of the interlayer and its' importance will be addressed later in this section.) The total net inplane forces between these layers are self-equilibrating. At the free-edge of the bolt hole, all normal and shear stresses are identically zero. Hence there is a boundary layer of stresses that exist where load transfer between layers occurs (i.e. regions of shear stress and deformation). These interactions can be explained in a step-by-step analysis highlighting the effect of Poisson ratio, tensile strains, inplane stresses attributed to adjacent constituents and friction influences.

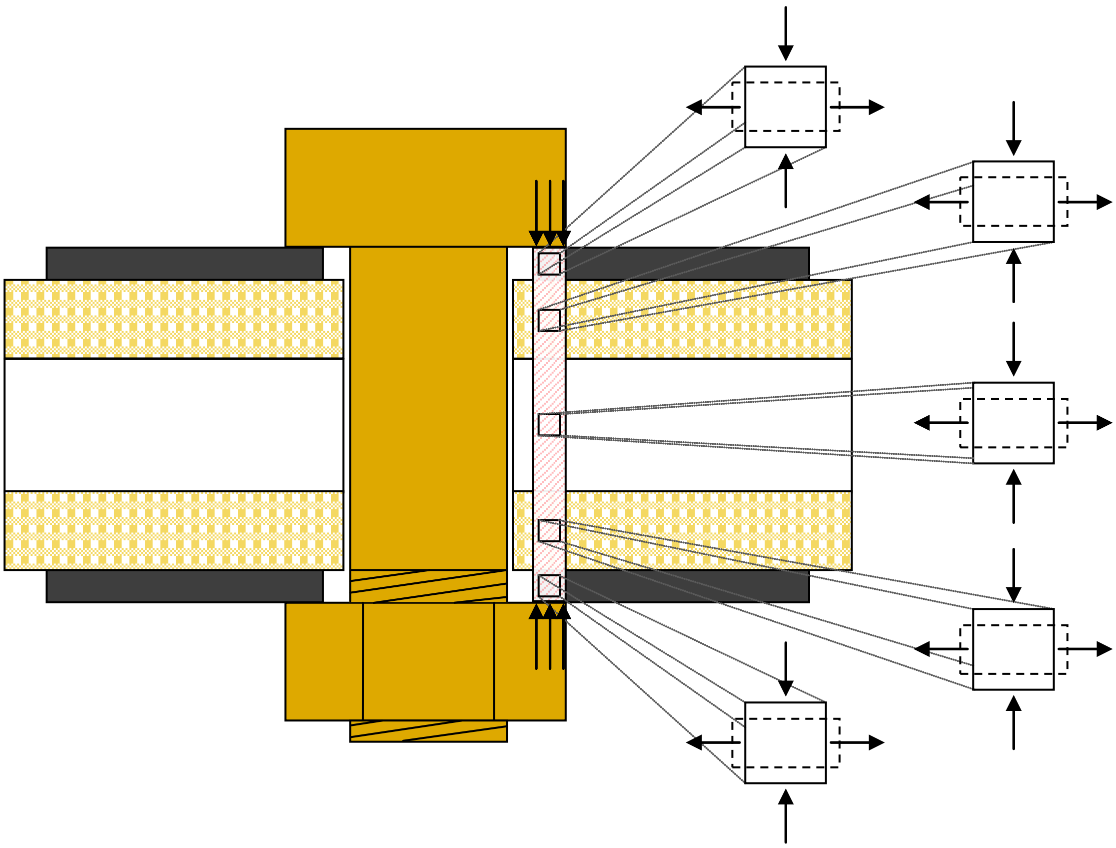

Figure 4.17: Free Body Diagram of DCCS Structure under Clamp Load at the Joint

Consider the DCCS Structure such that it was fabricated without the adhesive interlayer and there was no bonding between the face sheet and ceramic tile; applying a uniform compression on the DCCS joint (with the absence of the interlayer) may look like Figure 4.18. Note that the face sheet exhibits the most inplane tensile strain, followed by the washer and face sheet, for the reasons stated previously. Next, assume that the face sheet and ceramic tile are completely bonded and allow no movement relative to one another. In this case, the face sheet has a tendency to induce inplane tensile stresses on the ceramic tile and increase the inplane strain, whereas the ceramic tile induced inplane compressive stresses on the face sheet, reducing the inplane strain. As a result, the true strain experienced at the interface of the face sheet and ceramic tile occurs somewhere between the strain that the face sheet and tile would experience without bonding. This proposed situation is diagrammed in Figure 4.19. The next hypothetical scenario introduces a friction force between the face sheet and washer. Because the face sheet has a tendency to show greater inplane strains than the washer, the friction force resists this tendency to expand. Now, the face sheet's inplane growth is being restrained by the friction force inflicted by the washer, along with the bond of the ceramic tile. This confines the face sheet on both surfaces, and hypothetically, would reduce the amount of inplane strain inflicted on the ceramic tile, as proposed in the prior case. Figure 4.20 shows the deformed shape of this case. The last scenario to consider is to include the presence of the interlayer. Due to its' compliant nature, the interlayer will be inclined to shear along the face sheet – ceramic tile interface, allowing both to revert closer to their original deformed state shown in Figure 4.18. This leads to the image seen in Figure 4.21. According to these basic mechanical features, it has been shown that hypothetically, friction between the washer and face sheet restricts the inplane strain of the face sheet, potentially reducing strains in the ceramic tile; and the interlayer creates a compliant interface between the face sheet and ceramic tile, also reducing the effect of strain discrepancies and preventing additional strain in the ceramic tile.

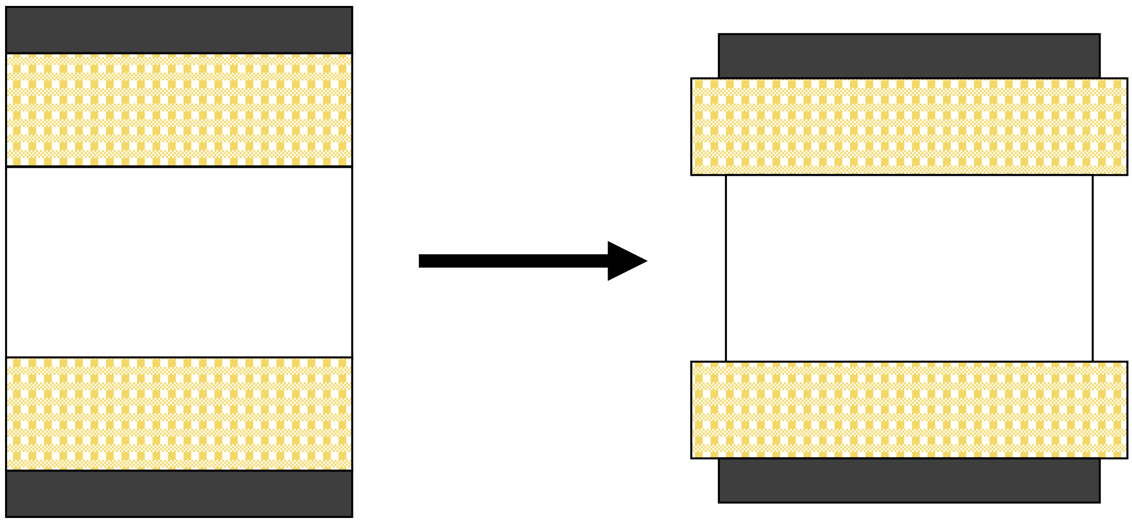

Figure 4.18: Mechanics of Un-bonded DCCS Structure Due to Uniform Compression (without Interlayer)

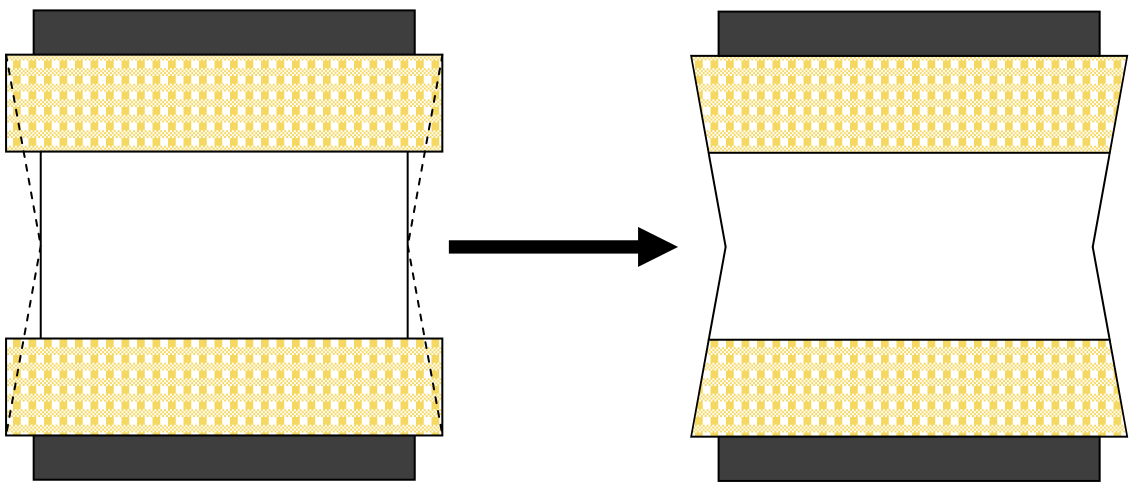

Figure 4.19: Mechanics of Bonded DCCS Structure Due to Uniform Compression (without Interlayer)

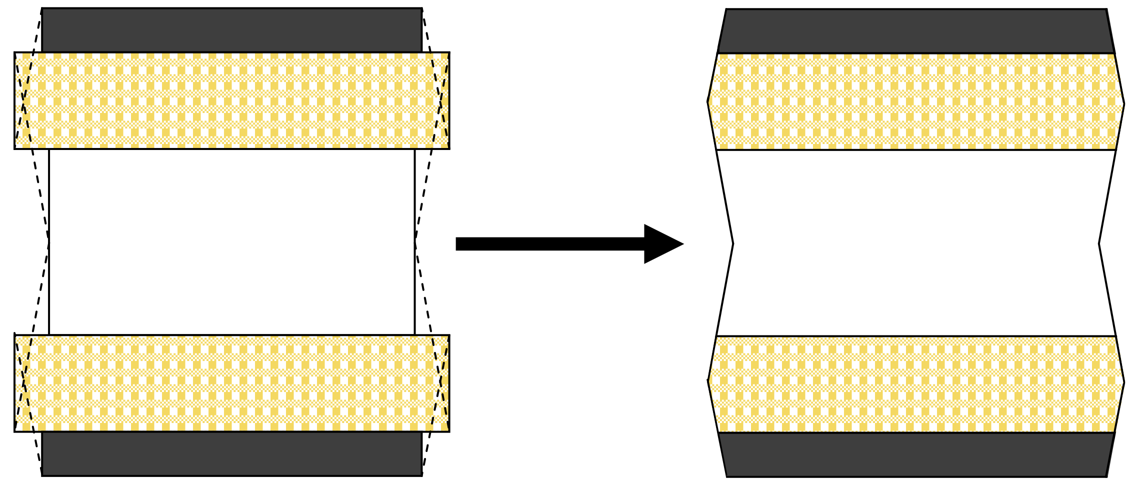

Figure 4.20: Mechanics of Bonded DCCS Structure with Friction Coefficient Due to Uniform Compression (without Interlayer)

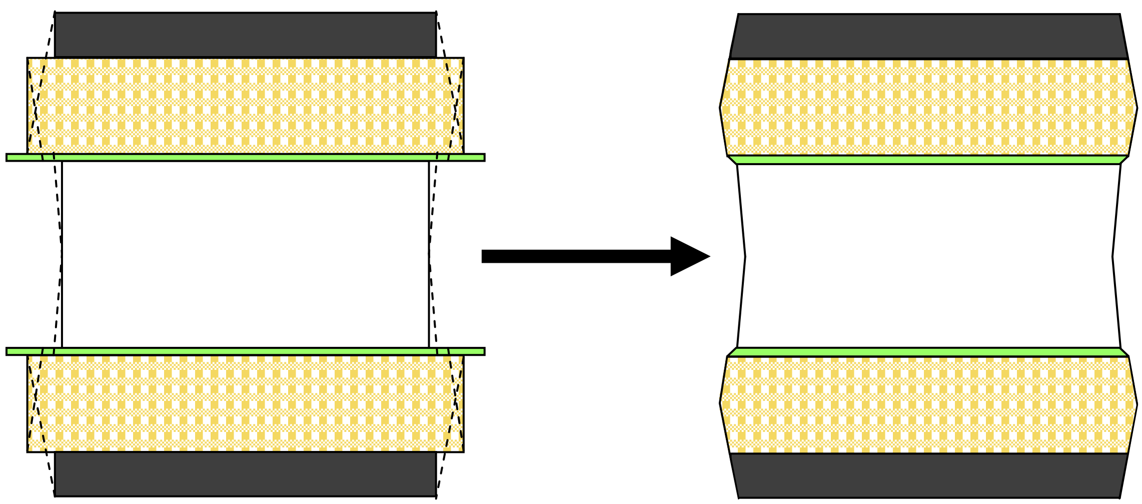

Figure 4.21: Mechanics of Bonded DCCS Structure with Friction Coefficient Due to Uniform Compression (with Interlayer)

Understanding the basic mechanics of the interaction between constituents under uniform compression can only explain part of the reaction in the joint due to the clamping force. Because the force is not uniformly distributed over the joint surface, there exists a compression-shear interaction along the force boundaries, and friction parameters control the amount of sliding between the face sheet and washer, inducing some rotation caused by the combination of the friction force and compression-shear interaction. To visualize the stress distribution throughout the joint due to the clamping force, a finite element model was created. Like the previous analysis, one model was created without the interlayer to attain a basic premise as to the interaction between the face sheet and ceramic tile, and a second model incorporated the interlayer into the DCCS Structure to identify its' influence on the compressive stress distribution.

The model was created in CATIA, "Computer-Aided Three-dimensional Interactive Application" software targeted at product design, engineering and manufacturing, and equipped with finite element analysis tools. The model utilized a ¼ symmetric design, capable due to the thru-thickness and in-plane symmetry of the DCCS Structure. Reducing the size of the model conserved computation time during the solver process. Each constituent of the model was created separately as a CATIA Part, and assembled together as a CATIA Product. The face sheet was modeled as 4 inches long (101.6 mm) by 2 inches wide (50.8 mm) by 0.247 inches thick (6.27 mm). The adhesive interlayer was modeled as 4 inches long (101.6 mm) by 2 inches wide (50.8 mm) by 0.02 inches thick (0.508 mm), when present in the model. Each ceramic tile was modeled as 4 inches long (101.6 mm) by 2 inches wide (50.8 mm) by 0.2 inches thick (5.08 mm). The ceramic tile, interlayer, resin gap, washer and bolt were designated as isotropic materials, using properties defined in Table 4.9. The face sheet was designated as a 3D orthotropic material, using the properties from Table 4.10. These properties were determined in a mechanical characterization testing program performed by Dr. John W. Gillespie Jr. and Chris Arvanitelis at the Center for Composite Materials, University of Delaware.

Table 4.9: Material Properties Used for FEA Modeling (Ceramic Tile, Adhesive Interlayer, Resin Gap, and Steel Bolt/Washer)

Material	Units	Modulus	Poisson Ratio
Ceramic Tile	US	51.0 Msi	0.22
	metric	350 GPa	0.22
Adhesive Interlayer	US	71.0 Ksi	0.35
	metric	.489 GPa	0.35
Resin Gap	US	71.0 Ksi	0.35
	metric	.489 GPa	0.35
Steel Washer	US	29.0 Msi	0.25
	metric	200 GPa	0.25
Steel Bolt	US	Rigid	0.25
	metric	Rigid	0.25

Table 4.10: Material Properties for FEA Modeling (Face Sheet Only)

Inplane		**Interlaminar**	
Tension		Tension	
E_1^T (Msi)	3.25	E_3^T (Msi)	1.70
E_2^T (Msi)	3.34	S_3^T (Ksi)	1.21
υ_{12}^T	0.11	ε_3^T (%)	0.07
υ_{21}^T	0.10	υ_{31}^T	0.13
X_1^T (Ksi)	69.6	υ_{32}^T	0.18
X_2^T (Ksi)	87.2		
ε_1^T (%)	2.56		
ε_2^T (%)	2.84		
Compression		Compression	
E_1^C (Msi)	3.66	E_3^C (Msi)	1.79
E_2^C (Msi)	4.19	S_3^C (ksi)	43.5
X_1^C (Ksi)	39.2	ε_3^C (%)	2.44
X_2^C (Ksi)	30.8	υ_{31}^C	0.19
ε_1^C (%)	1.02	υ_{32}^C	0.21
ε_2^C (%)	0.74		
Shear (1-2) (2 Rail)		V-Notch (1-3)	
G_{12} (Msi)	0.42	G_{13} (Msi)	0.43
S_{12} (Ksi)	5.47	S_{13} (Ksi)	5.03
γ_{12} (%)	4.89	γ_{13} (%)	>5.0
		V-Notch (2-3)	
		G_{23} (Msi)	0.44
		S_{23} (Ksi)	5.16
		γ_{23} (%)	4.58

Meshes were assigned to each individual part; the face sheet, ceramic tile, and interlayer were designed with a surface mesh that was refined with smaller elements near the joint hole; the built-in Sweep function was used to extrude 10 evenly-spaced three-dimensional elements to replicate the surface mesh through the thickness of the face sheet and ceramic tile; the same function was used to create 3 evenly-spaced three-dimensional elements through the thickness of the interlayer; an octahedral three-dimensional mesh was assigned to the bolt and washer using mesh sizes of 0.4 inches and 0.15 inches, respectively. A fastened connection mesh was used to connect the interface between the face sheet and ceramic tile within the first model; fastened connection meshes connected the face sheet and interlayer, and interlayer and ceramic tile in the second model. A contact connection mesh was used to connect the interface between the washer and face sheet; the friction component of this connection was varied to examine the influence of various magnitudes of friction coefficients on the hoop stress in the ceramic tile. Frictionless contact connection meshes, which prevent embedment between interfaces, were used between the bolt shank and the face sheet, interlayer, and ceramic tile along the bearing surface. The bolt was restricted from moving in the x- and y-directions, but allowed to expand in the z-direction due to the axial load applied to the shank to simulate the clamping force. Other restraints applied to the model to simulate symmetry were located on the bottom of the model in the z-direction, and along the edge of the model in the y-direction. A pressure load was applied on the end of the bolt shank to simulate the equivalent of 90 ft-lbs of torque.

The first model was computed without the interlayer, but used variable friction parameters. These included no friction between the washer and face sheet, friction ratios of 0.1, 0.3 and 0.5, and then a fastened connection which prevented any sliding at the interface. The purpose of this analysis was to examine the direct impact of friction on hoop stresses, and finalizing an appropriate coefficient of friction for further models. Figure 4.22 displays the hoops stress in the ceramic tile using the various friction effects. The peak hoop stress occurs at mid-tile in each circumstance, with approximately 2000 psi discrepancy between the highest resulting hoop stress (fastened model) and the lowest (frictionless model). According to the plot, hoop stresses increase with an increase in the friction, with a friction coefficient of 0.5 falling almost directly between the fastened and frictionless model. As stated before, several interactions between compression-shear planes and friction surfaces influence the deformation of the joint. To visualize this deformation, Figure 4.23 is presented with displacement on a 10:1 scale in the thru-thickness direction and a 100:1 scale in the transverse direction. These scales allow for the deformation to be easily identified, since the magnitude of displacement is typically not visible to the human eye. It can be seen from the plot that the face sheet nearest the hole boundary undergoes the most compressive displacement, whereas the regions near the outer diameter of the washer experience very little compression. Because the clamping force is applied on the innermost portion of the washer surface, the washer tends to rotate, with the interface of the washer and face sheet moving away from the hole. Due to the friction at this interface, the face sheet accompanies the washer in this rotation. With increased friction between the washer and face sheet, the more the face sheet is pulled from original hole boundary. And because the face sheet is being pulled outward, the ceramic tile inherently experiences the same reaction. This is the cause for increased hoop stress when the friction coefficient is increased.

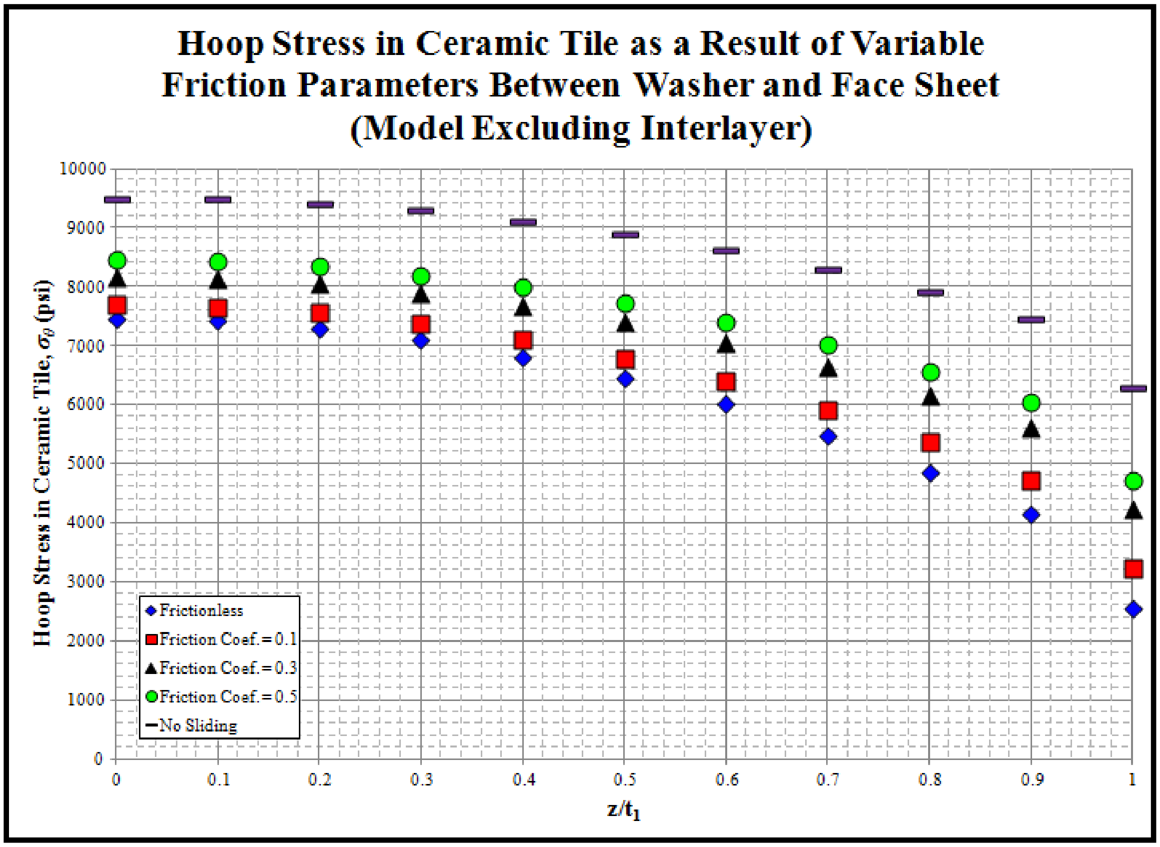

Figure 4.22: Effect of Friction Coefficient between Face Sheet and Washer on Hoop Stress in Ceramic Tile (Model without Interlayer)

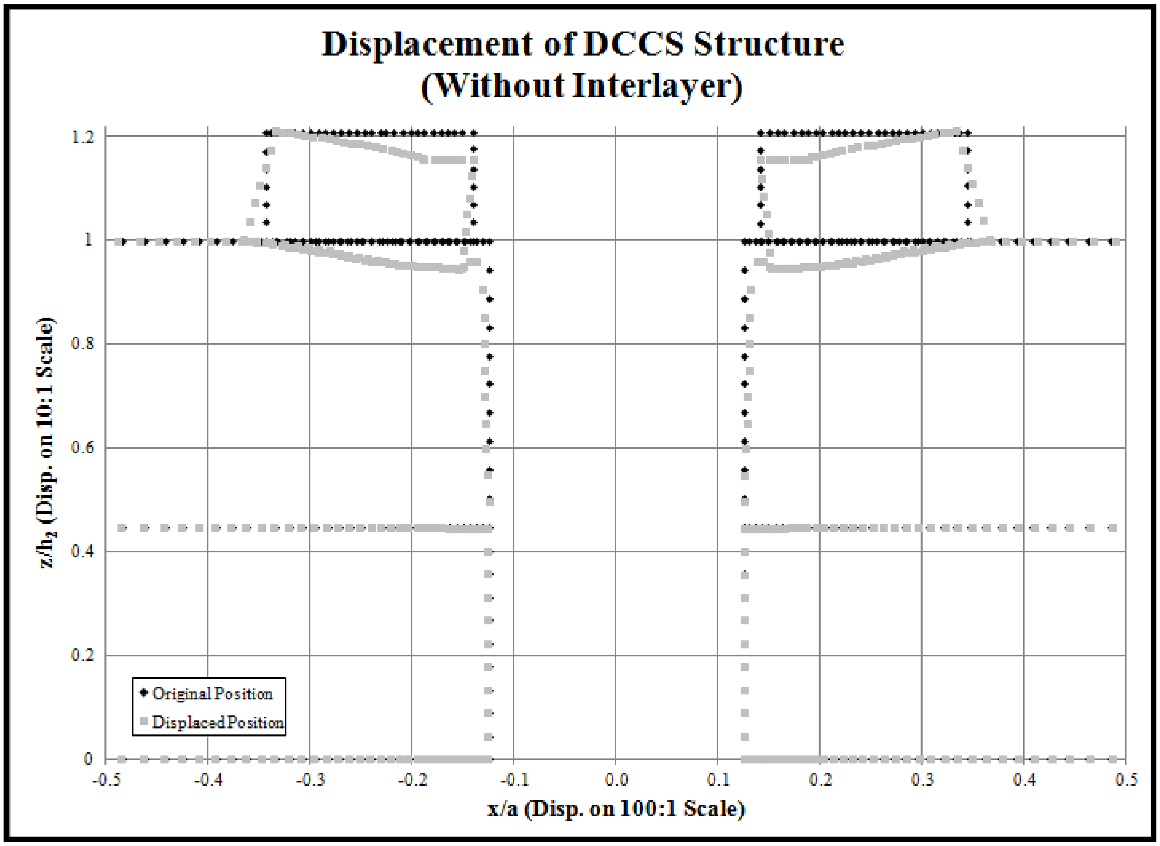

Figure 4.23: Displacement of DCCS Structure with Friction Ratio of 0.5 (Model without Interlayer)

The second model incorporates the presence of the interlayer between the face sheet and ceramic tile. The same analysis was performed regarding the friction parameters, and similar results were seen. Though the discrepancy was not as large, the model with the fastened interface between face sheet and washer exhibited that largest hoop stress at mid-tile (see Figure 4.24). Again, the model with a friction coefficient of 0.5 appeared to fall directly between the fastened and frictionless models, proving to be the appropriate property to apply to further models. Additionally, the magnitude of hoop stresses was found to be significantly less as a result of the interlayer. This confirms that the compliant nature of the interlayer allows the face sheet and ceramic tile to displace more independently. This can be seen in Figure 4.25, where a plot of the deformed joint shows noticeable differences in comparison to the model without the interlayer. The face sheet appears to be further from the joint (as a result of the friction between the washer and face sheet) than in the simplified model from earlier, yet the ceramic tile experiences less radial displacement and circumferential stresses. The low stiffness properties in the interlayer allows it to shear and compress considerably more than the other constituents, and ultimately reduces the out-of-plane stresses in the face sheet and ceramic tile.

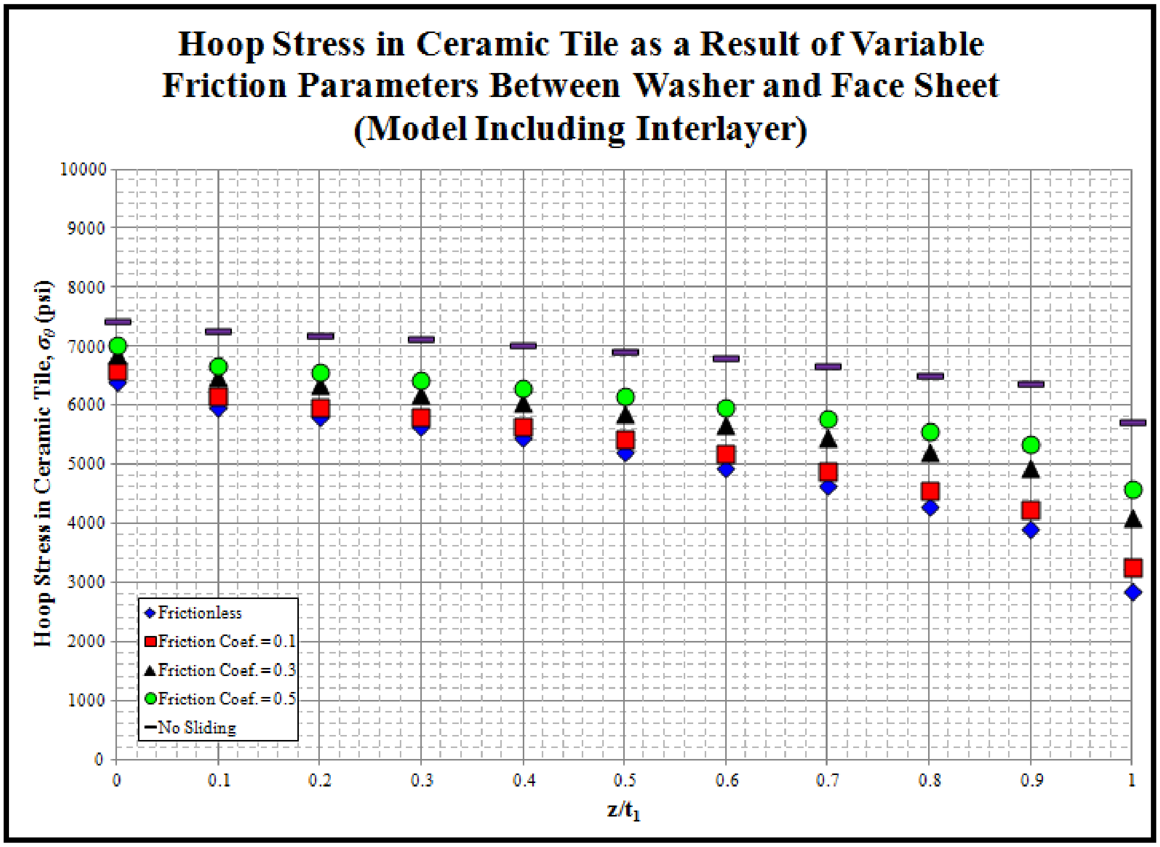

Figure 4.24: Effect of Friction Coefficient between Face Sheet and Washer on Hoop Stress in Ceramic Tile (Model with Interlayer)

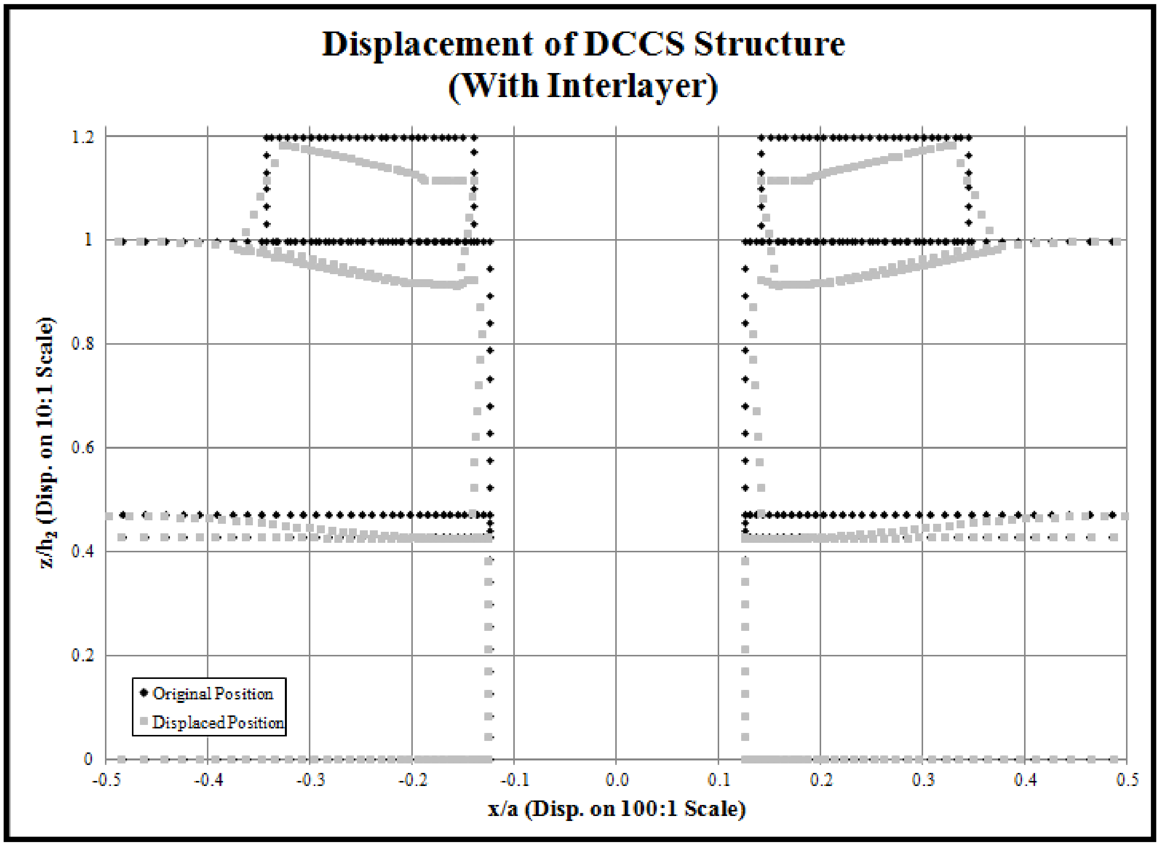

Figure 4.25: Displacement of DCCS Structure with Friction Ratio of 0.5 (Model with Interlayer)

It was discussed in Section 4.1 that under the expected clamping force, the interlayer would likely yield. However, in the finite element models presented thus far, the interlayer has been modeled as a linear elastic material, thus negating the effects of yielding and plastic non-linearity. To simulate the present state of yield that would be expected after 90 ft-lbs of torque, the elastic modulus of the interlayer was reduced to the point such that the compressive stress in the interlayer was equivalent to the yield stress. The revised modulus for the interlayer was found to be 21.0 ksi (as opposed to the defined modulus of 71.0 ksi). The model was re-computed with the new interlayer, resulting in the hoop stresses seen in Figure 4.26. Note that the reduced modulus resulted in a less stiff interlayer, and consequently, more compliant and further reducing the hoop stress in the ceramic tile. At this point, it can be predicted that the hoop stress causing cracks during the torque process are a result of tensile stresses between 6000 and 7000 psi. This is significantly less than the reported tensile strength of the tile, which is 36.0 ksi. However, brittle materials like ceramics are extremely defect-sensitive, and can fracture at much lower strengths if imperfections are present along the ceramic surface. (Reference Chapter 5.5 for the finite element analysis of the DCCS joint subjected to a far field tension load for pinned and clamped conditions. Analyses were performed at multiple far field loads, representing the absolute minimum and average strengths to cause net tension failure in the ceramic tile. Tensile stresses at the hole boundary are provided, and stresses causing failure at absolute minimum strengths can be compared to the hoop stresses causing fracture of the joint. These stresses should be on the same magnitude and because both represent the approximate experimental tensile stresses which caused fracture, they should hypothetically be close to equal.) In addition, the machining of the hole in the ceramic (see Chapter 2.3) could result in surface damage that could reduce the tensile stress required to propagate the radial cracks observed due to bolt torque.

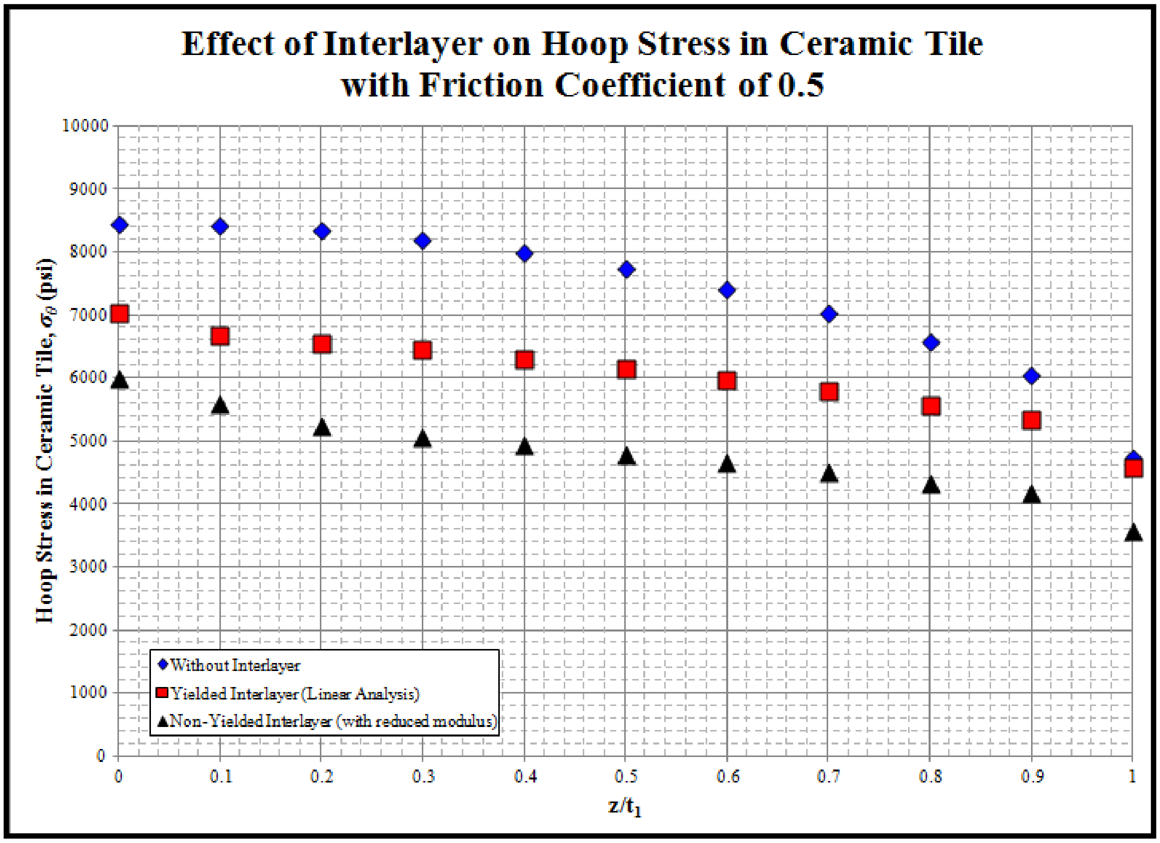

Figure 4.26: Effect of Interlayer on Hoop Stress in Ceramic Tile

In previous sections, it was explained that compression of viscoelastic materials resulted in a distinctive amount of stress relaxation based on the material properties. In Section 4.2, it was assumed that a clamping force of 10800 lbs (90 ft-lbs of torque resulted in compressive stresses of 8735 psi, assuming that the clamping force was evenly distributed through the surface area of the washer (1.236 in^2), and remained uniform through the thickness of the DCCS Structure. Further analysis of the DCCS joint in Section 4.4 revealed that the torque coefficient for the joint in question was calibrated to be 0.251, as opposed to the assumed torque coefficient of 0.20. Thus, instead of a clamping force of 10800 lbs, the true clamping force at 90 ft-lbs of torque was 8610 lbs. This force was resolved into a pressure applied at the end of the bolt shank. According to the previous premise, 8610 lbs of force distributed over 1.236 in^2 would result in a uniform compressive stress of 6960 psi. This rudimentary analysis provides an estimate for the expected compressive stresses experience in the DCCS Structure. However, Bickford provides a schematic highlighting the expected distribution of compressive stresses in a clamped joint (Figure 4.27). This diagram shows that compressive stresses are concentrated at the surface of the joint members where the load is applied, with the greatest stresses located near the corner of the joint at the hole boundary. The stresses ultimately distributed and lessen near the mid-point of the joint members. If the stresses in the DCCS joint distributed in a similar fashion, then the above approach cannot produce an accurate estimate of the compressive stresses at the different layers in the DCCS Structure.

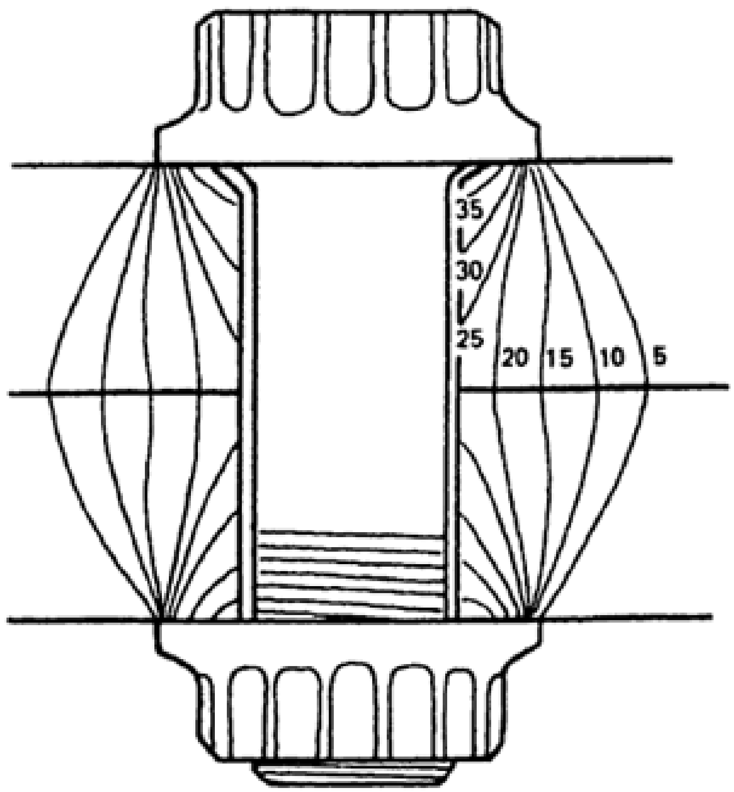

Figure 4.27: Lines of Compressive Stress in Joint Members under a 100 kip Clamping Load (Bickford)

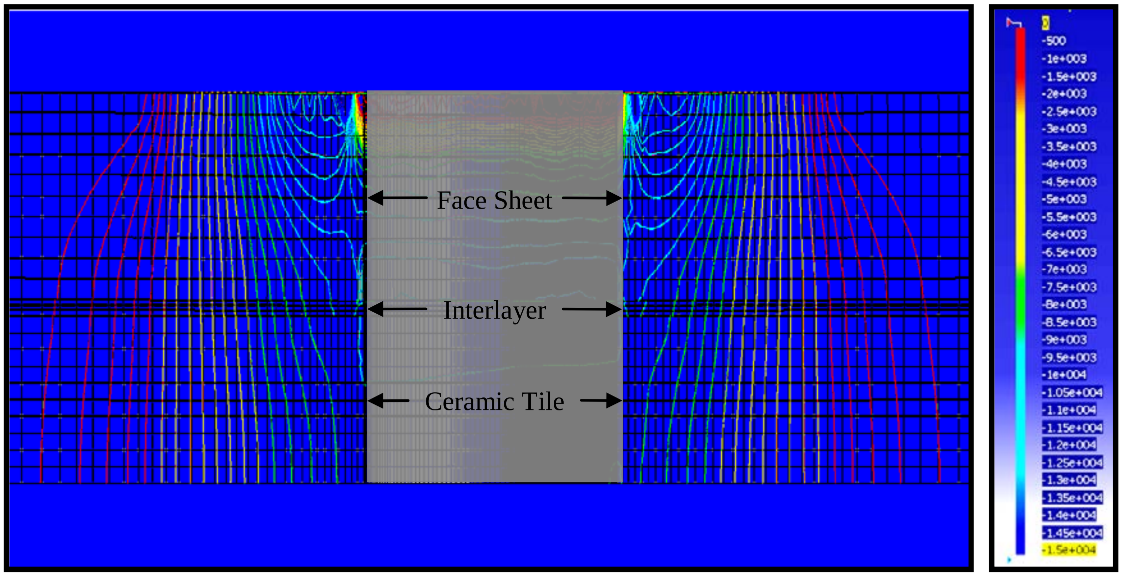

Figure 4.28: Lines of Compressive Stress in DCCS Joint using CATIA

Using the same finite element model as before, the compressive stresses were plotted (Figure 4.28) and exhibited the same general distribution that was seen in the diagram provided by Bickford. The blue and turquoise lines represent high compressive stresses and the yellow and red lines represent low compressive stresses. The face sheet, interlayer and ceramic tile have been indicated, though the lines of compressive stress do not appear to vary through the constituents. The peak stresses in the joint are seen in the face sheet at the interface with the washer's inner edge. The stresses in the interlayer are of the utmost concern, as the interlayer was predicted to yield due to the clamping force. As expected, the peak stresses in the interlayer are approximately 9000 psi at the hole boundary, before slowly dissipate further from the joint. Once the interlayer yields, it cannot be expected to transfer stress between the face sheet and ceramic tile as it would under elastic conditions. Since the model was analyzed as linear-elastic, this change in stress transfer effectiveness is not incorporated. However, this model does allow for the determination of the extent of interlayer yield. Figure 4.29 plots the normalized compressive stress (with respective to torque magnitude) against the distance from the center of the joint. The dotted line represents the hole boundary, with subsequent solid lines representing the extent of the yielded interlayer for various torque levels. The lower the torque and clamping force, the lesser the extent of yielded interlayer from the hole boundary, and vice versa. (Note that the inside perimeter of the washer is located at x/a = 0.14 and the outside perimeter is located at x/a = 0.34.)

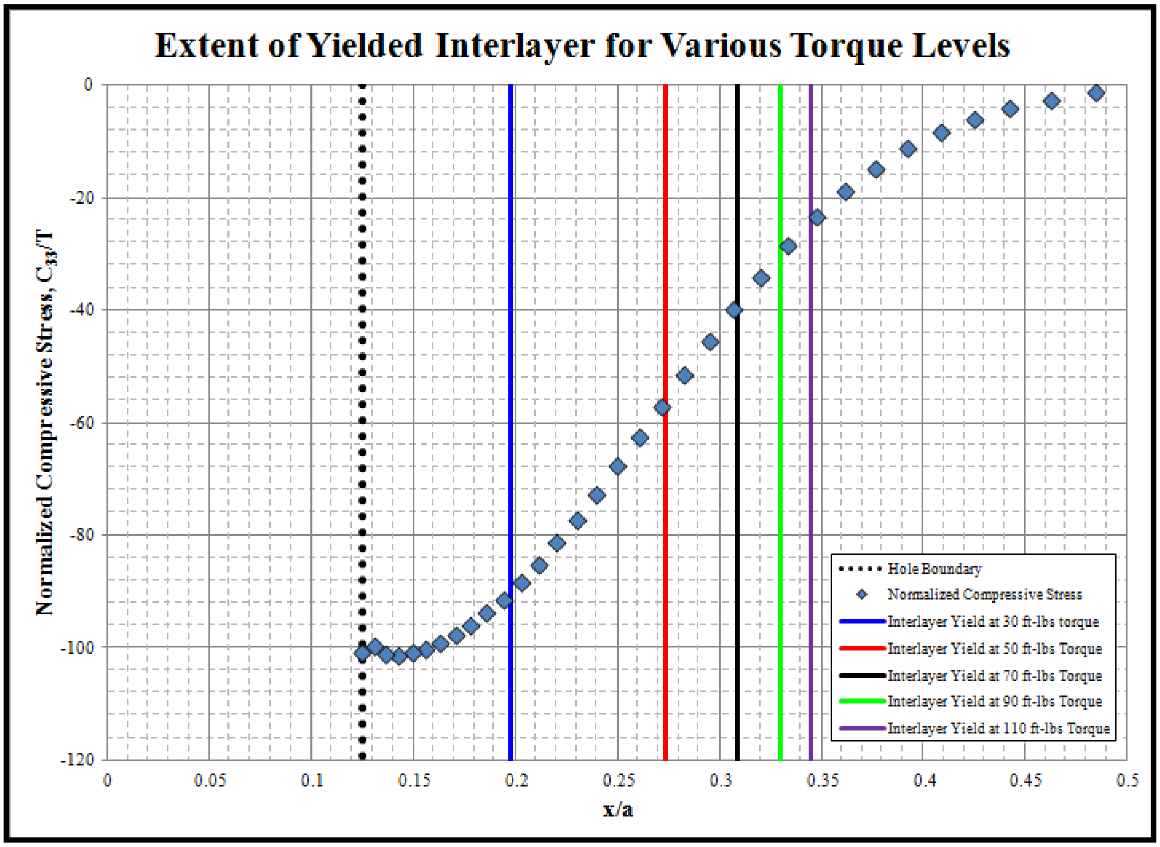

Figure 4.29: Extent of Yielded Interlayer around DCCS Joint for Various Torque Levels

Since it is unclear of the magnitude of hoop stresses that cause fracture, in part due to the fact that machining defects vary from specimen to specimen, the torque will be reduced from 90 ft-lbs by increments of 10 ft-lbs until a suitable torque is found that causes fracture in only a small fraction of the joints. Recall from Section 4.1 that the recommended range of torque for optimal performance was from 85 – 106 ft-lbs. Torque levels below the recommended torque raise concerns about self-loosening, slippage, fatigue, etc. These sources for clamp loss will need to be monitored closely for lower magnitudes of torque.

4.6 <u>Results from Washer Load Cell Relaxation Tests</u>

To reduce the magnitude of hoop stresses in the ceramic tile, the initial torque was refined to 80 ft-lbs (clamping force of 7650 lbs). Relaxation tests at this torque did not demonstrate cracks in the ceramic tile, and was used for the remainder of stress relaxation testing. Four different relaxation tests of the joint were performed with 80 ft-lbs of torque; they included testing the mechanical joint with a piece of steel substituted for the DCCS Structure, the DCCS Structure, the DCCS Structure with Loctite applied to the bolt threads, and the DCCS Structure with the joint being re-torqued after 5 minutes. Testing of the mechanical joint will allow for the amount of relaxation due to mechanical components, including embedment, thread slippage, creep, settling, etc., to be quantified. Loctite is a thread sealant that is applied prior to tightening the joint. Once the sealant fully cures, the threads are “locked” into place, preventing accidental loosening or slippage. Re-torquing will theoretically reduce the amount of relaxation over time, in particular, reducing the magnitude of initial loss that occurs within the first minute. This theory is supported by the stress-strain plot in Figure 4.30. If the joint was re-torqued to the prevailing baseline stress after the DCCS Structure reached the equilibrium or “rubbery” moduli, the amount of relaxation after re-torque would be half of the relaxation achieved with a single torque.

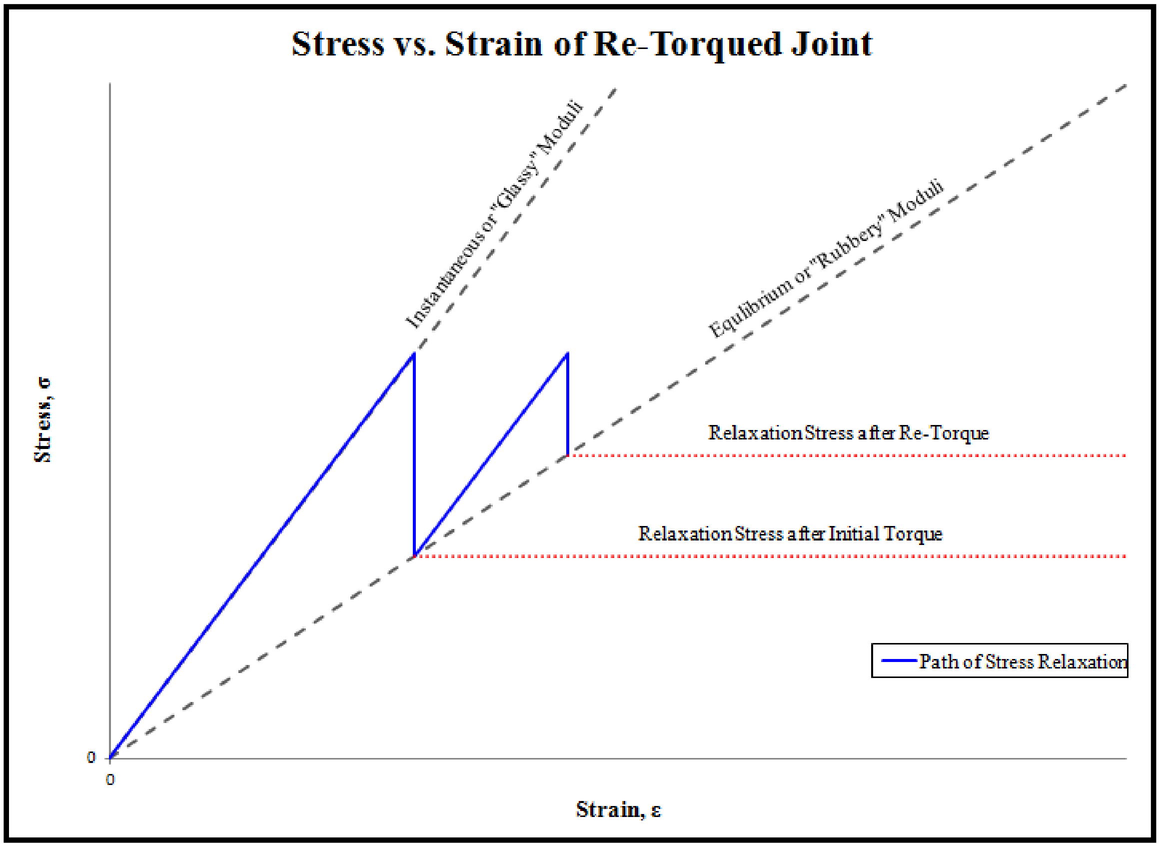

Figure 4.30: Stress Relaxation using Method of Re-Torque

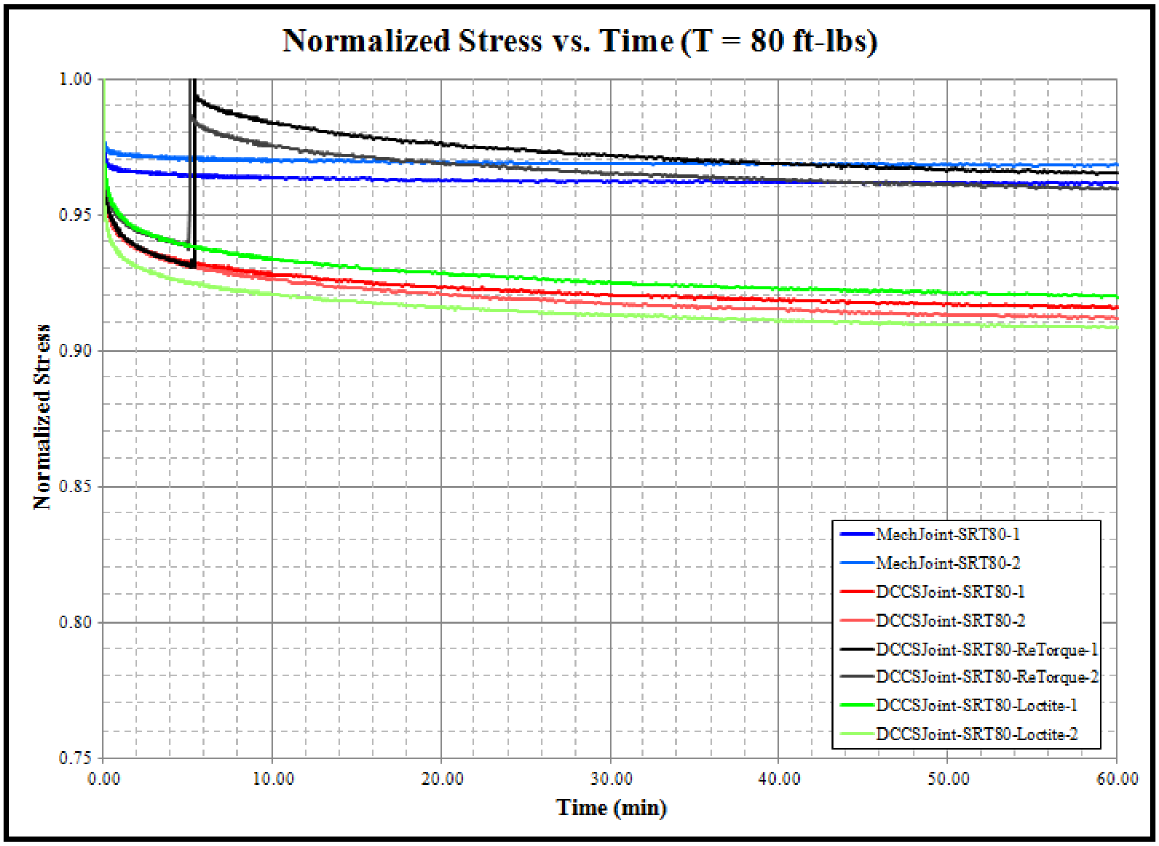

Figure 4.31: Stress Relaxation of DCCS Joint with Various Methods to Reduce Stress Relaxation

Figure 4.31 shows the results of the four joint relaxation tests. The mechanical joint experiences a 3 – 4 percent loss of stress immediately after application, and then maintains that stress through the remainder of the test. The majority of this loss can be attributed to embedment, where the rough thread surfaces of the bolt and nut embed into one another. This is more common with new joint parts than re-used components. The DCCS Structure exhibits a stress loss of approximately 8 – 9 percent over the first 60 minutes, and although the rate of stress loss is decreasing, the DCCS Structure has yet to reach the equilibrium moduli. Using

Loctite, there is no discernible improvement of short-term stress relaxation; however, the use of Loctite may be more effective for long-term relaxation, once the sealant has time to fully cure. The method of re-torque displayed a stress loss of 3 – 4 percent. Looking at Figure 4.31, the curve from the re-torque method appeared to be identical to that of the regular torque method, with the exception that the re-torque curve was shifted upward due to the secondary application of stress, correlating to a lower stress loss. The next step is comparing the relaxation models with the actual relaxation of the joint to see if they are accurate depictions of stress loss in the DCCS joint.

4.7 Compare Results from Instron Machine and Washer Load Cell

Comparing the stress relaxation between the two testing methods and the empirical models, the stress losses demonstrated under the washer load cell relaxation tests were much less than those of the Instron test. These losses can be explained by looking at the true stresses experienced by the DCCS constituents subjected to a clamping force. Originally, it was assumed that the clamping load would result in an equivalent pressure over the contact area between the washers and face sheet of the DCCS Structure. This stress would be equal and uniform through the thickness of the DCCS Structure. The first testing method using the Instron machine employed this rudimentary philosophy, exposing each of the constituents to a stress of 8735 psi, based on a clamp load of 10800 lbs over a washer with a surface area of 1.236 in^2. Transitioning to the joint, it is evident that because the clamping pressure is not applied over the entire surface of the DCCS Structure, but only locally at the joint, the stress distribution is not apparent without developing a finite element model.

According to the schematic provided by Bickford (Figure 4.27) and the compressive stress distribution diagram provided by the finite element model to validate Bickford's schematic (Figure 4.28), the maximum stresses occur at the perimeter of the joint hole directly beneath the nut and bolt head. This stress dissipates toward the mid-section of the joint member and radially away from the joint hole. Given that the stresses are not constant through the thickness of the DCCS Structure, the empirical models formulated from the data of the Instron testing cannot be expected to represent the stress relaxation at the joint.

Under an even distribution of compressive stress, the DCCS Structure experienced a relaxation of 25 percent. As stated previously in this Chapter, the interlayer, despite comprising less than 5 percent of the total thickness of the DCCS Structure, contributes a large majority to the overall relaxation of the DCCS Structure. The DCCS joint, whose distribution of compressive stresses is not implicitly known without finite element analysis, experienced a relaxation of approximately 8 percent. (Because the stress losses are a function of normalized values, and it was proven that these stresses are in the linear viscoelastic range of each constituent, the losses can be directly compared to one another despite one test simulating a torque of 90 ft-lbs and the other utilizing a torque of 80 ft-lbs.) Based on the fundamental stress distribution profile provided by Figures 4.28 and 4.29, it shows that compressive stresses in the region of the face sheet are greater than those in the region of the interlayer. Comparatively lower stresses in the interlayer would have a significant effect on the overall relaxation of the DCCS Structure, and could be one of the contributing factors as to why the relaxation was less in the DCCS joint. One other reason for the reduced relaxation values is the period of time over which the torque/stress was applied. The

Instron machine applied the load instantaneously, providing a stress-strain plot accurately depicting the true glassy modulus of the DCCS Structure. This allowed for the maximum amount of relaxation to occur between the glassy and rubbery moduli. Using a torque wrench to apply torque increased the time over which load was applied, allowing for relaxation to occur during the loading period. It was demonstrated that the method of re-torque was a valuable method to reduce the total amount of relaxation. The time it took to torque the joint to full capacity was essentially the re-torque method concentrated to a few seconds, thus eliminating much of the initial relaxation seen during that time.

Applying all the information collected from the compressive stress relaxation experiments and the finite element analysis, several conclusions and recommendations can be made. First, an appropriate torque coefficient was evaluated using the washer load cell and DCCS joint. This revised coefficient allows for more accurate clamping loads to be determined based on a given torque. Stress relaxation testing using the washer load cell determined that the original baseline of 90 ft-lbs led to the onset of cracks in the ceramic tile at the joint location. These cracks were found to be caused by hoop stresses, contributed to by the natural compression of the DCCS Structure and the mismatch in inplane strains between constituents. Consequently, the baseline torque was reduced to 80 ft-lbs, which reduced stresses enough to subside cracking of the tile. Several methods were evaluated to reduce the effect of stress relaxation, with the method of re-torque being the most successful. Further experimentation of the DCCS joint, including inplane static and fatigue testing, will utilize an effective torque of 80 ft-lbs, and tightening will be conducted at a slow pace, with a second tightening performed within five minutes after the initial torque.

According to the experiments performed in Section 4.5, this should limit the amount of stress relaxation to less than 5 percent of the overall torque. Establishing a repeatable and consistent method of tightening is important to the evaluation of the DCCS joint. Slight changes in the tightening process can directly affect the performance of the joint and the overall effectiveness of Discontinuous Ceramic Cored Sandwich Structure.

Chapter 5

STATIC TENSION/BEARING TEST IN DISCONTINUOUS CERAMIC CORED SANDWICH STRUCTURES

Discontinuous Ceramic Cored Sandwich Structures combine the respective strengths of multiple constituents to create a unique hybrid composite structure. The added complexity from the interaction of the constituents leads to more advanced failure mechanisms than seen in typical thin laminates. Static tension testing has been performed in preliminary research utilizing a pinned joint (Weidner et al). The current testing will incorporate a clamping force at the joint to further understand the performance of bolted joints in the DCCS Structure. First, pinned and clamped joints will be directly compared to understand the benefits and detriments of introducing external clamping forces around the perimeter of the joint. This comparison will be supported by data representing strength and stiffness differences, as well as a finite element model quantifying the bearing stresses experienced at the bolt hole due to far field loads/stresses. Further testing will be conducted to determine a range of clamping forces that will provide the optimal strength and stiffness properties of the joint. The various failure modes, including their location and the loads in which they occurred, will be detailed thoroughly throughout the Chapter. The conclusions established from the static tension testing of clamped joints will contribute to the final recommendation of the DCCS Structure joint properties.

5.1 Static Testing Set-Up

Obtaining quality data is a function of several components. First and foremost, proper machining and fabrication of the composite is required. Secondly, a reliable and easily replicable testing procedure must be prepared, in addition to selecting an experimental fixture that is most appropriate for the specific test. These topics and their importance in providing valid results were discussed in detail in Chapter 2 and Chapter 3, respectively. The test fixture and testing procedure used for all static tension tests was derived from ASTM D 5961/D 5981-M-05 "Standard Test Method of Bearing Response for Polymer Matrix Composite Laminates," and used in research conducted by Weidner et al on DCCS Structures. The double-lap test fixture used in this study was uniquely designed by Weidner to accommodate the thicker DCCS Structure. Weidner originally used a single 0.5 inch (12.70 mm) pin made of 17-4 PH stainless steel to conduct static tension testing of the joint. The tolerance between the steel pin and the machined joint ranged between 0.003 – 0.007 inches (0.076 – 0.178 mm). It is important to maintain a low tolerance without creating an interference fit. An interference fit could potentially cause local damage to the joint, whereas a high tolerance reduces the contact area, consequently increasing bearing stresses (McCarthy et al 1415 – 1431). The testing set-up utilizing a pinned joint, as performed by Weidner, is seen in Figure 5.1.

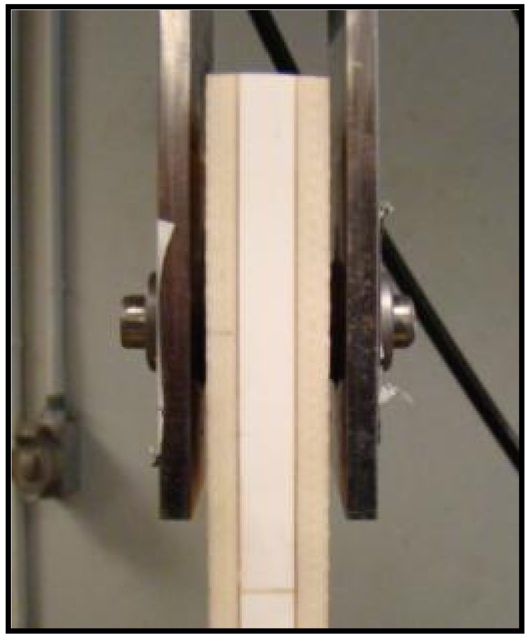

Figure 5.1: Static Testing Set-Up (Pinned)

Several minor changes in the testing set-up were required in transitioning from a pinned joint to a clamped joint. First, an equivalent bolt with threads had to be substituted for the stainless steel pin. A Grade 8 bolt most closely resembled the properties of the steel pin used in prior tests. The properties of the two materials are compared in Table 5.1. The tolerance between the Grade 8 bolt and the machined joint is slightly more than that seen with the steel pin, as bolt diameters are typically manufactured marginally less than the claimed dimension. The bolts had a diameter of 0.4950 inch +/- 0.001 inch (12.57 mm +/- 0.0254 mm), creating a tolerance in the range of 0.007 – 0.013 inches (0.178 – 0.330 mm).

Table 5.1: 17-4 pH Stainless Steel Pin vs. Grade 8 Bolt

Property Description	Units	17-4 pH Stainless Steel Pin	Grade 8 Bolt
Ultimate Tensile Strength	US	142 – 185 ksi	150 ksi
	Metric	0.979 – 1.28 MPa	1.03 MPa
Yield Strength	US	110 – 160 ksi	130 ksi
	Metric	0.758 – 1.10 MPa	0.896 MPa
Modulus of Elasticity	US	28500 ksi	29000 ksi
	Metric	197 MPa	200 MPa

Next, in order to accurately resemble a mechanically fastened joint in its' actual application, a washer is incorporated into the joint. Khashaba et al and Yan et al both found the optimal washer size for bolted composite joints had an outer diameter-to-inner diameter ratio in the range of 3.0. A black luster-coated washer, with an outer diameter of 1.375 inch (34.93 mm) and an inner diameter of 0.5625 inch (14.29 mm) was selected, in accordance with ASME standards. This provides an OD-to-ID ratio of 2.44, and although slightly less than the recommended ratio of 3.0, the washer size selected will provide a greater clamping pressure, yet maintain a sufficient area for lateral restraint to prevent delamination and bearing failure. The testing set-up utilizing a clamped joint is seen in Figure 5.2.

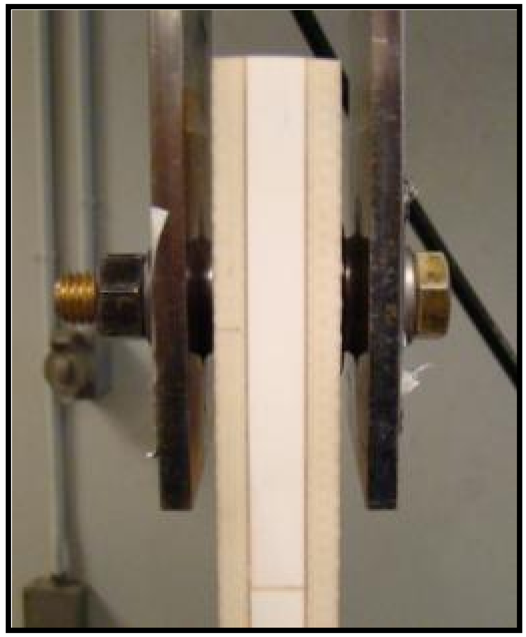

Figure 5.2: Static Testing Set-Up (Clamped)

Pinned tests were performed to corroborate the findings of Weidner et al and provide reliable data to compare with further test specimens. Initially, pinned tests will be compared with baseline torque tests of 90 ft-lbs (122 N-m), or an equivalent clamp load of 8610 lbs (38300 N). (Due to the fixture set-up, approximately 5 – 10 ft-lbs of torque is required in order for the side laps to reduce the clearance between the washers and DCCS specimen to zero. Thus it was assumed that the baseline torque of 90 ft-lbs would compensate for this additional torque, and the effective torque would only be approximately 80 ft-lbs, as determined in Chapter 4). Pinned and clamped tests will follow the same testing procedure, including a loading rate of 0.01 in/min (0.254 mm/min), LVDT's as the primary method of measuring displacement, and the application of blue dye to locate damage in the testing specimen throughout the duration of the test. The test fixture in full can be seen in Figure 3.10.

5.2 Results/Comparison of Pinned and Clamped Joints

The failure modes documented for test specimens with pinned and clamped joints followed the same sequence that was documented by Weidner et al. The net tension failure mode, shown in the clamped testing set-up in Figure 5.3, occurred first in the ceramic tile. Cracks were visible extending from the joint hole to the far edges of the ceramic tile, typically in the range of 60-90 degrees from the direction of the applied load. These cracks initiated, on average, at 4698 lbs (bearing stress of 10213 psi) under pinned joint conditions, with a standard deviation of 716 lbs (1557 psi); and at 4427 lbs (9624 psi) under baseline torque conditions, with a standard deviation of 270 lbs (587 psi). Net tension cracks continued to appear at an increased angle from the preceding crack until a final net tension crack formed at 90 degrees. These subsequent cracks were found to occur between 6000 – 20000 lbs (13043 – 43478 psi), with as many as three additional cracks and as few as zero additional cracks. A more detailed discussion on the mechanics that cause each of the failure modes and the influence of a clamping force will be included later in this section.

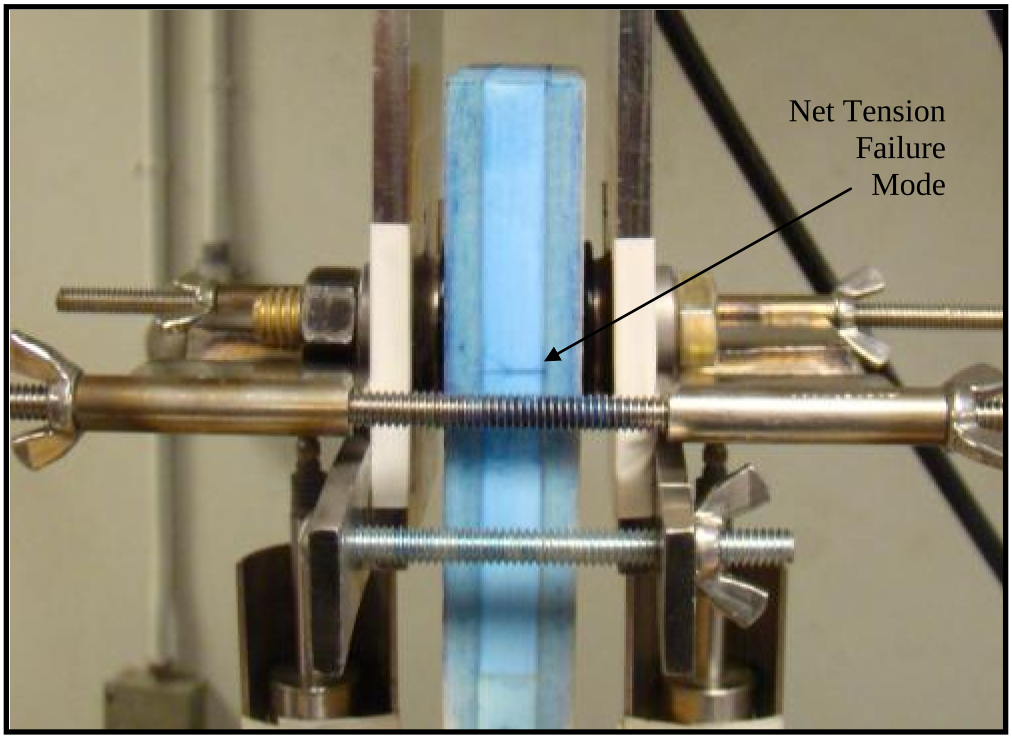

Figure 5.3: Typical DCCS Structure first failure mode (Net Tension)

The second failure mode of both pinned and clamped test specimens was the bending/shear failure mode, seen in Figure 5.4. This failure mode occurred as the joint stiffness rapidly deteriorated, when the joint began to experience a higher rate of displacement per additional loading. There was a significant variance in the pinned and clamped tests, leading to the conclusion that applying a clamping force at the joint supplemented the resistance of the bending/shear crack. For the pinned joint condition, the bending/shear crack formed at an average load of 21177 lbs (46037 psi), with a standard deviation of 3391 lbs (7372 psi). The average elongation of the joint when this crack occurred was 0.0373 inches. The baseline torque condition experienced a bending/shear crack at an average load of 34462 lbs (74917 psi), with a standard deviation of 403 lbs (876 psi). This crack occurred at an average joint elongation of 0.1627 inches. Both the load attained prior to the bending/shear crack and the joint elongation at the time of the failure mode were notably greater under the baseline torque condition. The explanation for this achievement in additional strength will be discussed later in the section. However, in both cases, the bending/shear crack was associated with an immediate loss of between 8 – 12 % of the achieved load, before stabilizing and gaining additional load.

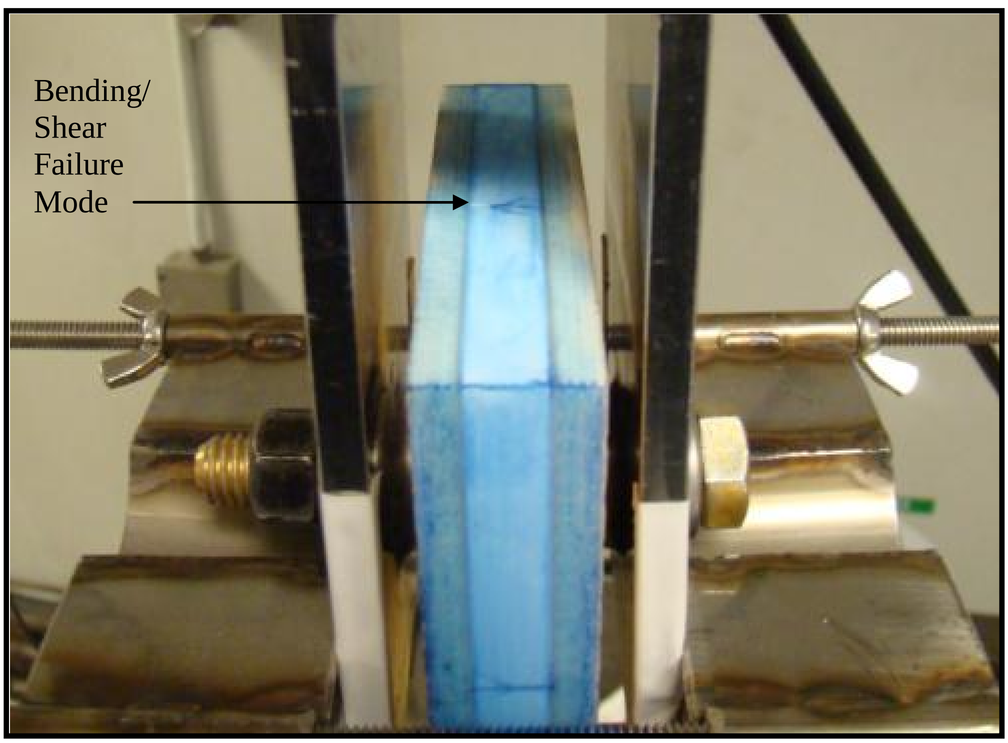

Figure 5.4: Typical DCCS Structure second failure mode (Bending/Shear)

After the bending/shear crack, specimens from both test cases begin to experience bearing failure of the face sheet and significant elongation of the joint hole. During bearing failure, the adhesive bond between the face sheet, interlayer and ceramic tile begins to weaken before catastrophically failing throughout the entire shear region of the specimen, seen in Figure 5.5. This final failure can be classified in five ways: delamination of plies within the face sheet, adhesive bond failure between the face sheet and interlayer, interlayer yielding, adhesive bond failure between the interlayer and ceramic tile, or tensile failure of the ceramic tile. Of these failures, adhesive bond failure between the face sheet and interlayer, and between the interlayer and ceramic tile were most prevalent, with a few cases experiencing tensile failure of the ceramic tile. It should be noted that any combination of those three failures were seen in a single failed specimen. Once delamination occurs, the two outer face sheets provide the full bearing capacity of the DCCS Structure. For the pinned joint condition, this ultimate failure occurred at an average load of 28739 lbs (62476 psi), with a standard deviation of 769 lbs (1672 psi). This was a strength of 20 – 50% greater than when the bending/shear failure occurred in the same specimens. Additionally, the average joint displacement at ultimate failure was 0.1089 inches. For the baseline torque condition, ultimate failure occurred at an average load of 32283 lbs (70180 psi), with a standard deviation of 734 lbs (1596 psi). This was a strength of 5 – 8% less than when the bending/shear failure occurred in the same specimens. The average joint displacement at ultimate failure was 0.1965 inches. The reason for differences between the pinned and clamped cases will be addressed later in this section.

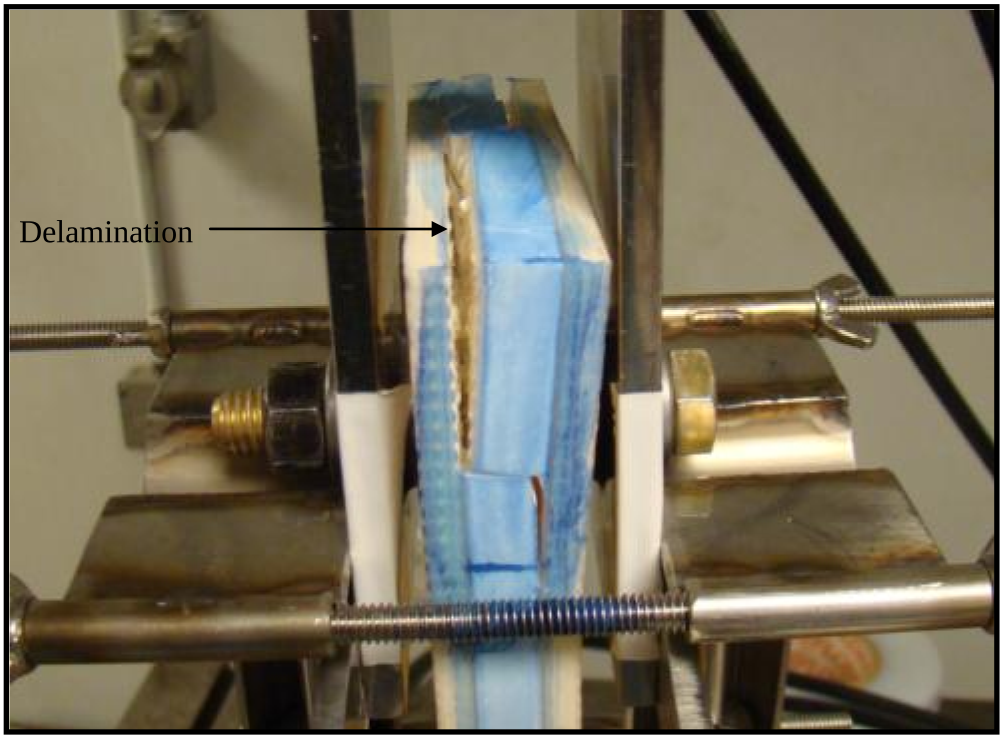

Figure 5.5: Typical DCCS Structure final failure mode (Delamination of Ceramic Tile, Interlayer and Face Sheet)

A graphic comparison between the pinned and baseline torque tests in the form of a load vs. displacement curve is found in Figure 5.6, along with a quantitative comparison of strength and displacement data in Table 5.2. The pinned data is comparable to that recorded in research performed by Weidner et al under the same testing conditions.

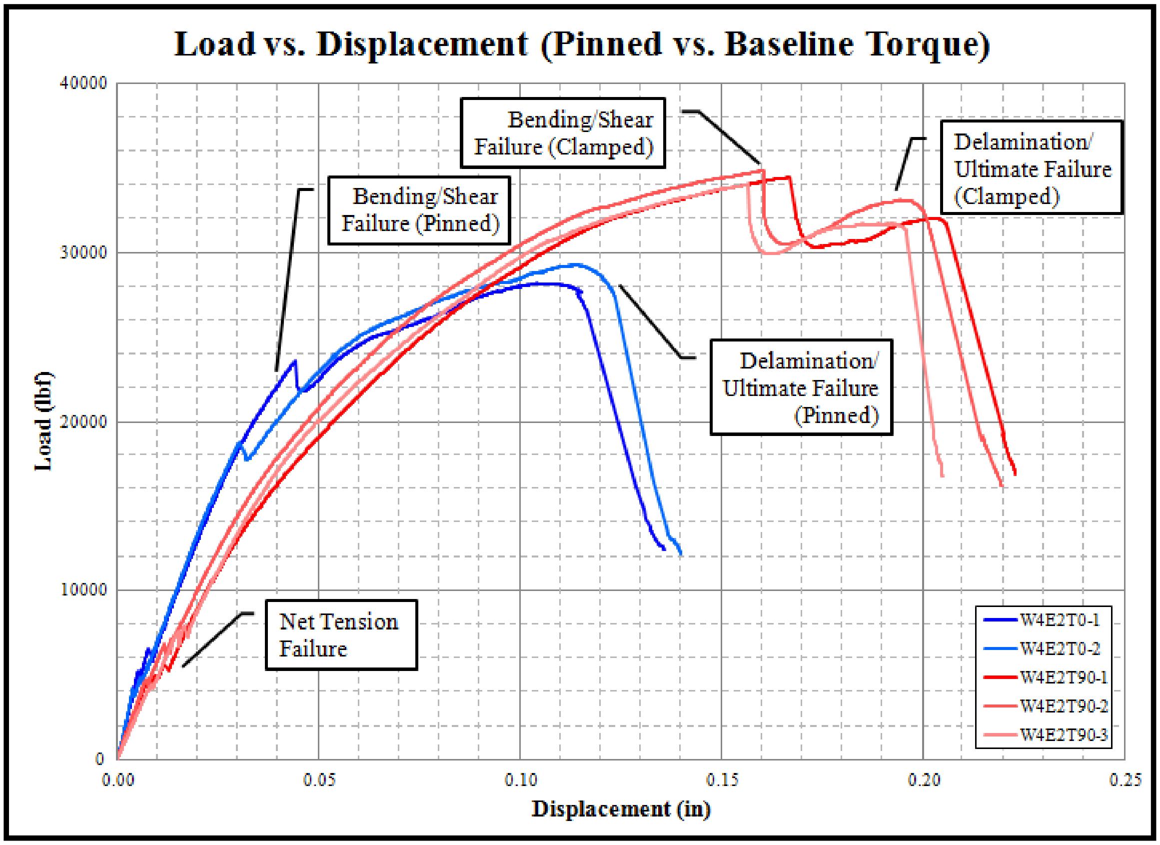

Figure 5.6: Load vs. Displacement Curve for Pinned and Baseline Torque Specimens (W4E2T0 and W4E2T90)

Table 5.2: Strength and Displacement Comparisons (Pinned vs. Baseline Torque)

Sample #	Strength at First Damage (Net Tension)	Strength at Bending/Shear Failure	Strength at Ultimate Failure	Displacement at Ultimate Failure
W4E2T0-1	5204 lbs	23574 lbs	28195 lbs	0.1041 in
	23150 N	104860 N	125420 N	2.644 mm
W4E2T0-2	4192 lbs	18779 lbs	29283 lbs	0.1137 in
	18650 N	83530 N	130260 N	2.888 mm
W4E2T90-1	4624 lbs	34465 lbs	32028 lbs	0.2027 in
	20570 N	153310 N	142470 N	5.149 mm
W4E2T90-2	4539 lbs	34864 lbs	33111 lbs	0.1945 in
	20190 N	155080 N	147290 N	4.940 mm
W4E2T90-3	4119 lbs	34058 lbs	31710 lbs	0.1922 in
	18320 N	151500 N	141050 N	4.882 mm

Studies performed on the effect of clamping forces in thin laminate joints have come to the conclusion that the addition of a clamping force improves joint strength and stiffness (Khashaba et al 310 – 317). These beliefs were founded on the concept that clamping forces suppress delamination and fiber-matrix splitting around the joint, improving the localized strength of the composite, and decreasing the amount of elongation of the joint hole. However, these assumptions cannot be directly applied to the DCCS Structure due to its' complex structural design and the unique interaction between the three primary constituents. In comparing the initial joint stiffness between the pinned and clamped test cases, pinned joints had a significantly greater stiffness prior to the first failure mode. Gawandi et al determined that the adhesive interlayer has the most influence over the stiffness of the DCCS Structure. A more compliant, thinner interlayer enhances stress transfer between the face sheet and ceramic tile. The ceramic tile has a notably higher modulus of elasticity, and provides almost half of the contact area between the bolt and joint hole; consequently, the pinned joint stiffness in the DCCS Structure is more characteristic of the stiffness of the ceramic tile because the interlayer directs the majority of the bearing load through the face sheet into the ceramic tile. Introducing a clamping force reduces the compliance of the interlayer at the joint (i.e. adhesive yielding around the bolt hole due to the bolt torque occurs), reducing the rate of stress transfer from the face sheet to the ceramic tile. As a result, clamped test cases inherently have a lower stiffness, as the overall stiffness of the DCCS Structure tends to resemble somewhere between the stiffness of the ceramic tile and face sheet.

Taking into account all static tension tests performed in this study, the first net tension crack on either side of the joint occurred at an average load of 4267 lbs (9276 psi) with a standard deviation of 683 lbs (1485 psi). However, the locations net tension cracks are extremely sensitive to specimen symmetry and off-axis loading. Figure 5.7 shows a specimen with a single net tension crack on the left edge and four net tension cracks on the right edge. Several specimens displayed the same tendency of a single net tensions crack on one edge and multiply cracks on the other edge. In the majority of specimens that experienced this trend, the first overall crack took place approximately 65 – 70 degrees from the loading angle, on the side that eventually showed multiple cracks. The second overall crack took place on the opposite edge, typically at 90 degrees from the loading angle. The slightest amount of off-axis loading caused the first crack to occur at an angle less than 90 degrees, where the greatest tensile stresses are expected (Weidner et al). Once this crack occurs, the stresses are redistributed around the circumference of the joint hole, where the largest tensile stress is experienced precisely at 90 degrees on the opposite side. As loading is increased and the hole elongates, the outer face sheets experience peak tensile stresses at +/- 90 degrees. On the one side, this tensile stress in the ceramic tile has already been relieved by the second overall crack. On the other side, these tensile stresses from the face sheet are still transmitted into the ceramic tile. They are relieved by secondary net tension cracks in the ceramic tile until all tensile stresses have been relieved with a final crack at 90 degrees. These secondary cracks took place at approximately the following average load levels: a second crack at 9745 lbs (21185 psi) with a standard deviation of 2857 lbs (6211 psi); a third crack at 15606 lbs (33926 psi) with a standard deviation of 4986 lbs (10839 psi); and a fourth crack at 20017 lbs (43515 psi) with a standard deviation of 2434 lbs (5291 psi).

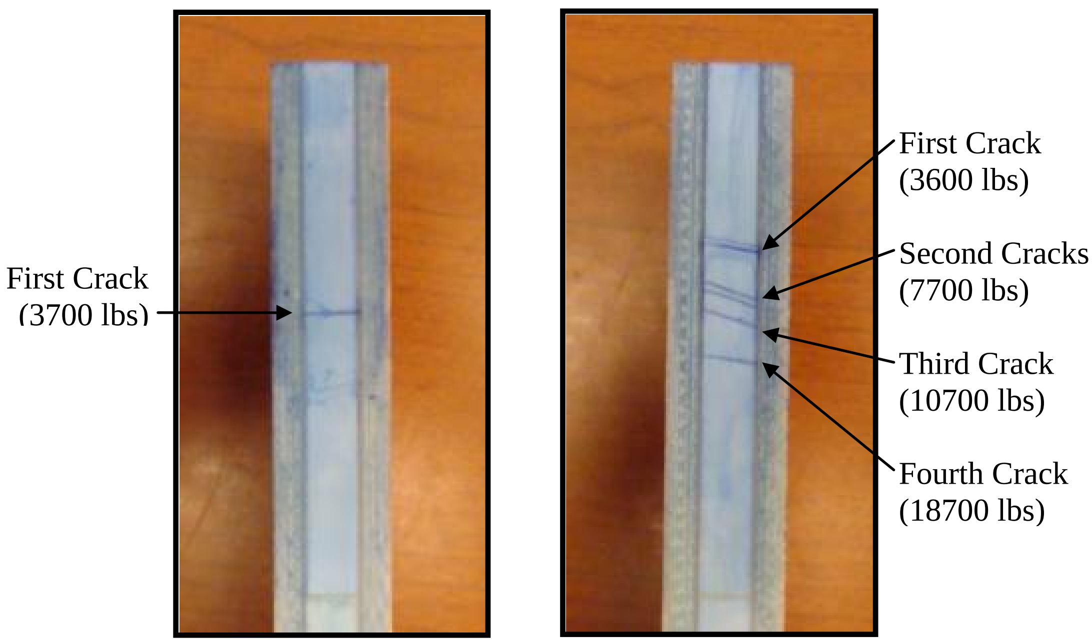

Figure 5.7: Net Tension Cracks in Tile prior to Ultimate Failure (horizontal views looking at left and right edges of specimen)

Weidner submitted the schematic in Figure 5.8 (to the left) to describe the bending/shear failure mode for pinned cases. The modified schematic on the right represents the bending/shear failure mode for clamped cases. After the ceramic tile fails in net tension, the upper portion of the tile, which is exposed to the bearing load from the bolt, acts like a beam in bending. The bearing load, shown as blue arrows applied at the joint hole, force the center of the ceramic tile upward, causing the deformed shape represented by the dashed lines. However, the ceramic tile is resisted by the interlayer, which transfers load between the tile and the outer face sheets. This resistance is spread across the entire face of the ceramic tile, shown as red arrows in the schematic. With increased load, the ceramic tile bends more significantly, with the maximum tensile stresses located at the top of the tile, directly above the joint hole. Once the tensile stresses exceed the strength of the tile, the bending/shear crack forms somewhere within the shaded region of the schematic. The DCCS Structure utilizes the interlayer's high strain-to-failure characteristic in order to continue transferring load between the face sheet and ceramic tile, even after the tile has experienced net tension and bending/shear cracks. The presence of the compliant interlayer prevents either failure modes from being catastrophic. When a clamping force is present at the joint, the ceramic tile is restricted from bending as dramatically. While some of the bearing load is still transferred into the tile, resulting in a given amount of bending, the face sheet is prone to carry more of the load, resulting in greater tensile stresses at +/-90 degrees and consequently, significantly more separation of the net tension cracks. The schematics in Figure 5.8 show a direct comparison of a pinned and clamped specimen under a hypothetically equivalent bearing load. The clamped specimen shows much greater separation in the net tension cracks, however the ceramic tile does not experience as much bending. It takes a much larger bearing load for the ceramic tile in the clamped specimen to achieve the deformed shape and tensile stresses experienced in the pinned specimen, resulting in higher strengths at the bending/shear failure mode.

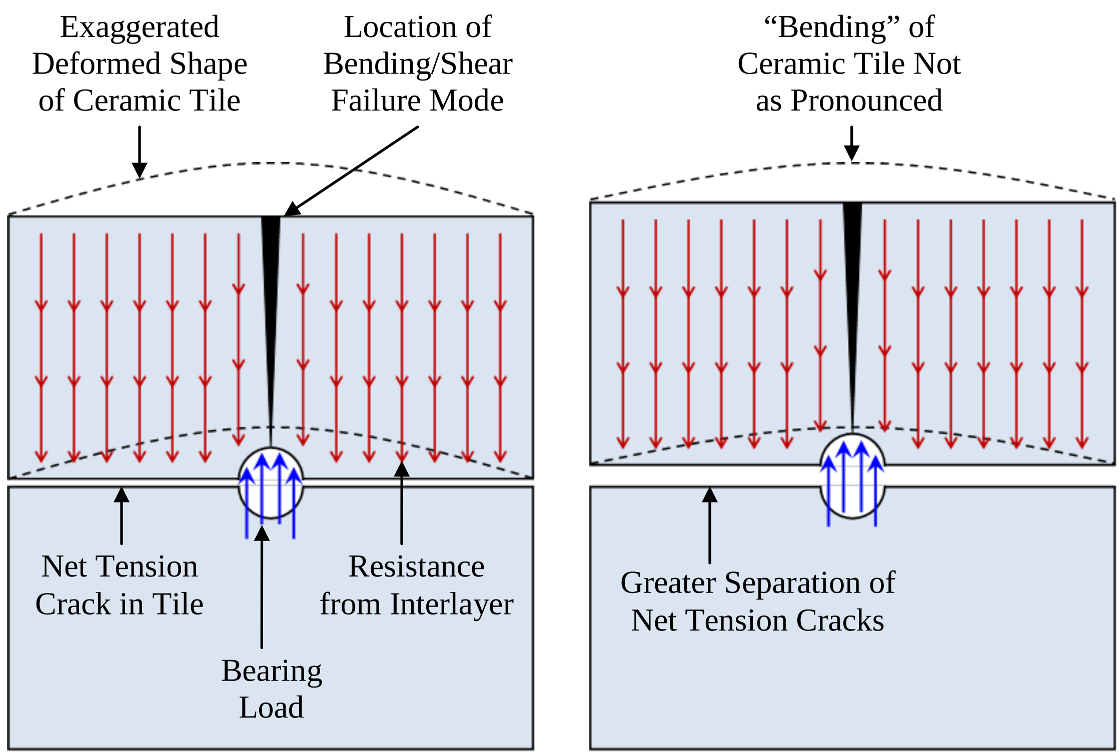

Figure 5.8: Bending/Shear Failure Mode Schematic – Pinned on left (Weidner); Clamped on right

After the ceramic tile fails in bending/shear, more bearing load is transferred into the face sheets. Since the face sheet material is considerably more pliable than the ceramic tile, the rate of loading becomes much less and the majority of the joint displacement takes place during this time frame. The center of the ceramic tile, at the bending/shear failure crack, begins to protrude from the top of the specimen with increased load. This indicates that the interlayer is yielding, weakening the adhesive bond strength between the three constituents in the entire DCCS Structure. As a response to the ceramic tile protruding, the face sheet is inclined to bow outward, away from the tile. This interaction causes a sudden and catastrophic failure of the specimen. This failure is classified as adhesive bond failure between the ceramic tile and interlayer, adhesive bond failure between the interlayer and face sheet, and in some cases, tensile failure along the top edge of the ceramic tile. Figure 5.9 shows the top edge of a specimen after ultimate failure. This particular specimen two of the three potential catastrophic failure modes: delamination of the interlayer and face sheet, and delamination of the ceramic tile and interlayer. The bending/shear failure crack can be seen as well.

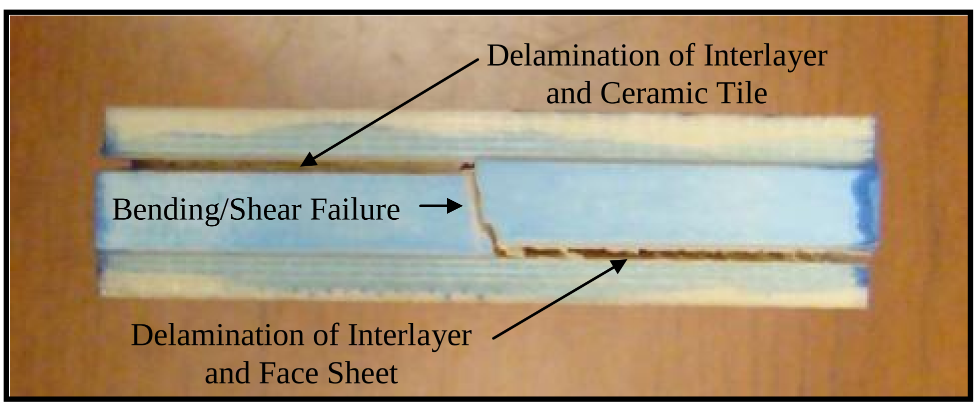

Figure 5.9: Bending/Shear Crack in Tile and Delamination of Ceramic Tile, Interlayer and Face Sheet (vertical view looking down on top edge of specimen; pin loaded normal to current view)

After the test specimens were removed from the fixture, there was evidence of bearing failure in the face sheet, seen in Figure 5.10. This was presumed to have occurred mostly between bending/shear failure and ultimate failure, with a small portion of fiber buckling and joint elongation coming in the time immediately after ultimate failure, before the test was halted. After bending/shear failure occurred, there were multiple instances of acoustic emissions without visible external damage. These acoustic emissions can be attributed to further degradation of the ceramic tile in the bearing region at the joint, or fiber buckling in regions of maximum bearing stress. Both pinned and clamped cases experienced bearing failure; however, for clamped tests, bearing damage was seen outside the contact area between the washer and the face sheet (noted in Figure 5.10), whereas bearing damage was much closer to the joint hole under pinned conditions.

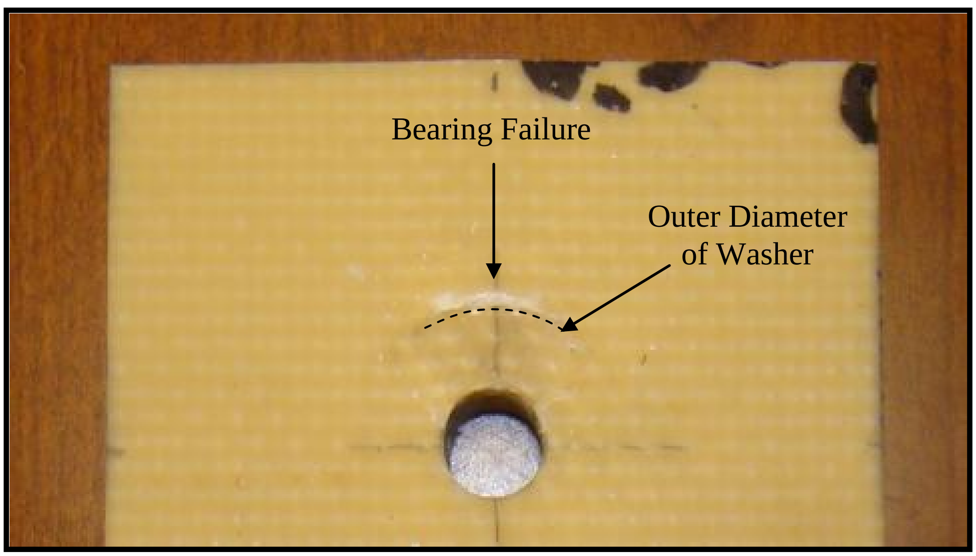

Figure 5.10: Bearing Failure in Face Sheet

There was also significant plastic deformation of the bolt after removal from the test fixture (Figure 5.11). Due to the placement of the LVDT's in conjunction with the test fixture, the bolt bending was accounted for in the joint displacement measurements. If a stronger bolt was substituted for the current Grade 8 bolt, the measured displacements would be significantly less and provide a more accurate value for the displacement of the joint due to failure of the DCCS Structure. Finding an alternatively stronger bolt could also be beneficial in terms of installation applications in the future.

Figure 5.11: Plastic Deformation of Grade 8 Bolt

Given the substantial increase in strength from clamping forces, the results support the recommendation to use clamped joints over pinned joints in the DCCS Structure. However, the baseline torque was selected entirely based on theoretical approaches. Testing various levels of torque will provide quantifiable and comparable data to make a firm recommendation on the optimal torque/clamping forces that should be applied to the joint.

5.3 <u>Clamped Joint Test with Varying Torque</u>

The baseline torque of 90 ft-lbs (an equivalent clamp load of 8610 lbs) was chosen based off careful consideration of many factors, including bolt strength, compressive composite strength, thread stripping strength, self-loosening, fatigue factors, torsion factors, and the effects of external loads. Earlier in this chapter, it was determined that a clamping force provided significantly greater overall strength to the DCCS joint, in the range of 15-25% higher than the pinned case. To determine the optimal clamping force that provides the greatest strength, several different torque levels were tested. The first torque level of 10 ft-lbs (960 lbs) was chosen to simulate the equivalent to hand-tightening. This case would be the next immediate step up from the pinned case, and will provide valuable information on the effects of providing suppressive support at the joint, without exerting excessive clamping forces. Each subsequent torque level was increased in increments of 20 ft-lbs, resulting in torque levels of 30 ft-lbs (2870 lbs), 50 ft-lbs (4780 lbs), 70 ft-lbs (6690 lbs), and 110 ft-lbs (10520 lbs). Testing six torque levels will provide sufficient data to evaluate the progressive change in failure modes, loads and displacements, and allow for a conclusive recommendation to be made.

5.3.1 Results (Torque = 10 ft-lbs)

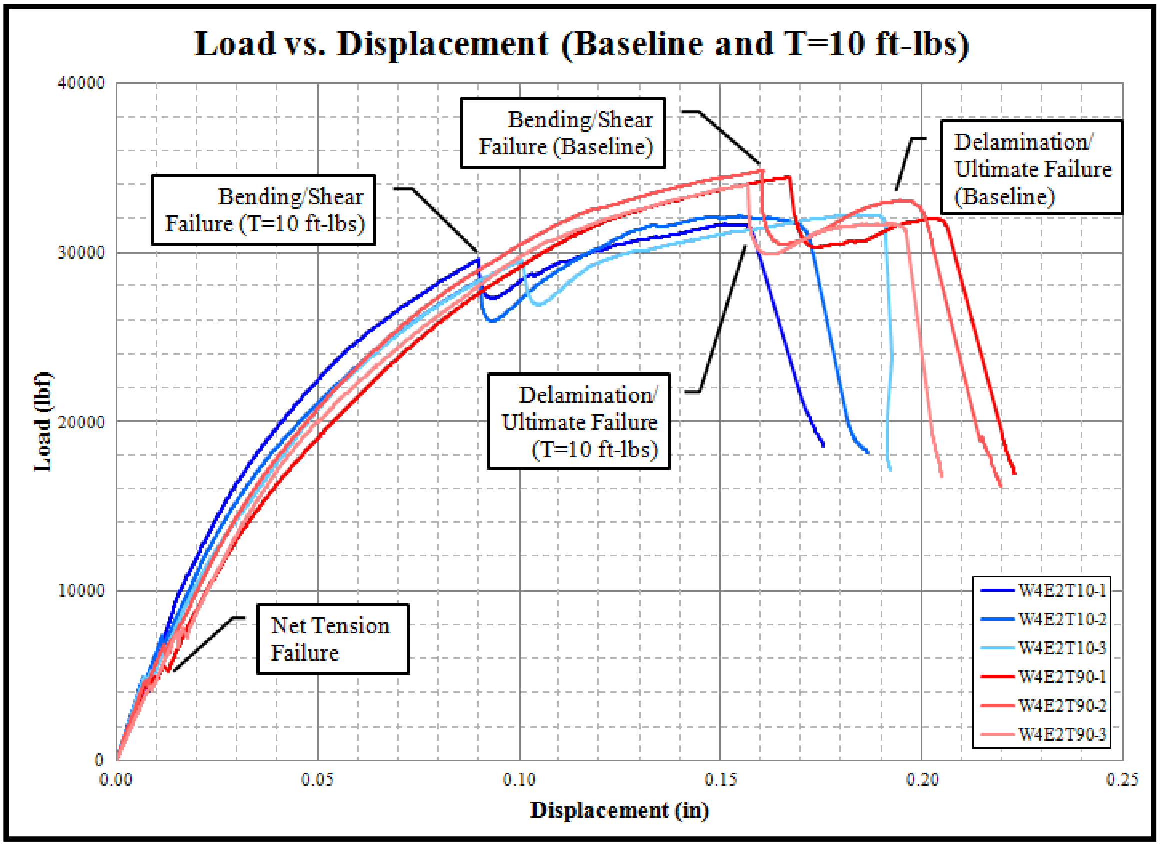

Figure 5.12: Load vs. Displacement Curves for Baseline Torque and Torque = 10 ft-lbs (W4E2T90 and W4E2T10)

With an initial torque of 10 ft-lbs, the first net tension crack occurred on average at 4541 lbs (9872 psi), with a standard deviation of 684 lbs (1487 psi). This average is slightly lower than that seen for the pinned and baseline torque cases; however, Table 5.3 shows that the third sample experienced first damage at a slightly lower load than the first two tests with 10 ft-lbs of torque. Any imperfection in the ceramic tile due to machining processes of the joint could have caused early crack initiation, resulting in the lower damage load. The bending/shear failure mode occurred at an average load of 29180 lbs (63435 psi), with a standard deviation of 683 lbs (1485 psi). This is approximately a 40% gain in strength from the pinned case for the same failure mode; however, it is much less than what the baseline torque experienced. It is presumed that the magnitude of clamping forces applied at the joint have a progressive effect on the strength at bending/shear failure. Ultimate failure and delamination of the DCCS Structure occurred at an average load of 32041 lbs (69654 psi), with a standard deviation of 312 lbs (678 psi). The average joint displacement at ultimate failure was 0.1647 inches. Like the bending/shear failure mode, ultimate failure for specimens with an initial torque of 10 ft-lbs occurred at a greater load and displacement than pinned specimens, however, they were only marginally less than the baseline torque of 90 ft-lbs. This implies that the magnitude of clamping force at the joint may not have a significant impact on the final failure mode, only that, as long as a clamping force exists, the strength at ultimate failure is improved. This claim will be confirmed or refuted by the results of the remaining torque levels.

Table 5.3: Strength and Displacement Comparisons (Torque = 10 ft-lbs)

Sample #	Strength at First Damage (Net Tension)	Strength at Bending/Shear Failure	Strength at Ultimate Failure	Displacement at Ultimate Failure
W4E2T10-1	4976 lbs	29533 lbs	32264 lbs	0.1839 in
	22130 N	131370 N	143520 N	4.671 mm
W4E2T10-2	4895 lbs	28393 lbs	32174 lbs	0.1549 in
	21770 N	126300 N	143120 N	3.934 mm
W4E2T10-3	3753 lbs	29615 lbs	31684 lbs	0.1554 in
	16690 N	131730 N	140940 N	3.947 mm

5.3.2 Results (Torque = 30 ft-lbs)

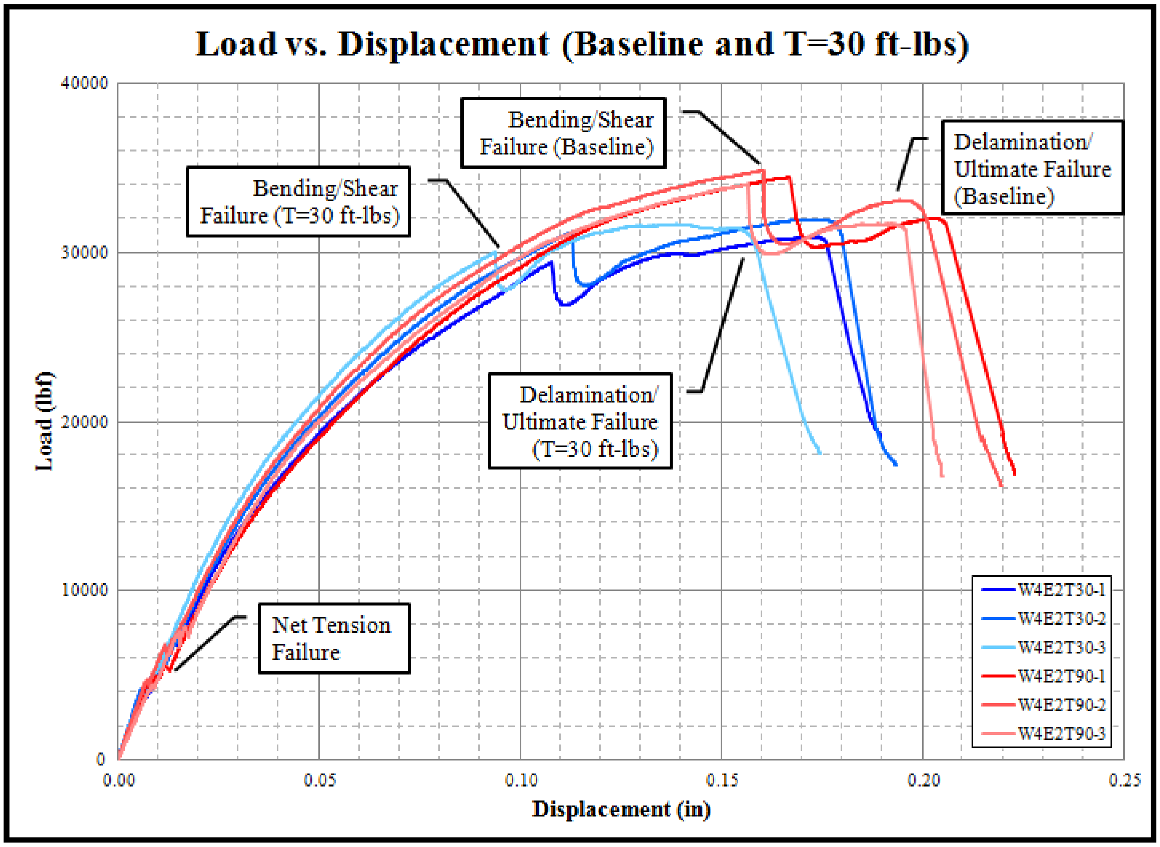

Figure 5.13: Load vs. Displacement Curves for Baseline Torque and Torque = 30 ft-lbs (W4E2T90 and W4E2T30)

With an initial torque of 30 ft-lbs, the first net tension crack occurred on average at 3775 lbs (8207 psi), with a standard deviation of 612 lbs (1330 psi). Not only is the average much lower than the averages seen in the pinned, baseline torque, and first torque level (10 ft-lbs), but individually, each specimen performed poorly in comparison to specimens from prior cases (Table 5.4). However, the initial joint stiffness for specimens with an initial torque of 30 ft-lbs was no different than the stiffness in the prior clamped cases. This raises the importance of quality joint machining; these results could signify the use of an old, worn-down drill bit, causing slight imperfections within the joint walls, ultimately leading to premature crack formation. This reinforces the need for drill bits to be replaced on a consistent basis to ensure pristine joints. The bending/shear failure mode occurred at an average load of 30253 lbs (65767 psi), with a standard deviation of 933 lbs (2028 psi). This supports the hypothesis that increased clamping forces increases the joint strength prior to bending/shear failure; the average load of bending/shear failure in joints with a torque of 30 ft-lbs is greater than the average load with 10 ft-lbs of torque, but less than the average load with the baseline torque of 90 ft-lbs. Ultimate failure and delamination of the DCCS Structure occurred at an average load of 31494 lbs (68465 psi), with a standard deviation of 593 lbs (1289 psi). The average joint displacement at ultimate failure was 0.1620 inches. These values were in a similar range as those seen with initial torques of 10 ft-lbs and 90 ft-lbs, supporting the theory that magnitude of clamping force may have no effect on the strength at ultimate failure.

Table 5.4: Strength and Displacement Comparisons (Torque = 30 ft-lbs)

Sample #	Strength at First Damage (Net Tension)	Strength at Bending/Shear Failure	Strength at Ultimate Failure	Displacement at Ultimate Failure
W4E2T30-1	4025 lbs	29422 lbs	30827 lbs	0.1752 in
	17900 N	130880 N	137130 N	4.450 mm
W4E2T30-2	4222 lbs	31263 lbs	31961 lbs	0.1719 in
	18780 N	139060 N	142170 N	4.366 mm
W4E2T30-3	3077 lbs	30075 lbs	31695 lbs	0.1389 in
	13690 N	133780 N	140990 N	3.528 mm

5.3.3 Results (Torque = 50 ft-lbs)

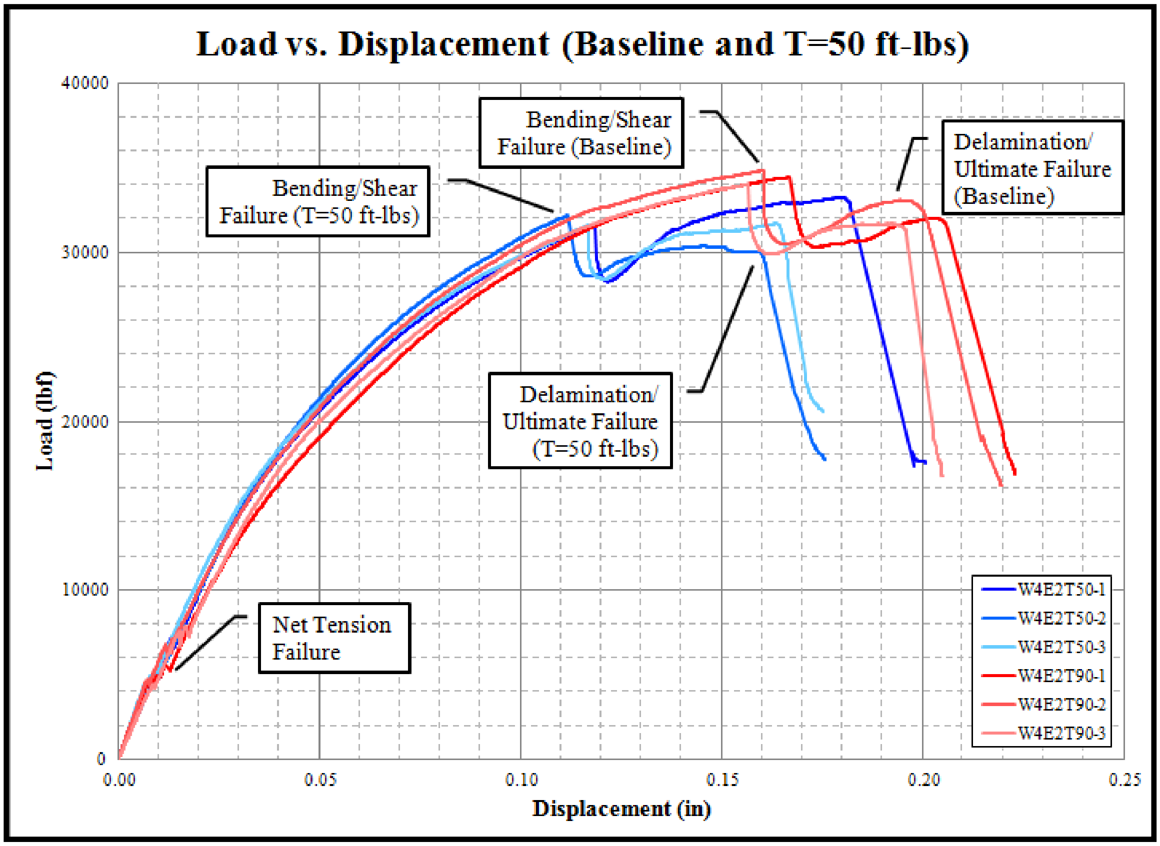

Figure 5.14: Load vs. Displacement Curves for Baseline Torque and Torque = 50 ft-lbs (W4E2T90 and W4E2T50)

With an initial torque of 50 ft-lbs, the first net tension crack occurred on average at 3994 lbs (8683 psi), with a standard deviation of 884 lbs (1922 psi). As evidence by the high standard deviation, this average was lowered by the second test sample (see Table 5.5). The first and third specimens experienced net tension failure at strengths comparable to those noted in previous cases. The bending/shear failure mode occurred at an average load of 31841 lbs (69220 psi), with a standard deviation of 333 lbs (724 psi). In conjunction with strength data from the first and second torque levels (10 ft-lbs and 30 ft-lbs), the strength at bending/shear failure for an initial torque of 50 ft-lbs continues to gradually increase as the clamping force increases. It is clearly evident that there is a correlation between clamping force and the strength at bending/shear failure in the ceramic tile. Ultimate failure and delamination of the DCCS Structure occurred at an average load of 31789 lbs (69107 psi), with a standard deviation of 1416 lbs (3078 psi). The average joint displacement at ultimate failure was 0.1627 inches. Again, these results are comparable to the first two torque levels, despite more variability in the strength at ultimate failure. Since ultimate failure is dependent on the adhesive bond strength between the constituents, strength at this failure mode is a direct function of the quality of fabrication; hence some amount of variability can be expected. Also, this was the first time where a specimen did not recoup the load lost at bending/shear failure before ultimately failing, signifying an important transition in the failure mode representing ultimate joint capacity.

Table 5.5: Strength and Displacement Comparisons (Torque = 50 ft-lbs)

Sample #	Strength at First Damage (Net Tension)	Strength at Bending/Shear Failure	Strength at Ultimate Failure	Displacement at Ultimate Failure
W4E2T50-1	4629 lbs	31665 lbs	33244 lbs	0.1791 in
	20590 N	140850 N	147880 N	4.549 mm
W4E2T50-2	2985 lbs	32225 lbs	30415 lbs	0.1455 in
	13280 N	143340 N	135290 N	3.696 mm
W4E2T50-3	4368 lbs	31634 lbs	31709 lbs	0.1637 in
	19430 N	140720 N	141050 N	4.158 mm

5.3.4 Results (Torque = 70 ft-lbs)

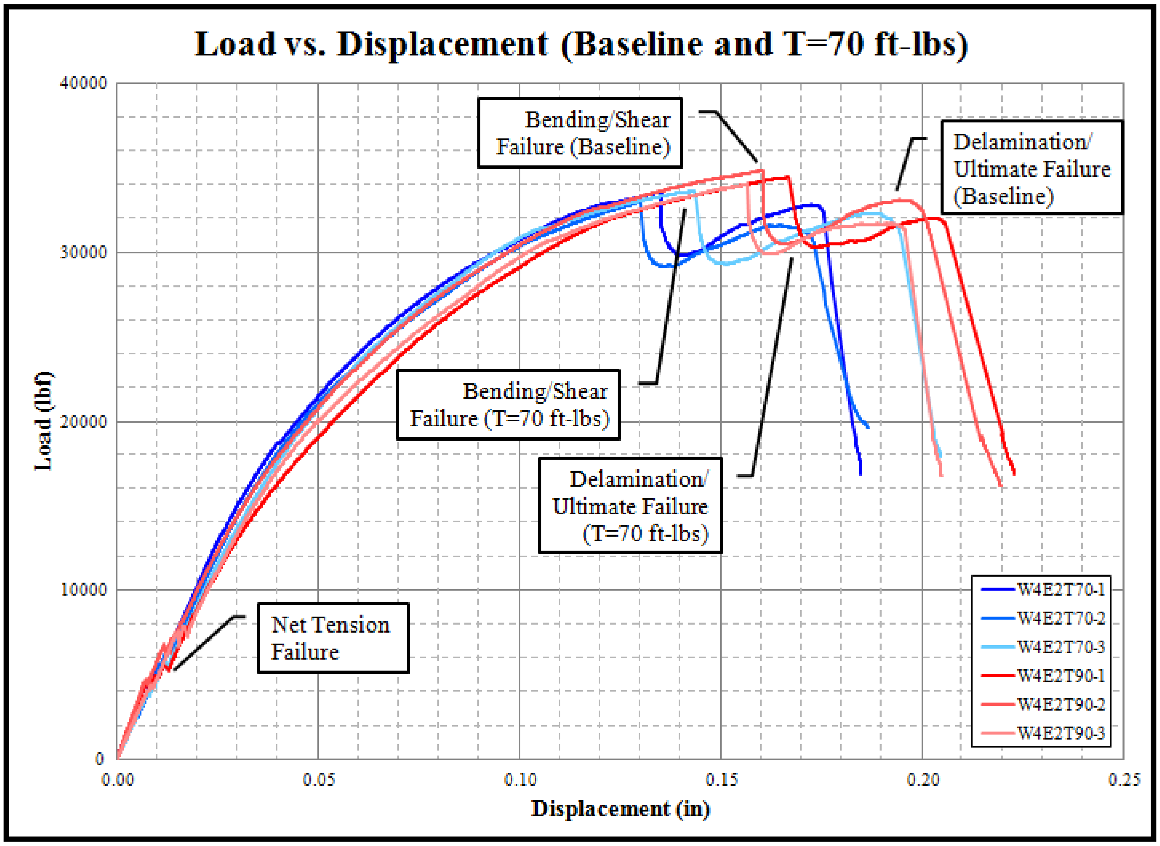

Figure 5.15: Load vs. Displacement Curves for Baseline Torque and Torque = 70 ft-lbs (W4E2T90 and W4E2T70)

Based on the data/results accumulated thus far from previous torque levels, the performance of the remaining torque levels (70 ft-lbs and 110 ft-lbs) is quite predictable. With an initial torque of 70 ft-lbs, the first net tension crack occurred on average at 3803 lbs (8267 psi), with a standard deviation of 939 lbs (2041 psi). The second test specimen experienced a below average strength at net tension failure, resulting in the reduced average and high standard deviation (Table 5.6). The bending/shear failure mode occurred at an average load of 33421 lbs (72654 psi), with a standard deviation of 360 lbs (783 psi). This value fell between the averages seen with initial torques of 50 ft-lbs and 90 ft-lbs. Ultimate failure and delamination of the DCCS Structure occurred at an average load of 32265 lbs (70141 psi), with a standard deviation of 610 lbs (1326 psi). The average joint displacement at ultimate failure was 0.1752 inches. This was the first torque level where the prevailing joint strength was governed by the strength at bending/shear failure as opposed to delamination of the DCCS Structure. This transition point is very important depending on the method of loading. All static tests in this study were conducted in a displacement-controlled manner. It has been apparent that in terms of displacement, bending/shear failure occurs at much smaller displacements than ultimate failure. However, if loading was applied by a load-controlled manner, bending/shear failure would also initiate delamination and ultimate failure in the DCCS Structure.

Table 5.6: Strength and Displacement Comparisons (Torque = 70 ft-lbs)

Sample #	Strength at First Damage (Net Tension)	Strength at Bending/Shear Failure	Strength at Ultimate Failure	Displacement at Ultimate Failure
W4E2T70-1	4549 lbs	33611 lbs	32828 lbs	0.1725 in
	20230 N	149510 N	146030 N	4.381 mm
W4E2T70-2	2749 lbs	33005 lbs	31617 lbs	0.1652 in
	12230 N	146810 N	140640 N	4.169 mm
W4E2T70-3	4112 lbs	33646 lbs	32350 lbs	0.1877 in
	18290 N	149660 N	143900 N	4.768 mm

5.3.5 Results (Torque = 110 ft-lbs)

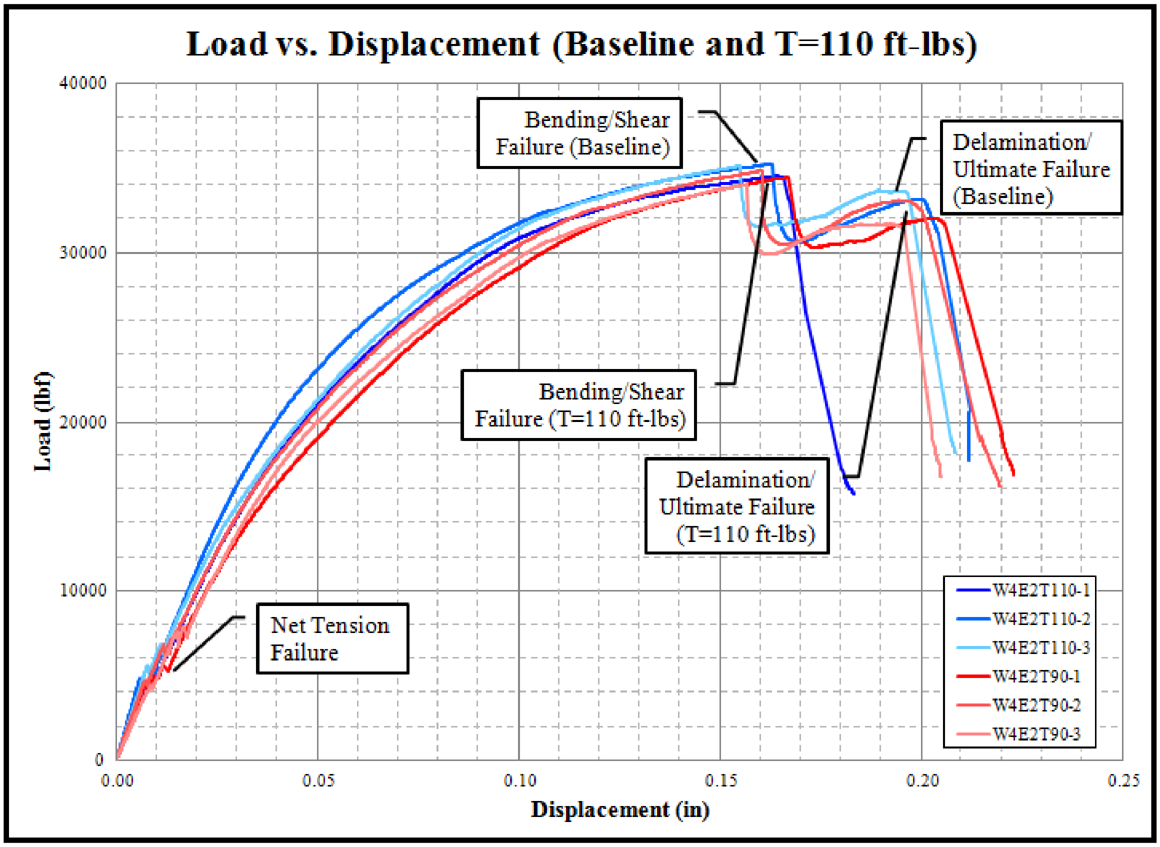

Figure 5.16: Load vs. Displacement Curves for Baseline Torque and Torque = 110 ft-lbs (W4E2T90 and W4E2T110)

With an initial torque of 110 ft-lbs, the first net tension crack occurred on average at 4972 lbs (10809 psi), with a standard deviation of 622 lbs (1352 psi). This falls into the expected range of net tension failure, and the standard deviation shows that there are no significant outliers of the three test samples (Table 5.7). The bending/shear failure mode occurred at an average load of 34987 lbs (76059 psi), with a standard deviation of 355 lbs (772 psi). Based on the trajectory of increased joint strength with an increase in clamp load, the average load of bending/shear failure appears to be reaching a plateau at the torque level of 110 ft-lbs. This was also the first torque level where a specimen built up enough potential energy in the DCCS Structure and stress in the interlayer prior to bending/shear failure that delamination occurred simultaneously. Ultimate failure and delamination of the DCCS Structure occurred at an average load of 33813 lbs (73507 psi), with a standard deviation of 687 lbs (1493 psi). The average joint displacement at ultimate failure was 0.1844 inches. These numbers were distorted based on the results of the first test specimen, which failed catastrophically when the second failure mode (bending/shear) occurred. Consequently, it raised the average strength of ultimate failure (based on the progression of previous torque levels, strength at ultimate failure would have been less than the strength at bending/shear failure) and decreased the total joint displacement (joint typically displaces due to bearing failure in the time between bending/shear failure and ultimate failure).

Table 5.7: Strength and Displacement Comparisons (Torque = 110 ft-lbs)

Sample #	Strength at First Damage (Net Tension)	Strength at Bending/Shear Failure	Strength at Ultimate Failure	Displacement at Ultimate Failure
W4E2T110-1[1]	4399 lbs	34555 lbs	34555 lbs	0.1642 in
	19470 N	153710 N	153710 N	4.171 mm
W4E2T110-2	4883 lbs	35251 lbs	33198 lbs	0.1994 in
	21720 N	156800 N	147670 N	5.065 mm
W4E2T110-3	5634 lbs	35156 lbs	33686 lbs	0.1895 in
	25060 N	156380	149840 N	4.813 mm

[1] Bending/Shear Failure occurred simultaneously with Delamination/Ultimate Failure

5.4 <u>Comparison of Various Torque Levels</u>

Collectively, the six different torque levels tested (the baseline torque and five subsequent levels) lend plenty of evidence to understand and accurately predict the performance of joints exposed to various clamping forces. A summary of results can be seen in Table 5.8, which includes the average strength at all three failure modes, the joint displacement at ultimate failure, along with the standard deviation of each strength and displacement at its' respective level of torque. (These results will be referenced throughout the remainder of this section.) Statistically speaking, the mean (or average) simply provides a baseline such that 50 percent of all specimens fail above the mean strength and 50 percent fail before reaching that strength. In terms of design, the higher the mean strength of failure does not necessarily represent the best design. Predictability of failure is a major component of design methodologies, consequently, having a lower variability in failure strength ranges (ie. smaller standard deviations), is often a better alternative than selecting the option that provides the most strength, albeit at more unpredictability. A common method of comparing design loads is subtracting three times the standard deviation from the mean; this typically requires many data points for a comprehensive statistical analysis, but it will be a sufficient method of comparison for this study. Another deciding factor in selecting the optimal torque is the progression of failure of the DCCS Structure. Progressive failure that provides an indication that ultimate failure is imminent is more advantageous compared to sudden, catastrophic failures. When there is forewarning to ultimate failure, the DCCS Structure can be repaired or replaced without being entirely exposed to additional impact loads. These thought processes will be employed when evaluating the optimal level of torque according to static testing.

Table 5.8: Strength and Displacement Comparisons (All Clamped Tests - Averages)

Sample #	Strength at First Damage (Net Tension)	Strength at Bending/Shear Failure	Strength at Ultimate Failure	Displacement at Ultimate Failure
W4E2T10	4541 lbs (± 684 lbs)	29180 lbs (± 683 lbs)	32041 lbs (± 312 lbs)	0.1647 in (± 0.0166 in)
	20200 N (± 3043 N)	129800 N (± 3038 N)	142530 N (± 1388 N)	4.183 mm (± 0.421 mm)
W4E2T30	3775 lbs (± 612 lbs)	30253 lbs (± 933 lbs)	31494 lbs (± 593 lbs)	0.1620 in (± 0.0201 in)
	16790 N (± 2722 N)	134570 N (± 4150 N)	140090 N (± 2638 N)	4.115 mm (± 0.511 mm)
W4E2T50	3994 lbs (± 884 lbs)	31841 lbs (± 333 lbs)	31789 lbs (± 1416 lbs)	0.1627 in (± 0.0168 in)
	17770 N (± 3932 N)	141640 N (± 1481 N)	141400 N (± 6299 N)	4.133 mm (± 0.427 mm)
W4E2T70	3803 lbs (± 939 lbs)	33421 lbs (± 360 lbs)	32265 lbs (± 610 lbs)	0.1752 in (± 0.0115 in)
	15120 N (± 9177 N)	148660 N (± 1601 N)	143520 N (± 2713 N)	4.450 mm (± 0.292 mm)
W4E2T90	4427 lbs (± 270 lbs)	34462 lbs (± 403 lbs)	32283 lbs (± 734 lbs)	0.1965 in (± 0.0055 in)
	16920 N (± 1201 N)	153290 N (± 1793 N)	143600 N (± 3265 N)	4.991 mm (± 0.140 mm)
W4E2T110	4972 lbs (± 622 lbs)	34987 lbs (± 355 lbs)	33813 lbs (± 687 lbs)	0.1844 in (± 0.0182 in)
	22120 N (± 2767 N)	155630 N (± 1579 N)	150410 N (± 3056 N)	4.684 mm (± 0.462 mm)

One of the earliest differences between the pinned and baseline clamped condition was the stiffness of the joint. This was attributed to the clamping force changing the compliance of the adhesive interlayer and reducing the amount of stress transfer from the face sheet into the ceramic tile. After testing various clamping forces, the magnitude of clamping force did not appear to have a significant influence on the stiffness of the joint. The joint stiffness from the twelve test performed at varying torques ranged from 540540 lbs/in to 750940 lbs/in, with an average of stiffness of 656236 lbs/in and a standard deviation of 64580 lb/in. This compared to an average stiffness of 1065925 lbs/in for pinned tests, provides evidence that the presence of a clamping force has a larger impact on the stiffness than the magnitude of torque.

The same reasoning behind the constant stiffness can describe the presence of the first net tension cracks in the ceramic tile occurring at approximately the same strength and displacement across all torque levels. The first visible cracks occurred within the range of 2749 lbs to 5634 lbs, with an average load of 4252 lbs and a standard deviation of 740 lbs. Many of the specimens on the lower end of this range may have cracked prematurely as a result of poorly machined joints. This raises into question the structural integrity of joints machined with old, worn drill bits. The use of such bits can cause burning of the interlayer, imperfections in the ceramic tile, and frayed edges at the surface of the face sheet. Any of these conditions can have an impact on the strength of the joint. For this reason, drill bits should be periodically checked and replaced, as needed. Based on the results, it is safe to conclude that the strength of the joint at first failure is more of a function of the quality of the joint, than the applied clamping force. According to the means and standard deviations from Table 5.8, there was no direct correlation between the strength at net tension failure and the amount of clamping force; however, if there was a method to machine the joint such that the quality was more consistent from specimen to specimen, this could provide for a better opportunity to examine effect of torque on the first failure mode.

The second failure mode, bending/shear cracking of the ceramic tile, appears to be directly affected by the magnitude of the clamping force. With increased clamping force, the mean strength and displacement at which bending/shear failure occurs continually increases. The increased displacement is visible by increasingly larger separation of the net tension cracks during loading. At the same time, the clamping force reduces the bending of the ceramic tile, by effectively reducing stress transfer from the face sheet to the tile. This leads to a greater bearing load required to cause the necessary bending and tensile stresses in the ceramic tile to cause bending/shear failure.

Using data from Table 5.8, the strengths at bending/shear failure can be compared using the methodology described earlier, reducing the mean strength by three standard deviations to eliminate the variability exhibited at each torque level. This resulted in the following reduced strengths for each torque level: 10 ft-lbs of torque – 27131 lbs; 30 ft-lbs of torque – 27454 lbs; 50 ft-lbs of torque – 30842 lbs; 70 ft-lbs of torque – 32341 lbs; 90 ft-lbs of torque – 33253 lbs; 110 ft-lbs – 33922 lbs. Torque levels below 30 ft-lbs did not show much difference in strength at this failure mode. Recall from Chapter 4, this range of torque levels did not see yielding of the interlayer, meaning the transfer of stresses between the face sheet and ceramic tile was not inhibited, and the ceramic tile likely carried the same bearing load for both the 10 and 30 ft-lb torque levels. Between 30 and 110 ft-lbs of torque, there was a markedly large increase in the bending/shear failure strength. This was accompanied by yielding of the interlayer, as seen in Figure 4.29. Note that the largest increase in strength between adjacent torque levels occurred between 30 and 50 ft-lbs of torque, which, according to Figure 4.29, also exemplified the most significant expansion of the yielded interlayer, in terms of extent from the hole boundary. As the extent of the yielded interlayer became less between each subsequent torque level, the increase in the failure strength also became less. It should also be noted, that one specimen pre-loaded with 110 ft-lbs of torque, failed catastrophically due to simultaneous bending/shear failure and delamination failure. This nature of failure provides an early indication of the upper torque limit for static loading; this will be discussed in more detail in the final design recommendation later in this Section.

After bending/shear failure, specimens from all torque levels experience a significant loss of bearing load due to the release of stored energy in the tile. As the bearing load increases, it becomes evident that the joint stiffness has been greatly reduced. Given the location of the cracks in the ceramic tile, the tile can no longer carry a large part of the bearing load, and the face sheet is relied to carry the majority of the load. During this stage of loading, the face sheet begins to experience bearing failure, as acoustic emissions of the from fiber damage become frequent. The upper two quadrants of the ceramic tile begin to protrude from between the face sheets, causing the face sheets to bow outward. The interlayer begins yielding where the net tension cracks are fully separated and at the top of the specimen where the tile is protruding. The adhesive bond finally fails between the ceramic tile and interlayer, and the interlayer and face sheet, resulting in catastrophic failure within the entire shear area of the specimen. Delamination and de-bonding begin along the top edge of the specimen, thus are a function of the fabrication of the DCCS Structure, not the clamping force. This explains why ultimate failure occurred at approximately the same mean strength for all torque levels. Joint displacement at ultimate failure increased marginally at torque levels above 50 ft-lbs, but this was primarily a result of increased displacement when bending/shear failure occurred. Delamination and ultimate failure occurred within the range of 30415 lbs to 34555 lbs, with the average failure strength of 32281 lbs and a standard deviation of 1014 lbs. This range is partially misleading, as the specimen experiencing ultimate failure at 34555 lbs failed in conjunction with bending/shear failure. Removing this specimen from the above range, the next highest strength to achieve ultimate failure was 33686 lbs.

Manipulating the strengths by reducing the mean strength by three standard deviations can provide a more introspective view into the strength by taking into account the variability of the strengths at failure. In doing this, the revised strengths for each stress level are: 10 ft-lbs of torque – 31105 lbs; 30 ft-lbs of torque – 29715 lbs; 50 ft-lbs of torque – 27541 lbs; 70 ft-lbs of torque – 30435 lbs; 90 ft-lbs of torque – 30081 lbs; 110 ft-lbs of torque – 31752 lbs. With the exception of the 50 ft-lb torque level, the reduced strengths all fall within a range between 29700 lbs to 31800 lbs, within no evident trend between the magnitude of torque and strengths in that range. However, the significantly higher variability of the 50 ft-lb torque level was no coincidence. As the torque level is increased, the peak joint strength demonstrated in any test specimen transitions from occurring between bending/shear and delamination failure strengths, to the bending/shear failure strength. This transition occurs at a torque level of approximately 50 ft-lbs. The average bending/shear failure at this level occurred at a strength of 31841 lbs, before drastically falling after this failure mode. The strength gradually recovered prior to ultimate failure, reaching an average strength of 31789 lbs. Because these failure modes occur so close in proximity in terms of strength, the onset of delamination failure may begin before or after bending/shear failure. If delamination has already begun, the energy released during bending/shear failure likely accelerates delamination, causing lower ultimate failure strengths. If delamination has not begun prior to bending/shear failure, the ultimate strength at delamination is likely to govern as the peak strength of that particular specimen. Note that a certain balance exists at torque levels greater than 50 ft-lbs where delamination and debonding likely initiates prior to bending/shear failure. Because the strength to cause bending/shear failure increases with increased torque, more internal debonding is likely to occur. This debonding begins along the top edge of the specimen and expands to regions closer to the joint with greater loads; however, increasing torque also suppresses delamination at the joint, thus allowing for bending/shear failure to always occur first, followed by delamination/debonding.

In torque levels below 50 ft-lbs, lower strengths at bending/shear failure are exhibited, thus peak strengths occurred just prior to delamination/ultimate failure. Torque levels greater than 50 ft-lbs experienced higher strengths at bending/shear failure, which resulted in the peak overall strength of the specimens. This transition becomes important in that, under load-controlled conditions (as opposed to displacement-controlled), these higher levels would cause simultaneous catastrophic failure of bending/shear and delamination, much like the second specimen at the 110 ft-lb torque level. This type of catastrophic failure is particularly disconcerting because it occurs unexpectedly and without warning. Under displacement-controlled settings, the torque level of 110 ft-lbs would preferably be avoided, citing the previous statement about catastrophic failures. Instead, the optimal torque likely lies somewhere between 90 ft-lbs and 110 ft-lbs.

5.5 <u>Finite Element Analysis of Clamped Joints in DCCS Structures</u>

Experimental testing is a useful method to monitor the progressive failure of DCCS joint specimens and quantify the strength at each respective failure mode. However, to gain a better understanding of the distribution of stresses throughout the DCCS Structure, a finite element model becomes necessary. Weidner et al utilized a finite element model of a pinned joint in the DCCS Structure to show how geometric parameters affected stress distribution around the joint. His baseline model consisted of geometrical ratios of e/D = 4.0 and w/D = 8.0, the same used in the current study. In order to easily compare the pinned joint case to the present clamped joint, the existing model was adapted to simulate the baseline clamping forces used in experimentation.

Like the finite element model discussed in Chapter 4, this model will also utilize CATIA as the primary program solver. The model created by Weidner was a ¼ symmetric design, on the same accord as the model constructed to simulate the clamping force, which greatly reduced computation time and produced equally adequate results. The face sheet was modeled as 12 inches long (304.8 mm) by 2 inches wide (50.8 mm) by 0.247 inches thick (6.27 mm). The adhesive interlayer was modeled as 12 inches long (304.8 mm) by 2 inches wide (50.8 mm) by 0.02 inches thick (0.508 mm). Each ceramic tile was modeled as 4 inches long (101.6 mm) by 2 inches wide (50.8 mm) by 0.2 inches thick (0.508 mm). The resin gaps located between adjacent tiles was modeled as 2 inches long (50.8 mm) by 0.2 inches deep (5.08 mm) by 0.02 inches thick (0.508 mm). The ceramic tile, interlayer, resin gap, washer and bolt were designated as isotropic materials, using properties defined in

Table 4.9. The face sheet was designated as a 3D orthotropic material, using the properties from Table 4.10.

Meshes were assigned to each individual part; the face sheet, ceramic tile, and interlayer were designed with a surface mesh that was refined with smaller elements near the joint hole and the resin-filled gaps; the built-in Sweep function was used to extrude 8 three-dimensional replicated elements of the surface mesh through the thickness of the face sheet and ceramic tile, spaced at gradually decreasing increments in the direction of the interlayer; the same function was used to create 3 evenly-spaced three-dimensional elements through the thickness of the interlayer; an octahedral three-dimensional mesh was assigned to the bolt and washer using mesh sizes of 0.4 inches and 0.15 inches, respectively. Fastened connection meshes were used to connect the interface between the face sheet and interlayer, interlayer and ceramic tiles, interlayer and resin gaps, and ceramic tiles and resin gaps. A contact mesh with a friction ratio of 0.5 was used to connect the interface between the washer and face sheet. Frictionless contact connection meshes, which prevent embedment between interfaces, were used between the bolt shank and the face sheet, interlayer, and ceramic tile along the bearing surface. The bolt was restricted from moving in the x- and y-directions, but allowed to expand in the z-direction due to the axial load applied to the shank to simulate the clamping force. Other restraints applied to the model to simulate symmetry were located on the bottom of the model in the z-direction, and along the edge of the model in the y-direction. A pressure load was applied on the end of the bolt shank to simulate the equivalent of 90 ft-lbs of torque. Another pressure load was applied on the far edge of the face sheet, forcing the applied load to be distributed through the interlayer into the ceramic tile, creating a bearing load on the joint (as the bolt restricted the DCCS Structure from moving along the x-axis. An example of the model constraints and loading are shown in Figure 5.17 and Figure 5.18, respectively.

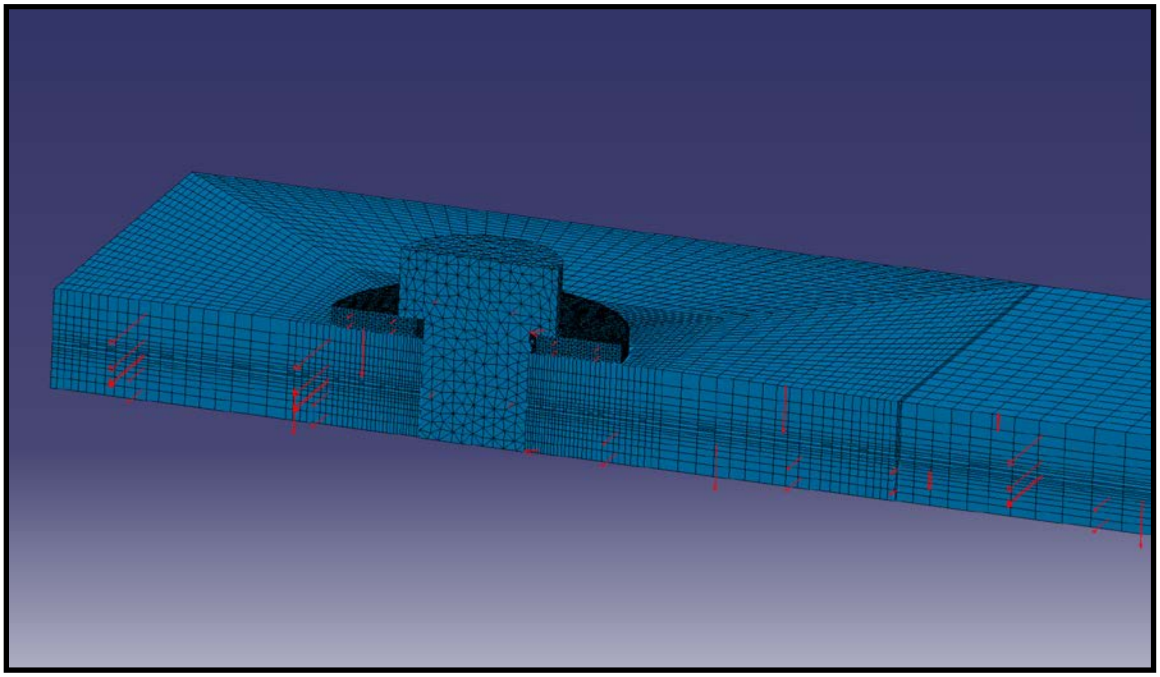

Figure 5.17: Constraints used for Quarter-Symmetric Finite Element Model

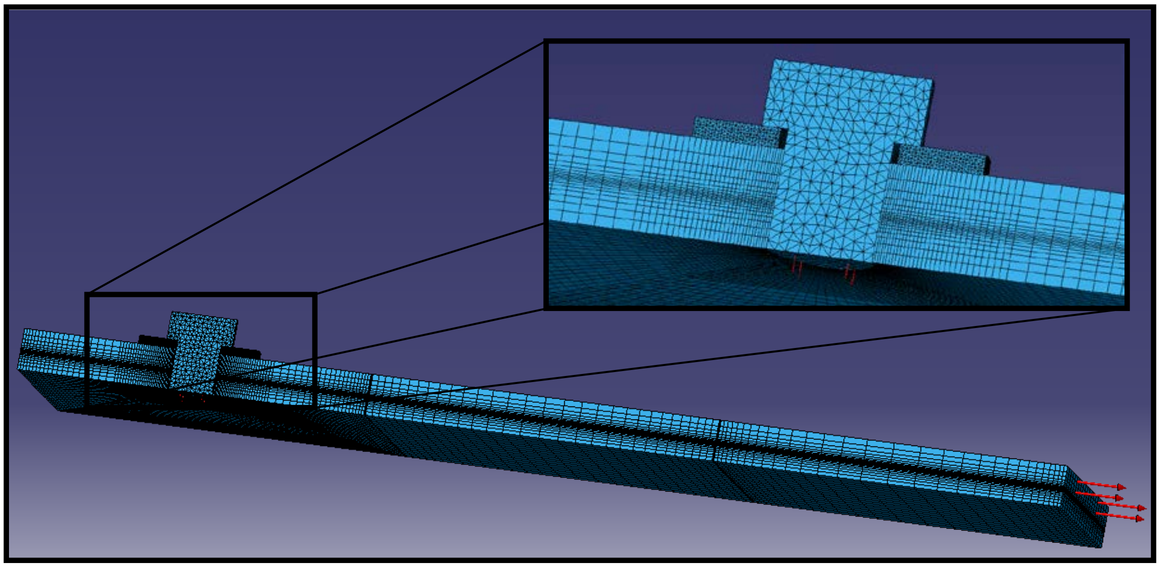

Figure 5.18: Loading used for Finite Element Model of Clamped Case

Experimental test results revealed that the average loading exhibiting visible damage to the DCCS Structure was approximately 4250 lbs (bearing stress of 9239 psi). To gain an understanding of the stresses causing this failure and the distribution of stresses, a far field pressure of 2125 psi was applied on the far edge of the face sheet to simulate 4250 lbs. The same far field load was applied to the pinned case model to allow direct comparison between the pinned and clamped case models. Figures 5.18 and 5.19 compare the hole boundary stresses in the face sheet and ceramic tile for both cases.

Earlier, it was discussed that clamped specimens exhibited lower stiffness at the joint, which was attributed to less load being transferred from the face sheet to the ceramic tile because of the yielded interlayer, and frictional resistance between the face sheet and washer causing the face sheet to carry that additional load on the surface. This stiffness was calculated based on the secant modulus, which was taken from zero load until the load of the first net tension failure. The average stiffness seen in pinned joint specimens was approximately 1066000 lb/in, whereas clamped joint specimens exhibited an average stiffness of approximately 656000 lb/in. In the finite element model, Figure 5.18 shows significantly more stress is carried in the face sheet under clamped conditions, confirming one of the mechanisms of reduced stiffness exists. Using the same method of defining stiffness that was done experimentally, the pinned model demonstrated a stiffness of approximately 1395000 lb/in, compared to a stiffness of 1324000 lb/in in the clamped model. The stiffness for the pinned model is 30% greater than the experimentally measured stiffness. This discrepancy can be attributed to the model assuming a linear elastic response, whereas experimentally, the stress-strain plot is not perfectly linear. Because the stiffness was quantified using the secant modulus, this may provide a slightly reduced stiffness than if the response was linear. The experimental stiffness of the clamped joint was 40% less than that of the pinned joint; by comparison, the modeled stiffness of the clamped joint was only 5% less than the pinned joint. Again, this is a result from the model being linear elastic. The reduced stiffness was a direct effect of the yielded interlayer preventing load from being transferred from the face sheet into the ceramic tile. However, the model does not take into account the non-linear plastic deformation of the interlayer due to yielding, instead assuming that the interlayer performs linearly beyond its' yield stress and continues to serve as a functional path for stresses to travel between the face sheet and ceramic tile. The reduced stiffness demonstrated in the model comes from the interaction between the washer and face sheet; the friction due to the clamping force transfers some of the bearing load through the outer surface of the face sheet, but the magnitude of this load is limited to the amount of clamping force and the friction coefficient between the washer and face sheet.

It was also noted in Section 5.2 that the first net tension cracks were found to occur at a hole boundary location of approximately 65 – 70 degrees. Figure 5.19 compares the tensile stresses in the ceramic tile at the hole boundary, and the distribution of stresses indicate that peak tensile stresses in the clamped joint occur close to 80 degrees, as opposed to 90 degrees in the pinned joint. Additionally, it was determined experimentally that the onset of net tension cracks occurred at similar loads for both joint cases. According to Figure 5.19, by applying a far field load in the finite element model to simulate the approximate average strength required to cause the first net tension crack, the inplane tensile stress in the ceramic tile was nearly the same for pinned and clamped joints. Multiple figures are presented to provide a visual representation of the stress distribution around the hole boundary for both models. In Figure 5.20 and 5.21, the blue regions indicate areas of compression and red regions indicate areas of tension. In both representations, tensile stresses are shown to be concentrated along the perimeter at a location of approximately 90 degrees, whereas, compressive stresses can be seen in the bearing region at approximately 0 degrees. The arrangement of stress concentrations are similar in the face sheet and interlayer, however, they exist on a much lower magnitude. In an attempt to get a better visualization of the tensile stresses, Figure 5.22 and 5.23 show only tensile stresses in the DCCS joint. This alternative approach reduces the range of stresses, and in doing so, allows the tensile stresses in the face sheet to become more apparent. The color designations are the same (dark blue indicates any part in compression, and a progression of light blue, yellow, orange and finally red for the peak tensile stresses).

These figures show areas of significantly higher tension in the clamped model than in the pinned model.

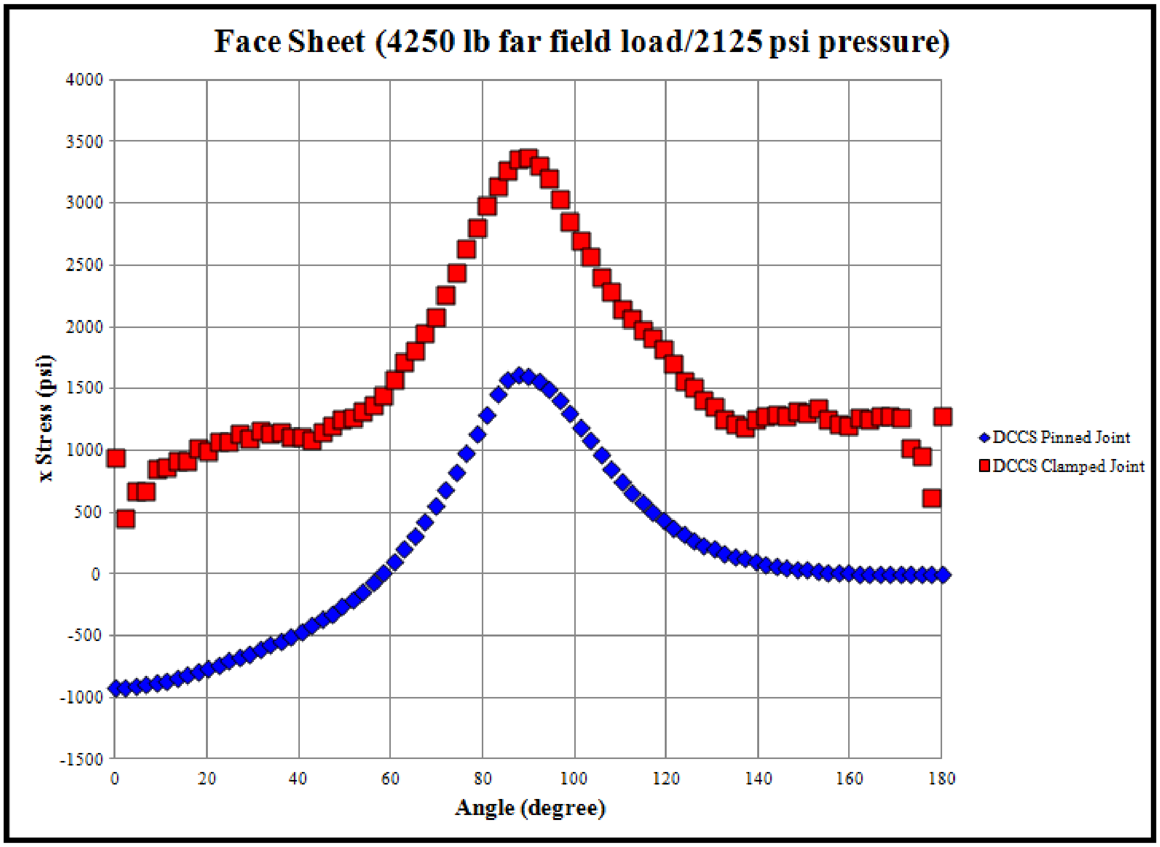

Figure 5.18: Comparison of hole boundary x stresses between pinned and baseline torque for the Face Sheet in DCCS Structure Modeling (Applied 4250 lb far field load/2125 psi pressure)

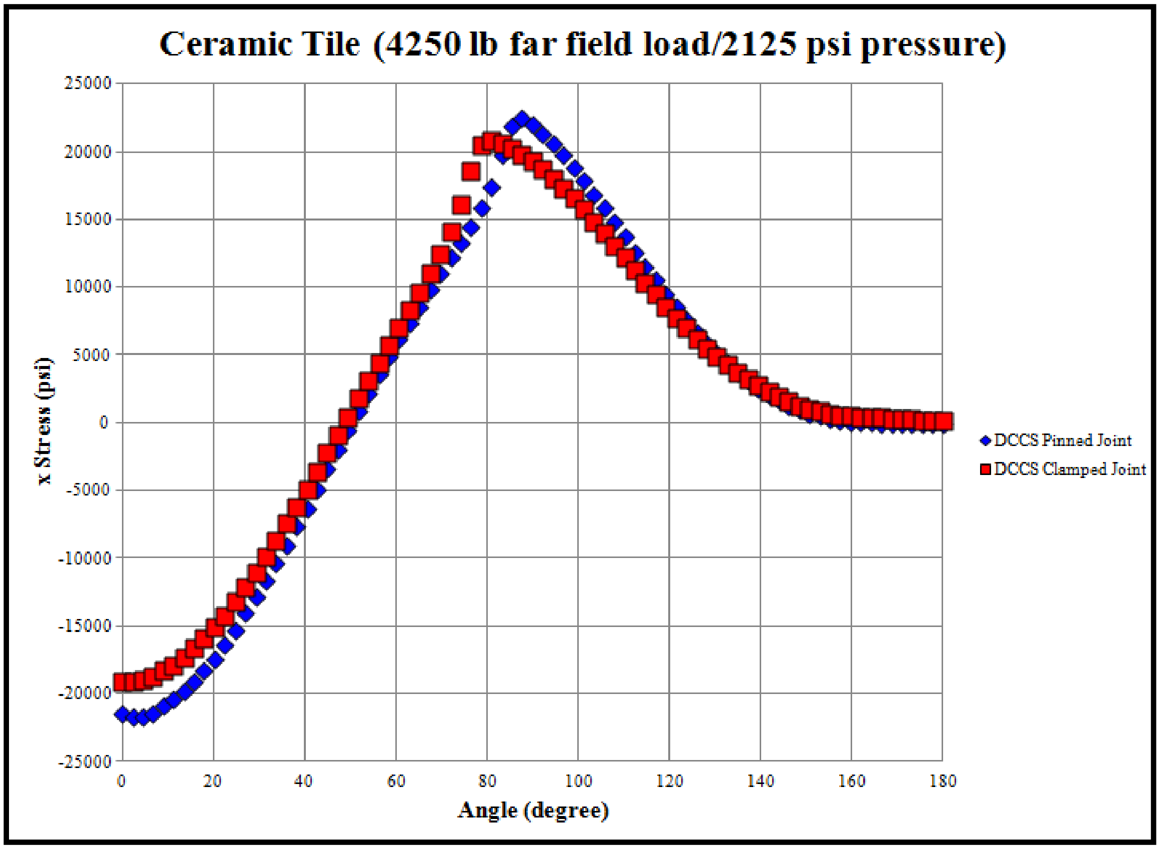

Figure 5.19: Comparison of hole boundary x stresses between pinned and baseline torque in the Ceramic Tile in DCCS Structure Modeling (Applied 4250 lb far field load/2125 psi pressure)

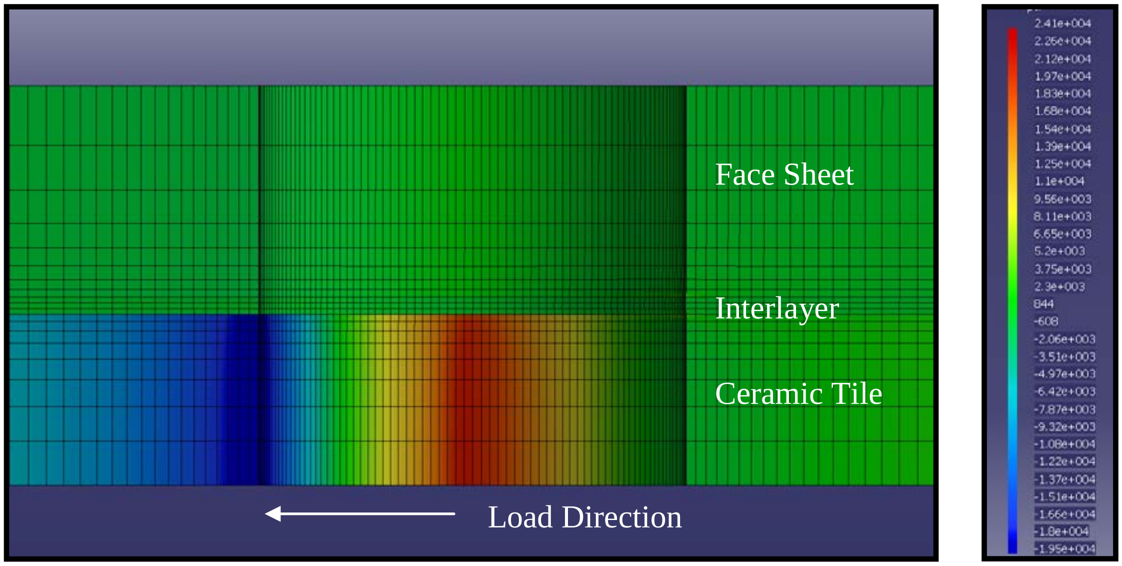

Figure 5.20: Pinned Joint Finite Element Model, x Stresses

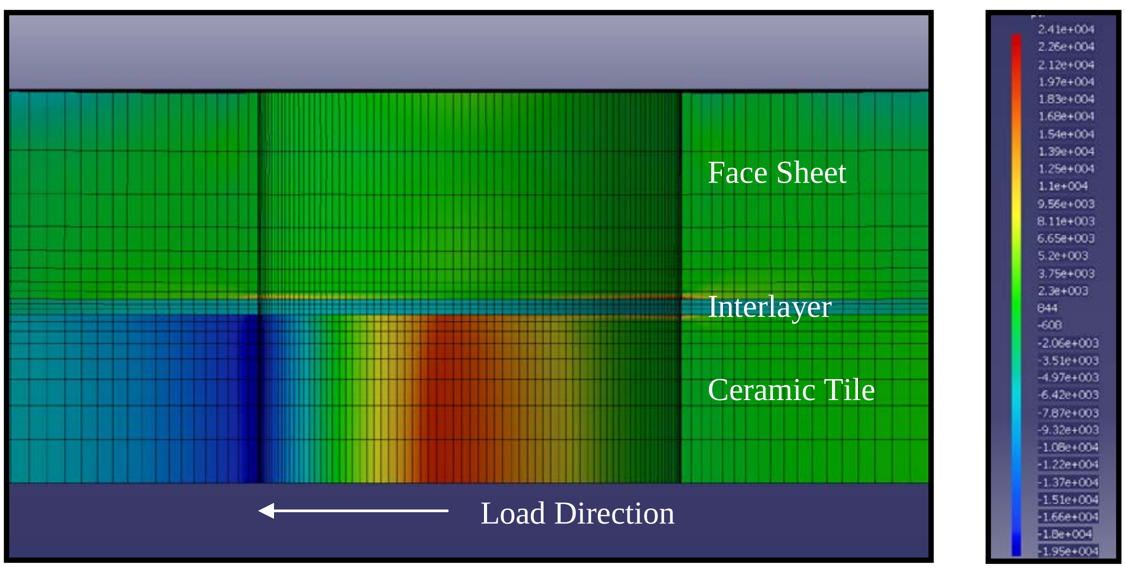

Figure 5.21: Clamped Joint Finite Element Model, x Stresses

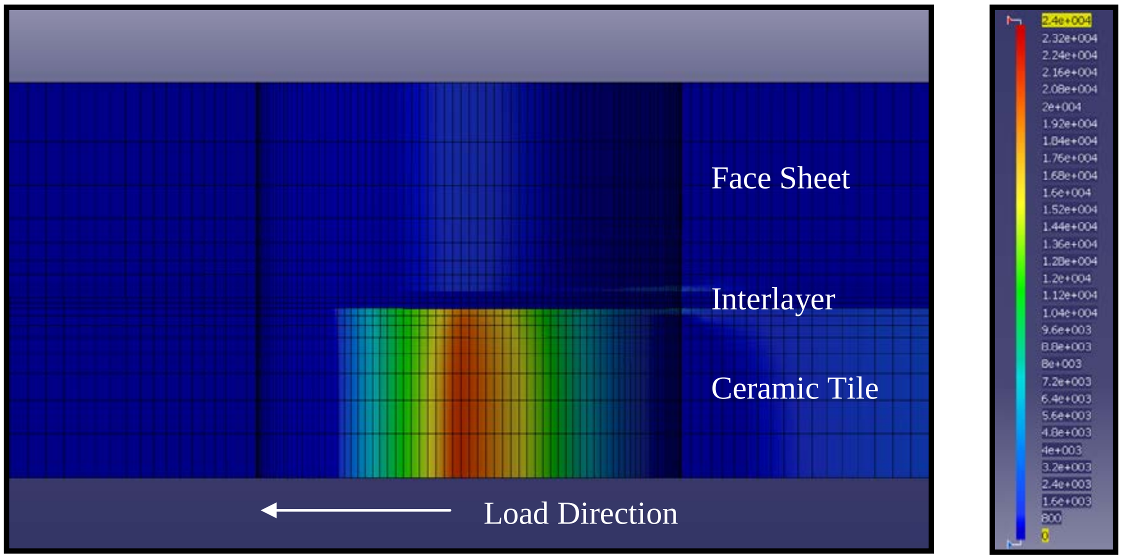

Figure 5.22: Pinned Joint Finite Element Model, x Stresses (Tension only)

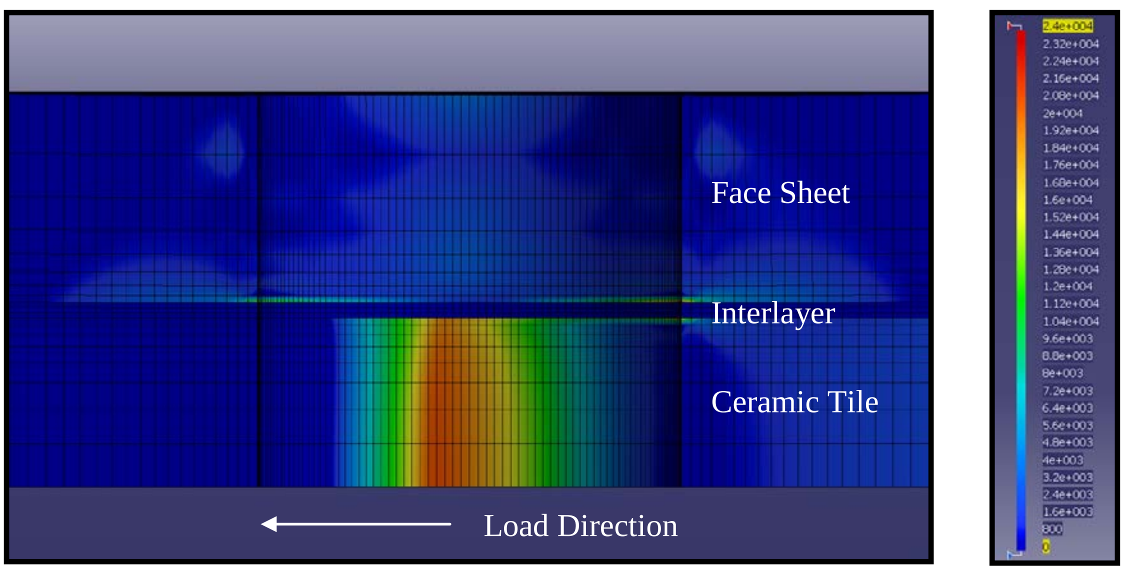

Figure 5.23: Clamped Joint Finite Element Model, x Stresses (Tension Only)

Accurately modeling the progressive failure of the DCCS joint becomes difficult after the first net tension crack. First, there is the presence of multiple net tension cracks in the ceramic tile, where the number of cracks and exact location can only be approximated. Secondly, Weidner et al confirmed that the interlayer yields and fails in the regions adjacent to the resin gaps between ceramic tiles. There is also the issue of the effect that the yielded interlayer has in the hole region due to the initial clamping force. These issues were not addressed in the current model, as the interlayer was assumed to be elastic and maintain loads in the linear region of the stress-strain relationship, and discontinuities within the ceramic tile at the joint were not considered. In order to model the DCCS joint beyond the first net tension crack and through ultimate failure, the interlayer must be modeled in its true non-linear nature by assuming elastic-plastic properties. To do this, the model will require the analysis function in ABAQUS, which can be run through the CATIA program. Other considerations that should be made to complete failure analysis of the DCCS joint include the addition of net tension and bending/shear cracks in the ceramic tile, and incorporating the non-linear nature of the face sheet. Completing an analysis that fully details progressive failure will enhance the ultimate understanding of joints in Discontinuous Ceramic Cored Sandwich Structures.

Static experimental testing and a finite element analysis provided a glimpse into the progression from pinned to clamped joints and the evolving interaction between constituents in the two test cases. The progression of failure remained the same in the transition from pinned to clamped joints, though the peak strength achieved varied depending on the magnitude of torque. Increased clamping forces result in progressively greater peak loads, before plateauing between 90 and 110 ft-lbs of torque. As joint strength increases, the location of the peak strength on the load-displacement curve takes place at different points in the progression of failure. In pinned joints and joints with under 50 ft-lbs of torque, the peak strength occurs just prior to delamination/debonding failure, whereas joints with torque greater than 50 ft-lbs experience the peak strength immediately prior to bending/shear failure. These developments were attributed to the reduced efficiency of the interlayer in its' ability to share load between the face sheet and ceramic tile, due to excessive clamping forces causing yielding of the interlayer. This phenomena also reduced joint stiffness in the DCCS Structure, prior to the first net tension failure. A finite element analysis was used to help describe the joint prior to this first failure mode. The pinned joint stiffness between the experimental results and the finite model were comparable, with the discrepancy resulting from restrictions of the model to a linear analysis. This restriction caused a larger discrepancy in the stiffness range of the clamped joint, as the model did not simulate the interlayer yielding, assuming an entirely elastic response and allowing for continuous load-sharing between the face sheet and ceramic tile. Experimentally, net tension failure occurred at the same strength in pinned and clamped test specimens; using the finite element analysis, it was proven that the tensile stress in the tile at the mean strength to cause failure (4250 lbs) was nearly identical between pinned and clamped specimens. The tensile stress to cause failure in both cases was approximately 21000 psi, compared to a prescribed tensile strength of 36000 psi. Additionally, the minimum strength to cause net tension failure was 2700 lbs, which equates to a tensile stress of approximately 13000 psi in the ceramic tile. These values are considerably lower than the ceramic tensile strength, a reduction caused by machining and surface defects along the perimeter of the joint. This poses the need for a more reliable, effective method of machining to reduce the amount and size of the defects. Despite the variability in joint strength at net tension failure, there are no residual effects of premature failure; instead, specimens demonstrate very similar load-displacement curves beyond net tension failure. Thus, the primary design consideration focuses around the peak joint strength. The experimental testing found this strength to occur at approximately 95 ft-lbs of torque, or an effective torque of 85 ft-lbs, taking into account the torque required in the experimental set-up to close the side laps of the test fixture. Under displacement-controlled loading conditions, this torque level demonstrated a failure sequence of net tension – bending/shear – delamination/debonding failure. However, under load-controlled conditions, bending/shear and delamination/debonding failure would occur simultaneously, in part because bending/shear failure represent the peak strength at this torque level. To prevent catastrophic failure of the DCCS joint under this loading condition, experimental testing showed that torque levels below 50 ft-lbs (effective torque of 40 ft-lbs) demonstrated peak strengths to occur at delamination/debonding failure, after bending/shear failure. This provides reduced joint strength, but allows for a more progressive failure prior to ultimate failure.

Static testing is a useful technique in evaluating and understanding the progressive failure modes and failure strengths for design. Modeling the DCCS Structure and stress interactions at the joint provides valuable information that can be applied to the design, as well. Future applications of the DCCS Structure have the potential for a variety of loading patterns, in addition to static loads. Cyclic and fatigue loading is very common, often resulting from vibrations, temperature differential and other environmental effects. Examining the long-term efficiency of the DCCS Structure is an important component in design. Chapter 6 will investigate the performance of clamped and pinned joints in the Discontinuous Ceramic Cored Sandwich Structure exposed to various fatigue levels.

Chapter 6

FATIGUE TESTING ON DISCONTINUOUS CERAMIC CORED SANDWICH STRUCTURES

In addition to static loading conditions, the performance of DCCS Structures exposed to fatigue loading is also important in design. Fatigue loading can come from any number of sources, including external sources, such as vehicle vibrations, travel on uneven terrain, or intense weather conditions, or internal sources like a mismatch in coefficients of thermal expansion between constituents. Under conditions with higher fatigue loads, damage may be detected visually, and monitored through the fatigue lifetime. Other conditions may expose the DCCS Structure to lower fatigue loads, where damage is not visible. However, this does not preclude the structure from experiencing a loss of stiffness or strength. Understanding the joint performance under high and low cyclic fatigue loading is imperative to enhance the long term durability of the DCCS Structure. Using results presented in Chapter 5, fatigue stress levels were determined under two primary states: high level stresses which exceed the strength of the joint at first damage, and low level stresses which do not experience visible damage under the initial load sequence. This will provide a comprehensive analysis of the effect of various fatigue levels on the progressive failure and residual strength of the DCCS Structure. Fatigue testing on the Discontinuous Ceramic Cored Sandwich Structure began with in-plane tension-tension testing of one inch wide specimens (Gillespie et al). It was concluded from these tests that fatigue initially caused gap failure in the discontinuous core, before showing signs of debonding of the face sheet/ceramic tile interface. Propagation of this fatigue crack significantly reduced the stiffness of the DCCS Structure over time. Weidner et al followed this research by conducting fatigue tests on pinned joints at low level stresses; this process will be repeated with clamped joints at both low and high level stresses, as well as with pinned joints at high level stresses. Combined with the results from Chapter 5, this will provide a complete comparison of pinned and clamped joints for the DCCS Structure.

6.1 <u>Fatigue Testing Set-Up</u>

To ensure comparable results for all fatigue testing, including the results obtained by Weidner et al using low level fatigue stresses with pinned joints, a rigid testing procedure and experimental set-up must be maintained. The double-lap test fixture used for static testing will be implemented for fatigue testing. The baseline specimen geometry, as determined by Weidner et al to be w/D = 8 and e/D = 4, will remain constant for all fatigue tests. The intent of high level fatigue testing was to determine the number of cycles required to cause catastrophic failure in the DCCS Structure, and at what stress level the DCCS Structure could survive despite net tension failure in the ceramic tile, which was expected at these levels. The intent of low level fatigue testing was to determine if/when net tension failure would occur in the ceramic tile when exposed to different stress levels, and the limiting stress level that resisted all stiffness and residual strength loss of the joint. The high level and low level stresses were derived from the results of the static testing in Chapter 5. These stress levels are documented in Tables 6.1. The average load to cause catastrophic failure of the DCCS Structure under clamped conditions was 32281 lbs (70176 psi), and 28739 lbs (62476 psi) under pinned conditions. The minimum load to cause failure between both cases was 28330 lbs (61587 psi). Since both conditions will be tested at high level fatigue stresses, fatigue results will be much easier to compare using the same stress levels. Stress Level 5 (high level) was determined as 90 percent of the minimum load to cause catastrophic failure, with each subsequent stress level a reduction of 20 percent of Stress Level 5. Low level stresses were based on the load to cause net tension failure in the ceramic tile. The average load to cause net tension failure was 4252 lbs (9243 psi), with a minimum load to cause failure of 3750 lbs (8152 psi). Low level were stresses were determined in the same manner as high level stresses, with Stress Level 5 verified to be outside the standard deviation of loads to cause each respective failure.

Table 6.1: Loads and Bearing Stresses for Fatigue Tests

		Maximum Load		Minimum Load		Percent of Level 5
Low Level Fatigue Stresses	Stress Level 1	680 lbs	1478 psi	68 lbs	148 psi	20
		3024 N	10.19 MPa	302.4 N	1.019 MPa	
	Stress Level 2	1360 lbs	2956 psi	136 lbs	296 psi	40
		6050 N	20.38 MPa	605.0 N	2.038 MPa	
	Stress Level 3	2040 lbs	4435 psi	204 lbs	444 psi	60
		9074 N	30.58 MPa	907.4 N	3.058 MPa	
	Stress Level 4	2720 lbs	5913 psi	272 lbs	591 psi	80
		12099 N	40.77 MPa	1209.9 N	4.077 MPa	
	Stress Level 5	3400 lbs	7391 psi	340 lbs	739 psi	100
		15123 N	50.96 MPa	1512.3 N	5.096 MPa	
High Level Fatigue Stresses	Stress Level 1	5120 lbs	11130 psi	512 lbs	1113 psi	20
		22775 N	76.74 MPa	2277.5 N	7.674 MPa	
	Stress Level 2	10240 lbs	22261 psi	1024 lbs	2226 psi	40
		45550 N	153.5 MPa	4555.0 N	15.35 MPa	
	Stress Level 3	15360 lbs	33391 psi	1536 lbs	3339 psi	60
		68325 N	230.2 MPa	6832.5 N	23.02 MPa	
	Stress Level 4	20480 lbs	44522 psi	2048 lbs	4452 psi	80
		91100 N	307.0 MPa	9110.0 N	30.70 MPa	
	Stress Level 5	25600 lbs	55652 psi	2560 lbs	5565 psi	100
		113874 N	383.7 MPa	11387.4 N	38.37 MPa	

Minimum loads for each stress level were determined based on the recommended force (stress) ratio of 0.1 provided by ASTM Standard D6873-03 for tension-tension fatigue testing. Specimens were set to test up to one million cycles, or until catastrophic failure occurred. The loading rate varied between 1 and 3 Hertz, based on the amplitude between the maximum and minimum loads. Stress Levels 4 and 5 under high level fatigue were performed at 1 Hertz; Stress Levels 2 and 3 under high level fatigue were performed at 2 Hertz; Stress Level 1 under high level fatigue and all low level stresses were performed at 3 Hertz. The variation in frequency was based on the desire to minimize the time required to complete one million cycles without causing overheating and energy loss at the joint. To assure that no energy was lost from the system due to friction or heat, the energy put into the system must equal the energy output. Several verification methods were taken to assure this was the case. Figures 3.2, 3.3, and 3.4 show sine waves with frequencies of 3 Hertz (Stress Level 1 – high level), 2 Hertz (Stress Level 3 – high level), and 1 Hertz (Stress Level 5 – high level). These figures show that the sine waves were completed at the required minimum and maximum loads within the expected period. This fact coupled with Figure 6.1, which shows that the minimum and maximum loads for Stress Level 2 (high level) were maintained through one million cycles, verify that the input was equal to the output. An infrared camera was used to monitor the temperature of the specimen and joint components to ensure no overheating occurred over the duration of the test. Not only could overheating at the joint create energy loss in the system, but additional heating could change properties of the DCCS Structure. Figure 3.5 shows an infrared image taken at Stress Level 5 (high level) prior to catastrophic failure in the specimen. This image verifies that overheating was not present at the highest fatigue level, and it was confirmed that overheating did not occur at an of the lower stress levels, despite higher frequencies.

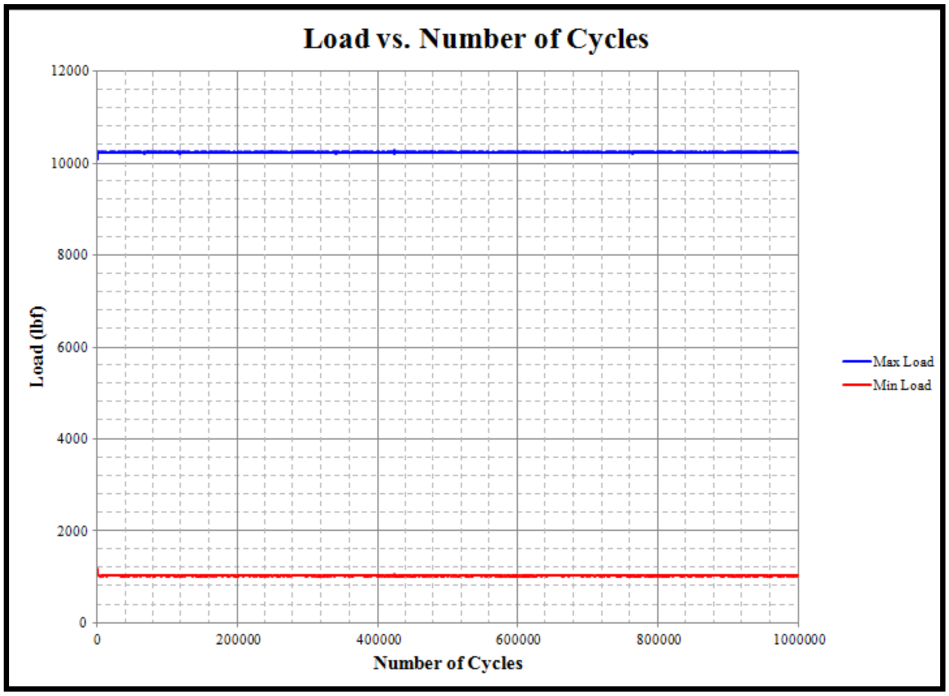

Figure 6.1: Load vs. Number of Cycles (Stress Level 2 – High Level)

Specimens were inspected continuously through the first 1000 cycles and subsequently at cycle 10000, 100000, and every 100000 cycles thereafter when convenient. Blue dye was used to locate cracks in the ceramic tile and damage in the interlayer and face sheet. Photographs were taken with each progressive failure to document the sequence of damage and at the conclusion of each test. Stress Levels that withstood one million cycles were repeated with periodic load-unload sequences. Tests were momentarily stopped at cycle 10000, 20000, 30000, 50000, 100000, 200000, 300000, 500000, and 1000000 to gather tracking data from a load-unload sequence. This data provided a better representation of progressive stiffness loss and permanent displacement at the joint. For specimens that failed catastrophically during fatigue testing, the number of cycles to failure and the method of failure were documented. Catastrophic failure was primarily in the form of delamination, either adhesive failure between the face sheet and interlayer, adhesive failure between the interlayer and ceramic tile, or interlayer yielding at tile crack locations. In some case, this was accompanied by bending/shear/tearout failure of the ceramic tile. Specimens that completed one million fatigue cycles underwent residual strength tests to compare to baseline static tests. These tests can determine the overall effect of fatigue on the strength and stiffness of the structure, and the progressive failure of the joint. In terms of design evaluation, it is important to determine the stress limit that allows for infinite survival with structural damage and the stress limit that does not demonstrate stiffness or strength loss.

The best method to assess fatigue resistance of the joint is quantifying the progressive stiffness loss over the duration of the fatigue test. Stiffness can be calculated either as the slope tangent to the load-displacement curve at a given point or the difference in load divided by the difference in displacement over a particular load range. These two calculations are defined as the tangent modulus and secant modulus, respectively. Figure 6.2 demonstrates the variations of these moduli, depending on the selected point or load range. The plot on the left demonstrates the secant modulus taken over the load (stress) range S_1, with a displacement (strain) of e_1; the tangent modulus is taken at the same point. Notice that the tangent modulus is much less than the secant modulus, as the material depicted is not linear-elastic, and the load-displacement curve demonstrates yielding/plasticization beyond the linear region. The plot on the right uses the same range for the secant modulus; however the tangent modulus is take at zero load, zero displacement. In this scenario, the tangent modulus is slightly greater than the tangent modulus, but the two resemble each other very closely. This knowledge can be applied to the data reduction in this study. At low fatigue stress levels, where the load-displacement curve is nearly linear, the tangent modulus taken at zero load, zero displacement and the secant modulus taken over the defined range of max/min fatigue loads will be nearly identical. At higher fatigue stress levels, the secant modulus is expected to be much lower than the tangent modulus at zero load, zero displacement. Under these circumstances, the secant modulus may be more revealing in terms of understanding fatigue resistance.

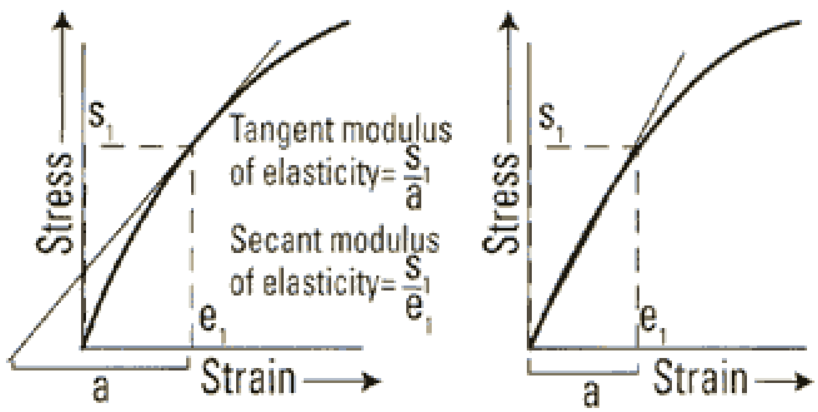

Figure 6.2: Tangent and Secant Modulus (Instron)

Initially, each stress level will be tested, stiffness will be calculated according to both tangent and secant moduli, and the progressive stiffness loss will be determined. Testing will continue using progressively lower fatigue stress levels, to the point where no stiffness or residual strength loss is detected. When comparing stiffness loss of different fatigue stress levels, stiffness must be defined in the same manner for all levels. For instance, the tangent modulus must be taken at the same load within each test, or the secant modulus must be taken over the same load range. This will provide an understanding of the progressive stiffness loss over a range of fatigue stress levels. The comparison will be made at the conclusion of all fatigue testing. Finally, all the data collected will be compiled into design table, allowing the designer to select the appropriate design based on three parameters: design load, factor of safety, and stiffness loss. This will be discussed in detail in Chapter 7.

6.2 High Level Fatigue Residual Strength and Stiffness

Prior to the commencement of the first fatigue cycle, each specimen was statically loaded at a constant loading rate and returned to zero load. This prevented a dynamic loading effect, which could exceed the expected maximum stress, from occurring on the first cycle. High level fatigue tests were performed with pinned and clamped joint conditions for Stress Levels 1 – 5. A summary of the longevity of each test is found in Table 6.2.

Table 6.2: Summary of High Level Fatigue (Pinned and Clamped)

Sample #	Joint Type	Stress Level Classification	Failure Method	Cycles to Failure
FW4E2T0-1	Pinned	Stress Level 5	DCCS Structure	479
FW4E2T90-1	Clamped	Stress Level 5	DCCS Structure	1413
FW4E2T90-2	Clamped	Stress Level 5	DCCS Structure	1125
FW4E2T90-3	Clamped	Stress Level 5	DCCS Structure	1189
FW4E2T0-2	Pinned	Stress Level 4	DCCS Structure	6270
FW4E2T90-4	Clamped	Stress Level 4	DCCS Structure	6681
FW4E2T90-5	Clamped	Stress Level 4	DCCS Structure	7974
FW4E2T0-3	Pinned	Stress Level 3	Steel Pin	26121
FW4E2T90-6	Clamped	Stress Level 3	Grade 8 Bolt	42708
FW4E2T90-7	Clamped	Stress Level 3	Grade 8 Bolt	52426
FW4E2T90-8	Clamped	Stress Level 3	Grade 8 Bolt	24398
FW4E2T90-9	Clamped	Stress Level 3	Grade 8 Bolt	22573
FW4E2T0-4	Pinned	Stress Level 2	N/A	1000000
FW4E2T90-10	Clamped	Stress Level 2	N/A	1000000
FW4E2T90-11	Clamped	Stress Level 2	N/A	1000000
FW4E2T90-12	Clamped	Stress Level 2	Grade 8 Bolt	123692
FW4E2T90-13	Clamped	Stress Level 2	Grade 8 Bolt	159872
FW4E2T0-5	Pinned	Stress Level 1	N/A	1000000
FW4E2T0-6	Pinned	Stress Level 1	N/A	1000000
FW4E2T90-14	Clamped	Stress Level 1	N/A	1000000
FW4E2T90-15	Clamped	Stress Level 1	N/A	1000000
FW4E2T90-16	Clamped	Stress Level 1	N/A	1000000
FW4E2T90-17	Clamped	Stress Level 1	N/A	1000000

Under both joint conditions, the DCCS Structure failed when exposed to Level 4 and Level 5 stresses. The progression of failure was the same in all cases, with the number of cycles to failure being the only variation. With increased fatigue cycles, the net tension cracks that formed during the initial loading sequence began to visibly separate. As the net tension cracks separated, the tile could be seen protruding from the top of the DCCS Structure (Figure 6.3). The interlayer was noticeably yielding at the location of the net tension cracks and the top edge of the specimen. As the tile protrusion became excessive, the adhesive bond between the ceramic tile and interlayer failed at the top edge, and the tile began sliding up-and-down against the interlayer with each cycle of fatigue.

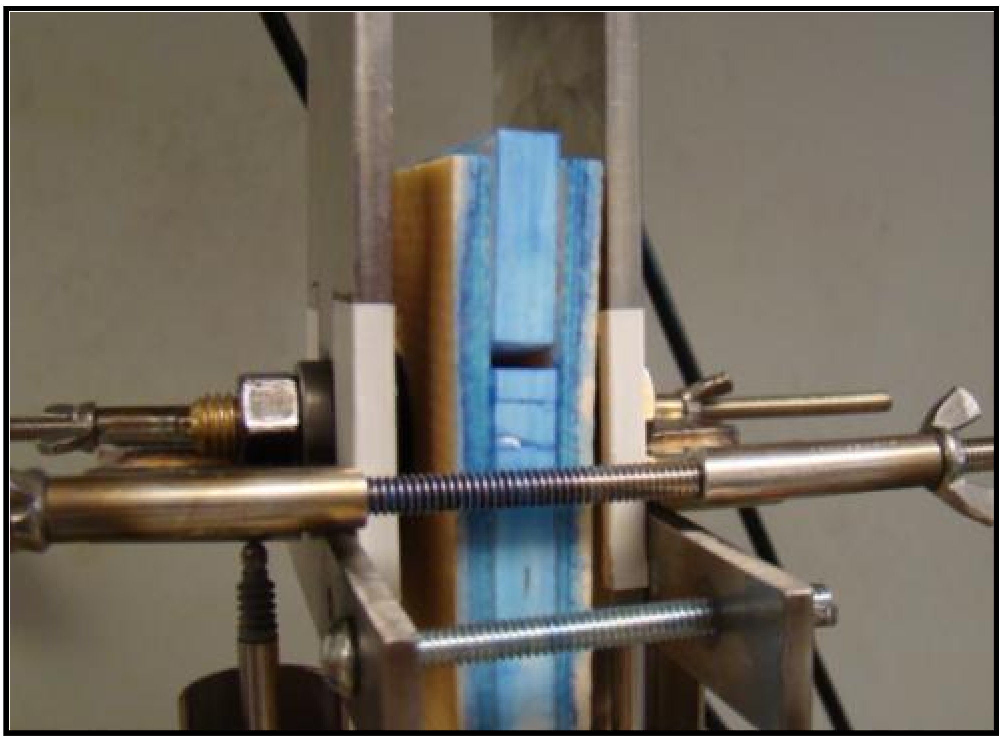

Figure 6.3: Increased Net Tension Displacement at Stress Levels 4 and 5

Not long after the adhesive bond began to fail, the face sheets could be seen bowing outward at the top of the specimen. This initiated full delamination of the DCCS Structure (Figure 6.4). Adhesive bond failure between the ceramic tile and interlayer was the major source of failure; however, in some regions that experienced yielding of the interlayer, the interlayer failed. This failure provided a transition for the interlayer to de-bond from the face sheet, as well. After delamination occurred, the load was transferred entirely into the face sheets. However, the face sheets could not resist the maximum loads from Stress Levels 4 and 5, and began to fail continuously in bearing.

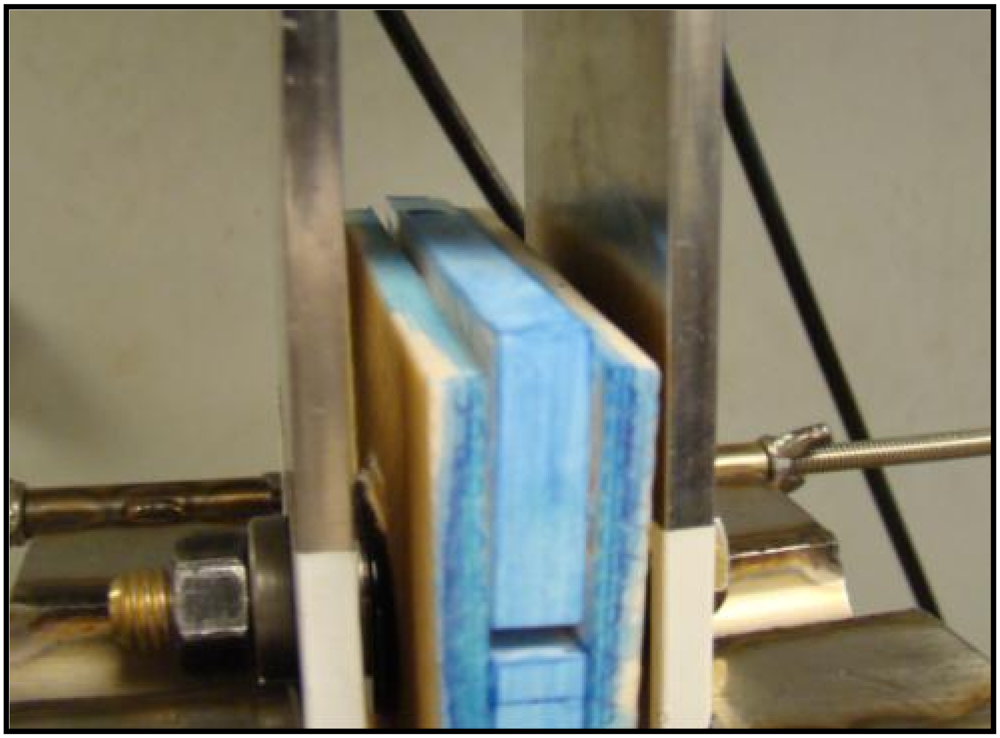

Figure 6.4: Tile Protruding after Delamination and Ultimate Failure at Stress Levels 4 and 5

The pinned joint experienced a fatigue life of 479 cycles at Stress Level 5 and 6270 cycles at Stress Level 4 before ultimate failure, while the clamped joint experienced an average fatigue life of 1242 cycles at Stress Level 5 and 7328 cycles at

Stress Level 4 before failure. It appears as if the clamping forces at the joint reduced the rate of elongation at the joint and limited interlayer yielding and separation of the net tension cracks. This provided a slightly longer fatigue life; however, the achieved lifetime was not acceptable in terms of meeting long-term durability and performance considerations.

Level 3 stresses led to a longer fatigue life for the DCCS Structure, but tests were stopped prematurely due to pin and bolt failure. These failures can be seen in Figure 6.5, and according to the location of the failure, it is evident that they both failed in bending. When the pin/bolt failed, it caused local bearing damage to the face sheet due to the natural bending motion of the pin. A replacement pin/bolt was installed to continue the fatigue testing; however, with local damage to the face sheet, the ceramic tile absorbed the full bearing load, causing bending/shear failure in the tile upon reloading. This led to premature delamination and ultimate failure in the DCCS Structure. It was assumed that if the local bearing damage was not present (a side-effect of a damaged or broken pin/bolt), and stronger fasteners were utilized, the DCCS Structure would exhibit a longer fatigue life than that monitored in this study. As it was, the pin failed after a fatigue life of 26121 cycles, and the bolt failed after an average fatigue life of 35526 cycles.

Figure 6.5: Failed Steel Pin/Grade 8 Bolt at Stress Level 3 (and during select cases at Stress Level 2)

Stress Level 2 was the first level to achieve one million cycles without consistent failure of the DCCS Structure or fastener. In addition to the visible damage caused by Level 2 stresses, specimens experience joint stiffness loss through the duration of the fatigue test. Figure 6.6 shows the normalized stiffness loss, in terms of secant modulus, from pinned and clamped joint specimens. The results for this chart were derived from the data acquisition system in the Instron machine. The max/min loads and displacements were recorded every 100 cycles, for the entirety of the test. Consequently, the load range used to calculate the secant modulus was based on the minimum load, 1024 lbs, to the maximum load, 10240 lbs. Recall, the minimum load was determined using an R value of 0.1 (ratio of minimum load to maximum load). After one million cycles, the pinned joint showed a stiffness loss of approximately 8 percent and the clamped joint showed a stiffness loss of 12 – 16 percent. Stiffness in terms of the secant modulus is one method to quantify stiffness loss. Calculating the tangent modulus of the initial slope (zero load, zero displacement) in a loading cycle is another method. The periodic load-unload sequences described in the previous section will allow for the progressive stiffness loss in terms of the tangent modulus to be quantified.

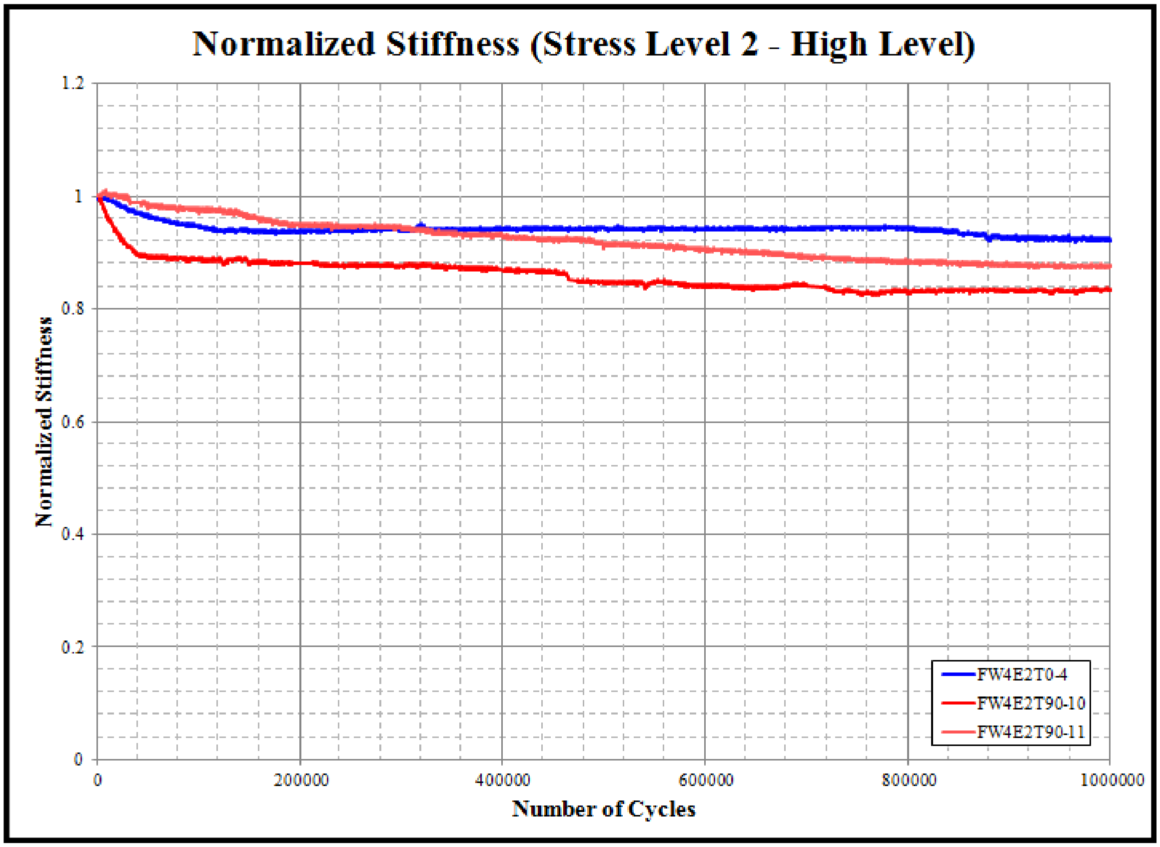

Figure 6.6: Normalized Fatigue Stiffness vs. Number of Cycles (Stress Level 2) based on Secant Modulus (defined from 1024 lbs to 10240 lbs)

Figures 6.7 and 6.8 illustrate the load-unload sequences for pinned and clamped joints, respectively. (It should be noted that displacements measured during fatigue testing came from the built-in displacement function within the Instron machine, and not from external LVDT's, as described in the static testing set-up. Consequently, displacement incurred in fatigue testing cannot be directly compared to static testing.) Both cases show that with an increase in the number of fatigue cycles, there is permanent elongation of the joint that occurred within the time of the previous load-unload sequence. This permanent elongation can be attributed to two potential causes. The first is the viscoelastic response of the adhesive interlayer and face sheet. By nature, hysteresis is observed in viscoelastic materials exposed to cyclic loading. This is a result of the materials viscous component, which in its' attempt to resist plastic deformation, loses energy through heat. As the elastic component attempts to restore the material to its' original form, creep caused by the viscous component allows for small amounts of temporary deformation, that are eventually restored over time. However, with continuous fatigue cycles at the magnitude of stresses seen in Level 2, deformation and elongation compounds itself, as demonstrated in both the pinned and clamped joint cases. The second scenario for permanent elongation is a difference in coefficients of thermal expansion between the face sheet and ceramic tile. During fabrication of the DCCS Structure, panels are post-cured at 300 degrees Fahrenheit. If the face sheet has a greater CTE than the ceramic tile, it will have a tendency to expand more during the post-cure process. Being bonded together, the face sheet transfers stresses into the ceramic tile, in an effort for the ceramic tile to expand beyond its' own thermal expansion properties, inherently putting the tile in tension. At the same time, the ceramic tile is resisting the stresses from the face sheet, inherently placing the face sheet in compression. These stresses remain present in the structure until they are tested. When the ceramic tile cracks in net tension, the residual tensile stress in the tile is released, and the compressive stress in the face sheet relaxes, resulting in the cracks to remain open with permanent deformation. However, this scenario only explains the permanent deformation from the first loading cycle when the initial cracks form. The deformation originated by fatigue loading is better explained by the viscoelastic properties of the interlayer and face sheet.

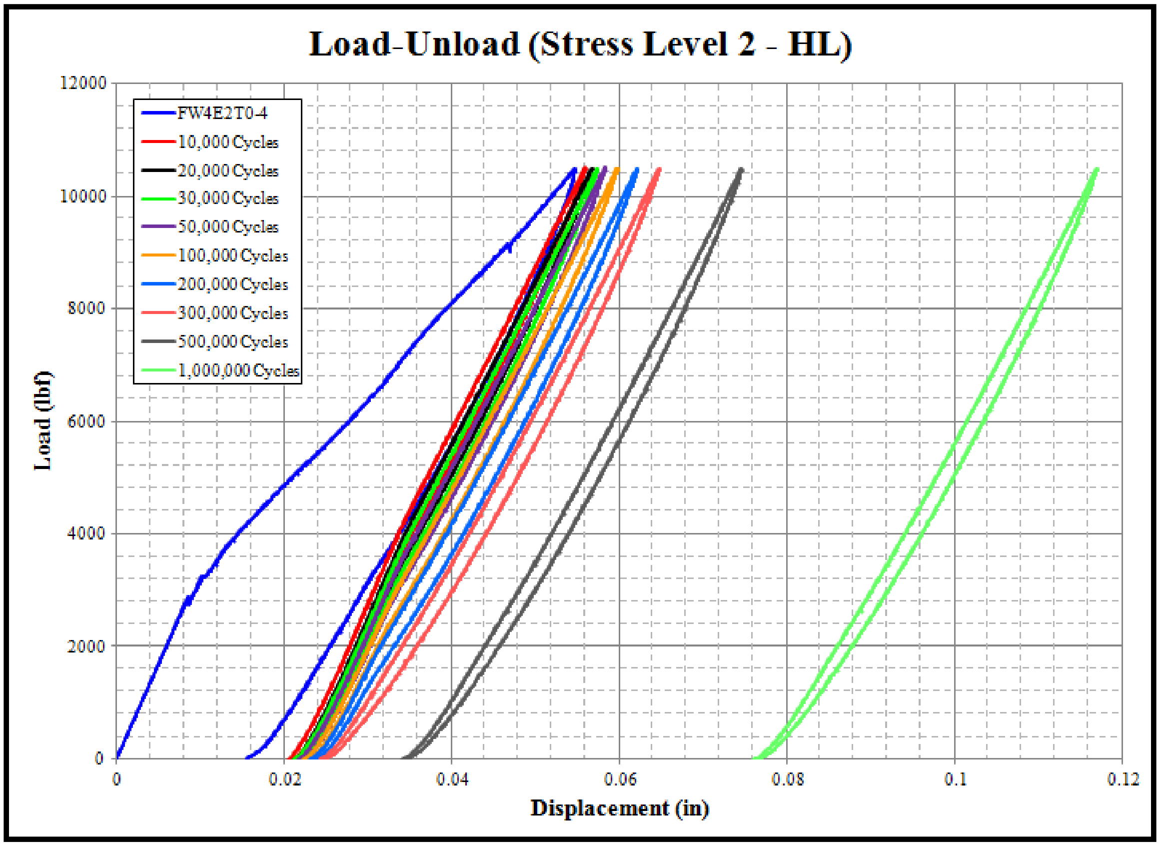

Figure 6.7: Periodic Hysteresis Curves for Stress Level 2 – Pinned Case

Table 6.3 quantifies the approximate stiffness loss according to the tangent (taken at zero load, zero displacement) and secant (over the load range 1024 lbs to 10240 lbs) loss of the pinned joint at Level 2 stresses. Stiffness loss based on secant modulus appeared to constantly increase over the course of one million fatigue cycles, losing 11 percent stiffness from the beginning of the test. The tangent modulus revealed significant jumps in stiffness loss between 30000 and 50000 cycles, 50000 and 100000 cycles, and 100000 and 200000 cycles. This range accounted for the majority of the 28 percent stiffness loss based on the tangent modulus.

There is a very noticeable difference in the load-displacement curves between the pinned joint (Figure 6.7) and the clamped joint (Figure 6.8). The total amount of hysteresis, or energy lost in the fatigue cycle of the clamped joint appears to be much greater than that of the pinned joint. Chapter 5 described the effects of the clamping force on the load distribution of the constituents. Those forces, which caused yielding of the interlayer, enhanced the ability for load to be transferred and shared more equally between the face sheet and ceramic tile, whereas, in the pinned case, the ceramic tile carried the majority of the bearing load up to bending/shear failure. Additionally, the clamping force provided a certain amount of friction force between the outer face sheet and the washer. This allowed for some of the bearing load to be transferred to the surface of the face sheet in terms of friction. With the face sheet carrying a greater portion of the bearing load, and the viscoelastic properties of the face sheet and interlayer causing the hysteresis during cyclic loading, it provides reason to believe that more energy is exerted and lost in an attempt for the materials to restore their original shape, hence a more pronounced phase lag between loading and unloading.

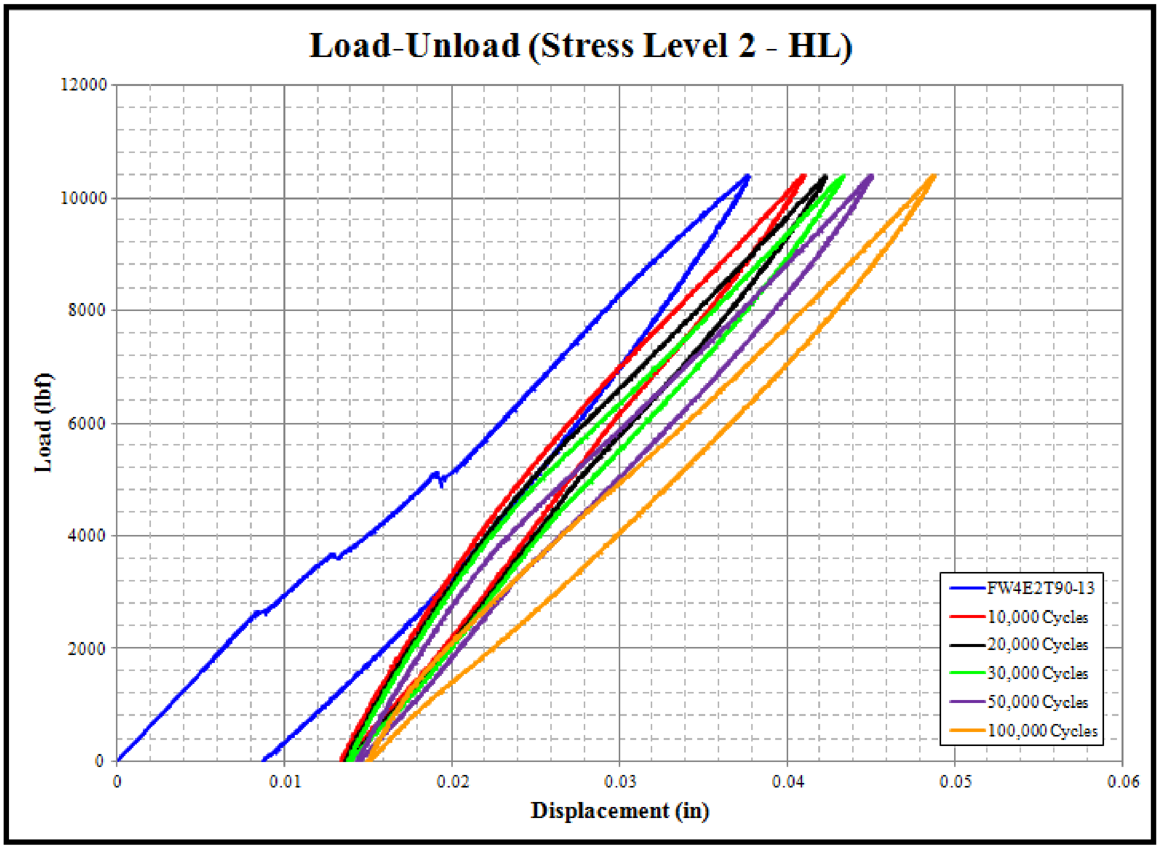

Figure 6.8: Periodic Hysteresis Curves for Stress Level 2 – Clamped Case

Table 6.3: Stiffness Loss according to Tangent Modulus (at zero load) and Secant Modulus (based on load range from 1024 lbs to 10240 lbs) for Stress Level 2 – Pinned

	Based on Secant Modulus		Based on Tangent Modulus	
Cycle	Stiffness (lb/in)	Stiffness Loss	Stiffness (lb/in)	Stiffness Loss
10,000	304067	0.00%	335645	0.00%
20,000	304568	-0.16%	335657	0.00%
30,000	299911	1.27%	329183	1.93%
50,000	295639	2.78%	309236	7.87%
100,000	288071	5.27%	283184	15.63%
200,000	277476	8.75%	247777	26.18%
300,000	271554	10.70%	243402	27.48%
500,000	273222	10.15%	244400	27.20%
1,000,000	270516	11.04%	240374	28.38%

Table 6.4 quantifies the approximate stiffness loss according to the tangent (taken at zero load, zero displacement) and secant (over the load range 1024 lbs to 10240 lbs) modulus of the clamped joint at Level 2 stresses. This particular test resulted in failure of the bolt (reference Table 6.2), one of two instances this occurred at Stress Level 2 for the bolted joint. The data acquired from this test still proved valuable and reliable (based on comparisons to subsequent stress levels). Stiffness loss based on the secant modulus was much more dramatic for the clamped case, resulting in a 19 percent loss after 100000 cycles, compared to an 11 percent loss for the pinned case through the full one million cycles. Conversely, the tangent modulus demonstrated more consistent losses, totaling 7 percent after 100000 cycles, compared to 15 percent for the pinned case after the same amount of time.

Table 6.4: Stiffness Loss according to Tangent Modulus (at zero load) and Secant Modulus (based on load range from 1024 lbs to 10240 lbs) for Stress Level 2 – Clamped

	Based on Secant Modulus		Based on Tangent Modulus	
Cycle	Stiffness (lb/in)	Stiffness Loss	Stiffness (lb/in)	Stiffness Loss
10,000	365503	0.00%	597349	0.00%
20,000	350240	4.18%	581879	2.59%
30,000	339489	7.12%	585022	2.06%
50,000	325703	10.89%	558811	6.45%
100,000	295760	19.09%	552138	7.57%
200,000	-	-	-	-
300,000	-	-	-	-
500,000	-	-	-	-
1,000,000	-	-	-	-

Residual strength tests were performed to assess the effect of fatigue on the overall strength and stiffness of the joint. (Residual strengths tests were performed using the same parameters as static tests in Chapter 5, thus allowing for results to be directly compared.) Figure 6.9 compares fatigued vs. non-fatigued specimens under pinned joint conditions and Figure 6.10 does the same for clamped joint specimens. Table 6.5 quantifies these results in terms of initial joint stiffness, strength at bending/shear failure and ultimate failure, and the total joint displacement at ultimate failure.

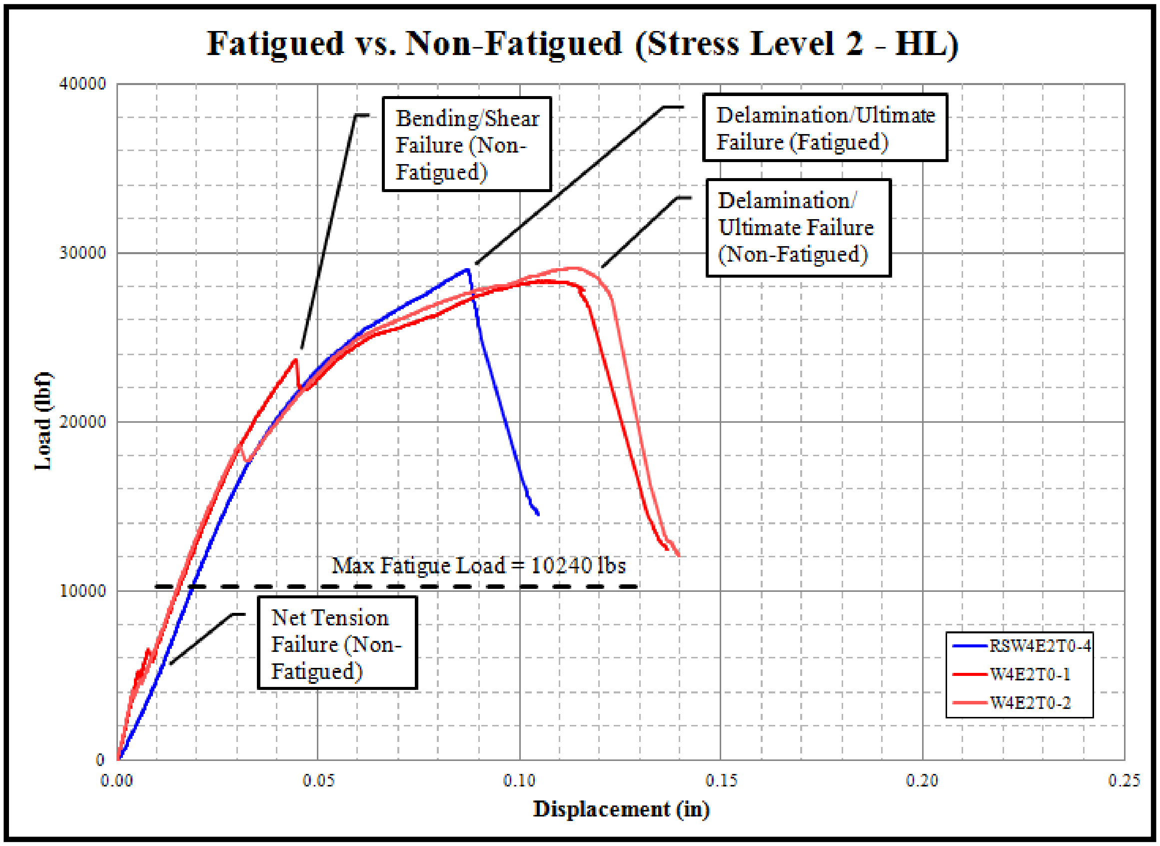

Figure 6.9: Fatigued vs. Non-Fatigued Specimens at Stress Level 2 – Pinned Case

Under non-fatigued pinned conditions, initial stiffness (according to the tangent modulus at zero load, zero displacement) of the joint was 1065925 lbs/in on average. Fatigued specimens exhibited an initial stiffness of 488172 lbs/in, significantly less than non-fatigued specimens. This can be attributed to the existing net tension cracks in the fatigued specimen. However, after net tension failure, which occurred in the first 0.01 inches of joint displacement in non-fatigued specimens, the load-displacement curves are nearly identical between the two cases. The only exception is that the fatigue load-displacement curve displays approximately 0.003

inches more displacement for an equivalent load than the non-fatigue load-displacement curve. This parallelism is maintained up through bending/shear failure of the non-fatigued specimens. Despite experiencing a greater displacement than non-fatigued specimens, bending/shear failure occurred at a higher strength under fatigued conditions. As explained in Chapter 5, once net tension cracks occur in the ceramic tile, the only way for the tile to absorb the bearing load is for the load to transfer from the face sheet, through the interlayer, into the tile. However, if the interlayer has residual damage due to fatigue loading, this can reduce the amount of bearing stress that is transferred into the ceramic tile. In a sense, the bearing load is now more distributed between the ceramic tile and face sheet, causing more separation of the net tension cracks and a higher strength prior to bending/shear failure. However, due to the weakened interlayer, delamination and ultimate failure occurred simultaneously with bending/shear failure of the ceramic tile. This happened at approximately the equivalent strength exhibited by non-fatigued specimens, albeit at a smaller joint displacement.

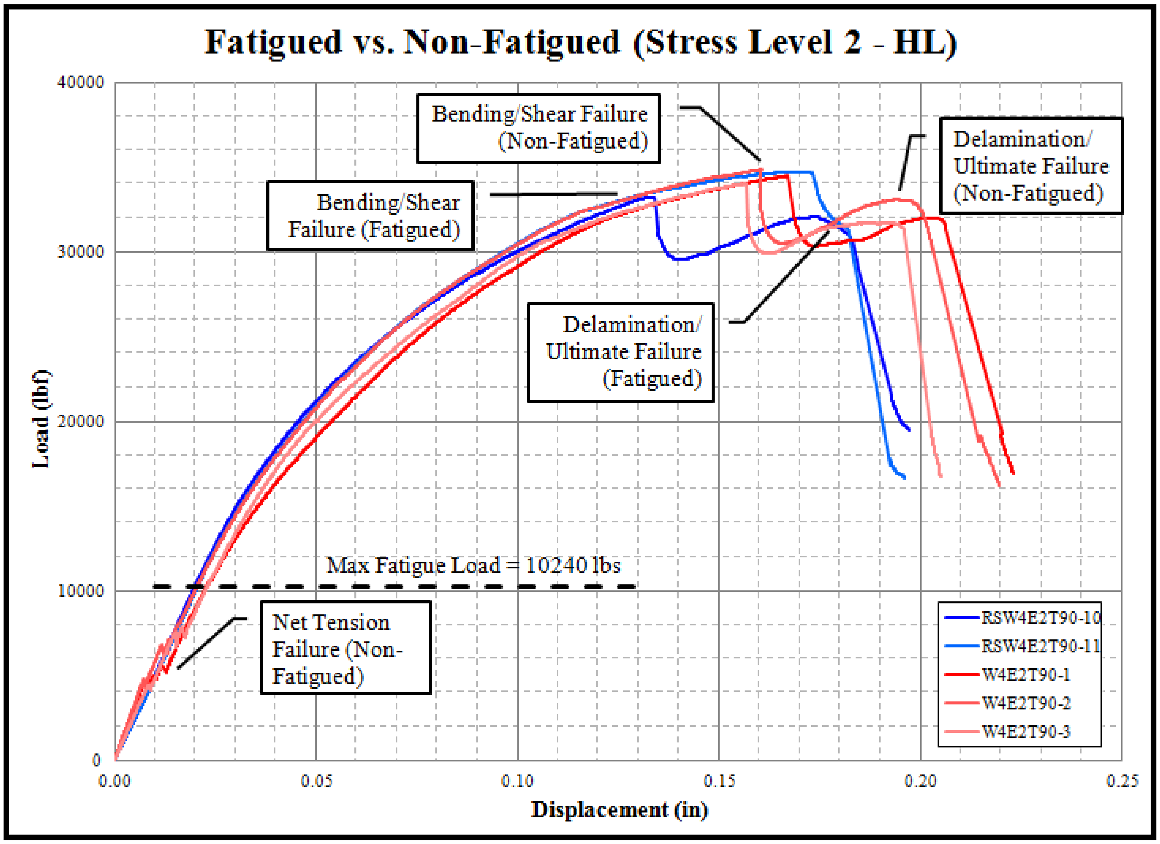

Figure 6.10: Fatigued vs. Non-Fatigued Specimens at Stress Level 2 – Clamped Case

The clamped joint specimens exposed to fatigue loading displayed two different modes of failure progression. At first, both followed nearly identical load vs. displacement curves. The fatigued specimens demonstrated an initial stiffness (according to the tangent modulus at zero load, zero displacement) ranging from 488540 lbs/in to 494290 lbs/in, a stiffness reduction of approximately 26 percent over the non-fatigued specimens. One specimen then exhibited a failure sequence resembling that achieved in non-fatigued tests, where bending/shear failure of the ceramic tile is followed by bearing failure in the face sheet before final delamination/ ultimate failure of the DCCS Structure. The primary difference between this specimen and the generic non-fatigued specimens was that marginally smaller strengths and displacement were achieved. The other fatigued specimen peaked at a strength equivalent to the non-fatigued specimens before the adhesive bond began to fail between the interlayer and ceramic tile. As the DCCS Structure de-bonded and lost strength, bending/shear/tearout failure of the ceramic tile occurred. This was not the characteristic single crack at 0 degrees seen in non-fatigued specimens, but instead cracks between 30 – 50 degrees on either side of the joint, more like tearout failure (Figure 1.3). Bending/shear failure was explained in Chapter 5 as being a result of bending in the ceramic tile, with the crack initiating along the top edge where the peak tensile stresses were located. In the case of fatigued specimens, the adhesive bond begins failing along the top edge of the tile, relieving those tensile stresses which would have led to the bending/shear crack. With the adhesive de-bonding at the top of the specimen, but maintaining cohesion along the sides and near the joint, tensile stresses began to increase in the ceramic tile at the joint. Since the stresses had already been partially released due net tension cracking at the beginning of the loading sequence, maximum tensile stresses were re-located above the net tension cracks, in the range of 30 – 50 degrees from the loading direction. As de-bonding spreads across the top edge of the tile, ultimate failure comes down to two final possibilities: full de-bonding and delamination of the DCCS Structure throughout the shear area, or tearout of the ceramic tile coinciding with the region of maximum tensile stress at the joint. At higher stress levels, where the interlayer is considerably weaker due to fatigue, de-bonding and delamination prevail. However, at Level 2 stresses, the interlayer remains strong enough to maintain cohesion closer to the joint, leaving tearout of the ceramic tile as the final catastrophic failure mode.

Table 6.5: Strength and Displacement Comparisons (Stress Level 2 Residual Strength vs. Pinned/Baseline)

Sample #	Initial Joint Stiffness	Strength at Bending/Shear Failure	Strength at Ultimate Failure	Displacement at Ultimate Failure
W4E2T0 (Averages)	1065925 lbs/in	21177 lbs	28739 lbs	0.1089 in
	186670 N/mm	94200 N	127840 N	2.766 mm
RSW4E2T0-4	488172 lbs/in	28983 lbs	28983 lbs	0.0868 in
	85490 N/mm	128920 N	128920 N	2.205 mm
W4E2T90 (Averages)	666020 lbs/in	34462 lbs	32283 lbs	0.1965 in
	116640 N/mm	153290 N	143600 N	4.991 mm
RSW4E2T90-10	494290 lbs/in	33222 lbs	32051 lbs	0.1747 in
	86560 N/mm	147780 N	142570 N	4.437 mm
RSW4E2T90-11[2]	488540 lbs/in	31063 lbs	34731 lbs	0.1680 in
	85560 N/mm	138180 N	154490 N	4.267 mm

All specimens tested at Stress Level 1 achieved one million cycles without experiencing further visible damage. However, like Stress Level 2, specimens experienced joint stiffness loss through the duration of the fatigue test. Figure 6.11 shows the normalized stiffness loss, in terms of secant modulus, from pinned and clamped joint specimens. The results for this chart were derived from the data acquisition system in the Instron machine. The max/min loads and displacements were recorded every 100 cycles, for the entirety of the test. Consequently, the load

[2] Bending/Shear Failure occurred after Delamination/Ultimate Failure began

range used to calculate the secant modulus was based on the minimum load, 512 lbs, to the maximum load, 5120 lbs. After one million cycles, the pinned joint showed a stiffness loss of 5 – 8 percent and the clamped joint showed a stiffness loss of 3 – 12 percent. Load-unload sequences were repeated at Stress Level 1 to better describe the effect of fatigue over the course of cyclic fatigue loading.

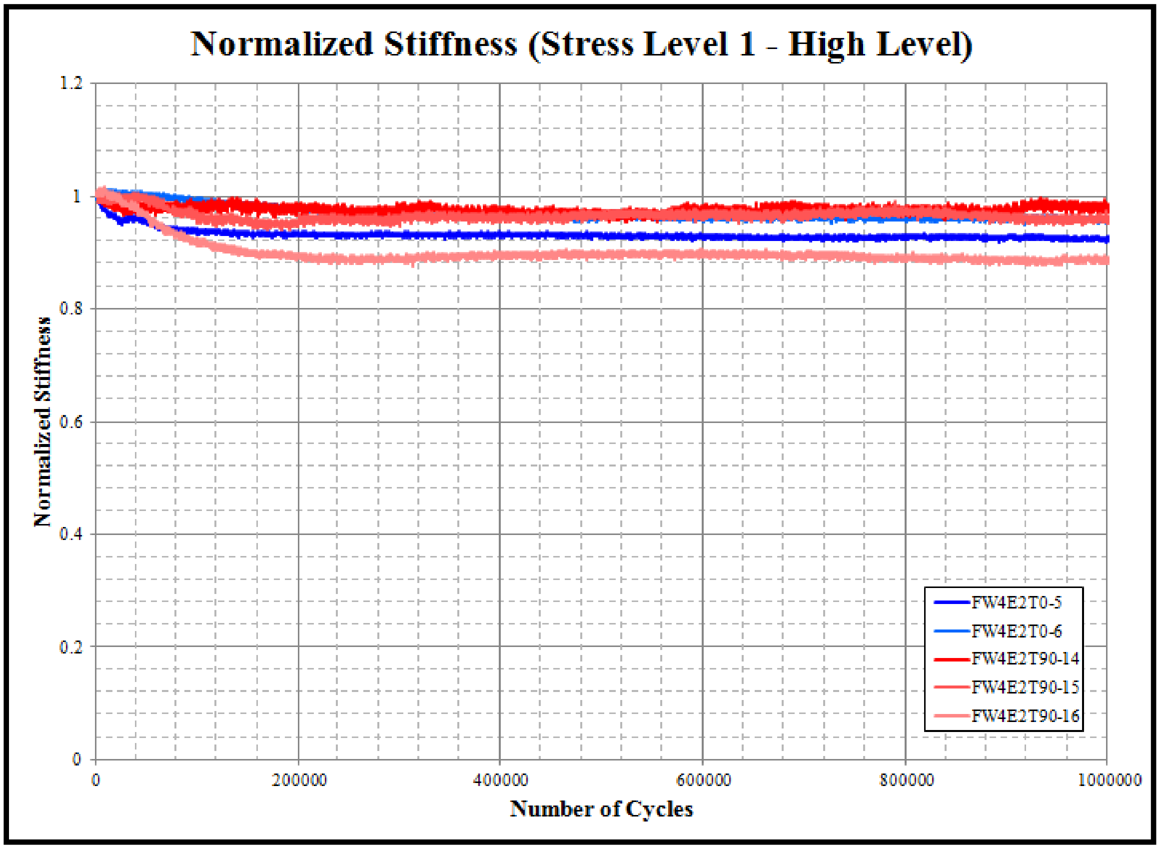

Figure 6.11: Normalized Fatigue Stiffness vs. Number of Cycles (Stress Level 1) based on Secant Modulus (defined from 512 lbs to 5120 lbs)

Figures 6.12 and 6.13 illustrate the load-unload sequences for pinned and clamped joints, respectively. Similar to specimens fatigued at Level 2 stresses, both pinned and clamped specimens show permanent elongation of the joint that increases with each subsequent load-unload sequence. Clamped joints also appeared to have larger phase lags, described earlier to be a result of more load-carrying responsibility of the viscoelastic face sheet material.

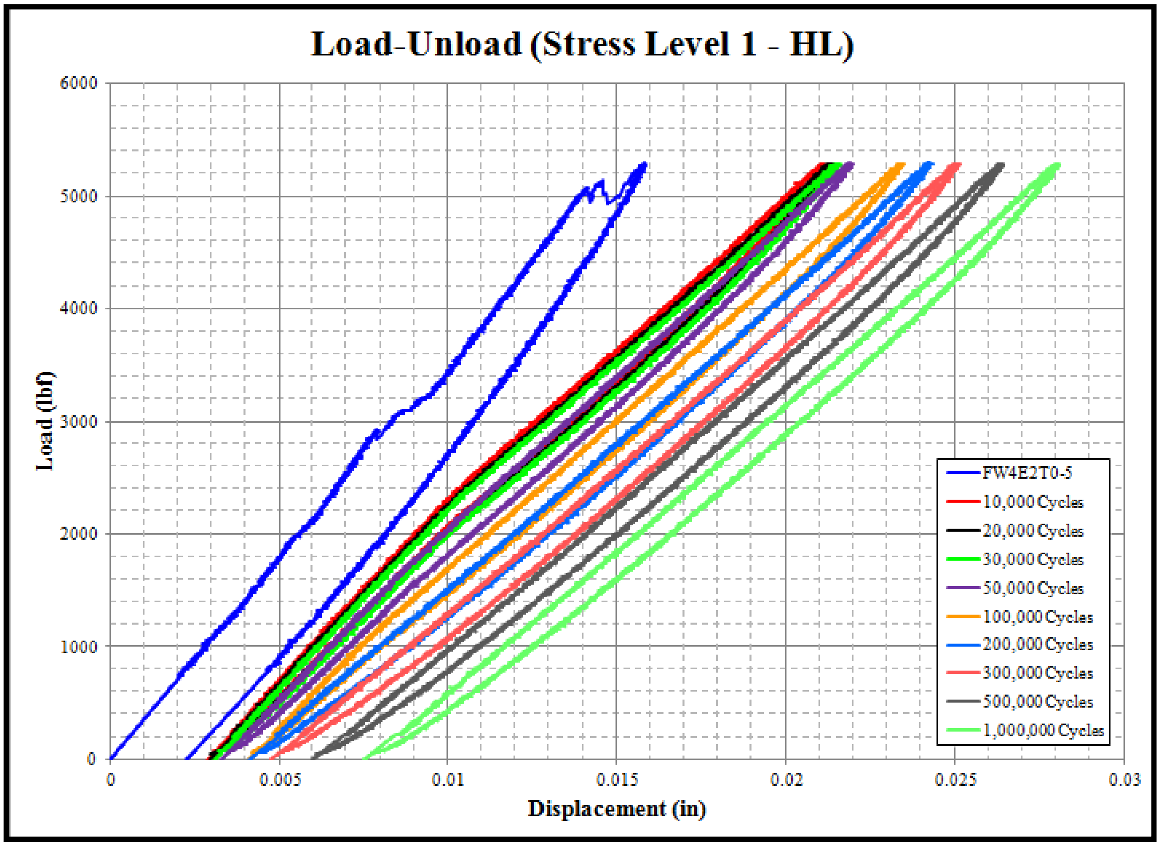

Figure 6.12: Periodic Hysteresis Curves for Stress Level 1 – Pinned Case

Table 6.6 quantifies the approximate stiffness loss according to the tangent (taken at zero load, zero displacement) and secant (over the load range 512 lbs to 5120 lbs) modulus loss of the pinned joint at Level 1 stresses. Stiffness loss based on secant modulus appeared to constantly increase over the course of one million fatigue cycles, losing 9 percent stiffness from the beginning of the test. The tangent modulus revealed significant jumps in stiffness loss between 50000 and 100000 cycles, and 100000 and 200000 cycles. This range accounted for the majority of the 24 percent stiffness loss based on the tangent modulus. Because the tangent modulus was taken at the same location of the load-displacement curve for fatigued specimens in Stress Level 2, the results from the two stress levels are comparable. Stress Level 2 fatigue specimens exhibited similar jumps in stiffness loss during the same time period of the test, which totaled a 28 percent stiffness loss, only marginally more than Stress Level 1 fatigue specimens.

Table 6.6: Stiffness Loss according to Tangent Modulus (at zero load) and Secant Modulus (based on load range from 512 lbs to 5120 lbs) for Stress Level 1 – Pinned

	Based on Secant Modulus		Based on Tangent Modulus	
Cycle	Stiffness (lb/in)	Stiffness Loss	Stiffness (lb/in)	Stiffness Loss
10,000	287826	0.00%	323821	0.00%
20,000	285967	0.65%	324457	-0.20%
30,000	283338	1.56%	319123	1.45%
50,000	282968	1.69%	314078	3.01%
100,000	270804	5.92%	291987	9.83%
200,000	261733	9.07%	246402	23.91%
300,000	260895	9.36%	237136	26.77%
500,000	261203	9.25%	239360	26.08%
1,000,000	261392	9.19%	244325	24.55%

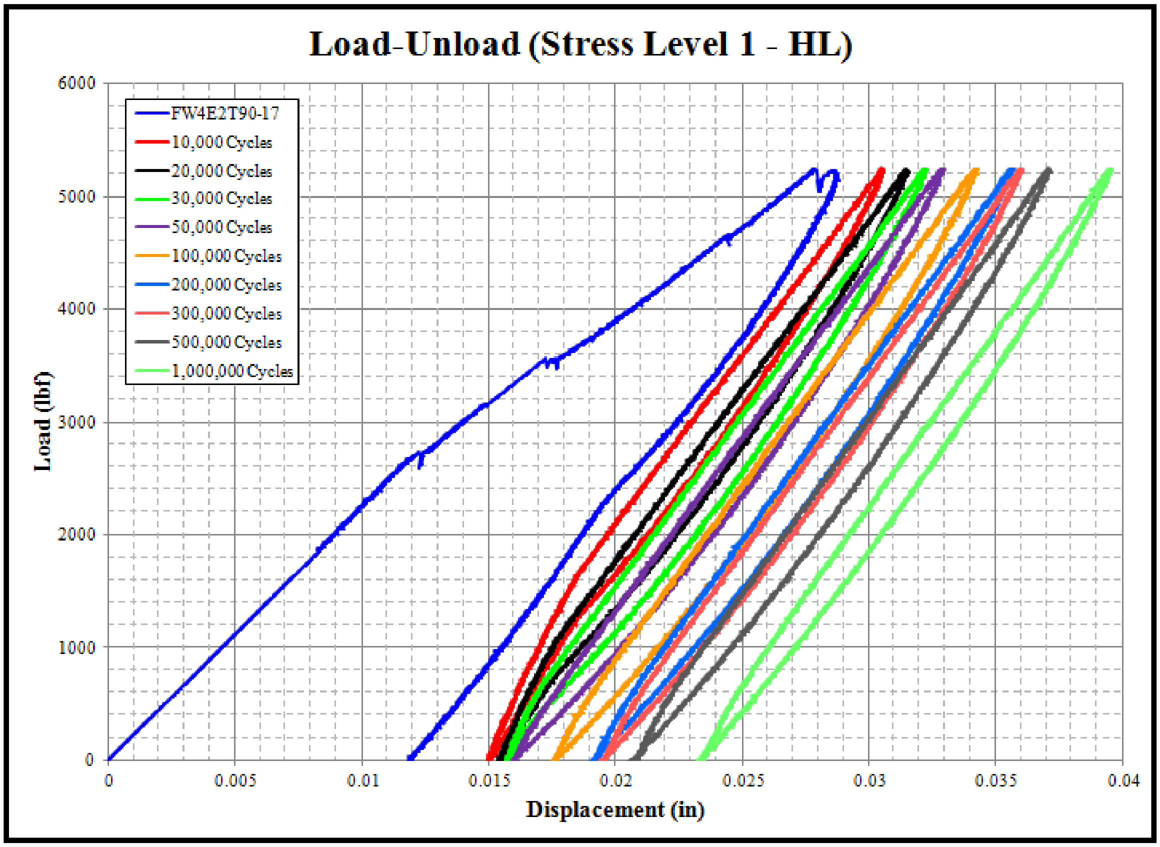

Figure 6.13: Periodic Hysteresis Curves for Stress Level 1 – Clamped Case

Table 6.7 shows the approximate stiffness losses of the clamped joint at Level 2 stresses. Stiffness loss based on the secant modulus (over the load range 512 lbs to 5120 lbs) was almost negligible for the clamped case, resulting in a fluctuation of 2 – 6 percent over the course of one million cycles. The total stiffness loss according to the tangent modulus (taken at zero load, zero displacement) was approximately 19 percent, with the majority of stiffness loss coming between 30000 and 50000 cycles, and 50000 and 100000 cycles. At 100000 cycles, the total stiffness loss was almost 18 percent, compared to 7 percent at the same point during the Stress Level 2 test. There is not a clear explanation for this difference, though it should be noted that the data used to determine the tangent modulus is based on the slope of the load vs. displacement curve within the first 500 lbs of the loading sequence, resulting in displacements in the range of one-thousandth of an inch. The slightest vibration or slip of the specimen in the test fixture can drastically affect the modulus, and potentially explain spikes in the stiffness between sequential load-unload cycles. Again, the displacement was measured by the built-in displacement function of the Instron machine. Consequently, the measured displacement accounts for all elongation within the specimen, including separation of the gap within the discontinuous tile core, thus values taken from this function are used solely to examine approximate stiffness loss, but cannot assume to be entirely accurate.

Table 6.7: Stiffness Loss according to Tangent Modulus (at zero load) and Secant Modulus (based on load range from 512 lbs to 5120 lbs) for Stress Level 1 – Clamped

	Based on Secant Modulus		Based on Tangent Modulus	
Cycle	Stiffness (lb/in)	Stiffness Loss	Stiffness (lb/in)	Stiffness Loss
10,000	324423	0.00%	530331	0.00%
20,000	313324	3.43%	518382	2.25%
30,000	306792	5.44%	503837	5.00%
50,000	304581	6.12%	564194	13.04%
100,000	307592	5.19%	435693	17.85%
200,000	312190	3.78%	431624	18.61%
300,000	312208	3.77%	423895	20.07%
500,000	312956	3.54%	422952	20.25%
1,000,000	316768	2.36%	428792	19.15%

Residual strength tests of specimens fatigued at Level 1 stresses can be seen in Figure 6.14, which compares fatigued vs. non-fatigued specimens under pinned joint conditions and Figure 6.15, which does the same for clamped joint specimens. Table 6.8 quantifies these results in terms of initial joint stiffness, strength at bending/shear failure and ultimate failure, and the total joint displacement at ultimate failure.

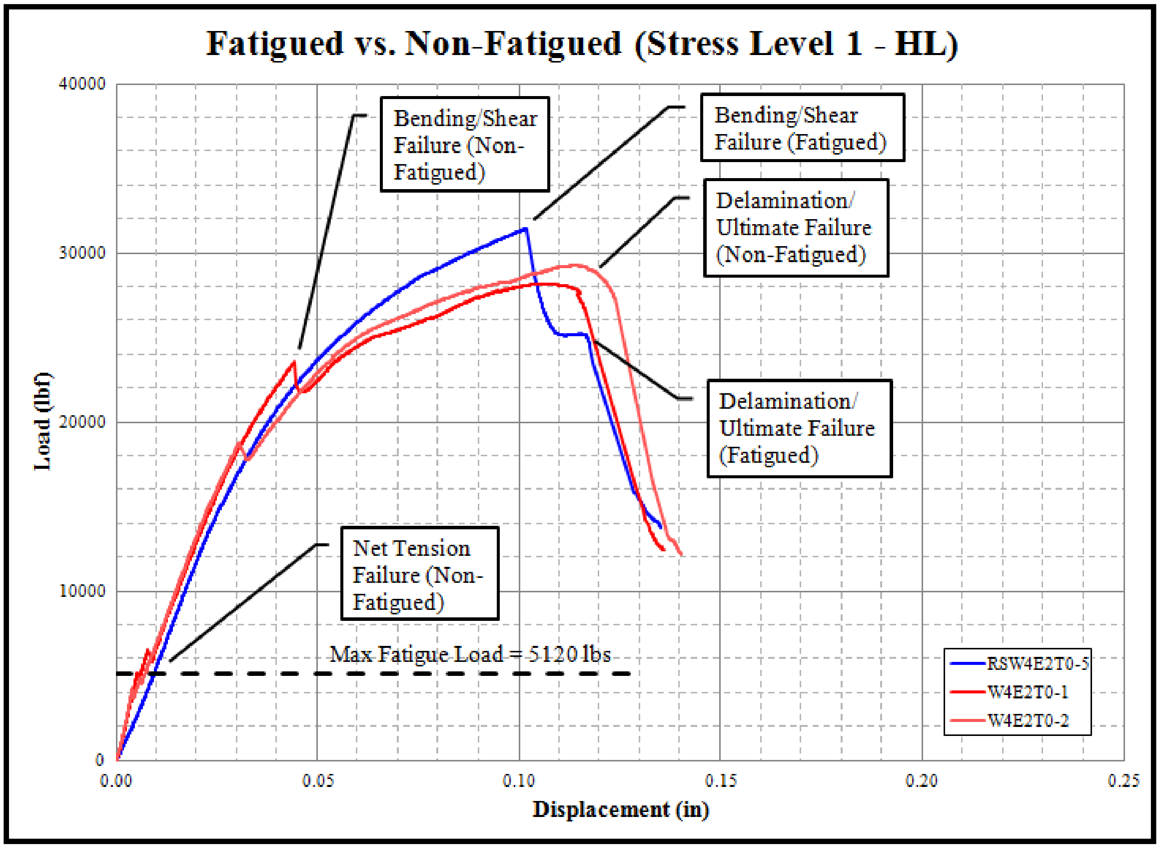

Figure 6.14: Fatigued vs. Non-Fatigued Specimens at Stress Level 1 – Pinned Case

Under non-fatigued pinned conditions, initial stiffness (according to the tangent modulus at zero load, zero displacement) of the joint was 1065925 lbs/in on average. Fatigued specimens exposed to Level 1 stresses exhibited an initial stiffness of 540900 lbs/in, significantly less than non-fatigued specimens, yet a slight improvement over the initial stiffness of 488172 lbs/in seen in fatigued specimens from Level 2 stresses. As described earlier in the explanation of Stress Level 2 fatigued pinned specimens, the load-displacement curves of the two cases are nearly identical after net tension failure of the non-fatigued specimens. Instead, the presence of the net tension cracks in the fatigued specimens caused an offset of approximately 0.002 inches in the load-displacement curve. Again, this parallelism is maintained through bending/shear failure of the non-fatigued specimens. This demonstrates that despite one million cycles of fatigue, little residual damage is found above the first failure mode as a result of fatigue. However, the weakened interlayer ultimately influenced the transfer of load between the face sheet and ceramic tile, resulting in a more balanced distribution of the bearing load between the face sheet and ceramic tile. This allows for the bending/shear crack to occur at a much greater strength in the ceramic tile for fatigued specimens. Unlike fatigued specimens at Stress Level 2, which failed due to simultaneous failure of the tile in bending/shear and the DCCS Structure in delamination, Stress Level 1 fatigued specimens followed the same progression of failure as non-fatigued specimens. After bending/shear failure in the ceramic tile, the fatigue specimen from Stress Level 1 began to regain strength before ultimately failing due to delamination. This occurred at approximately the same joint displacement as the non-fatigued specimens, but at a much smaller strength. This reduction in strength can be attributed to the weakened interlayer, causing premature failure of the bond line between the ceramic tile and interlayer, and between the interlayer and face sheet.

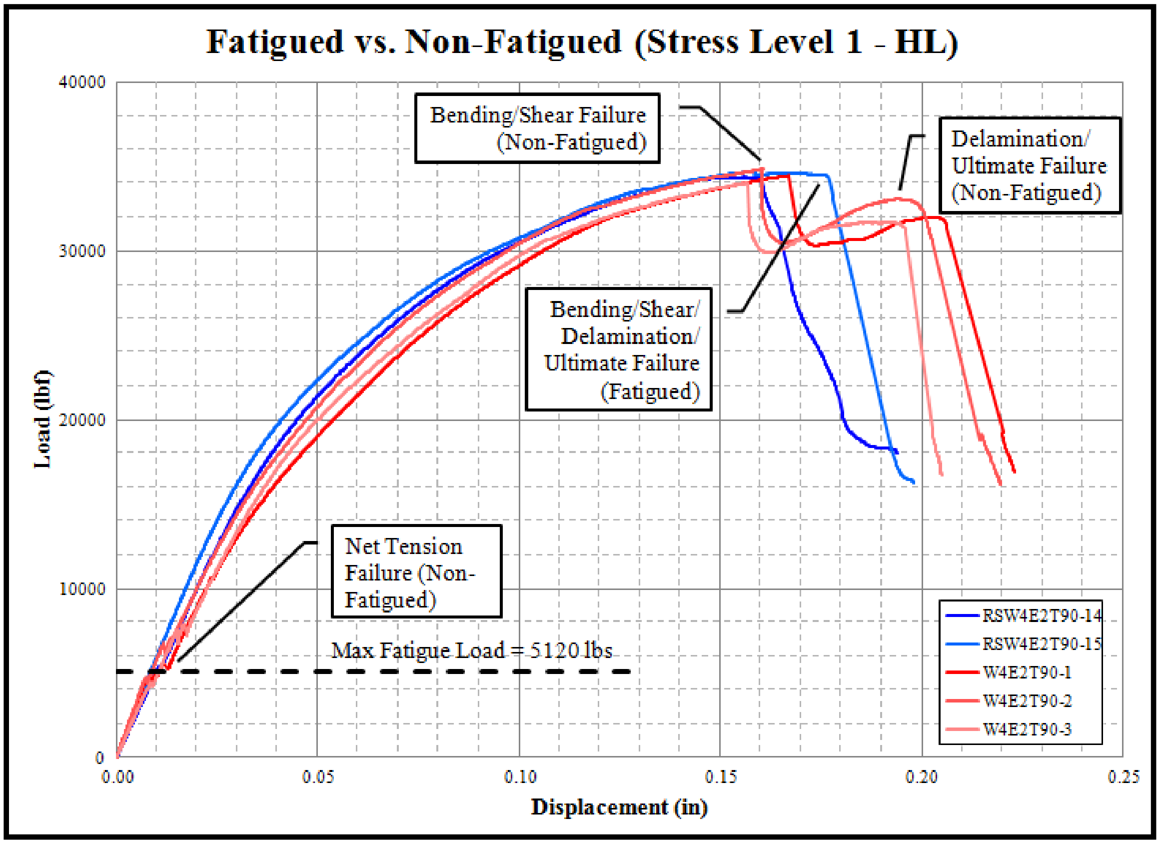

Figure 6.15: Fatigued vs. Non-Fatigued Specimens at Stress Level 1 – Clamped Case

Clamped joint specimens exposed to Level 1 stresses demonstrated an initial stiffness, calculated as the tangent modulus at zero load/displacement, ranging from 515570 lbs/in to 595520 lbs/in, resulting in an average stiffness reduction of 16 percent compared to non-fatigued specimens, and an improvement over the stiffness loss measured at Stress Level 2. Both residual strength specimens tested at Stress

Level 1 experienced progressive failure similar to that of the second specimen described at Stress Level 2. The load vs. displacement curves of fatigued specimens followed the same curve as that of non-fatigued specimens, even matching peak strength of the non-fatigued specimens. At this peak/ultimate strength, the DCCS Structure began to deteriorate, with frequent acoustic emissions coming from the structure due to the failing adhesive bond and disintegration of the ceramic tile at the joint. Not long after achieving ultimate strength, the DCCS Structure failed by a combination of tearout failure of the ceramic tile, and delamination and de-bonding of the constituents. With the exception of the initial stiffness, there was not a significant difference in failure progression between specimens fatigued at Level 1 and Level 2 stresses.

Table 6.8: Strength and Displacement Comparisons (Stress Level 1 Residual Strength vs. Pinned/Baseline)

Sample #	Initial Joint Stiffness	Strength at Bending/Shear Failure	Strength at Ultimate Failure	Displacement at Ultimate Failure
W4E2T0 (Averages)	1065925 lbs/in	21177 lbs	28739 lbs	0.1089 in
	186670 N/mm	94200 N	127840 N	2.766 mm
RSW4E2T0-5	540900 lbs/in	31461 lbs	25217 lbs	0.1155 in
	94730 N/mm	139950 N	112170 N	2.934 mm
W4E2T90 (Averages)	666020 lbs/in	34462 lbs	32283 lbs	0.1965 in
	116640 N/mm	153290 N	143600 N	4.991 mm
RSW4E2T90-14[3]	515570 lbs/in	34068 lbs	34380 lbs	0.1557 in
	90290 N/mm	151540 N	152930 N	3.955 mm
RSW4E2T90-15[3]	595520 lbs/in	34421 lbs	34746 lbs	0.1583 in
	104290 N/mm	153110 N	154560 N	4.021 mm

Over the course of five fatigue stress levels ranging from loads of 5120 lbs (11130 psi) at Stress Level 1 to 25600 lbs (55652 psi) at Stress Level 5, a well-defined progression of failure has been documented due to the effect of fatigue loading. Stress Level 5 and Stress Level 4 (load of 20480 lbs; bearing stress of 44522 psi) resulted in failure of the DCCS Structure by way of de-bonding of the face sheet, interlayer, and ceramic tile during the cyclic loading process. Stress Level 3 (15360 lbs; 33391 psi) transitioned from fatigue failure of the DCCS Structure to fatigue failure of the respective fastener in bending. Stress Level 2 (10240 lbs; 22261 psi) showed inconsistent results, with some specimens reaching the end of the one million cycle fatigue test, while others experienced fastener failure. Residual strength tests of

[3] Bending/Shear Failure occurred after Delamination/Ultimate Failure began

the fatigued specimens revealed changes in the structural integrity of the DCCS Structure, resulting in a change in failure progression of the specimens. All specimens tested at Stress Level 1 survived one million cycles, but like Stress Level 2, residual strength tests demonstrated structural damage within the test specimens. Overall, these results reveal a clearer picture of the performance of the DCCS Structure at high level fatigue stresses; low level fatigue testing will provide a complete understanding of the fatigue performance of the DCCS Structure.

6.3 <u>Low Level Fatigue Residual Strength and Stiffness</u>

The objective of low level fatigue testing is to determine the stress level that experiences no residual strength or stiffness loss in the DCCS structure and maintains the same failure progression as non-fatigued specimens. Weidner et al performed low level fatigue tests on pinned joint specimens, concluding that fatigue loads in the range of 1680 lbs began to show the initial stages of structural damage in the DCCS Structure. His conclusions will be used as a baseline means to compare the effect of clamping forces on fatigue damage and residual strength (however, his fatigue loads were slightly different than those used in this study, thus the quantified results cannot be compared directly).

Figure 6.16 shows the normalized stiffness loss according to the secant modulus over the course of one million cycles for specimens subjected to Level 5 stresses. The results for this chart were derived from the data acquisition system in the Instron machine. The max/min loads and displacements were recorded every 100 cycles, for the entirety of the test. Consequently, the load range used to calculate the secant modulus was based on the minimum load, 340 lbs, to the maximum load, 3400 lbs. The total stiffness loss ranged from 12 – 24 percent for clamped joints at this stress level. In the fatigue testing performed by Weidner et al on pinned joints, the max/min fatigue loads he utilized began with 2800/280 lbs. At this fatigue level, he noted a stiffness loss of 20 – 30 percent for pinned joints, calculated as the secant modulus using data supplied by the Instron data acquisition system. Because the load ranges used to calculate the stiffness are not equivalent between the pinned and clamped cases, the stiffness values cannot be directly compared. However, it should be noted that at this stress level in pinned joints, cracks were noticed in the ceramic tile at the joint. These cracks did not propagate to the outer edges of the tile during the fatigue process, thus were undetected while the test was ongoing. Despite being fatigued at higher loads, the clamped joints at Stress Level 5 showed no evidence of tile cracking at the joint during fatigue. This is due to the face sheet carrying a larger percentage of the bearing load resulting in lower tensile stresses in the ceramic tile compared to the pinned condition.

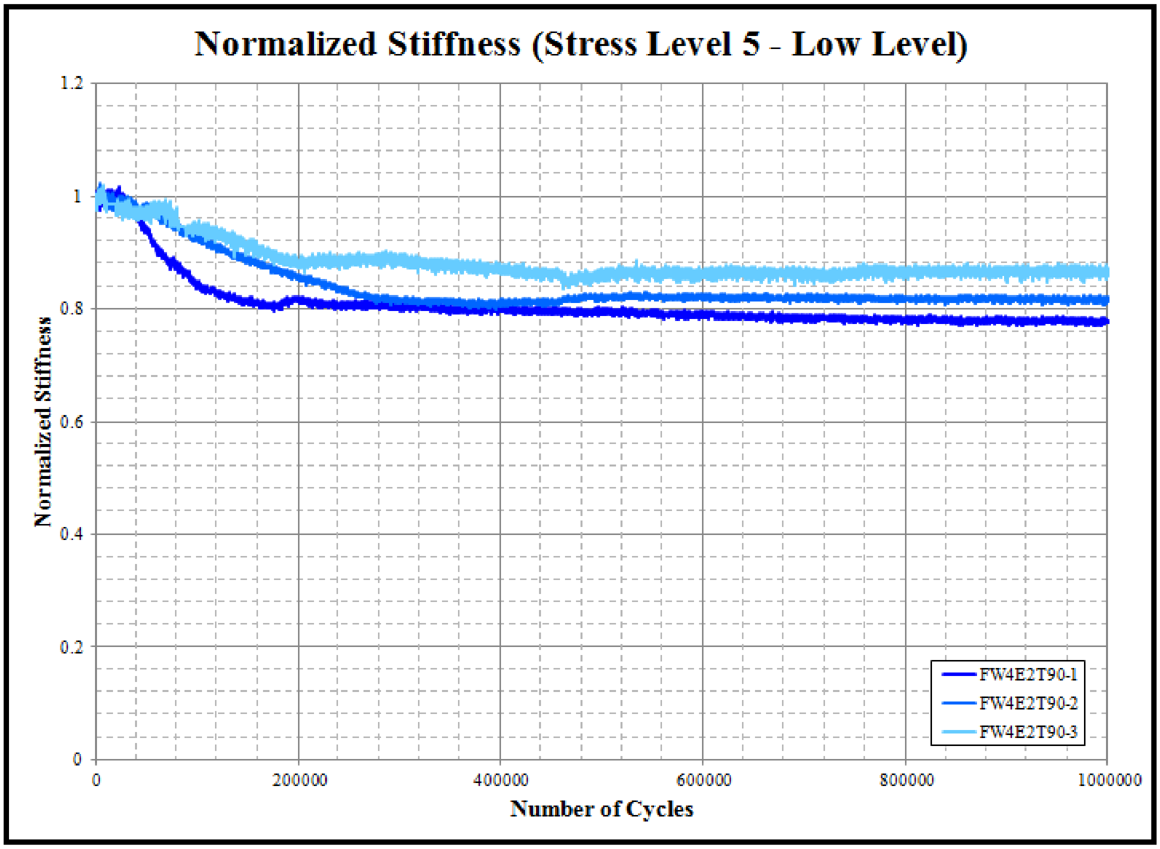

Figure 6.16: Normalized Fatigue Stiffness vs. Number of Cycles (Stress Level 5) based on Secant Modulus (defined from 340 lbs to 3400 lbs)

A load-unload sequence was performed periodically over the course of one million fatigue cycles to better define the progressive stiffness loss according to both the tangent and secant modulus. According to Figure 6.17, the initial loading sequence resulted in a significant amount of permanent displacement, despite no net tension cracks. This occurrence discounts the proposed theory of mismatching coefficients of thermal expansion as the source of permanent displacement, as this suggested the displacement was a result of released tensile stress in the ceramic tile by way of net tension cracks and the subsequent relaxing of the pre-compressed face sheet causing the net tension cracks to remain open. Instead, it supports the theory of a viscoelastic response from the face sheet and interlayer, preventing the specimen from fully recovering to its original position. The first 300000 fatigue cycles do not increase the magnitude of displacement; however, there is a noticeable change in the permanent displacement between 300000 and 500000 cycles, and again between 500000 and 1000000 cycles. There is also evidence of an increased phase lag in the final load-unload curve at one million cycles, signifying more energy was required (and lost) in order for the specimen to regain its original shape.

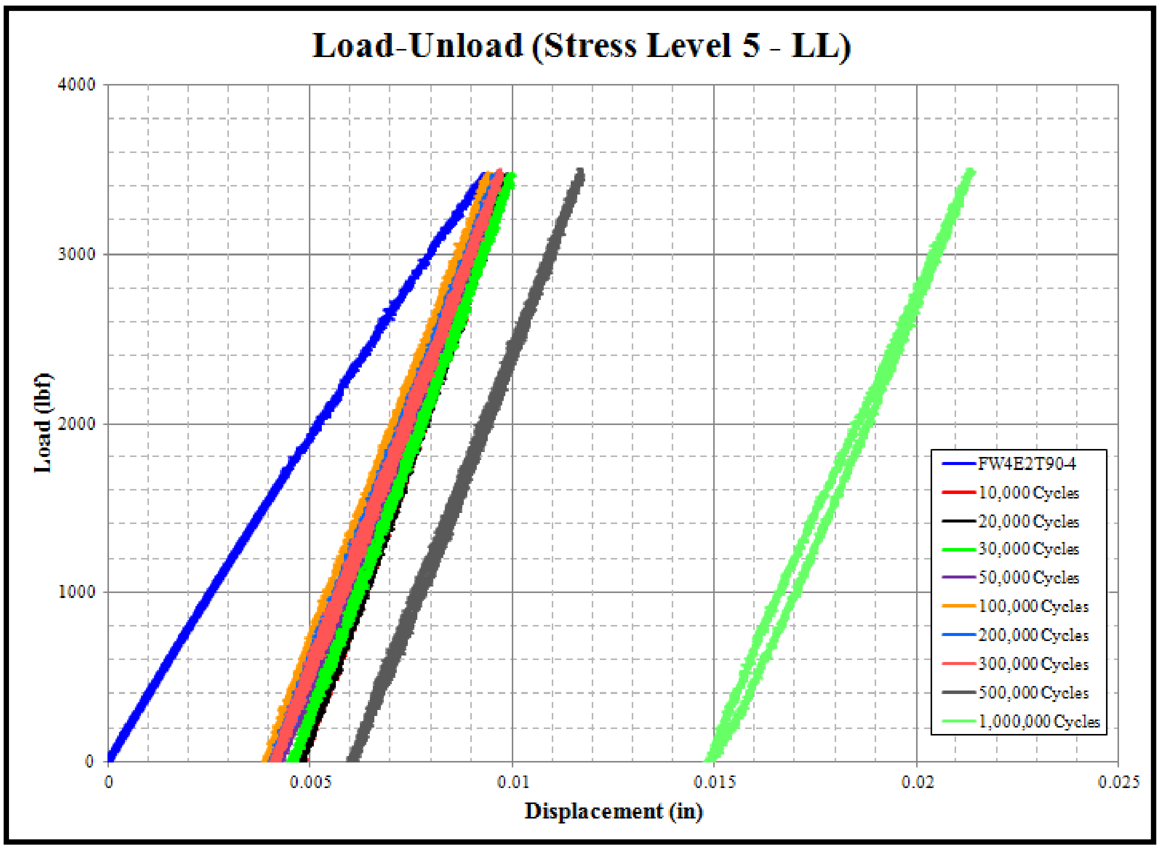

Figure 6.17: Periodic Hysteresis Curves for Stress Level 5 – Clamped Case

Table 6.9 quantifies the progressive stiffness loss from a specimen tested at Level 5 stresses. Stiffness according to the secant (over the load range 340 lbs to 3400 lbs) and tangent (taken at zero load, zero displacement) modulus are very representative of each other, with the measured stiffness and stiffness loss varying no more than one or two percent during each load-unload cycle. Losses appeared to be consistently progressive, with only relatively significant jumps occurring between 20000 and 30000 cycles, and again between 500000 and 1000000 cycles. The latter of the two could have been predicted based on Figure 6.17. It was at this time in the fatigue test that permanent displacement of the joint was taking place; so presumably, there was progressive structural damage at the joint to cause this change in displacement and stiffness. Over the course of one million cycles, there was an 18 and percent loss in joint stiffness based on the tangent and secant modulus, respectively.

Table 6.9: Stiffness Loss according to Tangent Modulus (at zero load) and Secant Modulus (based on load range from 340 lbs to 3400 lbs) for Stress Level 5 – Clamped

	Based on Secant Modulus		Based on Tangent Modulus	
Cycle	Stiffness (lb/in)	Stiffness Loss	Stiffness (lb/in)	Stiffness Loss
10,000	668199	0.00%	682407	0.00%
20,000	669770	-0.23%	682848	-0.06%
30,000	638335	4.47%	639989	6.22%
50,000	628242	5.98%	645365	5.43%
100,000	625983	6.32%	635460	6.88%
200,000	611782	8.45%	618086	9.43%
300,000	620432	7.15%	622275	8.81%
500,000	604772	9.50%	608702	10.80%
1,000,000	530979	20.54%	559619	17.99%

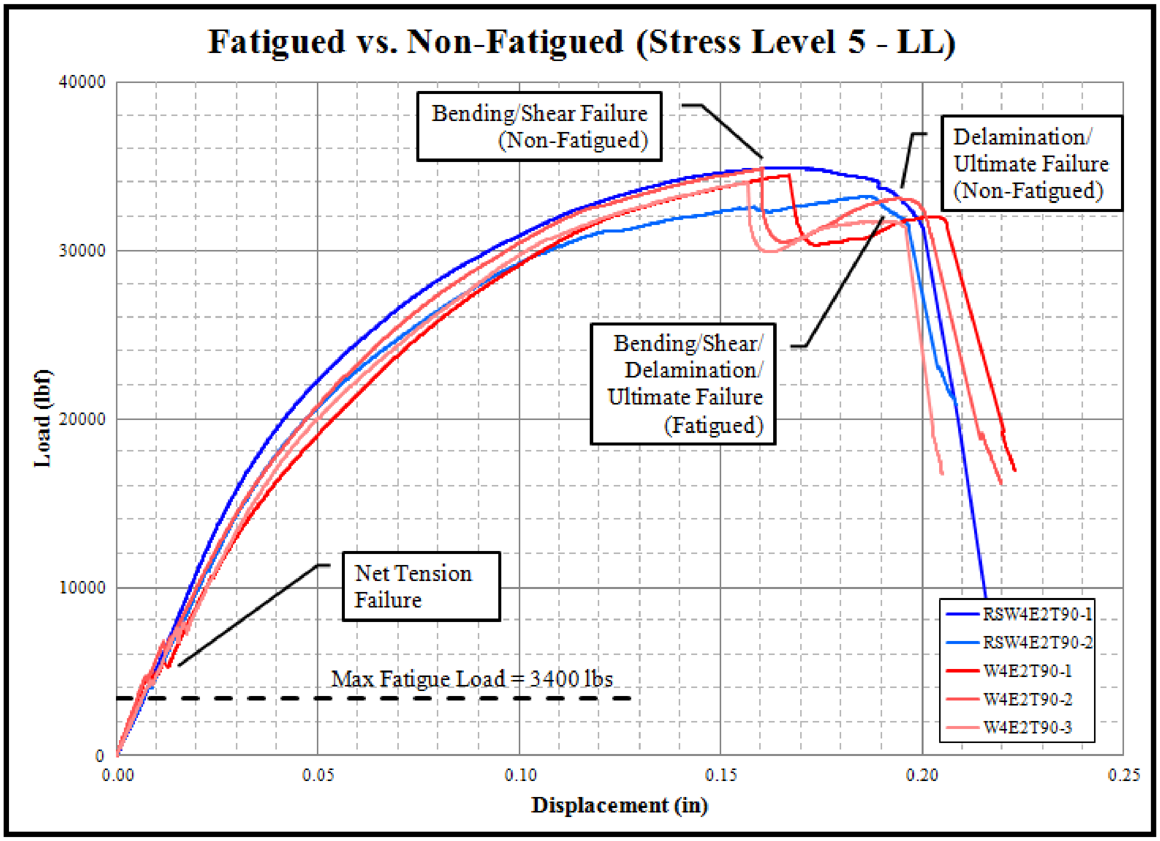

Figure 6.18: Fatigued vs. Non-Fatigued Specimens at Stress Level 5

Residual strength tests were performed on specimens tested at Level 5 stresses, with the results plotted against non-fatigued specimens in Figure 6.17, along with quantifiable comparisons of the initial stiffness, strength at bending/shear failure and ultimate failure and the overall joint displacement at ultimate failure. In these residual strength tests, the initial stiffness (calculated using the tangent modulus at zero load, zero displacement) ranged from 508230 lbs/in to 530093 lbs/in, an average stiffness reduction of approximately 22 percent over non-fatigued specimens (which exhibited an average stiffness using the tangent modulus of 666020 lbs/in). Load vs. displacement curves were very similar between fatigued and non-fatigued specimens as they ascended over 30000 lbs (65217 psi) of bearing load. At the time when the non-fatigued specimens typically experienced bending/shear failure of the ceramic tile, fatigued specimens had also reached their peak/ultimate strength, but were showing signs of imminent delamination failure. Acoustic emissions were audible as the joint displacement increased without an increase in strength. Eventually the load began to decline rapidly with further damage at the joint and initial de-bonding of the interlayer and ceramic tile. Ultimately, a combination of bending/shear failure of the ceramic tile and delamination of the DCCS Structure resulted in catastrophic failure of the specimen. In comparison with non-fatigued specimens, the fatigued specimens did not show a significant loss in overall strength, and failed at a marginally smaller joint displacement. The most significant difference was the catastrophic nature of failure due to delamination and bending/shear failure. Weidner et al saw the same phenomenon with pinned joints at Stress Level 5.

Table 6.10: Strength and Displacement Comparisons (Stress Level 5 Residual Strength vs. Baseline)

Sample #	Initial Joint Stiffness	Strength at Bending/Shear Failure	Strength at Ultimate Failure	Displacement at Ultimate Failure
W4E2T90 (Averages)	666020 lbs/in	34462 lbs	32283 lbs	0.1965 in
	116640 N/mm	153290 N	143600 N	4.991 mm
RSW4E2T90-1[4]	508230 lbs/in	32021 lbs	34902 lbs	0.1648 in
	89000 N/mm	142440 N	155250 N	4.186 mm
RSW4E2T90-2[4]	530093 lbs/in	31147 lbs	33176 lbs	0.1874 in
	92830 N/mm	138550 N	147570 N	4.760 mm

Figure 6.19 shows the normalized stiffness loss according to the secant modulus over the course of one million cycles for specimens subjected to Level 4 stresses. The results for this chart were derived from the data acquisition system in the Instron machine. The max/min loads and displacements were recorded every 100 cycles, for the entirety of the test. Consequently, the load range used to calculate the secant modulus was based on the minimum load, 272 lbs, to the maximum load, 2720 lbs. The total stiffness loss was negligent for clamped joints at this stress level. Additionally, this stress level was conducted using nearly the identical max/min fatigue loads as the first fatigue test conducted by Weidner et al (max/min of 2800/280 lbs), which resulted in a stiffness loss of 20 – 30 percent. This resounding difference exemplifies the effect of clamping forces on the joint. According to these results, it appears as though fatigue testing at Level 4 stresses does not have a resounding effect on the structural integrity of the joint. Fatigue testing with load-unload sequences will

[4] Bending/Shear Failure occurred after Delamination/Ultimate Failure began

be done to examine if the tangent modulus confirms no stiffness loss and residual strength tests will compare any change in the damage progression.

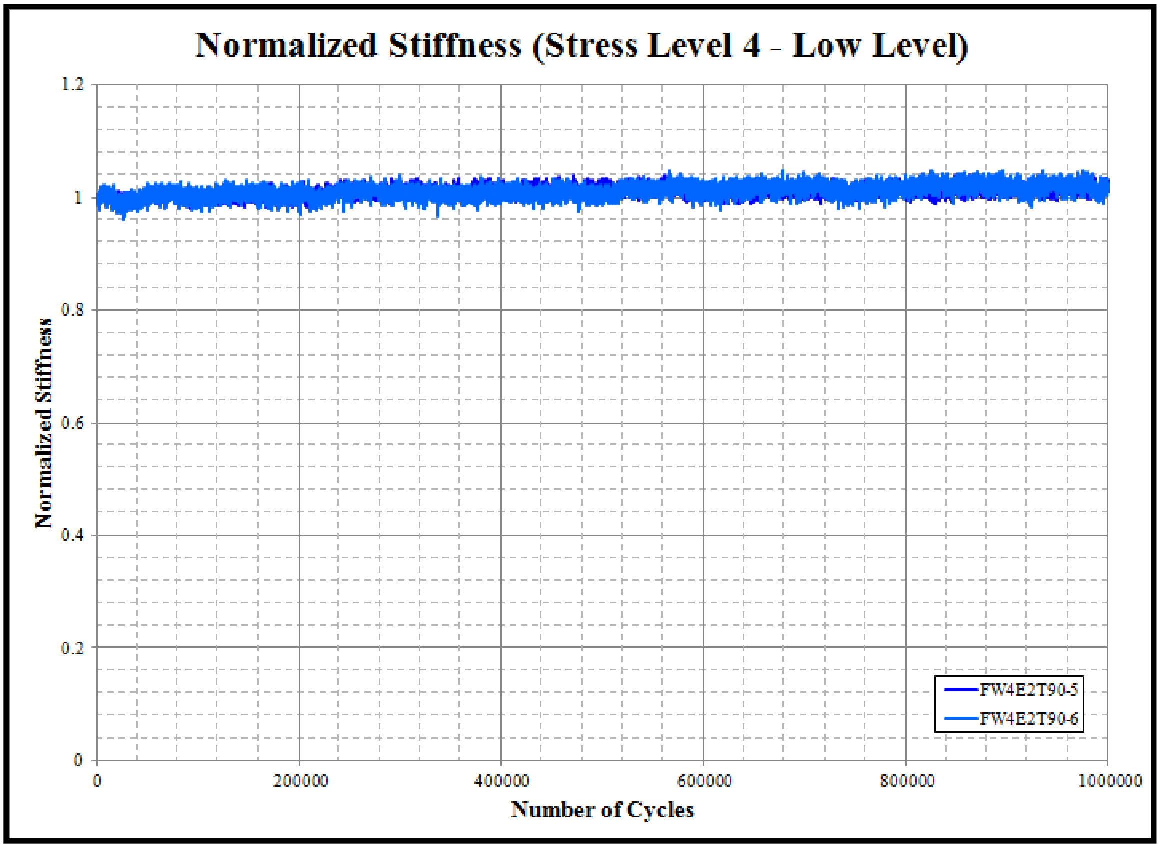

Figure 6.19: Normalized Fatigue Stiffness vs. Number of Cycles (Stress Level 4) based on Secant Modulus (defined from 272 lbs to 2720 lbs)

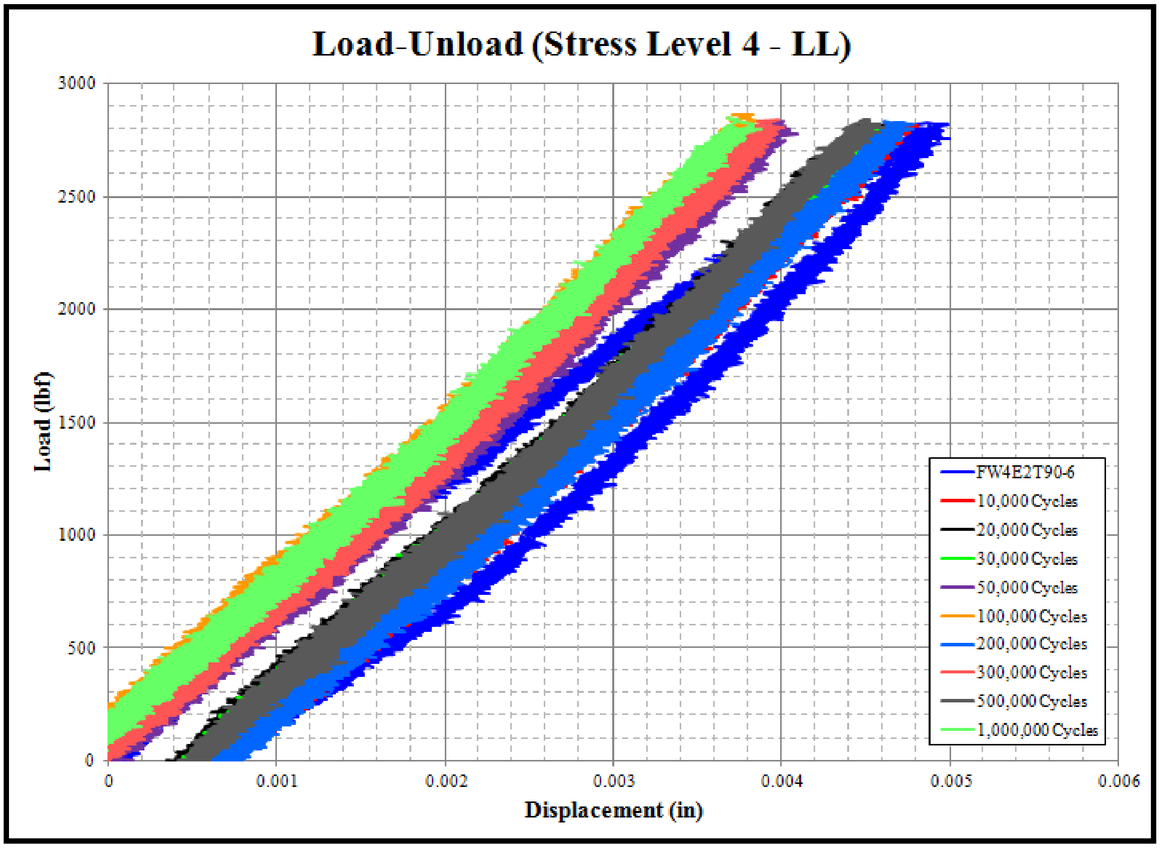

Figure 6.20: Periodic Hysteresis Curves for Stress Level 4 – Clamped Case

The load-unload cycles seen in Figure 6.20 show that with an increase in the number of fatigue cycles, there is no progressive deformation. Further examination shows that there appears to be some fluctuation in the permanent displacement over time, with some load-unload cycles recognizing the permanent displacement achieved from the first loading cycle, while others appear to have entirely restored this original displacement back to the initial shape. There appeared to be no consistency or pattern to these discrepancies, ruling out the possible role fatigue may have had on the differences. Inspection of the data output from the Instron machine revealed that the load-unload sequences were initiated at loads ranging from -20 to 20 lbs. While insignificant compared to the maximum fatigue load at Stress Level 4, this variability in initial load had a direct effect on the initial displacement values for each load-unload cycle. This variability went unnoticed in previous stress levels due to extensively larger overall displacements.

Table 6.11 quantifies the secant (over the load range 272 lbs to 2720 lbs) and tangent (taken at zero load, zero displacement) modulus stiffness loss of the specimen tested at Level 4 stresses. There was some fluctuation in each of the sets of values throughout the fatigue test; however over the course of one million cycles, there was no defined amount of stiffness loss. This validates the normalized stiffness losses seen in Figure 6.19. With no evidence of stiffness loss due to Level 4 stresses, residual strength tests will confirm if there was any loss in structural integrity due to fatigue.

Table 6.11: Stiffness Loss according to Tangent Modulus (at zero load) and Secant Modulus (based on load range from 272 lbs to 2720 lbs) for Stress Level 4 – Clamped

	Based on Secant Modulus		Based on Tangent Modulus	
Cycle	Stiffness (lb/in)	Stiffness Loss	Stiffness (lb/in)	Stiffness Loss
10,000	687421	0.00%	697399	0.00%
20,000	666843	3.00%	701870	-0.64%
30,000	687983	-0.08%	691253	0.88%
50,000	705736	-2.66%	732523	-5.04%
100,000	717191	-4.33%	741878	-6.38%
200,000	688778	-0.19%	745322	-6.87%
300,000	720709	-4.84%	659901	5.38%
500,000	698319	-1.58%	665644	4.55%
1,000,000	680034	1.08%	689761	1.10%

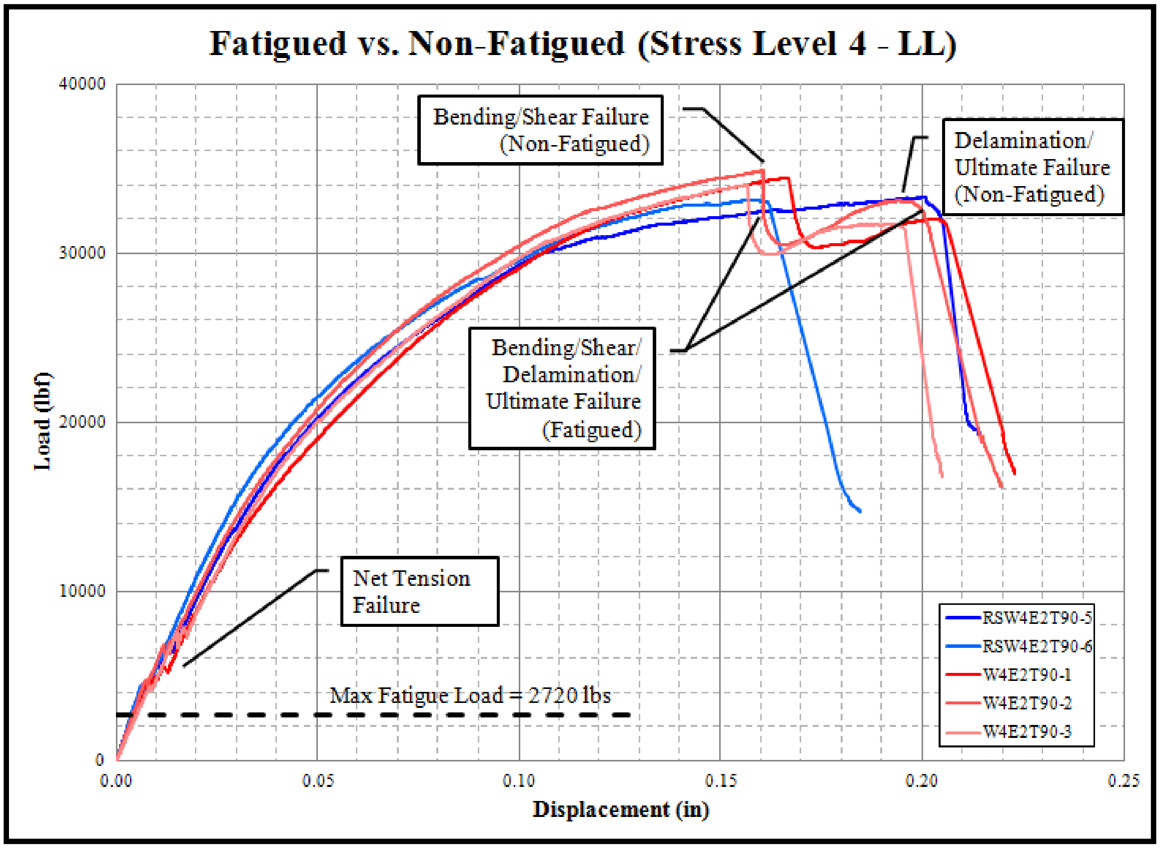

Figure 6.21: Fatigued vs. Non-Fatigued Specimens at Stress Level 4

Residual strength tests from Stress Level 4 are shown in Figure 6.21, plotted against non-fatigued specimens. The results are quantified in Table 6.12 according to joint stiffness, strength at bending/shear and ultimate failure, and displacement at ultimate failure. The initial joint stiffness for each fatigued specimen fell within the range of stiffness's calculated from non-fatigued specimens. As the bearing load increases, there is evidence that fatigue had an effect on the strength of the interlayer and adhesive bond between constituents. Acoustic emissions signified bond failure and deterioration within the joint, preventing the peak strength from matching that seen in the non-fatigued specimens. Displacement at ultimate failure became a function of the durability of the adhesive bond. The more extensive the damage of the interlayer, the sooner the bond failed, such was the case for the second fatigued specimen. The first fatigued specimen was able to retain slightly more strength in the adhesive, allowing for a greater displacement, but unsuccessful in increasing the ultimate capacity of the joint.

Residual strength tests conducted by Weidner et al on specimens exposed to lower fatigue stress levels displayed similar results to those of clamped joint specimens. He saw that in certain stress levels that exhibited little to no stiffness loss in residual strength tests, there was a tendency for structural damage, as evident based on the progression of failure. In particular, in pinned specimens tested for one million cycles using a fatigue load range of 224 lbs to 2240 lbs, he saw that two of the three residual strength specimens demonstrated simultaneous and catastrophic failure of the ceramic tile in bending/shear and of the full DCCS Structure due to delamination, while one specimen followed the baseline failure progression. This was the case for specimens tested at Stress Level 4 under clamped joint conditions.

Table 6.12: Strength and Displacement Comparisons (Stress Level 4 Residual Strength vs. Baseline)

Sample #	Initial Joint Stiffness	Strength at Bending/Shear Failure	Strength at Ultimate Failure	Displacement at Ultimate Failure
W4E2T90 (Averages)	666020 lbs/in	34462 lbs	32283 lbs	0.1965 in
	116640 N/mm	153290 N	143600 N	4.991 mm
RSW4E2T90-5[5]	705880 lbs/in	31969 lbs	33286 lbs	0.2007 in
	123620 N/mm	142210 N	148060 N	5.098 mm
RSW4E2T90-6[5]	730160 lbs/in	32887 lbs	33113 lbs	0.1594 in
	127870 N/mm	146290 N	147290 N	4.049 mm

Given that damage was not visible to the naked eye at Level 4 and Level 5 stresses, but there was documented stiffness loss at Stress Level 5, underwater ultrasonic C-Scan images were taken to compare specimens at both levels. Figure 6.22 shows two specimens, one exposed to one million cycles at Level 5 stresses and the other after one million cycles at Level 4 stresses. The images show a full ceramic tile with the centralized joint, while the resin-filled gap between tiles is also visible near the bottom of each image. Yellowish-orange is the basic coloration of a solid object with no voids; darker orange and red represent voids or areas of delamination. According to the two images below, Stress Level 5 exhibited damage around the full bearing edge of the joint all the way up to the top edge of the tile, whereas Stress Level 4 showed no discoloration or delamination. These differences explain the reason for the reduced stiffness at Level 5 stresses and no stiffness loss at Level 4 stresses.

[5] Bending/Shear Failure occurred after Delamination/Ultimate Failure began

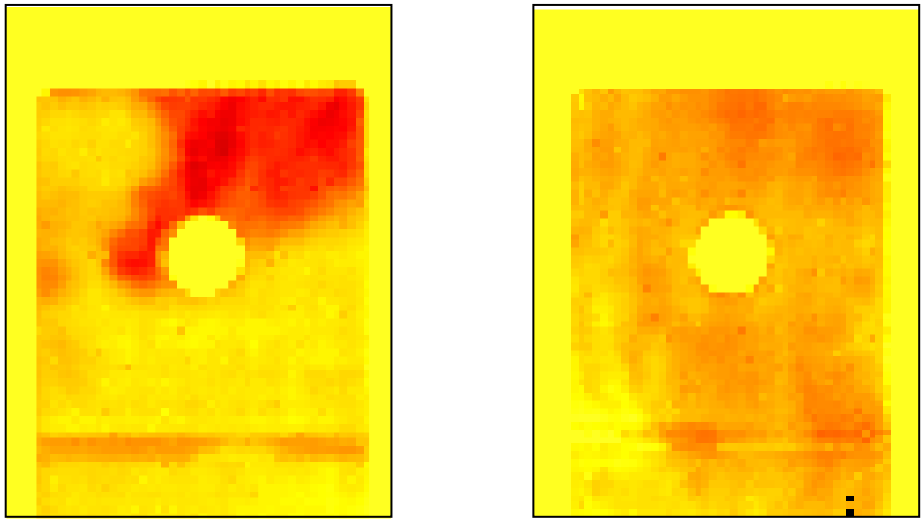

Figure 6.22: Underwater C-Scan Images of Fatigued Specimens at Stress Level 5 (left) and Stress Level 4 (right)

Based on the results of specimens fatigued at Level 4 stresses, it was determined that any fatigue stress below Stress Level 4 would result in no loss of joint stiffness. However, damage to the interlayer was still present, affecting the residual strength of the DCCS Structure. Fatigue testing at lower stress levels would be aimed at finding the limiting stress level that exhibited no change in residual strength from non-fatigued specimens.

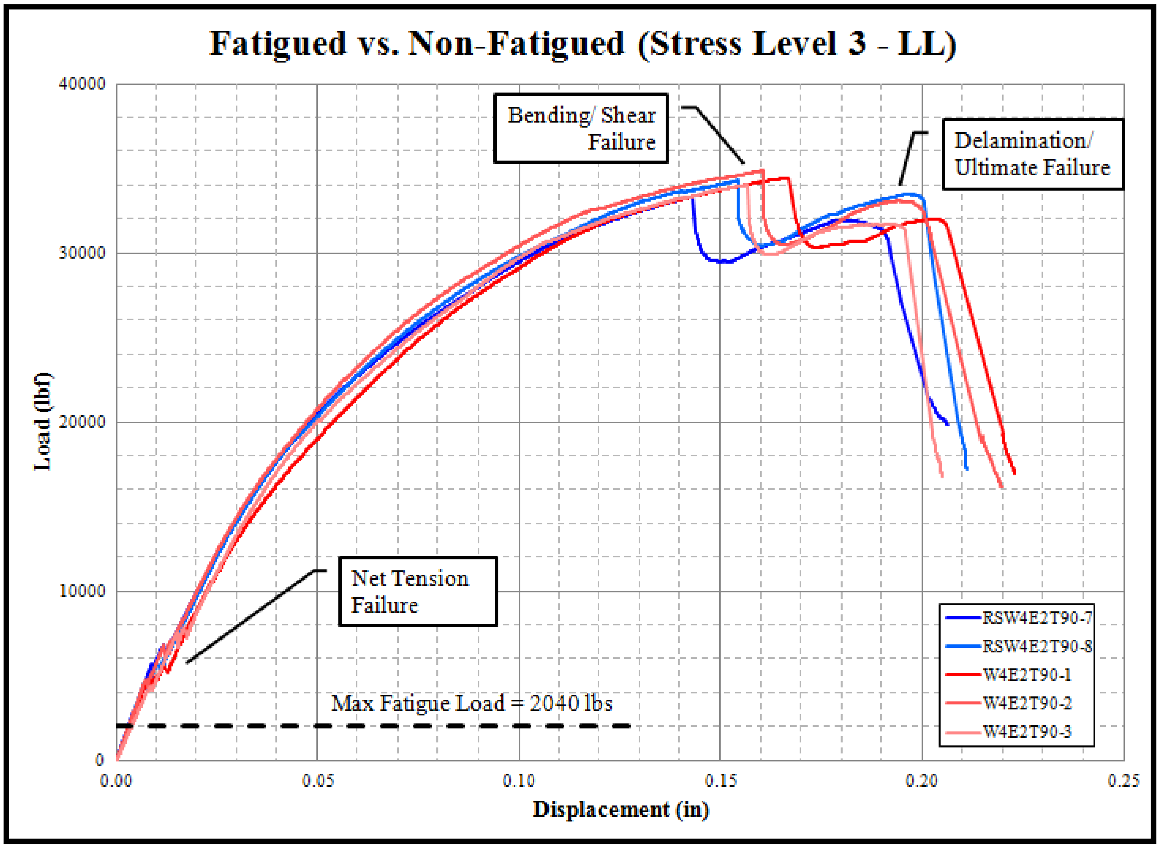

Figure 6.23: Fatigued vs. Non-Fatigued Specimens at Stress Level 3

Residual strength tests at Level 3 fatigue stresses, seen in Figure 6.23, reveal very similar results to those of non-fatigued specimens. Table 6.13 documents the strength and displacement comparisons between fatigued and non-fatigued specimens. Like Stress Level 4 specimens, Level 3 stresses resulted in no loss of joint stiffness. The progression of failure followed the baseline sequence of net tension cracks in the ceramic tile, bending/shear crack in the ceramic tile, and delamination/ ultimate failure of the DCCS Structure. Last these failure modes all occurred at approximately the same strengths and displacement as the average non-fatigued specimen. Weidner et al was in agreement that the progression of failure for pinned joints at Stress Level 3 followed the baseline failure progression of non-fatigued specimens. It was determined that although the initial stiffness (calculated using the tangent modulus at zero load, zero displacement) and displacements at ultimate failure remained consistent, ultimate strength of the fatigued joints were less than non-fatigued pinned specimens. For pinned joints, Weidner found that the fatigue stress level required to exhibit these same characteristics in pinned joints was at a min/max load of 112/1120 lbs.

Table 6.13: Strength and Displacement Comparisons (Stress Level 3 Residual Strength vs. Baseline)

Sample #	Initial Joint Stiffness	Strength at Bending/Shear Failure	Strength at Ultimate Failure	Displacement at Ultimate Failure
W4E2T90 (Averages)	666020 lbs/in	34462 lbs	32283 lbs	0.1965 in
	116640 N/mm	153290 N	143600 N	4.991 mm
RSW4E2T90-7	702190 lbs/in	33335 lbs	31928 lbs	0.1827 in
	122970 N/mm	148280 N	142020 N	4.641 mm
RSW4E2T90-8	674970 lbs/in	34285 lbs	33484 lbs	0.1970 in
	118210 N/mm	152510 N	148940 N	5.004 mm

When Level 3 stresses were determined to be the limiting stress that resulted in no residual strength or stiffness loss, Stress Levels 1 and 2 were disregarded to conserve test specimens. Results from low level fatigue tests were a continuation of the results from high level fatigue tests. Stress Level 5 (load of 3400 lbs; bearing stress of 7391 psi) demonstrated stiffness loss at the joint according to both the secant and tangent modulus, and a failure sequence of net tension cracks in the ceramic tile, de-bonding of the interlayer and ceramic tile, and ultimate failure by means of bending/shear failure in the ceramic tile and delamination of the DCCS Structure. Stress Level 4 (2720 lbs; 5913 psi) exhibited no stiffness loss after one million fatigue cycles, but continued to show structural damage within the interlayer, resulting in the same failure sequence seen in Stress Level 5. Stress Level 3 (2040 lbs; 4435 psi) reached the desired stress limit that demonstrated no joint stiffness loss or changes within the failure sequence of residual strength testing. Over the span of three low-level fatigue stresses and five high-level fatigue stresses, the performance at each stress level successfully bridged the gap between visibly damaged and internally damaged specimens, and allowed for a comprehensive analysis to be made on the effect of fatigue on DCCS Structures.

Comparisons between stress levels can be useful in understanding transition periods and progressive changes in fatigue resistance. The easiest method to do this is through visual inspection and quantifying stiffness loss. Visual inspection is a qualitative measurement of the degradation of fatigued specimens over the course of fatigue tests. High Stress Level 5 (max/min – 25600/2560 lbs) and Stress Level 4 (max/min – 20480/2048 lbs) both resulted in failed specimens after very short fatigue lives. High Stress Level 3 (max/min – 15360/1536 lbs) demonstrated failure of joint fastener. High Stress Level 2 (max/min – 10240/1024 lbs) and Stress Level 1 (max/min 5120/512 lbs) withstood one million fatigue cycles, demonstrating only net tension failure in the ceramic tile. Low Stress Level 5 (max/min – 3400/340 lbs), Stress Level 4 (max/min – 2720/272 lbs), and Stress Level 3 (max/min – 2040/204 lbs) showed no visual damage after one million cycles. In terms of stiffness loss, stiffness measured by the tangent modulus can be compared across the varying stress levels on the condition that the tangent slope is quantified at the same load for each test. Stiffness calculated according to the secant modulus must follow the same condition; all comparisons must utilize a secant modulus computed over an equivalent load range. Because the tangent modulus was taken at a specific point on the load-displacement curve, it did very little to explain the performance of specimens subjected to large fatigue loads. The secant modulus was much more effective in explaining the fatigue resistance at higher loads. One useful objective of the tangent modulus was demonstrating the initial stiffness loss between specimens fatigued below net tension failure in the ceramic tile, and those which exhibited several cracks after initial loading. The onset of net tension cracks significantly reduced the initial stiffness in these fatigued specimens; however, it was observed that despite these cracks, residual strength tests provided proof that beyond net tension failure, the tangent modulus was nearly identical in fatigued and non-fatigued specimens. In order to compare stiffness loss according to the secant modulus, an appropriate range must be determined to allow for consistency between stress levels. Low Stress Level 4 (max/min – 2720/272 lbs) was the first fatigue load that exhibited little to no stiffness loss, thus it was determined this would be the most advantageous range of loads to compare stiffness. Table 6.14 documents the four stress levels that achieved one million fatigue cycles, beginning with High Stress Level 2 and ending with Low Stress Level 4. According to the data, it appears as though reducing the fatigue load results in lower stiffness loss. After 100000 cycles, High Stress Level 2 (max/min – 10240/1024 lbs) experienced over 25 percent loss of stiffness; over the same time, High Stress Level 1 (max/min – 5120/512 lbs) experienced 13 percent loss of stiffness; Low Stress Level 5 (max/min – 3400/340 lbs) experienced 8 percent loss of stiffness; Low Stress Level 4 (max/min – 2720/272 lbs) did not record any loss in stiffness, only the casual fluctuation that can be expected when measuring displacements on the scale of thousandths of an inch. (Because of this, measured stiffness loss can be assumed to have a tolerance of ± 5 percent.) At this point in the fatigue test, stiffness loss appeared to plateau in each test (with the exception of High Stress Level 2, where the bolt failed). It should be noted that between 500000 and 1000000 cycles in the fatigue test at Low Stress Level 5, there is a significant loss of stiffness that could not be visually confirmed at the joint (no cracking of the ceramic tile or debonding at the face sheet-tile interface). This could be a result of damage elsewhere in the specimen, particularly at the gaps, or sliding between the washers and face sheet. Sliding may potentially develop due to a reduction in clamp load and friction force over time, ultimately becoming less than the applied far field load, which will allowing for sliding. This may not be an issue for other stress levels; higher levels likely experience this sliding as the applied load exceeds the resisting friction force, whereas lower fatigue loads are much less than friction force, thus preventing the occurrence of sliding.

Table 6.14: Stiffness Loss according to Secant Modulus (based on load range from 272 lbs to 2720 lbs) for all stress levels

	Stress Level 2 – High (max/min of 10240/1024)	Stress Level 1 – High (max/min of 5120/512)	Stress Level 5 – Low (max/min of 3400/340)	Stress Level 4 - Low (max/min of 2720/272)
Cycle	Stiffness Loss	Stiffness Loss	Stiffness Loss	Stiffness Loss
10,000	0.00%	0.00%	0.00%	0.00%
20,000	10.11%	8.55%	2.06%	3.00%
30,000	9.10%	13.00%	10.62%	-0.08%
50,000	13.51%	15.17%	10.24%	-2.66%
100,000	25.37%	13.23%	7.94%	-4.33%
200,000	-	13.36%	9.48%	-0.19%
300,000	-	13.30%	11.76%	-4.84%
500,000	-	13.18%	11.17%	-1.58%
1,000,000	-	10.89%	23.83%	1.08%

Several different experimental tests have been performed to examine the performance of bolted joints in Discontinuous Ceramic Cored Sandwich Structures. Stress relaxation testing evaluated the amount of clamping load expected to be lost in the near-term following joint tightening. Static testing provided a method of optimizing the clamp load to gain the most strength from the joint without causing initial damage to the joint upon tightening or creating a scenario of catastrophic failure without warning. Fatigue testing allowed a means for quantifying the fatigue resistance of the DCCS joint at various stress levels. Compiling these results into final design recommendations will assist future designers in selecting the appropriate design based on certain parameters.

Chapter 7

CONCLUSIONS AND RECOMMENDATIONS

In this study, testing was performed to gain a better understanding of the performance of clamped joints in Discontinuous Ceramic Cored Sandwich Structures. These tests included various stress relaxation tests to estimate the total relaxation in the clamping pre-load, static in-plane tension/bearing tests to obtain strength and stiffness properties of the joint, and fatigue testing to examine the resistance of the DCCS Structure to cyclic loading and quantify strength and stiffness loss at particular fatigue stress levels. Each individual test provided insight to design parameters, and collectively, allowed for a final recommendation to be made regarding the clamping properties of the joint. The design methodology developed in this study can be applied to future work involving the DCCS joint, including alternative loading conditions and joint characteristics to provide new perspectives of design.

7.1 Compressive Stress Relaxation in Discontinuous Ceramic Cored Sandwich Structures

Past research has shown that providing clamping forces on composite joints has been beneficial to joint strength and stiffness. This study focused on confirming these presumptions and optimizing the clamping force to obtain the best joint performance in the DCCS Structure. Part of the design methodology in determining the optimum clamping forces is quantifying the amount of relaxation, or stress loss that occurs at the joint. One source of relaxation that is unique to composite joints results from the viscoelastic nature of the matrix in the laminate. Additionally, the interlayer in the DCCS Structure possesses viscoelastic characteristics, providing two different materials within the structure that will have the tendency to relax when exposed to an initial compressive force. Experimental testing was performed on the DCCS Structure and its' constituents to gain a better understanding of the amount of stress lost over time, and several methods to mitigate this issue were investigated.

Before beginning stress relaxation tests, several parameters were required to provide the closest simulation of compressive stresses that would be present at the joint when torque is applied. These included selecting a suitable washer size for the extent of this study and a baseline torque, solely as an approximate starting point before a finalized torque is determined. Khashaba et al and Yan et al found that washer size influenced the distribution of compressive stresses through composite joints, and that an outer diameter-to-inner diameter ratio of 3.0 provided the optimal joint performance. These findings, in conjunction with ASME standards, led to the selection of a washer with an inner diameter of 0.5625 inches and an outer diameter of 1.375 inches (total surface area of 1.236 in^2). Under the assumption that the washer was completely rigid, compressive stresses in the DCCS Structure were calculated according to the magnitude of the torque/clamping load distributed evenly through the contact area between the washer and face sheet. Upper torque limits were established according to fastener and constituent strengths. The fastener was governed by the proof tensile strength of the bolt, which was achieved at a torque level of approximately 106 ft-lbs. The interlayer, whose compressive yield strength is only 2700 psi, governs between the three constituents of the DCCS Structure, and undergoes yield at torque levels above 27 ft-lbs. Selecting a lower torque limit is much more arbitrary, as the purpose of the lower limit is to account for stress losses, such as vibration and fatigue, embedment, material relaxation, etc. Bickford suggests a lower limit of 48 percent of the minimum tensile strength of the bolt, equating to a torque of 85 ft-lbs. This was notably greater than the torque limit established by the interlayer strength. It was concluded that yielding of the interlayer was a necessary sacrifice in order to ensure that the bolt did not loosen so much as to reduce the clamping force to zero over time. Thus, based on the prescribed torque range of 85 ft-lbs to 106 ft-lbs, a baseline torque of 90 ft-lbs was selected to begin testing.

Two experimental tests were designed to evaluate the stress loss in the joint under a torque of 90 ft-lbs. The first utilized core samples of the face sheet and DCCS Structure (nominal diameter of 0.447 inches; surface area of 0.1569 in^2) placed between two flat, rigid surfaces fixed to an Instron machine (see Figure 3.6 for test configuration). The specimens were instantaneously subjected to a uniform compressive stress equivalent to that of 90 ft-lbs (conversion from torque to equivalent stress documented in Chapter 4.2), wherein the strain was held constant and the stress loss was measured over time. This test showed the average stress loss in the face sheet was approximately 10 – 12 percent after one minute, 13 – 15 percent after 10 minutes, and 17 – 19 percent after 100 minutes; the average stress loss in the DCCS Structure was approximately 15 – 19 percent after one minute, 20 – 24 percent after 10 minutes, and 25 – 27 percent after 100 minutes. Using basics mechanics, a relationship between the DCCS Structure and its' constituents was defined such that the stress relaxation of the interlayer could be quantified (see Equation (7) in Chapter 4.3). This resulted in approximate stress loss in the interlayer of 77 – 78 percent after one minute, 79 – 80 percent after 10 minutes, and 83 – 84 percent after 100 minutes. In comparing the experimental results of the face sheet and DCCS Structure and the theoretical results of the interlayer, it was evident that the interlayer had a greater contribution than the face sheet to the overall relaxation of the DCCS Structure. This likely was attributed to the compressive yielding and compliant nature of the interlayer. Additionally, the results suggested that the majority of relaxation occurs closely after the application of the clamping force, a conclusion that influenced methods to help mitigate the effect of stress loss.

The second experimental test simulates the DCCS joint as it would be in a real-life application. Figure 3.7 shows the test set-up, which utilizes a 4 inch by 4 inch specimen with a centralized 0.5 inch hole, two washers protecting the joint and distributing compressive stresses around the joint, a stable fixture that allows for the joint to be tightened while restricting the bolt from turning during the tightening process, and a washer load cell to measure the clamping forces in the joint. The joint was initially clamped using the baseline torque of 90 ft-lbs, but the magnitude of this force caused radial cracks to form in the ceramic tile, beginning at the hole and extending radially away from the joint. An investigation into the cause of these cracks concluded that a mismatch of the inplane tensile strains caused by compressive forces led to hoop stresses in the ceramic tile. A finite element analysis determined the magnitude of these stresses; however, they did not exceed the tensile strength of the ceramic tile. The stresses were found to be on the same magnitude providing validity to the model, and leading to the belief that fracture strength in the tile was also a function of the size of defects caused by machining. Ceramics are extremely defect-sensitive because of their brittle nature; consequently, any type of machining is expected to result in minor imperfections, reducing the strength to cause fracture. To resolve this problem, the torque used for the remainder of the stress relaxation tests was reduced to 80 ft-lbs. Subsequent tests at the revised torque level displayed no evidence of radial cracking.

Four different relaxation tests were conducted with the washer load cell to measure the total stress relaxation over the first hour following tightening. The first test substituted a solid piece of steel for the DCCS Structure to measure the relaxation of the mechanical joint. The total relaxation of the mechanical components (embedment, thread slippage, creep, settling, etc.) was approximately 3 – 4 percent after one hour. The second test measured the relaxation of the DCCS Structure. This baseline test resulted in stress relaxation of approximately 8 – 9 percent after the first hour. A third test incorporated the use of Loctite, a thread sealant, to prevent thread slippage over time. There was very little difference in relaxation between this test and the baseline relaxation test of the DCCS Structure, with an average stress relaxation of 7 – 10 percent after one hour. Short-term relaxation was the primary focus of this study, negating the primary benefits of Loctite, which is most effective against fatigue and vibration loads over the long-term. Despite not demonstrating major benefits over the short-term, Loctite may still be advantageous for the prospect of reducing long-term relaxation. The final relaxation test called for an initial torque to the baseline of 80 ft-lbs, followed by a secondary torque after five minutes, to the same 80 ft-lb torque level. This resulted in a total relaxation of 3 – 4 percent over the first hour. This can be explained by Figure 4.30, where re-torquing the joint increases the total compressive strain at the joint, and reduces the amount of stress that can dissipate before the “rubbery” moduli is achieved.

Comparing the amount of relaxation exhibited by the DCCS Structure in the two experimental tests, the total relaxation after one hour according to the Instron set-up was in the range of 24 – 26 percent, whereas the total relaxation from the washer load cell arrangement was approximately 8 – 9 percent. This discrepancy can be attributed to the time required to apply the clamping force. The Instron set-up applied the force instantaneously, thus allowing for the all the relaxation to occur after clamping. The washer load cell arrangement required the use of a torque wrench, and tightening occurred over the span of several seconds. This time frame allowed for much of the immediate relaxation to occur, thus reducing the total amount of relaxation measured after the tightening concluded.

Collectively, the conclusions from each stress relaxation test provided adequate confirmation for a baseline torque and method of torque to be used through the remainder of this study. An original baseline of 90 ft-lbs of torque was found to be problematic with the introduction of radial stresses in the tile, thus a new baseline of 80 ft-lbs of torque was selected. This reduced the clamping forces and the magnitude of mismatch of in-plane tensile strains, such that hoop stresses at the joint did not cause fracture. Testing various methods of torque determined that the best method to mitigate stress loss was re-torquing the joint within five minutes following the initial torque. This recommendation provided the baseline tightening procedure for all static and fatigue tests performed.

7.2 <u>Bearing in Discontinuous Ceramic Cored Sandwich Structures</u>

The benefits of torque for composite joints has been well documented for thin laminates, however, very little research has been performed comparing pinned and clamped joints in thick, hybrid composite joints. Weidner et al studied various geometric ratios in relation to the DCCS Structure, modifying e/D and w/D ratios before concluding the optimal geometric configuration of e/D = 4.0 and w/D = 8.0. His conclusion was based on obtaining the maximum joint strength with loads applied in the in-plane tensile direction using pinned joints. Given an established geometric pattern, experimental testing was performed on DCCS joints to get a better understanding on the transition from pinned to clamped joints, with a focus on joint strength and stiffness, and the progression of failure.

Tests performed by Weidner et al were repeated to confirm his findings and ensure consistency and repeatability amongst static tests in this study. Static testing was conducted using a double lap test fixture designed by Weidner (see Figure 3.8), using a 4 inch wide by 12 inch long test specimen, machined with a 0.5 inch joint hole positioned at the center of the end tile. The end opposite the joint was milled to a smaller thickness to fit in the Instron grips; the final test configuration can be seen in Figure 3.9. Under pinned joint conditions, the sequence of failure began with net tension failure of the ceramic tile at an average load of 4698 lbs, with subsequent cracks forming over the next 15000 lbs, followed by bending/shear failure in the tile at an average load of 21177 lbs, before failing catastrophically due to delamination and debonding of the constituents at an average load of 28739 lbs. (These failure modes are well-documented in Chapter 5.2 and Appendix F.) Before first failure, the DCCS joint demonstrated relatively linear behavior, exhibiting a stiffness of approximately 1050000 lb/in.

Clamped joint tests were performed on the DCCS Structure with an applied torque of 90 ft-lbs. Due to the variable width of the DCCS Structure, the test fixture was design to accommodate specimens with thicknesses up to 0.94 inches, whereas many specimens left fabrication with thicknesses between 0.90 and 0.92 inches. This resulted in slight gaps between the specimen surface and the side laps of the fixture. Due to the rigidity and stiffness of 17-4 PH stainless steel, it was estimated that 5 – 10 ft-lbs of torque was required to close these gaps, resulting in an effective clamping force equal to approximately 80 ft-lbs, or the recommended torque according to findings from the stress relaxation tests. Clamped joint specimens exhibited the same sequence of failure as pinned joint specimens, beginning with net tension failure of the ceramic tile at an average load of 4427 lbs, bending/shear failure of the tile at an average load of 34462 lbs, and ultimately failure due to delamination/debonding at an average load of 32283. Like the pinned case, clamped joints were nearly linear with an approximate stiffness of 650000 lb/in prior to experiencing net tension failure.

To model the load-displacement curves of the DCCS joint specimens, the Ramberg-Osgood equation was utilized. Typically used to describe the transition between linear and non-linear regions of the stress-strain curve, the equation is slightly modified to illustrate the initial stiffness of the joint (prior to first damage), followed by a secondary stiffness (after first damage). The original Ramberg-Osgood equation is expressed as:

$$\varepsilon = \frac{\sigma}{E} + \alpha \frac{\sigma_0}{E} \left(\frac{\sigma}{\sigma_0}\right)^n \qquad (11)$$

where, ε = strain at a given time, σ = stress at a given time, E = modulus of elasticity of the material, σ_0 = yield stress, and α and n are material constants/parameters.

Revising the above equation to account for the distinct difference in pre- and post-damage material response, results in the following equation:

$$\delta = \left\{\frac{P_0}{k_0}\right\}_{Pre} + \left\{\frac{(P - P_0)}{k_1} + \alpha\frac{P_1}{k_1}\left(\frac{P - P_0}{P_1}\right)^n\right\}_{Post} \tag{12}$$

where, δ = displacement at a given time, P_0 = average load at first damage, k_0 = initial stiffness, P = load at a given time, k_1 = secondary stiffness after first damage, P_1 = load after first damage where non-linearity begins, and α and n are material constants/parameters. These values have been evaluated and fitted for pinned and clamped joint specimens, which can be found in Table 7.1. Figures 7.1 and 7.2 show the load vs. displacement curves of the pinned and clamped joint specimens, respectively, fitted with a Ramberg-Osgood line to compare the experimental strength with the theoretical plateau strength of the pinned joint.

Table 7.1: Fitting Parameters for Ramberg-Osgood Relationship

Fitting Parameters	k_0 (lb/in)	P_0 (lbs)	k_1 (lbs/in)	P_1 (lbs)	α ( )	n ( )
Pinned	1050000	4250	650000	1000	5.0×10^{-6}	4.95
Clamped	650000	4250	400000	1000	1.1×10^{-6}	5.00

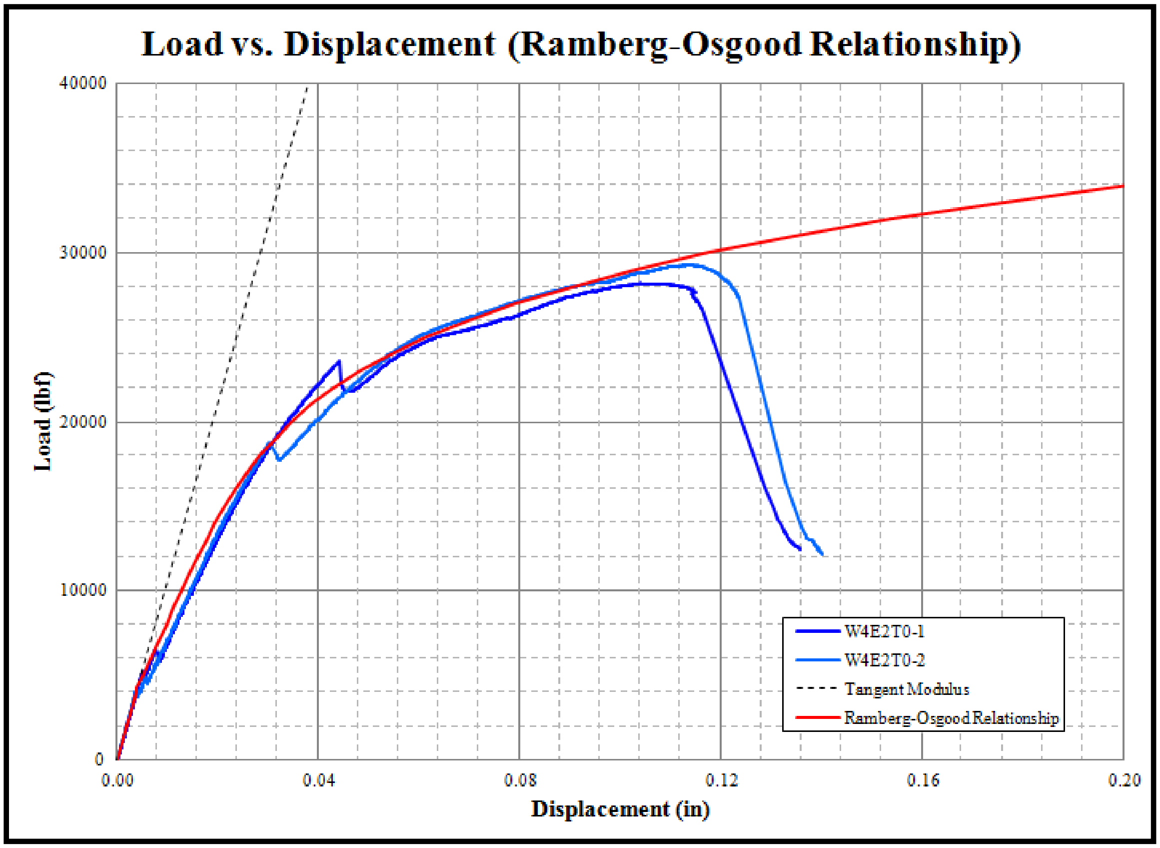

Figure 7.1: Ramberg-Osgood Relationship (Pinned)

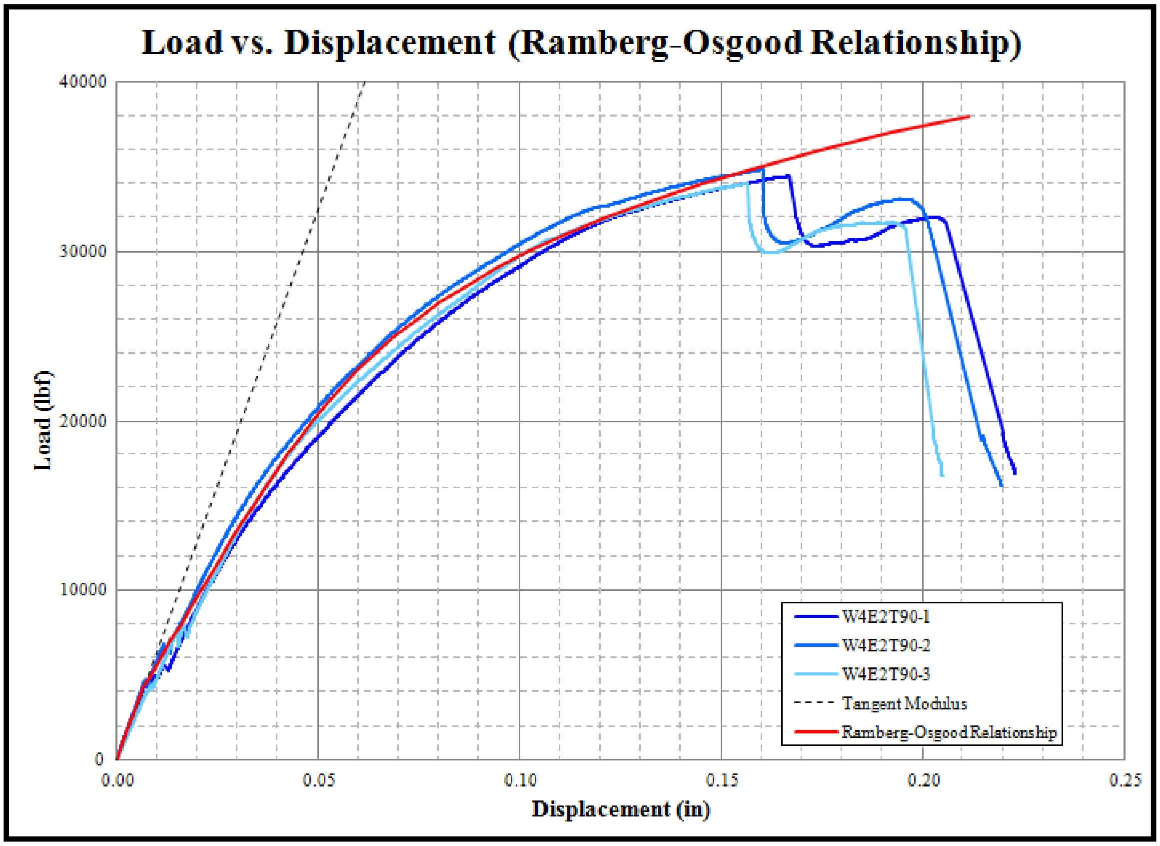

Figure 7.2: Ramberg-Osgood Relationship (Clamped)

There are several notable differences between the pinned and clamped joint specimens, beginning with the joint stiffness when no damage is present. Introducing clamping forces at the joint resulted in nearly a 50 percent reduction in joint stiffness, which was a direct result of the yielded interlayer. In pinned joints, the majority of the bearing load was transferred from the face sheet through the interlayer into the ceramic tile. Consequently, the DCCS Structure had a stiffness that closer resembled the ceramic tile than the face sheet. Under clamped joint conditions, the compressive forces caused the interlayer to yield, inhibiting some of the bearing load from being transferred from the face sheet, and allowing the bearing load to be more evenly shared between the face sheet and ceramic tile. In doing this, the stiffness of the DCCS Structure falls somewhere between the stiffness of the ceramic tile and face sheet, but significantly less than that exhibited in the pinned joint.

Another difference between the pinned and clamped joint tests was the strength at which bending/shear failure occurred in the ceramic tile. Clamped joints experienced bending/shear failure at a strength over 50 percent greater than that in pinned joints. Like the change in stiffness described earlier, the yielded interlayer was the primary cause of this change in failure strength. In the pinned case, the majority of the bearing load is transferred from the face sheet into the ceramic tile; after net tension failure, the top half of the ceramic tile begins to bend due to the applied bearing load at the center of the tile, ultimately leading to bending/shear failure. At this time in the pinned joint, the face sheet is carrying very little of the bearing load, except for tensile stress in the regions of ±90° where the ceramic tile has failed due to net tension. In clamped joint specimens, the yielded interlayer reduces the amount of bearing load transferred into the ceramic tile, reducing the stress in the tile to cause bending/shear failure. Because the tile carries a lower percentage of the total bearing load, it takes a larger overall load for the tile to reach the critical stress that causes bending/shear failure.

The location of the peak strength during the progression of failure also varies between pinned and clamped specimens. Following bending/shear failure in pinned specimens, loading in the specimen recovered beyond the strength to cause that failure, gradually losing stiffness until the loading nears its' strength plateau, before failing in delamination/debonding. In clamped specimens, bending/shear failure occurs at much higher strengths than pinned specimens, however, after this failure, loading does not recover and ultimately fails before achieving bending/shear failure strength. This transition becomes important depending on the method of loading; experimental tests were performed under displacement-controlled conditions, allowing for the load to drop off when energy is released during bending/shear failure. Under load-controlled conditions, bending/shear failure would cause a jump in the displacement, without any drop in load. Pinned specimens would continue to taking on additional load before ultimate failure, whereas clamped specimens would provide higher strengths but also exhibit bending/shear and delamination/debonding failure simultaneously. This type of catastrophic failure may want to be avoided depending on the parameters of the designer. To better define this transition of the peak strength location, several other torque levels were examined.

Torque levels of 10, 30, 50, 70 and 110 ft-lbs were tested to compare to the data collected from the baseline torque case. (Recall, all torque levels are effectively 5 – 10 ft-lbs less than the measured torque due the clamping force required to tighten the side laps of the test fixture.) Design charts pertaining to each failure mode were created to compare all torque specimens, beginning with net tension failure of the ceramic tile (Figure 7.3), bending/shear failure of the ceramic tile (Figure 7.4), and delamination/debonding of the face sheet, interlayer and tile (Figure 7.5). The magnitude of torque appeared to have very little effect on the strength at net tension failure. The average strength at net tension failure of all torqued specimens was 4252 lbs, with the majority of all specimens falling within one standard deviation of the mean. A few specimens failed prematurely, leading to the conclusion that the quality of the machined joint and the size of potential imperfections on the joint surface had a significant impact on when fracture occurred in the tile. Theoretically, larger defects lead to lower fracture stresses, while fewer, smaller defects allow for optimal strength. In order to successfully conclude whether torque magnitude effects joint strength at net tension failure, machining needs to be controlled for more precision to produce pristine joints, allowing for optimum strength at the joint. The baseline torque and pinned results provided sufficient evidence that the magnitude of torque directly affected the strength of bending/shear failure. According to the design chart, bending/shear strength increased linearly with an increase in torque (mean strength of 29180 lbs for 10 ft-lbs, 30253 lbs for 30 ft-lbs, 31841 lbs for 50 ft-lbs, 33421 lbs for 70 ft-lbs, 34462 lbs for 90 ft-lbs), before reaching the approximate plateau strength in the range of 35000 lbs, determined in part because specimens tested at 110 ft-lbs exhibited catastrophic failure (bending/shear and delamination/debonding failure occurred simultaneously). Using an approximate linear fit line of the failure strengths for specimens tested between 10 and 90 ft-lbs, and a horizontal plateau at the failure strength of 110 ft-lbs, the torque to achieve optimal joint strength is found to occur at 95 ft-lbs. Due to the fact that torque levels of 110 ft-lbs exhibited catastrophic behavior and torque levels of 90 ft-lbs continued to demonstrate progressive failure, this precise transition lies somewhere in between. Erring on the side of caution, it is recommended for design that torque levels not exceed 90 ft-lbs (an effective torque of 80 ft-lbs), with respect to bending/shear failure. The design chart for ultimate failure demonstrated no notable correlation between failure strength and magnitude of torque. One note that can be drawn from the chart is related to the variability of failure strength at the torque level of 50 ft-lbs. It was found that 50 ft-lbs was the transition point between the peak strength occurring immediately before ultimate failure and delamination/debonding (torque levels less than 50 ft-lbs) and peak strengths occurring at bending/shear failure (torque levels greater than 50 ft-lbs). When delamination/debonding failure initiates prior to bending/shear failure, the release of energy expedites the final failure mode, reducing ultimate failure strength. If bending/shear failure occurs prior to the commencement of delamination/debonding, ultimate failure strength tends to occur at a greater failure strength relative to the other scenario. Due to the amount of torque and clamping force applied at the joint, delamination and debonding is suppressed at the joint, even if debonding has initiated along the top edge of the specimen. Increased clamping force allows for more loading to exist prior to bending/shear failure, and conversely, more debonding; however there is also a greater amount of suppression at the joint, therefore always allowing bending/shear failure to occur prior to/or simultaneously with delamination/debonding.

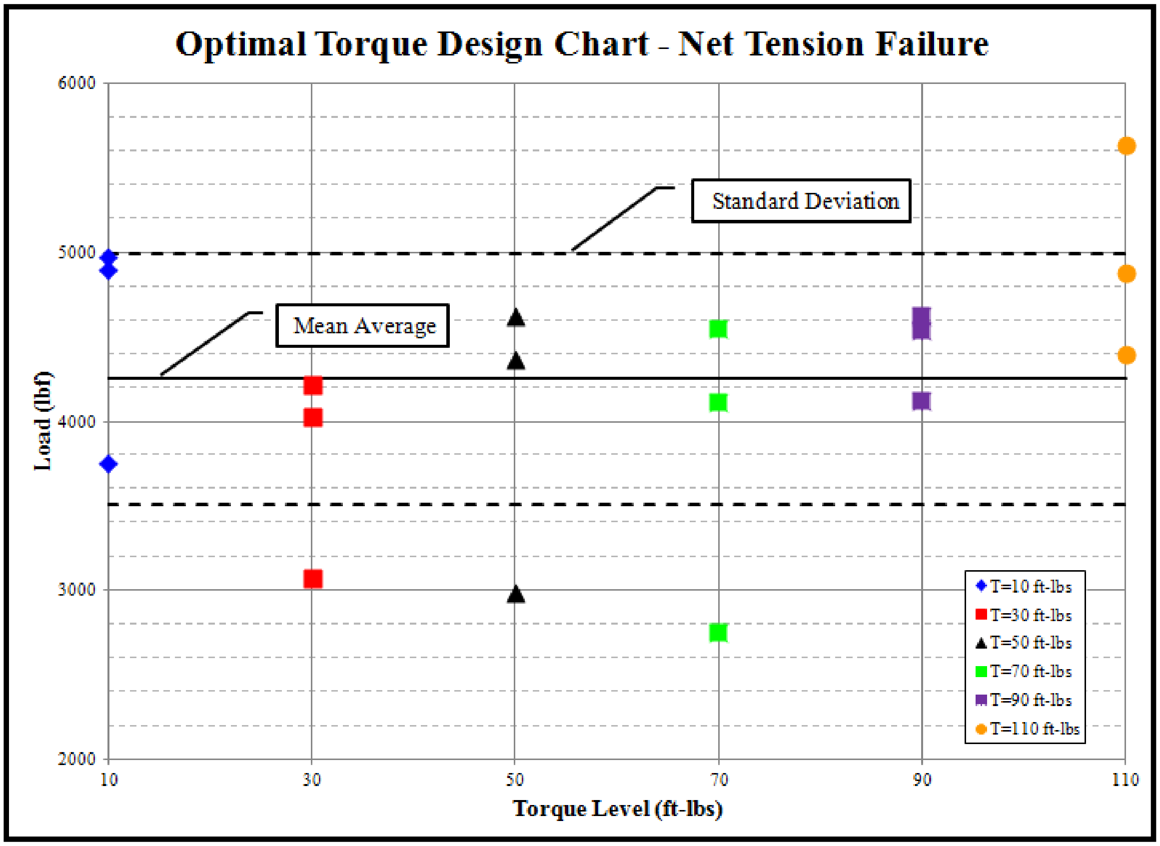

Figure 7.3: Torque Design Chart – Net Tension Failure Mode

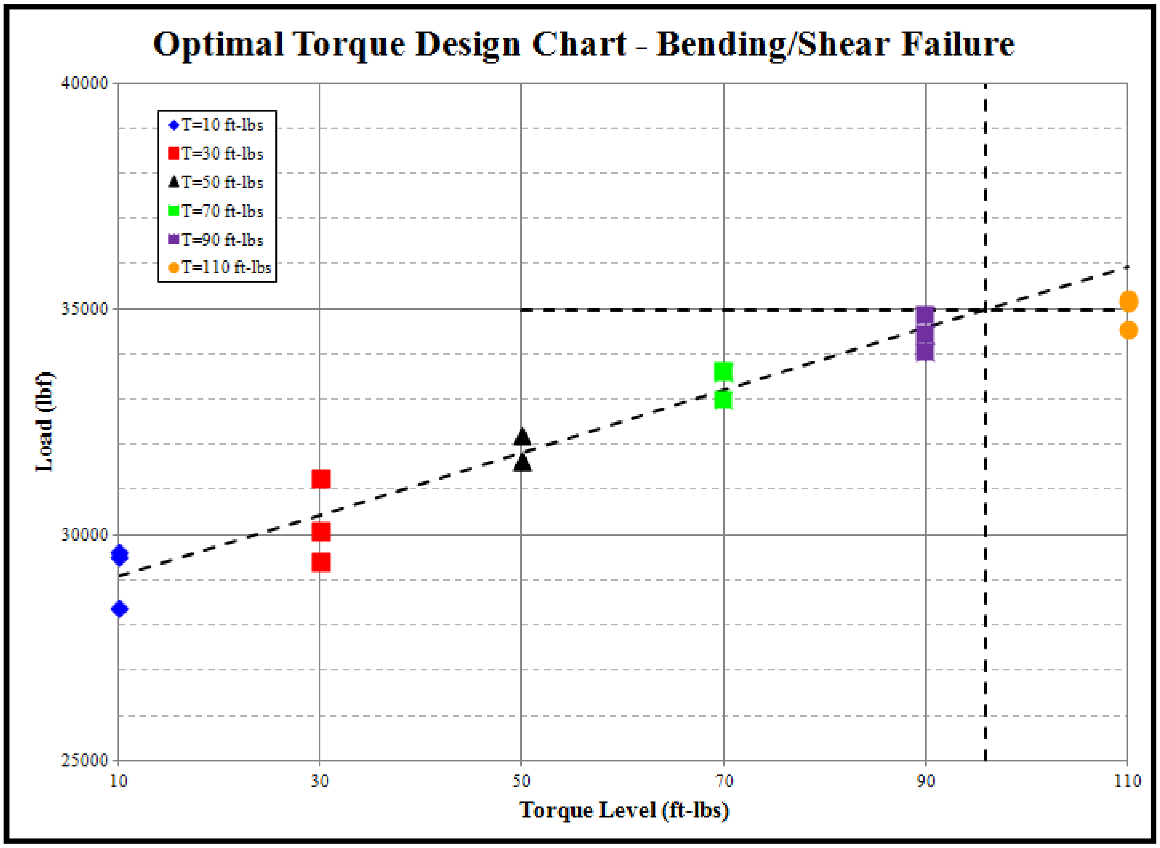

Figure 7.4: Torque Design Chart – Bending/Shear Failure Mode

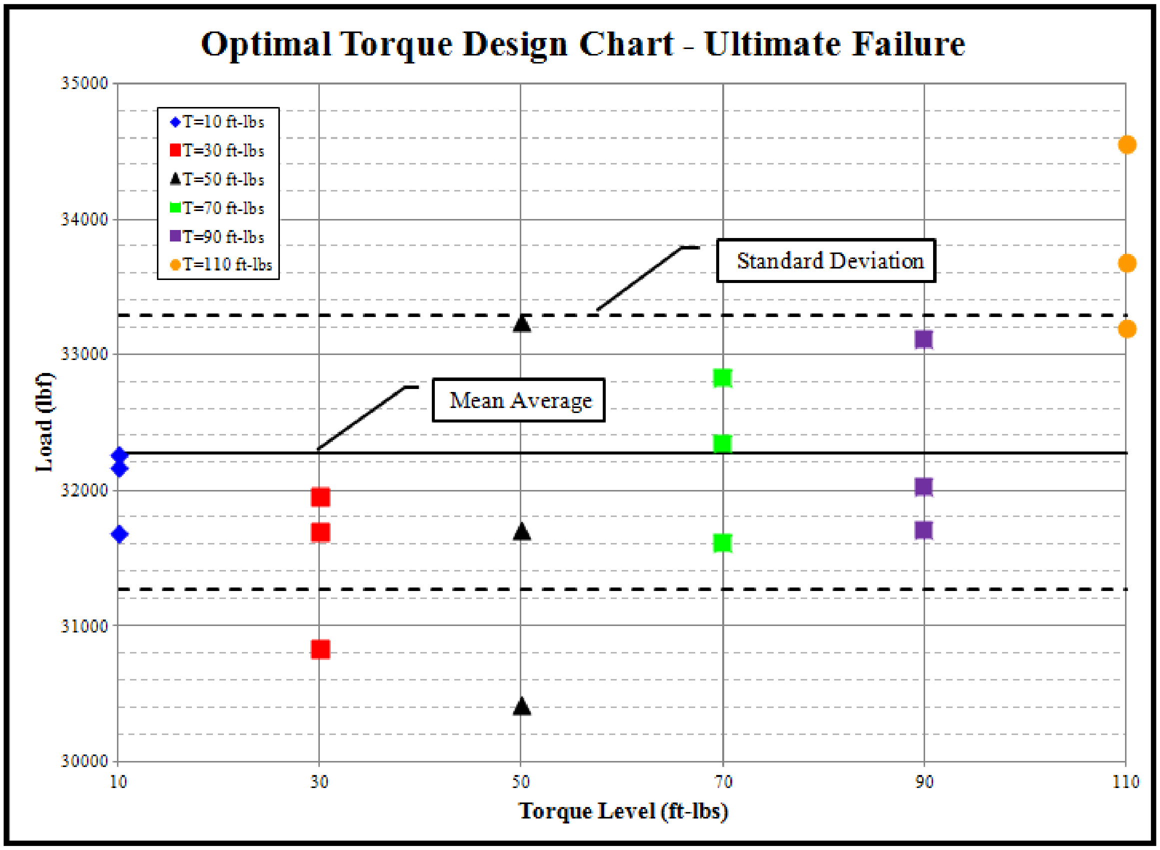

Figure 7.5: Torque Design Chart – Ultimate/Delamination Failure Mode

Collectively, the design charts can be used to select the appropriate torque according to the required design parameters. For joints designs requiring the maximum strength available, with no concern of failure mode or sequence, an effective torque greater than 85 ft-lbs provides approximately 35000 lbs of strength. For joint designs requiring the maximum strength with progressive failure (non-catastrophic, based on displacement-controlled loading), the optimal effective torque would be in the range of 75 – 85 ft-lbs, providing 34000 – 35000 lbs of strength. If a design calls for progressive failure based on load-controlled loading, the effective torque would be required to be less than 40 ft-lbs, resulting in an overall joint strength of 32000 lbs. Static experimental testing established a valuable design tool for optimizing the joint by selecting the appropriate torque according to design parameters. Fatigue testing will further develop the joint design methodology of the DCCS Structure.

7.3 <u>Fatigue on Discontinuous Ceramic Cored Sandwich Structures</u>

Evaluating joint performance under fatigue loading is an integral component of the design process. Repetitious loading patterns are common in many structural applications, and understanding the degradation of the composite joint that takes place during these situations will allow for adequate measures to be taken to reduce the risk of premature failure and strength loss. Using the same experimental set-up and test fixture used for static testing, the DCCS Structure was tested at various fatigue levels. The fatigue levels were broken into two categories: high level fatigue stresses, which were determined as a given percentage of the minimum load to cause failure in the DCCS Structure; and low level fatigue stresses, determined based on a given percentage of the minimum load to cause first damage at the joint. A total of five stress levels were established for each category. Each specimen tested was evaluated using visual inspection, calculating the stiffness loss according to the tangent modulus at zero load/zero displacement and the secant modulus over the respective fatigue load range, and performing a static test following one million cycles of fatigue to determine the residual strength of the specimen.

High level stresses exhibited a wide range of results, as can be expected given the magnitude of the fatigue loads. Stress Level 5 (max/min – 25600/2560 lbs) and Stress Level 4 (max/min – 20480/2048 lbs) led to ultimate failure of the DCCS Structure in the early stages of fatigue life. Stress Level 3 (max/min – 15360/1536 lbs) was terminated after failure of the bolt due to bending stresses combined with the initial preload due to torque. Stress Level 2 (max/min – 10240/1024 lbs) and Stress Level 1 (max/min – 5120/512 lbs) both achieved one million cycles, though Stress Level 2 experienced bolt failure in two cases. Figure 7.6 shows the fatigue life for the DCCS Structure and Grade 8 bolt, which are seen to cross between Stress Level 3 and 4. This diagram allows for the mode of joint failure to be identified, depending on the fatigue stress level. Ideally in design, only failure mode exists, either the fastener or the joint. In this case, the recommended maximum fatigue design levels will be between Stress Level 2 and Stress Level 3, where only bolt failure is a factor.

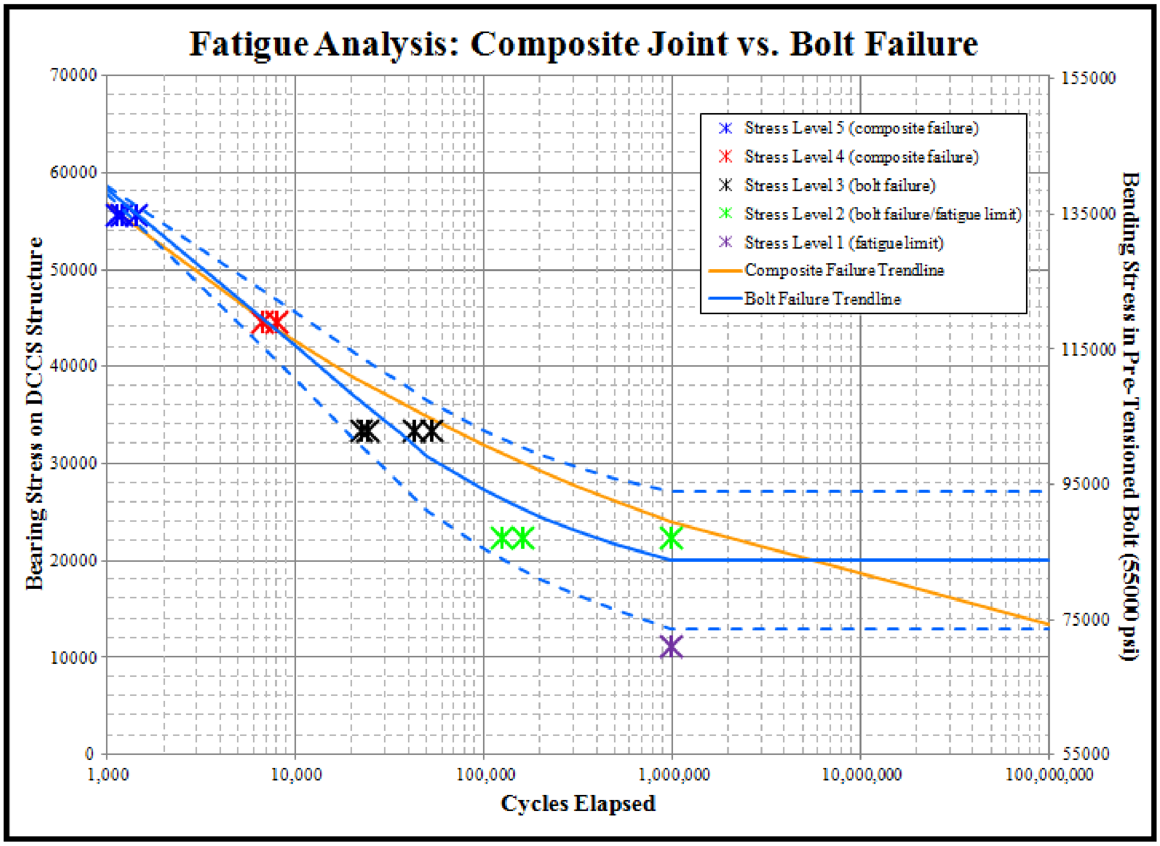

Figure 7.6: DCCS Joint Failure vs. Bolt Failure

All specimens tested at low level stresses, conducted at fatigue loads below the minimum load to cause first damage, achieved one million cycles without visible damage to any specimen. Stress Level 5 (max/min – 3400/340 lbs) experienced notable stiffness loss and demonstrated noticeable differences compared to non-fatigued specimens in residual strength tests. Stress Level 4 (max/min 2720/272 lbs) did not exhibit stiffness loss, though there remained some differences between the load-displacement curve of the residual strength test and non-fatigued tests. Stress Level 3 (max/min – 2040/204 lbs) did not show any stiffness or residual strength loss, consequently negating the need to test Stress Level 2 (max/min – 1360/136 lbs) and Stress Level 1 (max/min – 680/68 lbs).

The use of the tangent modulus as a method of measuring stiffness loss was found to provide very limited information on the overall fatigue resistance of the joints. Typically, the tangent modulus, when taken at zero load/zero displacement, only provides value when fatigue loads are small. However, for large fatigue load ranges, the secant modulus provides a better indication on the losses over the course of ongoing fatigue. Stiffness according to the tangent modulus was highly variable from one specimen to the next, but it did indicate that at high level stresses where net tension cracks in the ceramic tile are present, the initial stiffness was greatly reduced compared to non-fatigued specimens, and specimens fatigued at low level stress where no damage is present. The secant modulus over the fatigue load range at each stress level provided the most valuable stiffness data for design considerations. Figure 7.7 plots the stiffness loss versus the maximum fatigue load, beginning with the Low Stress Level 4, where little to not stiffness loss was documented, and ending with High Stress Level 2, which was the greatest fatigue load that completed all one million cycles. This chart can be used to estimate the appropriate fatigue levels when designing for an allowable stiffness loss. Taking this concept to full design, Table 7.2 incorporates stiffness loss/fatigue levels with safety factors and design loads to create a cumulative design chart. (Design loads are based on the average peak strength of DCCS Specimens with 80 ft-lbs of torque.) A designer can use this chart to select the design load and design fatigue load based on predetermined values for allowable stiffness loss and safety factor. Establishing a design table significantly simplifies the design process. However, this design table is limited to the joint parameters established earlier in this study. There are several alternative measures that can be taken to improve joint strength, along with additional loading conditions that can be tested to provide a better understanding of the performance of bolted joints in Discontinuous Ceramic Cored Sandwich Structures.

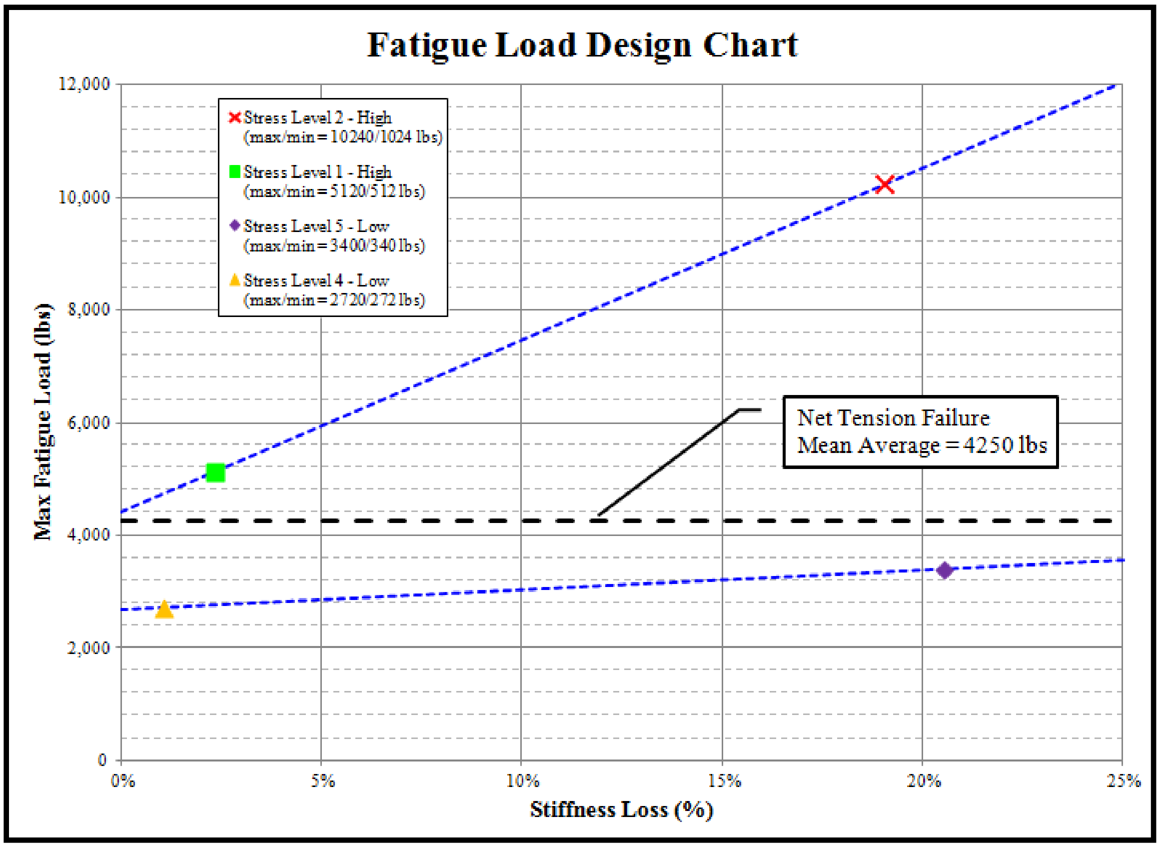

Figure 7.7: Fatigue Load Design Chart

Table 7.2: Fatigue Design Table – Design Load (lbs) and Max/Min Fatigue Load (lbs)

	Allowable Stiffness Loss (%)	Safety Factor[6] 1	1.5	2	2.5	3
Stress Levels prior to first damage (net tension failure)	0	34462	22975	17231	13785	11487
		2682/268	2682/268	2682/268	2682/268	2682/268
	5	34462	22975	17231	13785	11487
		2857/285	2857/285	2857/285	2857/285	2857/285
	10	34462	22975	17231	13785	11487
		3032/303	3032/303	3032/303	3032/303	3032/303
	15	34462	22975	17231	13785	11487
		3207/320	3207/320	3207/320	3207/320	3207/320
	20	34462	22975	17231	13785	11487
		3381/338	3381/338	3381/338	3381/338	3381/338
	25	34462	22975	17231	13785	11487
		3556/355	3556/355	3556/355	3556/355	3556/355
Stress Levels after first damage (net tension failure)	5	34462	22975	17231	13785	11487
		5928/592	5928/592	5928/592	5928/592	5928/592
	10	34462	22975	17231	13785	11487
		7459/745	7459/745	7459/745	7459/745	7459/745
	15	34462	22975	17231	13785	11487
		8990/889	8990/889	8990/889	8990/889	8990/889
	20	34462	22975	17231	13785	11487
		10521/1052	10521/1052	10521/1052	10521/1052	10521/1052
	25	34462	22975	17231	13785	11487
		12052/1205	12052/1205	12052/1205	12052/1205	12052/1205

[6] Design Load based on Ultimate Joint Strength of 34462 lbs for torque of 80 ft-lbs

7.4 <u>Directions Toward Future Work</u>

The current work performed on Discontinuous Ceramic Cored Sandwich Structures focused on the performance of pinned and clamped joints exposed to bearing and in-plane tensile loading conditions. Testing originally began with pinned joints to provide a basic understanding of failure modes and stress interactions in the DCCS Structure. However, the use of pinned joints was not a realistic method of fastening composite panels for their desired applications. The progression to clamped joints provides the necessary stability and support to mount the composite panels, but required further experimental testing to distinguish the difference in damage evolution and stress distribution from the pinned joint.

The conclusions and recommendations gathered from this study provide the groundwork for other methods of testing the DCCS Structure, primarily, transverse loading of the joints in the form of three-point bend testing. This method of testing transverse loads was initiated in conjunction with the current study and consisted of testing various support conditions (simple, pinned, and clamped) both statically and in fatigue. Figure 7.8 is a rendering of the test fixture designed specifically to allow pinned and clamped joint conditions, of which there was no specific ASTM Standard that described a fixture for such testing. Further testing remains to be completed using this test fixture, including four-point bend tests and dynamic impact testing. Also, a finite element model of the DCCS Structure has yet to incorporate the specific loading and support conditions exhibited with this experimental set-up. Studying bending of the DCCS Structure and transverse loading of the joint offers an alternative design perspective to tensile/bearing loading of the joint.

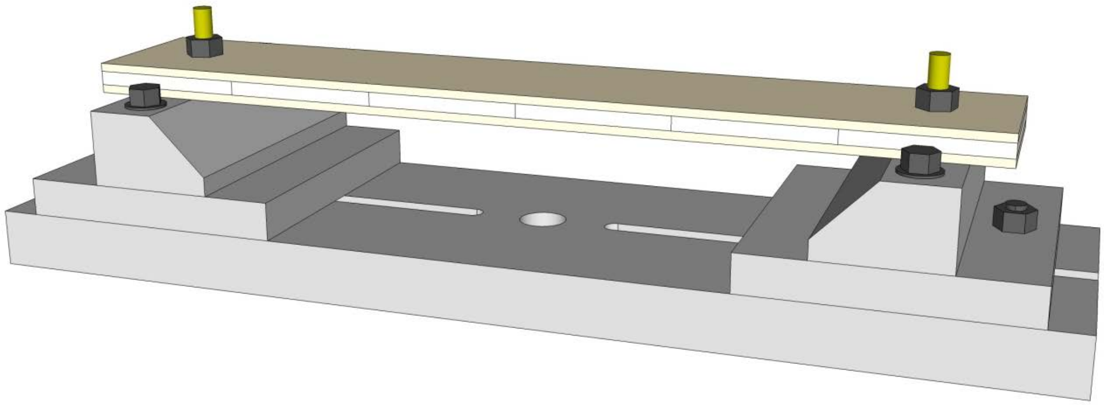

Figure 7.8: Test Fixture for Transverse Loading of DCCS Joint

Another consideration is the use of metallic inserts at the joint. Extensive research has been performed on the use of inserts for composite joints; however the majority has focused solely on thin laminates. Due to the complex nature of the DCCS Structure, the wide range of strength and stiffness properties of the constituents, and the overall thickness of the structure, experimental testing of the joint with the insert is necessary to verify that the presence of the insert is beneficial to the performance of the joint. Two of the major proponents to the inclusion of metallic inserts suggested by prior research are that they are much more effective in distributing and redistributing stresses with progressive loading, and they provide protection to the joint and reduce the likelihood of damage often prone to occur when fastener components are replaced on a frequent basis. These specific characteristics can be observed with experimental testing, in addition to monitoring changes in joint strength, stiffness, and failure progression, to better determine the effective of metallic inserts. (Figure 7.9 shows what a metallic insert may look like in the DCCS Structure;

details of the insert, including wall thickness, tapered vs. non-tapered edges, bonding agents, and the selection of the metal may all be investigated).

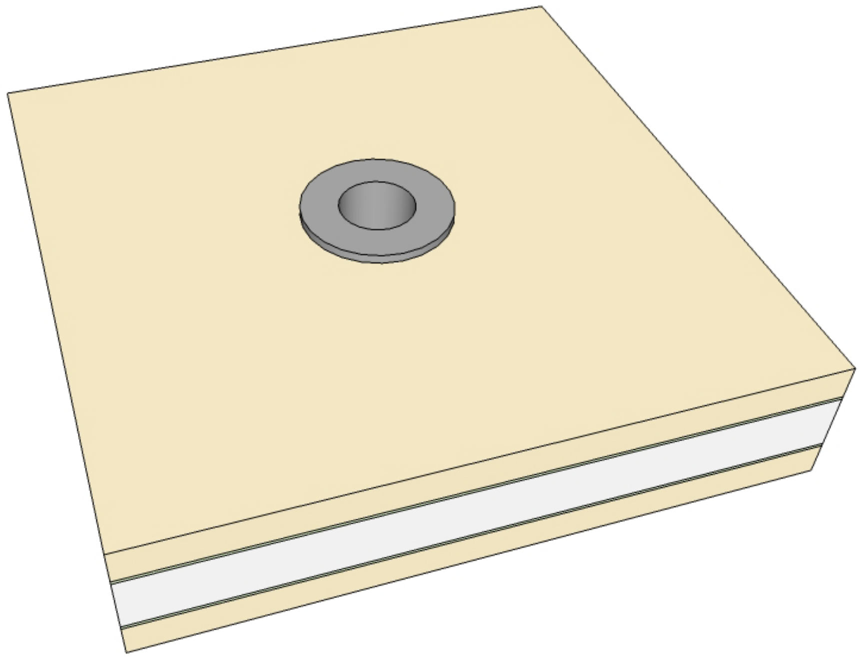

Figure 7.9: Metallic Insert in DCCS Joint

The recommendations provided in this study, along with further investigation into the joint regarding various loading conditions, analytical models, and metallic inserts, will provide valuable information in optimizing the efficiency and performance of joints in Discontinuous Ceramic Cored Sandwich Structures.

REFERENCES

"3 Dimensional Woven Fabrics." 3Tex Incorporated, Cary, NC. (2007) <http://www.3tex.com/node/3>

Banea, M. D., and L. F. M. da Silva. "Adhesively bonded joints in composites: an overview." *Proceedings of the Institution of Mechanical Engineers, Part L: Journal of Materials Design and Applications* 223 (2009): 1 – 18.

Bickford, John H. *An Introduction to the Design and Behavior of Bolted Joints*. Marcel Decker. New York, NY, (1974).

Bolick, Ronnie. "Composite fabrication via the VARTM process." Triangle Polymer Technologies, Inc/North Carolina A&T State University: STTR N064-040-0400. 1 – 7.

Camanho, P.P. and M. Lambert. "A design methodology for mechanically fastened joints in laminated composite materials." *Composites Science and Technology* 36 (2006): 3004 – 3020.

"Ceramic Armor." CoorsTek, Inc., Golden, CO. (2006) <http://www.coorstek.com/resources/8510-1091_Ceramic_Armor.pdf>

Echaabi, J., M.B. Nziengui, and M. Hattabi. "Compressibility and relaxation models for fibrous reinforcements in Liquid Composites Moulding." *International Journal of Material Forming* 1 (2008): 851 – 854.

Gawandi, Anis, Leif A. Carlsson, Travis A. Bogetti, and John W. Gillespie Jr. "Mechanics of discontinuous ceramic core sandwich structure: Influence of thermal and interlaminar stresses." *Composite Structures* 92 (2010): 164 – 172.

Gillespie Jr., John W. Class Lecture. Experimental Mechanics. University of Delaware, Newark, DE.

Gillespie Jr., John W. and Chris Arvanitelis. "Mechanical Properties of S-2 Glass 3Weave fabric 8084 Vinyl Ester Composites." University of Delaware: Center for Composite Materials. Newark, DE. (2007): 1 – 123.

Gillespie Jr., John W, Leif A. Carlsosn, Anis A. Gawandi, and Travis A. Bogetti. "Fatigue crack-growth at the face sheet-core interface in a discontinuous ceramic-tile cored sandwich structure." *Composite Structures* (2012).

Hou, Li, and Dashin Liu. "Size Effects and Thickness Constraints in Composite Joints." *Journal of Composite Materials* 37 (2003): 1921 – 1938.

Huang, X.G., J. W. Gillespie Jr., V. Kumar, and L. Gavin. "Mechanics of integral armor: discontinuous ceramic-cored sandwich structure under tension and shear." *Composite Structures* 36 (1996): 81 – 90.

Khashaba, U.A., H.E.M Sallam, A.E. Al-Shorbagy, and M.A. Seif. "Effect of washer size and tightening torque on the performance of bolted joints in composite structures." *Composite Structures* 73 (2006): 310 – 317.

Mahdi, S., B.A. Gama, S. Yarlagadda, and J.W. Jr. Gillespie. "Effect of the manufacturing process on the interfacial properties and structural performance of multi-functional composite structures." *Composites Part A: applied science and manufacturing* 34 (2003): 635 – 647.

Manzella, A.F., B.A. Gama, J.W. Gillespie Jr. "Effect of punch and specimen dimensions on the confined compression of S-2 glass/epoxy composites." *Composite Structures* 93 (2011): 1726 – 1737.

McCarthy, M.A., V.P. Lawlor, W.F. Stanley, and C.T. McCarthy. "Bolt-hole clearance effects and strength criteria in single-bolt, single-lap, composite bolted joints." *Composite Science and Technology* 62 (2002): 1415 – 1431.

Riccio, A. and L. Marciano. "Effects of Geometrical and Material Features on Damage Onset and Propagation in Single-Lap Bolted Composite Joints under Tensile Load: Part I – Experimental Studies." *Journal of Composite Materials* 39 (2005): 2071 – 2090.

Roylance, David. "Engineering Viscoelasticity." Massachusetts Institute of Technology: Department of Materials Science and Engineering. Cambridge, MA. (2001): 1 – 37.

Sen, F. and O. Sayman. "The influences of geometrical parameters on the failure response of two serial pinned/bolted composite joints." *Journal of Materials: Design and Application* 233 (2009): 169 – 181.

Steiner, Karl V., Rushad F. Eduljee, Xiaogang Huang, and John W. Gillespie Jr. "Ultrasonic NDE Techniques for the Evaluation of Matrix Cracking in Composite Laminates." *Composites Science and Technology* 53 (1995): 193 – 198.

Sun, C. T. and P. Wang. "Development of Improved Hybrid Joints for Composite Structures." University of Purdue: Joint Advanced Materials & Structures Center of Excellence. West Lafayette, IN. (2009): 1 – 20.

Thoppul, Srinivasa D., Joana Finegan, and Ronald F. Gibson. "Mechanics of mechanically fastened joints in polymer-matrix composite structures - A review." *Composites Science and Technology* 69 (2009): 301 – 329.

Wang, Michael L., Ian. M. McAninch, and John. J. La Scala. "Materials Characterization of High-Temperature Epoxy Resins: SC-79 and SC-15/SC-79 Blend." U.S. Army Research Laboratory. Aberdeen Proving Ground, MD. (2011): 1 – 26.

Weidner, Kris, John W. Gillespie, Jr. Nicholas Shevchenko. "Performance of bolted joints in Discontinuous Ceramic Cored Sandwich Structures – Static experimental testing." *Composite Structures* 93 (2011): 3175 – 3184.

Whitworth, H.A. "Fatigue Evaluation of Composite Bolted and Bonded Joints." *Journal of Advanced Materials* 30 (1998): 25 – 31.

Yan, Y., W.-D. Wen, F.-K. Chang, and P. Shyprykevich. "Experimental study on clamping effects on the tensile strength of composite plates with a bolt-filled hole." *Composites Part A: applied science and manufacturing* 30 (1999): 1215 – 1229.

Appendix A

DCCS STATIC COMPRESSION TEST GRAPHS

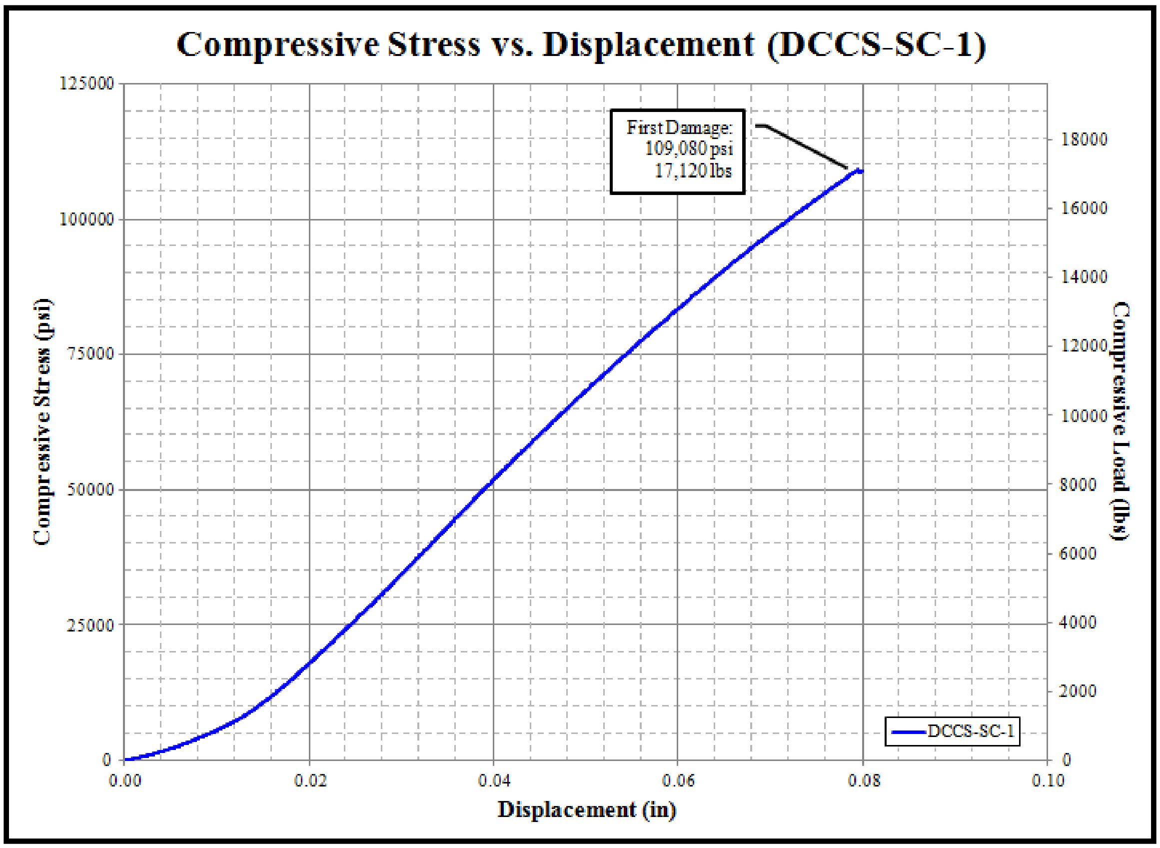

Figure A.1: Compressive Stress vs. Displacement (DCCS-SC-1)

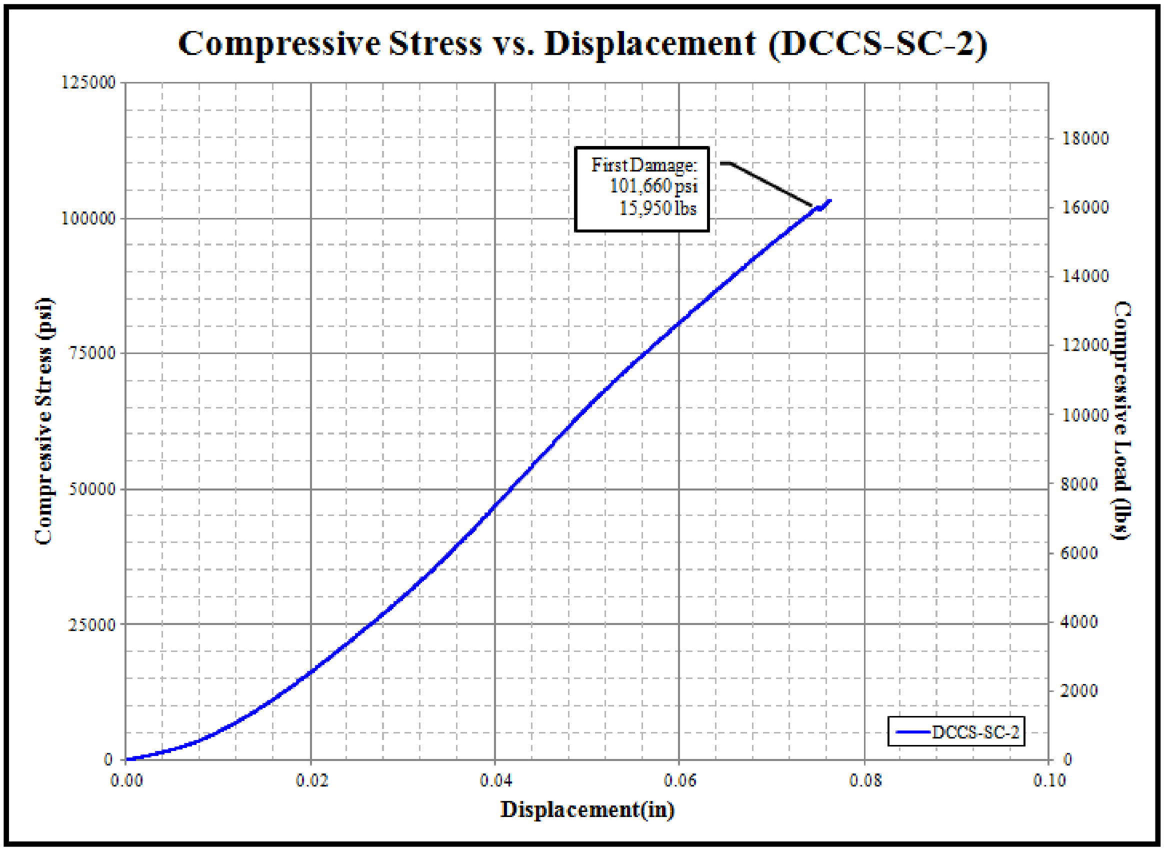

Figure A.2: Compressive Stress vs. Displacement (DCCS-SC-2)

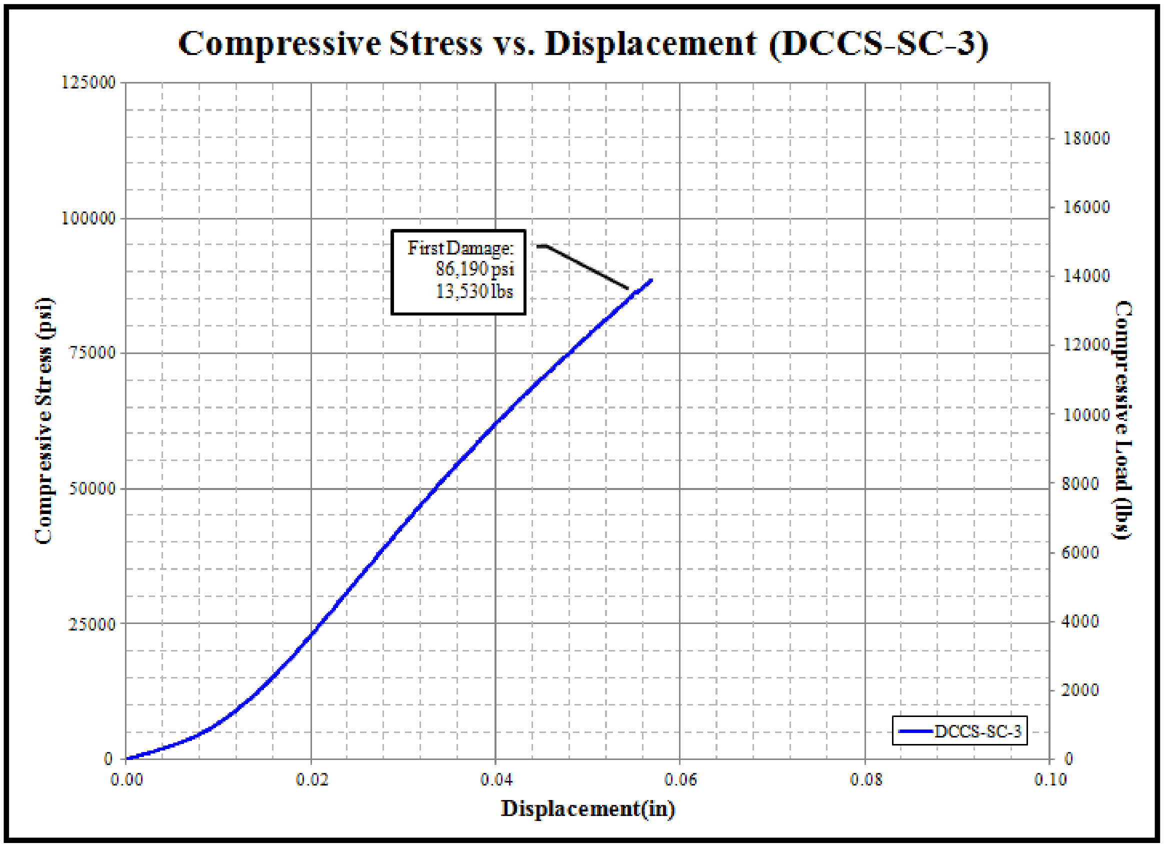

Figure A.3: Compressive Stress vs. Displacement (DCCS-SC-3)

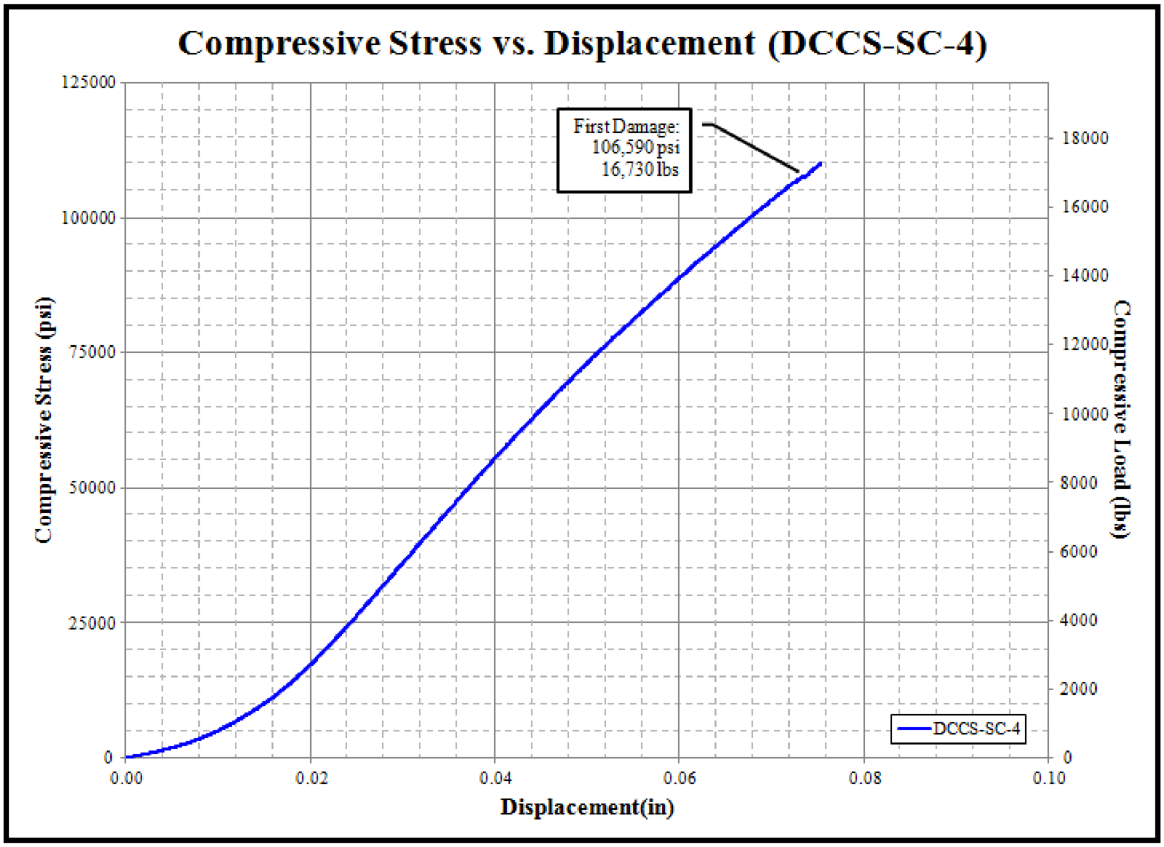

Figure A.4: Compressive Stress vs. Displacement (DCCS-SC-4)

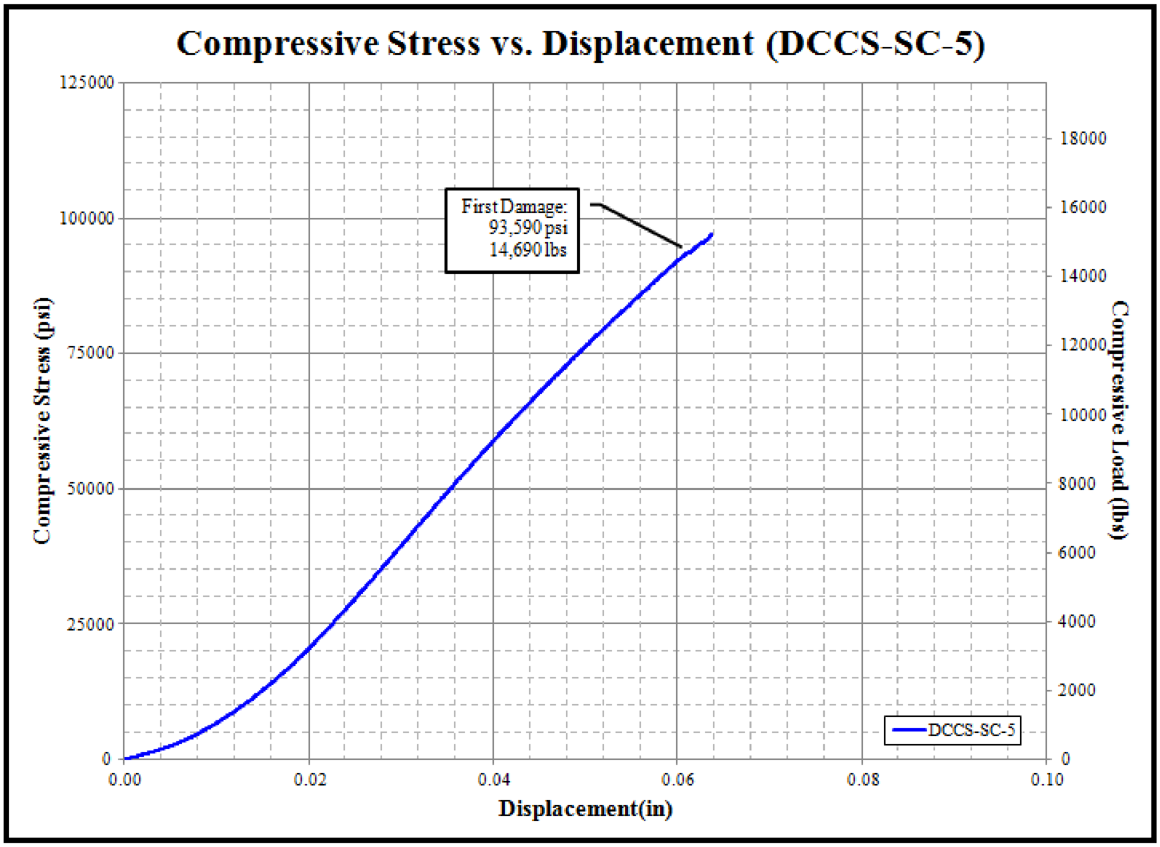

Figure A.5: Compressive Stress vs. Displacement (DCCS-SC-5)

Appendix B

FACE SHEET STRESS RELAXATION TEST GRAPHS

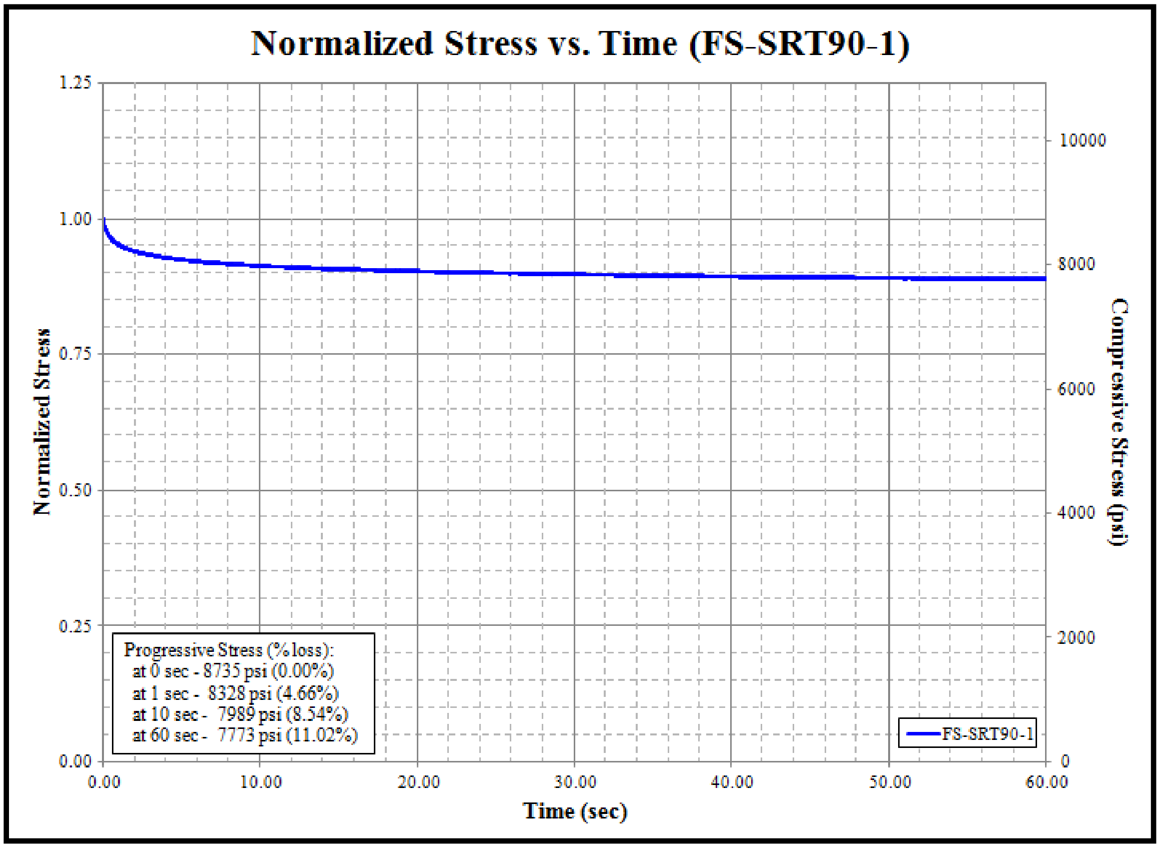

Figure B.1: Normalized Stress vs. Time (FS-SRT90-1)

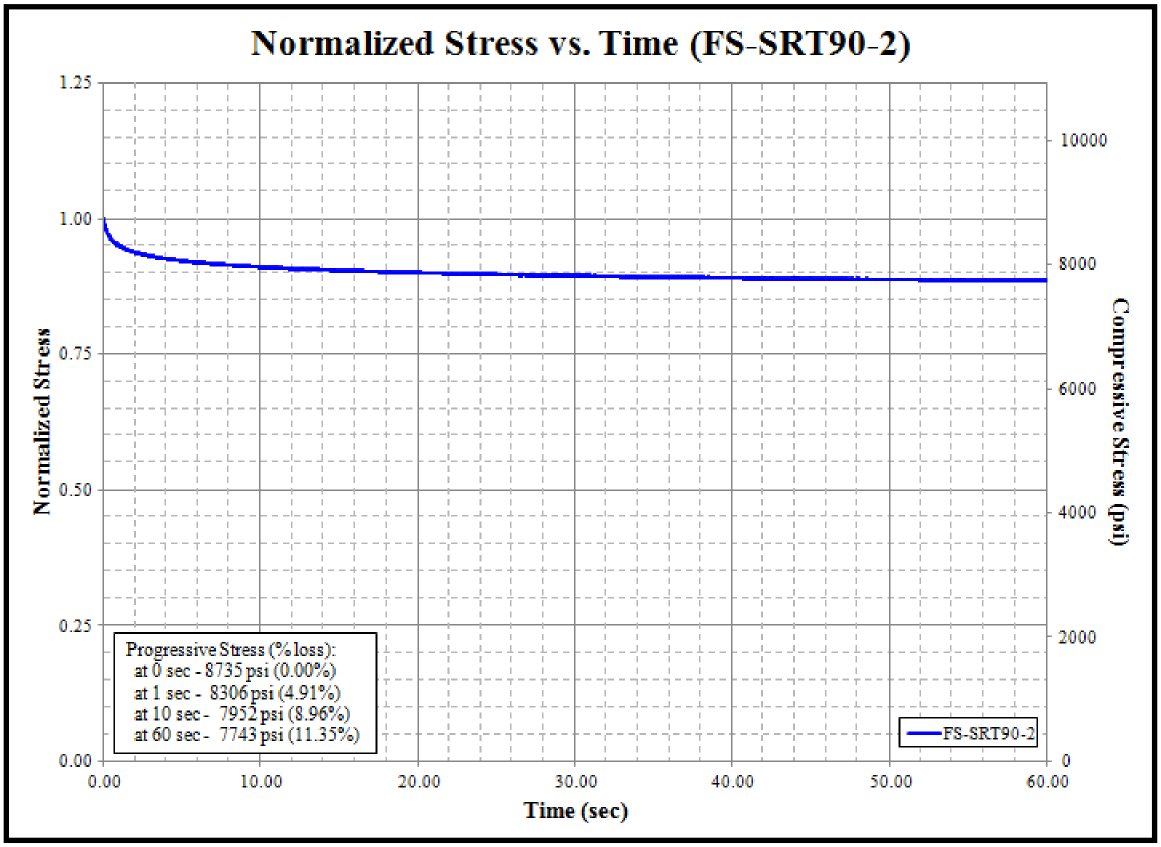

Figure B.2: Normalized Stress vs. Time (FS-SRT90-2)

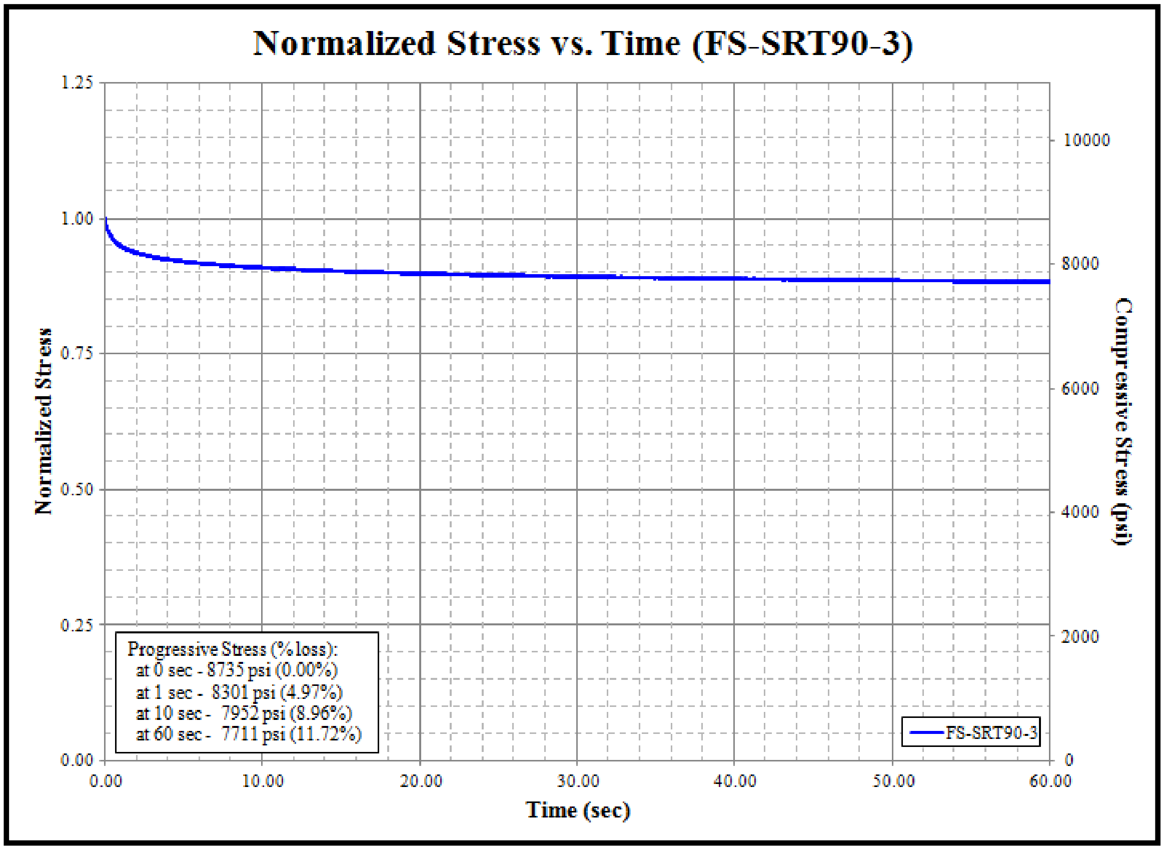

Figure B.3: Normalized Stress vs. Time (FS-SRT90-3)

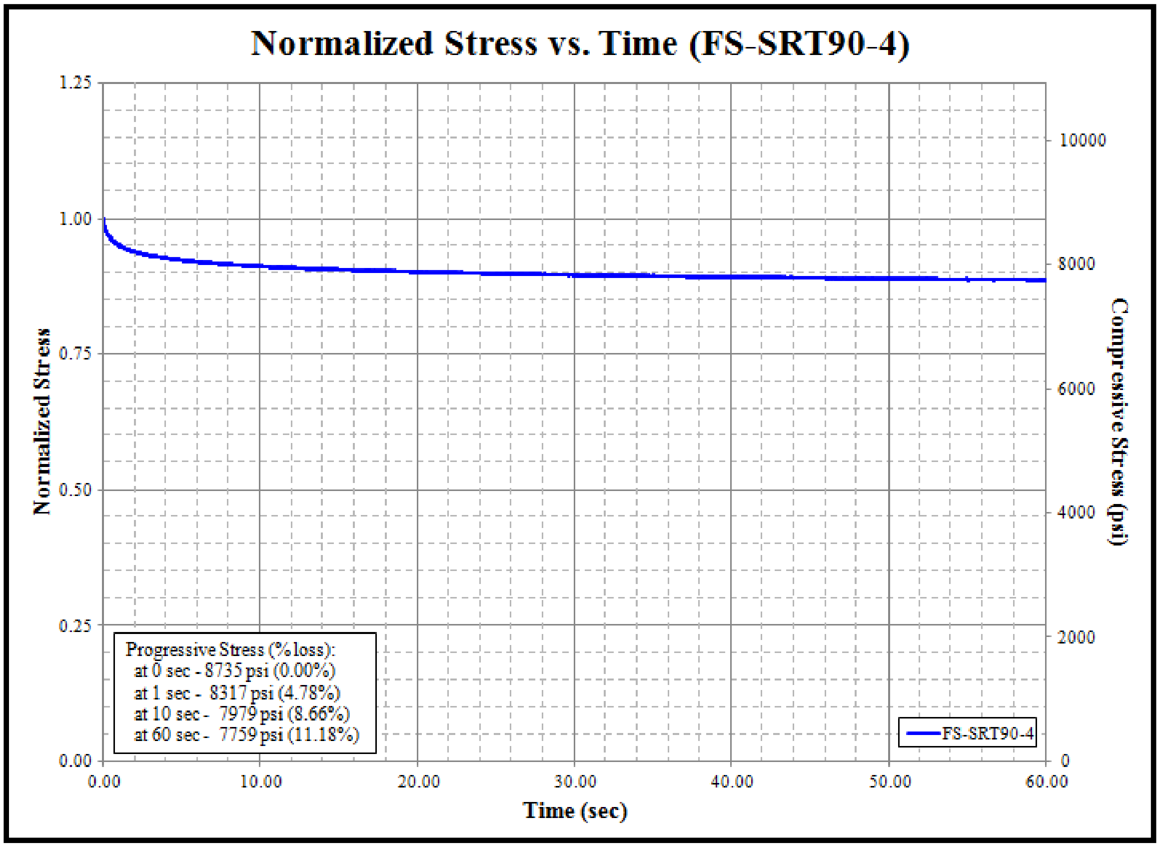

Figure B.4: Normalized Stress vs. Time (FS-SRT90-4)

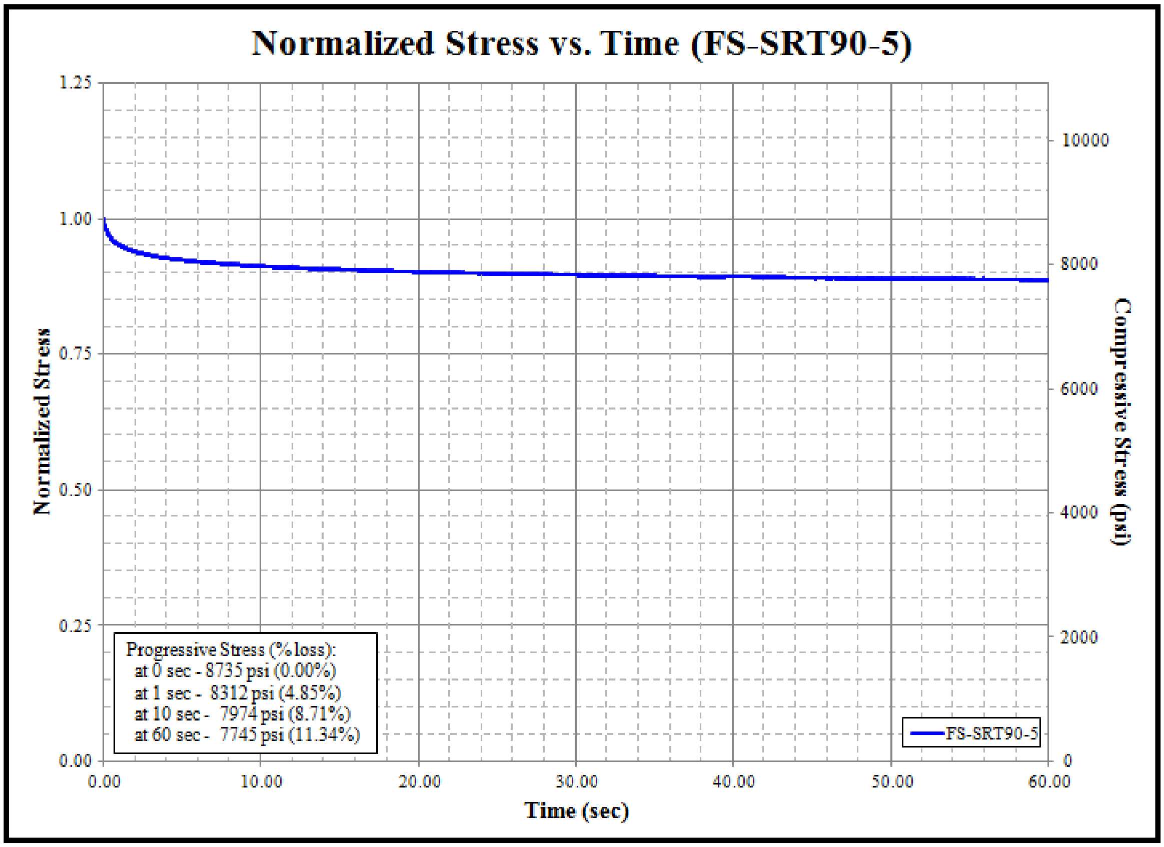

Figure B.5: Normalized Stress vs. Time (FS-SRT90-5)

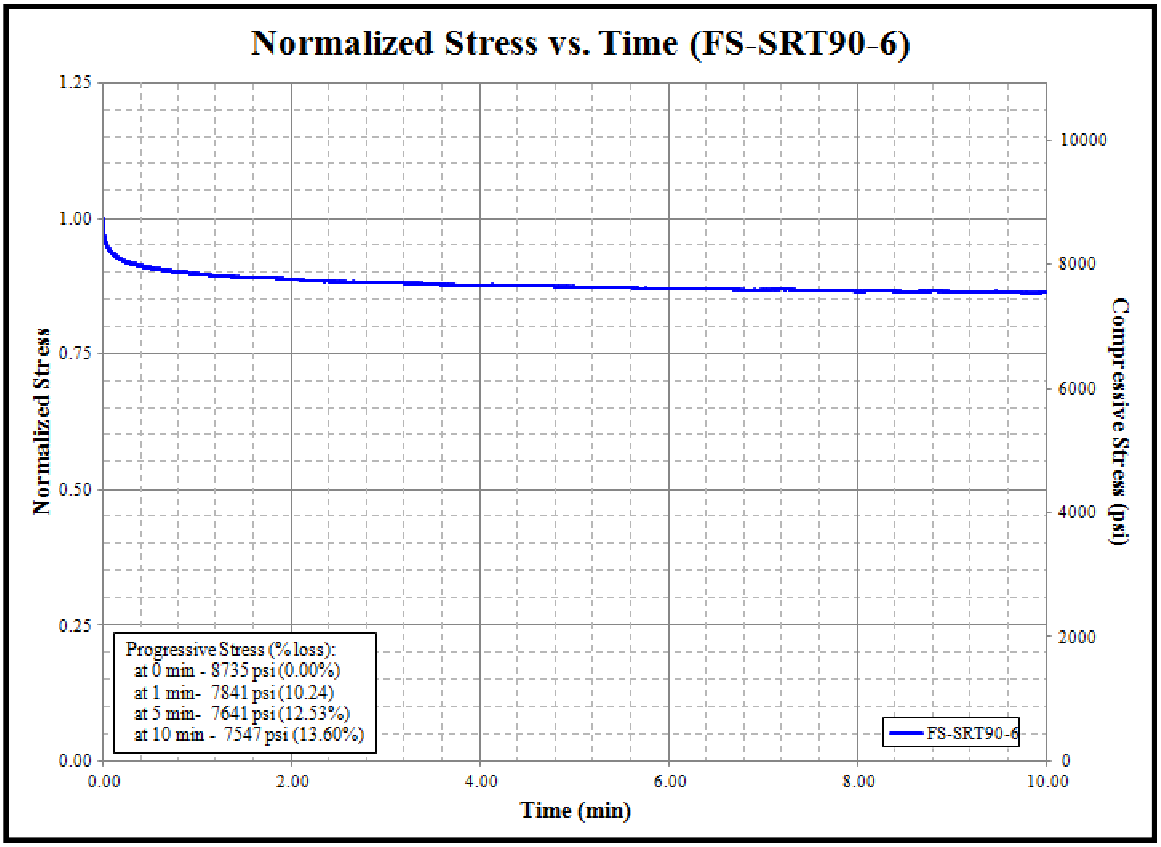

Figure B.6: Normalized Stress vs. Time (FS-SRT90-6)

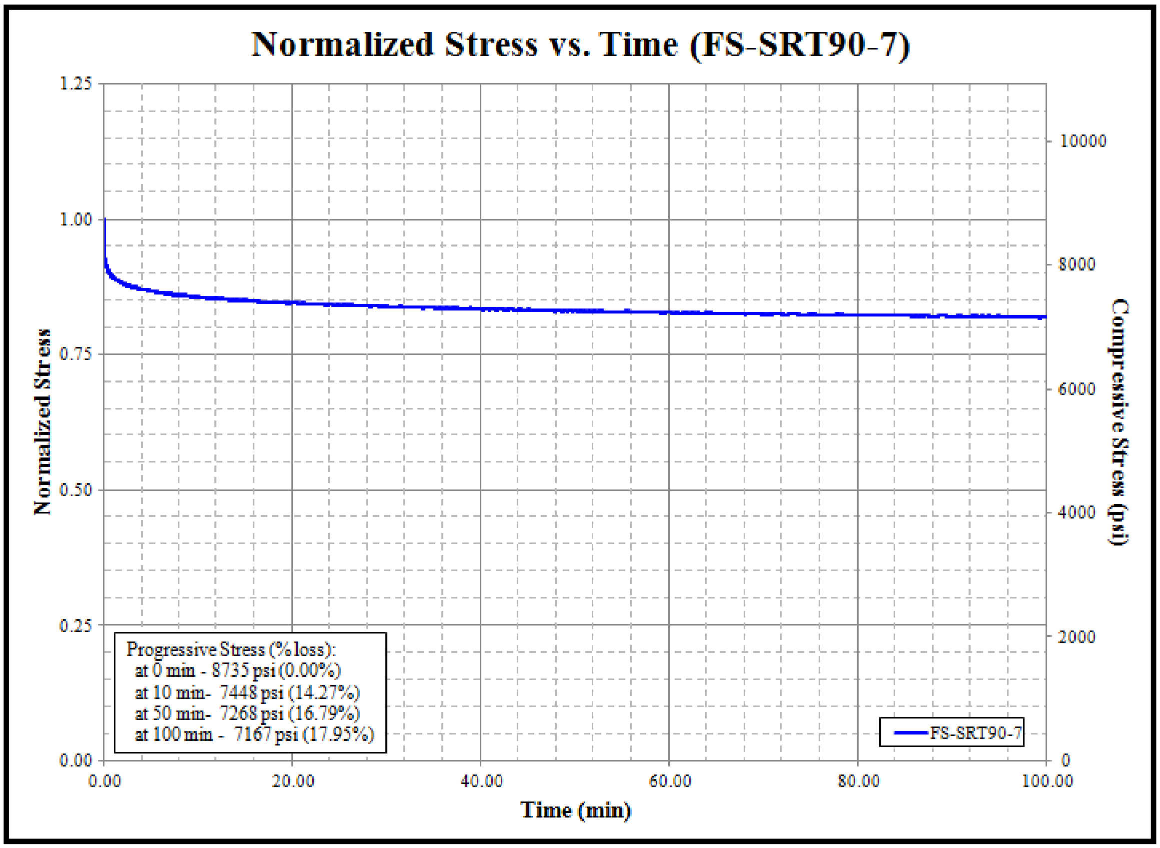

Figure B.7: Normalized Stress vs. Time (FS-SRT90-7)

Appendix C

DCCS STRUCTURE STRESS RELAXATION TEST GRAPHS

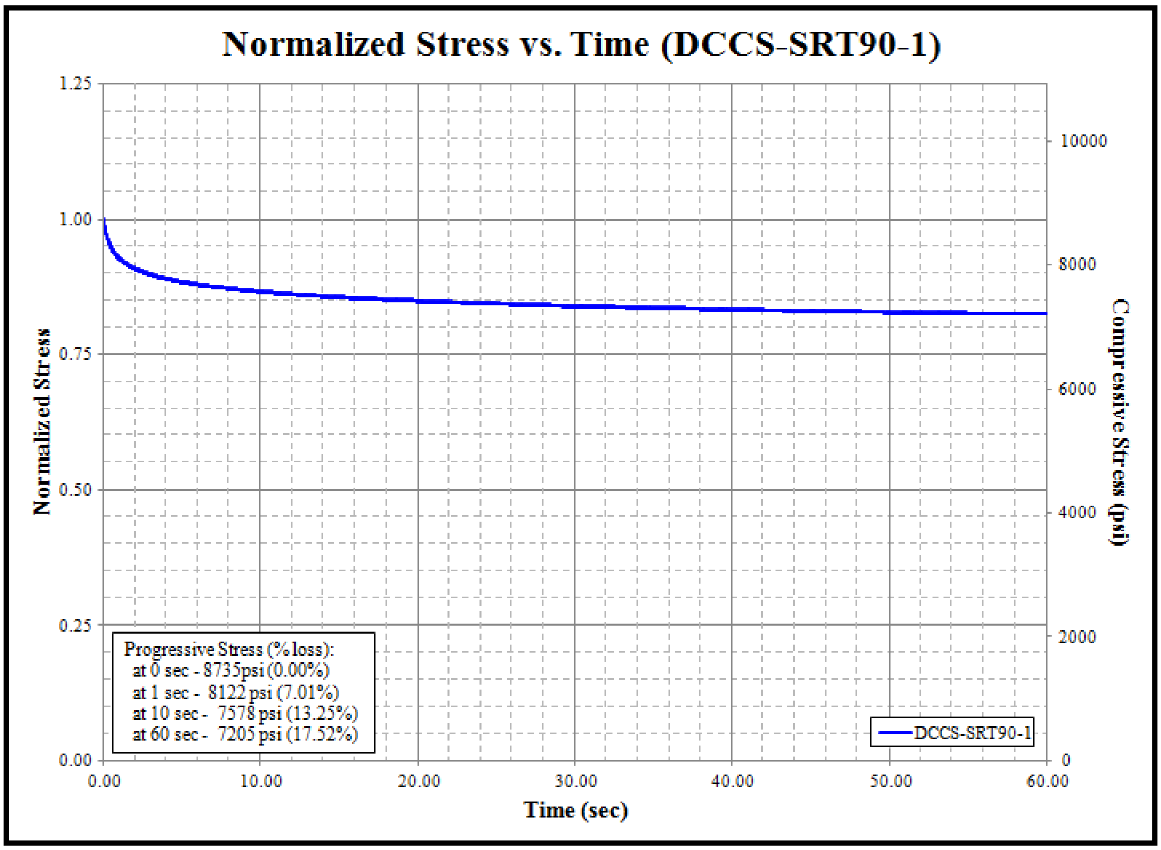

Figure C.1: Normalized Stress vs. Time (DCCS-SRT90-1)

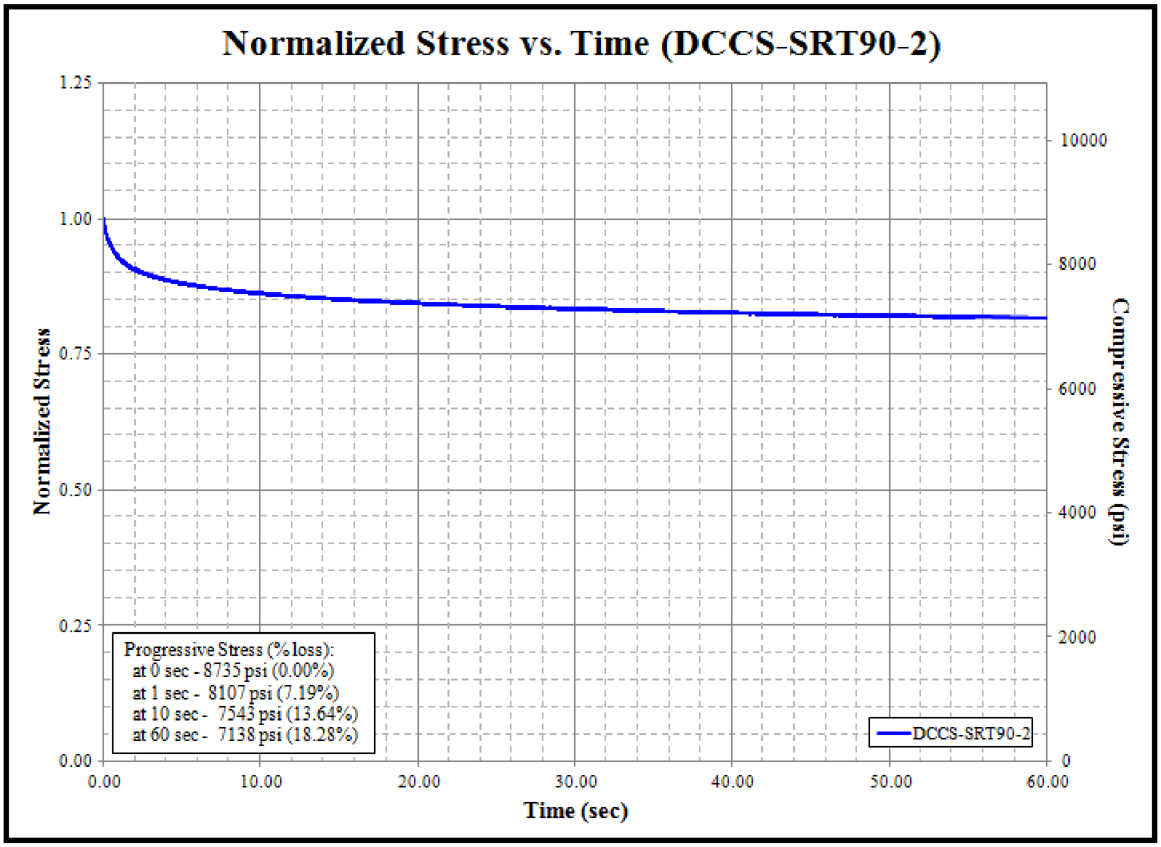

Figure C.2: Normalized Stress vs. Time (DCCS-SRT90-2)

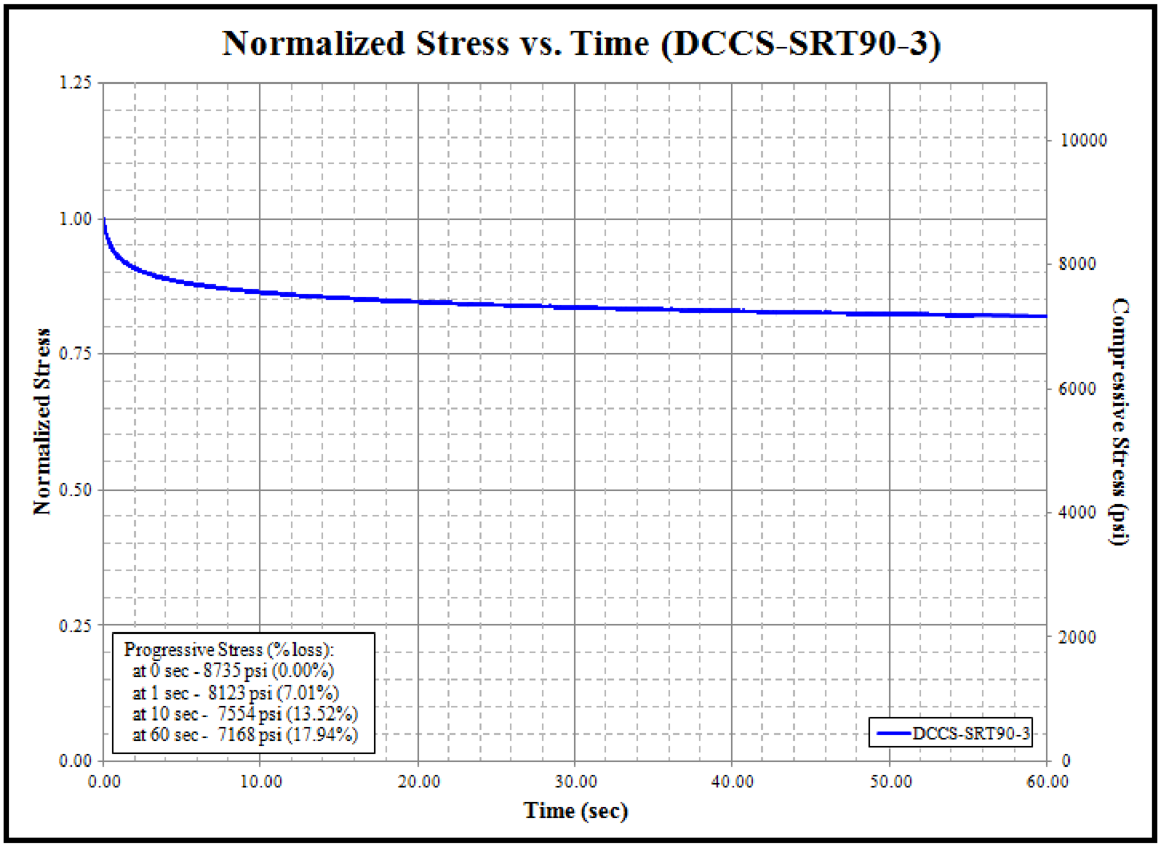

Figure C.3: Normalized Stress vs. Time (DCCS-SRT90-3)

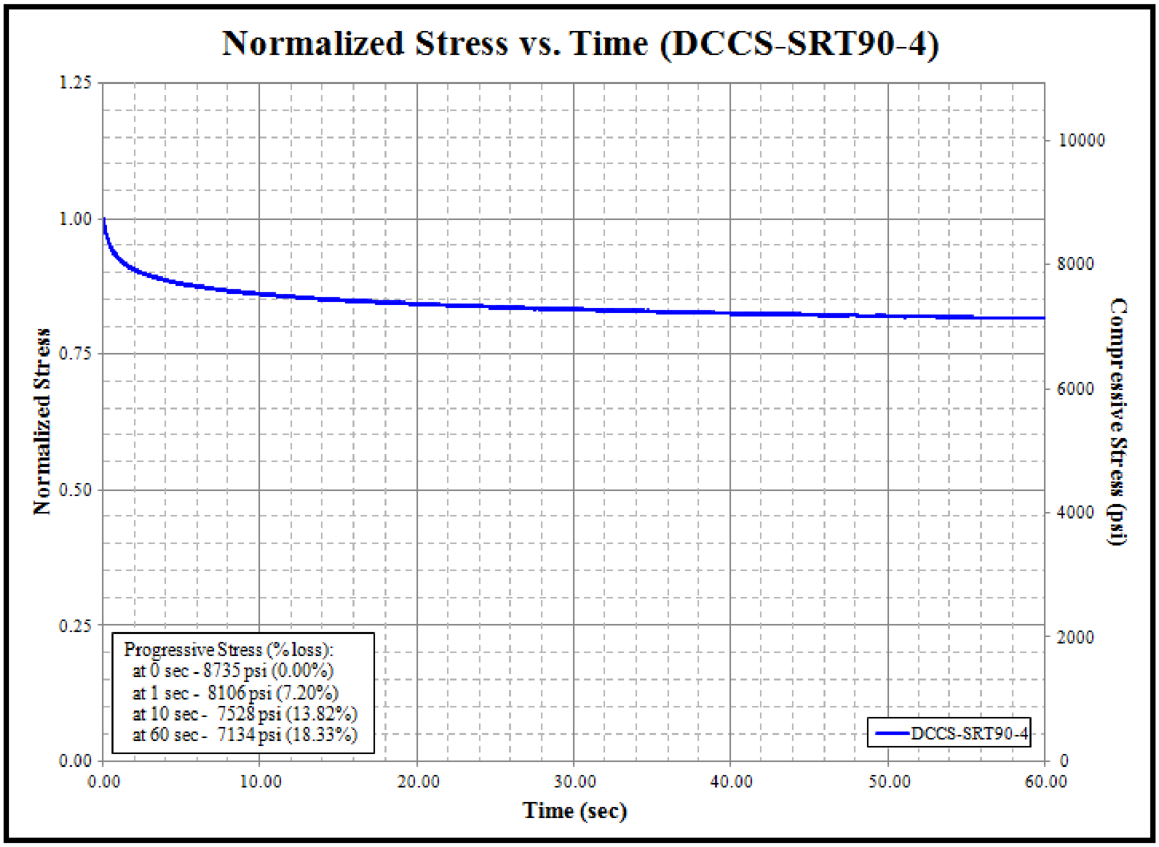

Figure C.4: Normalized Stress vs. Time (DCCS-SRT90-4)

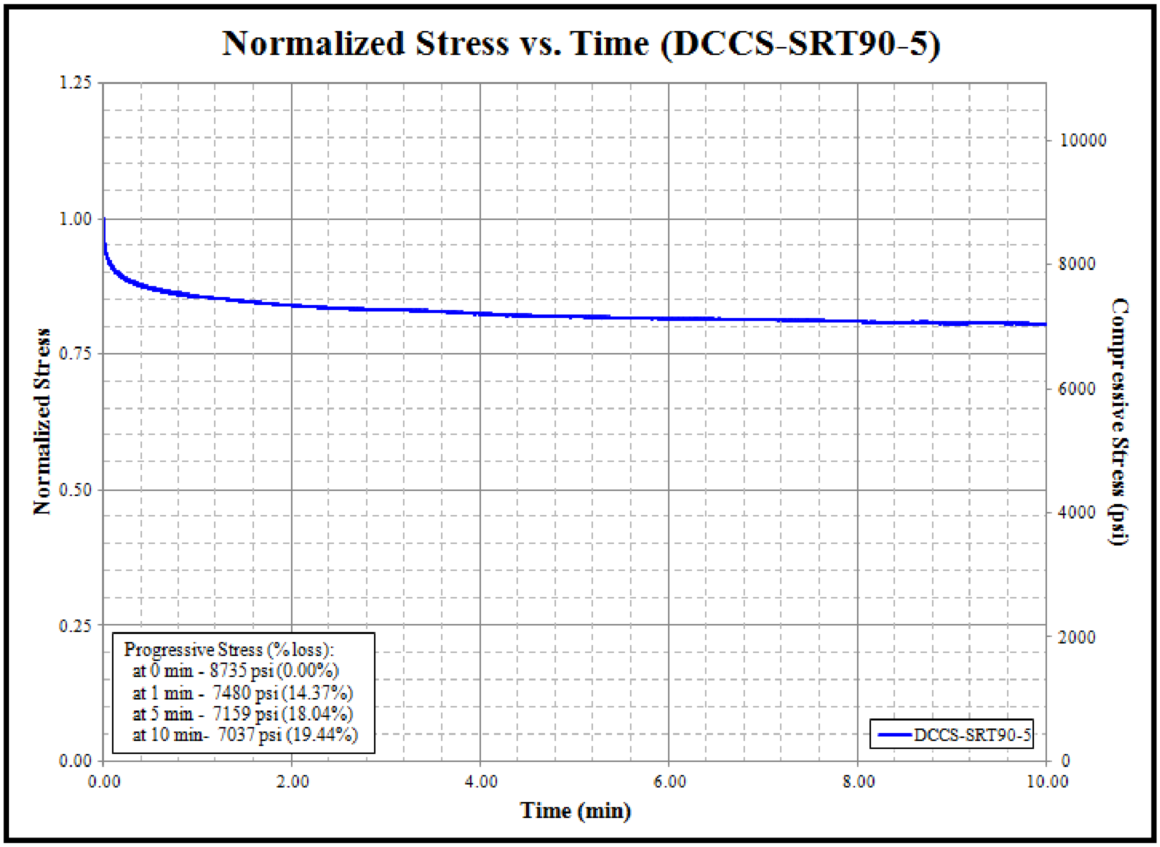

Figure C.5: Normalized Stress vs. Time (DCCS-SRT90-5)

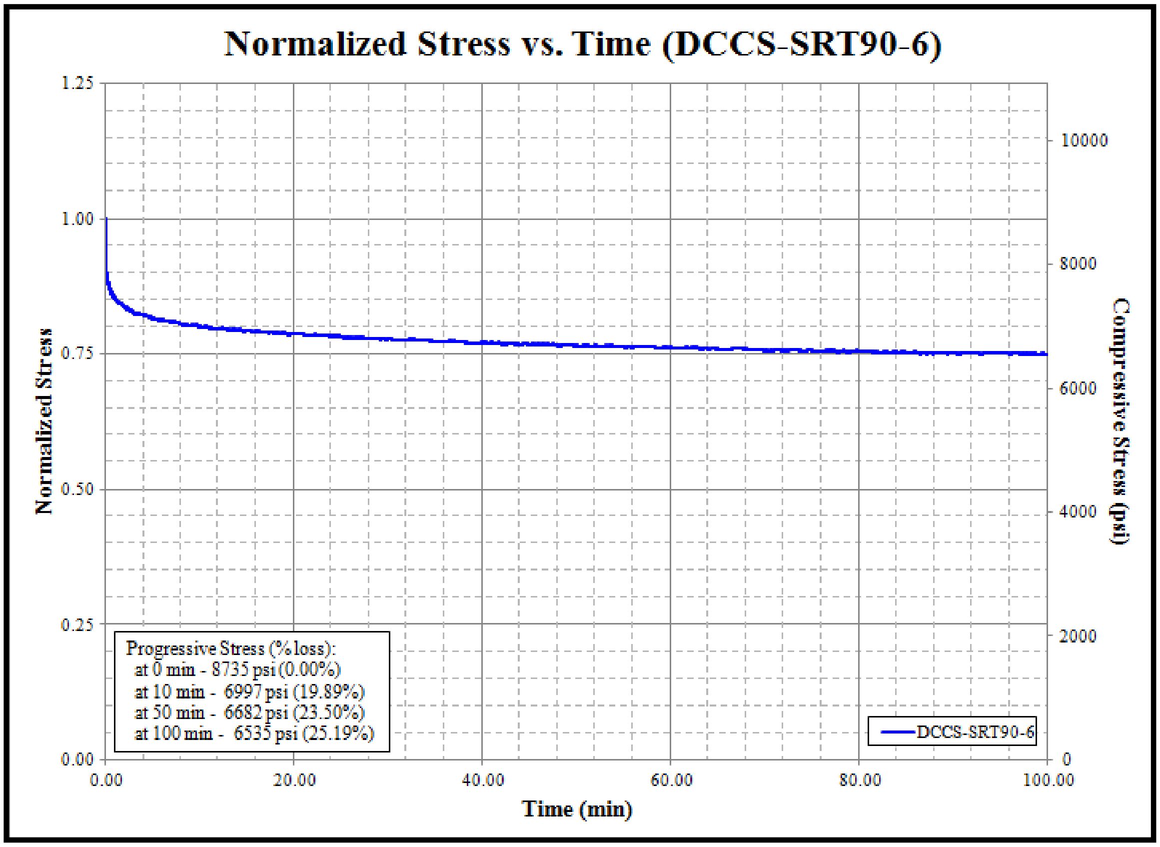

Figure C.6: Normalized Stress vs. Time (DCCS-SRT90-6)

Appendix D

STATIC/FATIGUE SPECIMEN GEOMETRIES

Table D.1: Pinned vs. Baseline Torque Test Specimen Geometries

Sample #		Width (w)	Length (L)	Edge Distance (e)	Distance to Gap	Hole Diam. (D)	Thickness (h)	w/D	e/D
Nominal	in	4.00	12.00	2.00	2.00	0.500	0.920	8.00	4.00
	mm	101.6	304.8	50.8	50.8	12.7	23.368	8.00	4.00
DCCS-W4E2T0-1	in	4.021	12.07	1.990	1.987	0.504	0.912	7.98	3.95
	mm	102.1	306.6	50.55	50.47	12.80	23.165	7.98	3.95
DCCS-W4E2T0-2	in	3.977	12.13	2.063	1.966	0.505	0.906	7.88	4.08
	mm	101.0	308.1	52.40	49.94	12.83	23.012	7.88	4.08
DCCS-W4E2T90-1	in	3.950	11.96	2.012	1.949	0.504	0.906	7.84	3.99
	mm	100.3	303.8	51.11	49.51	12.80	23.01	7.84	3.99
DCCS-W4E2T90-2	in	3.930	12.06	1.991	1.969	0.505	0.911	7.78	3.94
	mm	99.82	306.3	50.57	50.01	12.83	23.14	7.78	3.94
DCCS-W4E2T90-3	in	3.941	12.00	1.992	1.953	0.504	0.914	7.82	3.95
	mm	100.1	304.8	50.60	49.61	12.80	23.22	7.82	3.95

Table D.2: Variable Torque Test Specimen Geometries

Sample #		Width (w)	Length (L)	Edge Distance (e)	Distance to Gap	Hole Diam. (D)	Thickness (h)	w/D	e/D
Nominal	in	4.00	12.00	2.00	2.00	0.500	0.920	8.00	4.00
	mm	101.6	304.8	50.8	50.8	12.7	23.368	8.00	4.00
W4E2T10-1	in	3.938	12.01	2.014	1.969	0.504	0.916	7.81	4.00
	mm	100.0	305.1	51.16	50.01	12.80	23.27	7.81	4.00
W4E2T10-2	in	3.930	12.02	1.981	1.962	0.503	0.908	7.81	3.94
	mm	99.82	305.3	50.32	50.34	12.78	23.06	7.81	3.94
W4E2T10-3	in	3.929	12.01	1.995	1.964	0.503	0.909	7.81	3.97
	mm	99.80	305.1	50.67	49.89	12.78	23.09	7.81	3.97
W4E2T30-1	in	3.943	11.99	1.980	1.986	0.504	0.909	7.82	3.93
	mm	100.2	304.5	50.29	50.45	12.80	23.09	7.82	3.93
W4E2T30-2	in	3.933	11.98	1.998	1.945	0.505	0.905	7.79	3.96
	mm	99.90	304.3	50.75	49.40	12.83	22.99	7.79	3.96
W4E2T30-3	in	3.907	12.05	2.002	1.975	0.504	0.905	7.75	3.97
	mm	99.24	306.1	50.85	50.17	12.80	22.99	7.75	3.97
W4E2T50-1	in	3.924	11.98	2.002	1.961	0.503	0.913	7.80	3.98
	mm	99.67	304.3	50.85	49.81	12.78	23.19	7.80	3.98
W4E2T50-2	in	3.931	11.98	1.978	1.976	0.504	0.907	7.80	3.92
	mm	99.85	304.3	50.24	50.19	12.80	23.04	7.80	3.92
W4E2T50-3	in	3.940	12.02	1.968	1.987	0.503	0.917	7.83	3.91
	mm	100.1	305.3	49.99	50.47	12.78	23.29	7.83	3.91

Table D.2: Continued

Sample #		Width (w)	Length (L)	Edge Distance (e)	Distance to Gap	Hole Diam. (D)	Thickness (h)	w/D	e/D
Nominal	in	4.00	12.00	2.00	2.00	0.500	0.920	8.00	4.00
	mm	101.6	304.8	50.8	50.8	12.7	23.368	8.00	4.00
W4E2T70-1	in	3.932	12.05	1.986	1.982	0.506	0.911	7.77	3.92
	mm	99.87	306.1	50.45	50.34	12.85	23.14	7.77	3.92
W4E2T70-2	in	3.940	11.98	1.979	1.982	0.504	3.915	7.82	3.93
	mm	100.1	304.3	50.27	50.34	12.80	99.44	7.82	3.93
W4E2T70-3	in	3.928	12.02	1.989	1.977	0.504	0.919	7.79	3.95
	mm	99.77	305.3	50.52	50.22	12.80	23.34	7.79	3.95
W4E2T110-1	in	3.935	12.01	2.006	1.958	0.506	0.911	7.78	3.96
	mm	99.95	305.1	50.95	49.73	12.85	23.14	7.78	3.96
W4E2T110-2	in	3.933	11.99	1.975	1.991	0.504	0.910	7.80	3.92
	mm	99.90	304.5	50.17	50.57	12.80	23.14	7.80	3.92
W4E2T110-3	in	3.928	12.02	1.989	1.977	0.504	0.919	7.79	3.95
	mm	99.77	305.3	50.52	50.22	12.80	23.34	7.79	3.95

Table D.3: High Level Fatigue Test Specimen Geometries (Clamped)

Sample # (Stress Level)		Width (w)	Length (L)	Edge Distance (e)	Distance to Gap	Hole Diam. (D)	Thickness (h)	w/D	e/D
Nominal	in	4.00	12.00	2.00	2.00	0.500	0.920	8.00	4.00
	mm	101.6	304.8	50.8	50.8	12.7	23.368	8.00	4.00
FW4E2T90-1 (5)	in	3.933	11.75	2.025	1.916	0.504	0.914	7.80	4.02
	mm	99.90	298.5	51.44	48.67	12.80	23.22	7.80	4.02
FW4E2T90-2 (5)	in	3.942	12.01	2.039	1.917	0.501	0.918	7.87	4.07
	mm	100.1	305.1	51.79	48.69	12.73	23.32	7.87	4.07
FW4E2T90-3 (5)	in	3.925	12.02	1.991	1.984	0.507	0.914	7.74	3.93
	mm	99.70	305.3	50.57	50.39	12.88	23.22	7.74	3.93
FW4E2T90-4 (4)	in	3.955	12.02	1.978	1.944	0.504	0.910	7.85	3.92
	mm	100.5	305.3	50.24	49.38	12.80	23.11	7.85	3.92
FW4E2T90-5 (4)	in	3.924	11.98	2.022	1.934	0.505	0.916	7.77	4.00
	mm	99.67	304.3	51.36	49.12	12.84	23.27	7.77	4.00
FW4E2T90-6 (3)	in	3.924	11.99	2.012	1.927	0.506	0.923	7.75	3.98
	mm	99.67	304.5	51.11	48.95	12.85	23.44	7.75	3.98
FW4E2T90-7 (3)	in	3.933	12.02	2.000	1.960	0.504	0.901	7.80	3.97
	mm	99.90	305.3	50.80	49.78	12.80	22.88	7.80	3.97
FW4E2T90-8 (3)	in	3.935	12.01	1.975	1.971	0.506	0.906	7.78	3.90
	mm	99.95	305.1	50.17	50.06	12.85	23.01	7.78	3.90
FW4E2T90-9 (3)	in	3.926	11.99	2.009	1.951	0.504	0.903	7.79	3.99
	mm	99.72	304.5	51.03	49.56	12.80	22.94	7.79	3.99

Table D.3: Continued

Sample # (Stress Level)		Width (w)	Length (L)	Edge Distance (e)	Distance to Gap	Hole Diam. (D)	Thickness (h)	w/D	e/D
Nominal	in	4.00	12.00	2.00	2.00	0.500	0.920	8.00	4.00
	mm	101.6	304.8	50.8	50.8	12.7	23.368	8.00	4.00
FW4E2T90-10 (2)	in	3.908	12.08	2.013	1.946	0.504	0.922	7.75	3.99
	mm	99.26	306.8	51.13	49.43	12.80	23.42	7.75	3.99
FW4E2T90-11 (2)	in	3.913	12.02	2.028	1.926	0.505	0.915	7.75	4.02
	mm	99.39	305.3	51.51	48.92	12.83	23.24	7.75	4.02
FW4E2T90-12 (2)	in	3.930	12.03	1.985	1.968	0.503	0.910	7.81	3.95
	mm	99.82	305.6	50.42	49.99	12.78	23.11	7.81	3.95
FW4E2T90-13 (2)	in	3.941	12.01	2.018	1.946	0.504	0.908	7.82	4.00
	mm	100.1	305.1	51.26	49.43	12.80	23.06	7.82	4.00
FW4E2T90-14 (1)	in	3.930	12.00	2.045	1.931	0.504	0.922	7.80	4.06
	mm	99.82	304.8	51.94	49.05	12.80	23.42	7.80	4.06
FW4E2T90-15 (1)	in	3.924	12.01	1.989	1.990	0.506	0.908	7.75	3.93
	mm	99.67	305.1	50.52	50.55	12.85	23.06	7.75	3.93
FW4E2T90-16 (1)	in	3.931	11.99	2.021	1.962	0.507	0.912	7.75	3.99
	mm	99.85	304.5	51.33	49.84	12.88	23.17	7.75	3.99
FW4E2T90-17 (1)	in	3.903	12.06	1.989	1.950	0.506	0.910	7.71	3.93
	mm	99.14	306.3	50.52	49.53	12.85	23.11	7.71	3.93

Table D.4: High Level Fatigue Test Specimen Geometries (Pinned)

Sample # (Stress Level)		Width (w)	Length (L)	Edge Distance (e)	Distance to Gap	Hole Diam. (D)	Thickness (h)	w/D	e/D
Nominal	in	4.00	12.00	2.00	2.00	0.500	0.920	8.00	4.00
	mm	101.6	304.8	50.8	50.8	12.7	23.368	8.00	4.00
FW4E2T0-1 (5)	in	3.880	12.03	2.003	1.966	0.504	0.909	7.70	3.97
	mm	98.55	305.6	50.88	49.94	12.80	23.09	7.70	3.97
FW4E2T0-2 (4)	in	3.937	12.01	1.973	1.995	0.505	0.911	7.80	3.91
	mm	100.0	305.1	50.11	50.67	12.83	23.14	7.80	3.91
FW4E2T0-3 (3)	in	3.926	12.01	1.964	2.026	0.503	0.917	7.81	3.90
	mm	99.72	305.1	49.89	51.46	12.78	23.29	7.81	3.90
FW4E2T0-4 (2)	in	3.911	12.02	1.988	1.977	0.503	0.918	7.78	3.95
	mm	99.34	305.3	50.50	50.22	12.78	23.32	7.78	3.95
FW4E2T0-5 (1)	in	3.872	12.12	1.979	2.017	0.506	0.919	7.65	3.91
	mm	98.35	307.8	50.27	51.23	12.85	23.34	7.65	3.91
FW4E2T0-6 (1)	in	3.896	12.04	1.982	2.002	0.503	0.908	7.75	3.94
	mm	98.96	305.8	50.34	50.85	12.78	23.06	7.75	3.94

Table D.5: Low Level Fatigue Test Specimen Geometries (Clamped)

Sample # (Stress Level)		Width (w)	Length (L)	Edge Distance (e)	Distance to Gap	Hole Diam. (D)	Thickness (h)	w/D	e/D
Nominal	in	4.00	12.00	2.00	2.00	0.500	0.920	8.00	4.00
	mm	101.6	304.8	50.8	50.8	12.7	23.368	8.00	4.00
FW4E2T90-1 (5)	in	3.954	12.03	1.974	1.959	0.503	0.921	7.86	3.92
	mm	100.4	305.6	50.14	49.76	12.78	23.393	7.86	3.92
FW4E2T90-2 (5)	in	3.926	12.02	2.003	1.927	0.502	0.911	7.82	3.99
	mm	99.72	305.3	50.88	48.95	12.75	23.139	7.82	3.99
FW4E2T90-3 (5)	in	3.928	12.07	2.024	1.913	0.504	0.917	7.79	4.02
	mm	99.77	306.6	51.41	48.59	12.80	23.292	7.79	4.02
FW4E2T90-4 (5)	in	3.932	12.02	2.000	1.981	0.504	0.912	7.80	3.97
	mm	99.87	305.3	50.80	50.32	12.80	23.165	7.80	3.97
FW4E2T90-5 (4)	in	3.957	12.02	2.023	1.950	0.504	0.902	7.85	4.01
	mm	100.5	305.3	51.38	49.53	12.80	22.911	7.85	4.01
FW4E2T90-6 (4)	in	3.897	12.05	2.006	1.965	0.507	0.907	7.69	3.96
	mm	98.98	306.1	50.95	49.91	12.88	23.038	7.69	3.96
FW4E2T90-7 (3)	in	3.918	12.02	1.982	1.978	0.504	0.914	7.77	3.93
	mm	99.52	305.3	50.34	50.24	12.80	23.22	7.77	3.93
FW4E2T90-8 (3)	in	3.937	11.99	2.002	1.926	0.505	0.916	7.80	3.96
	mm	100.0	304.5	50.85	48.92	12.83	23.27	7.80	3.96

Appendix E

DCCS STRUCTURE BEARING TEST GRAPHS

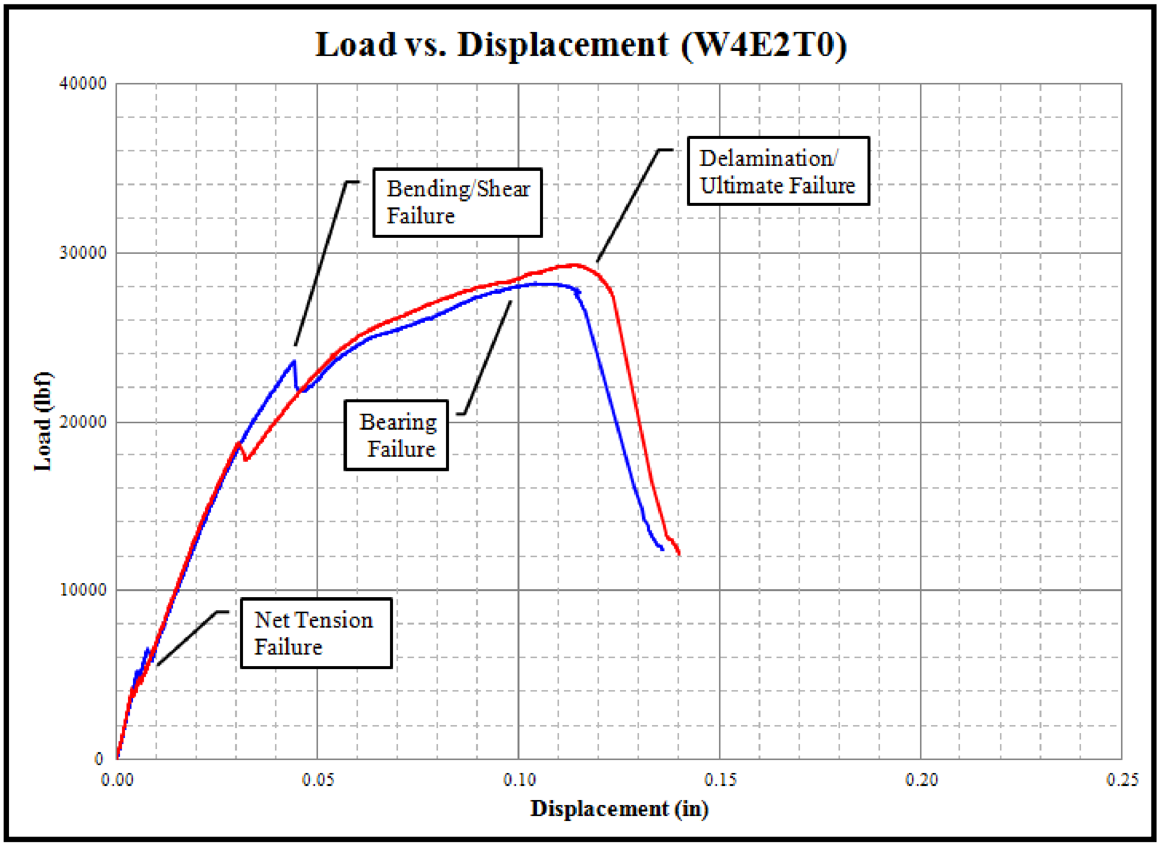

Figure E.1: Load vs. Displacement (W4E2T0)

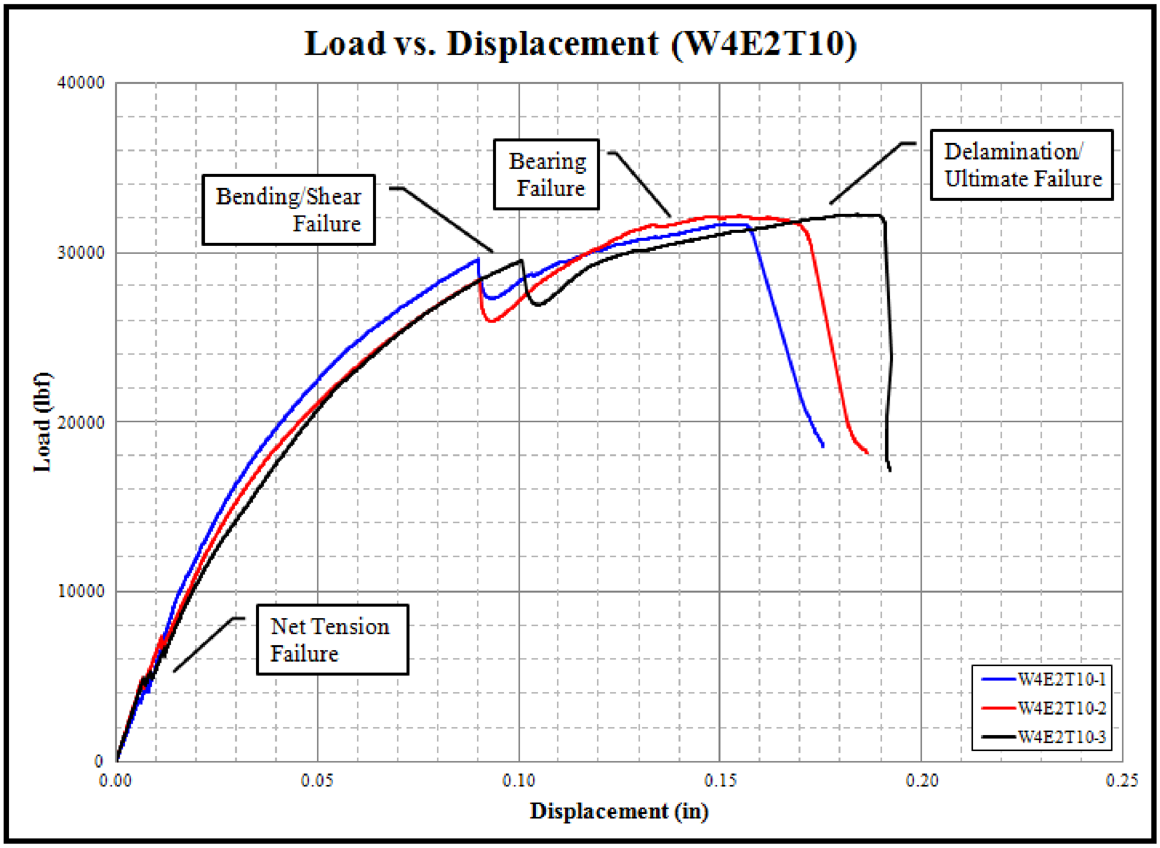

Figure E.2: Load vs. Displacement (W4E2T10)

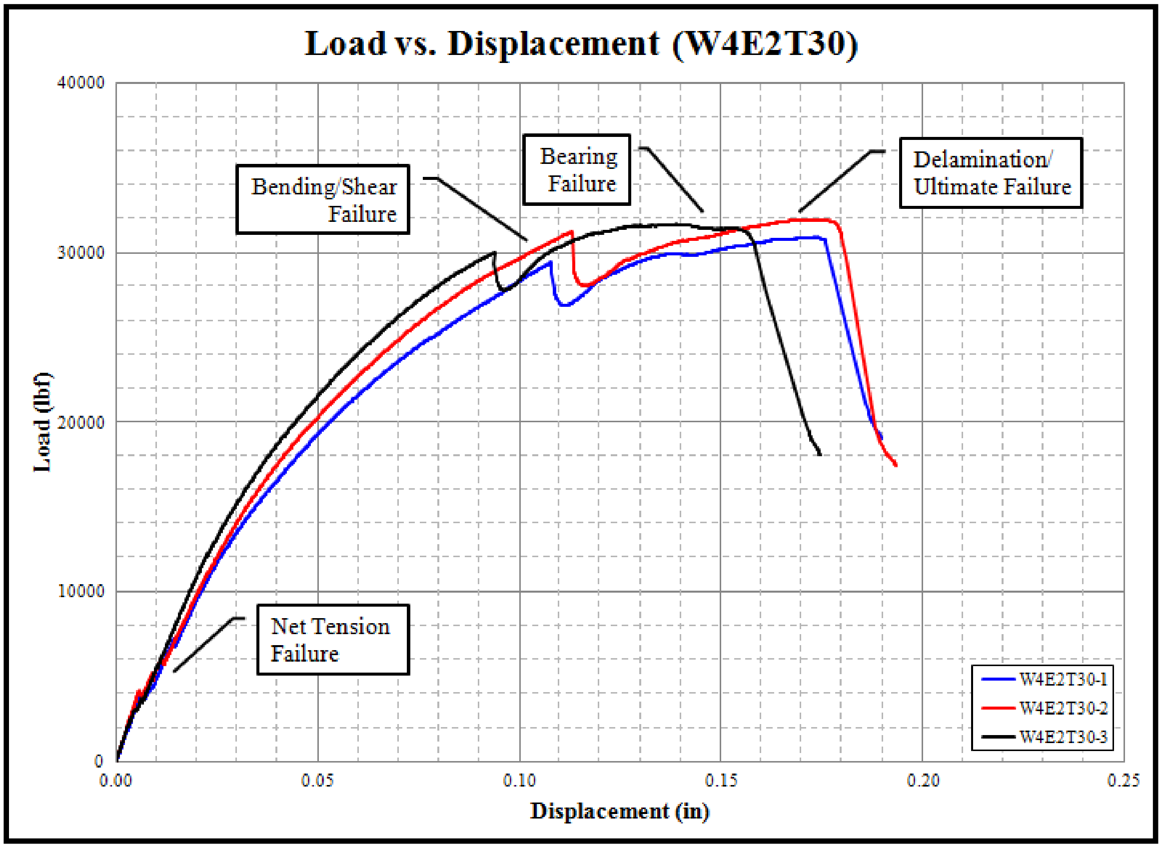

Figure E.3: Load vs. Displacement (W4E2T30)

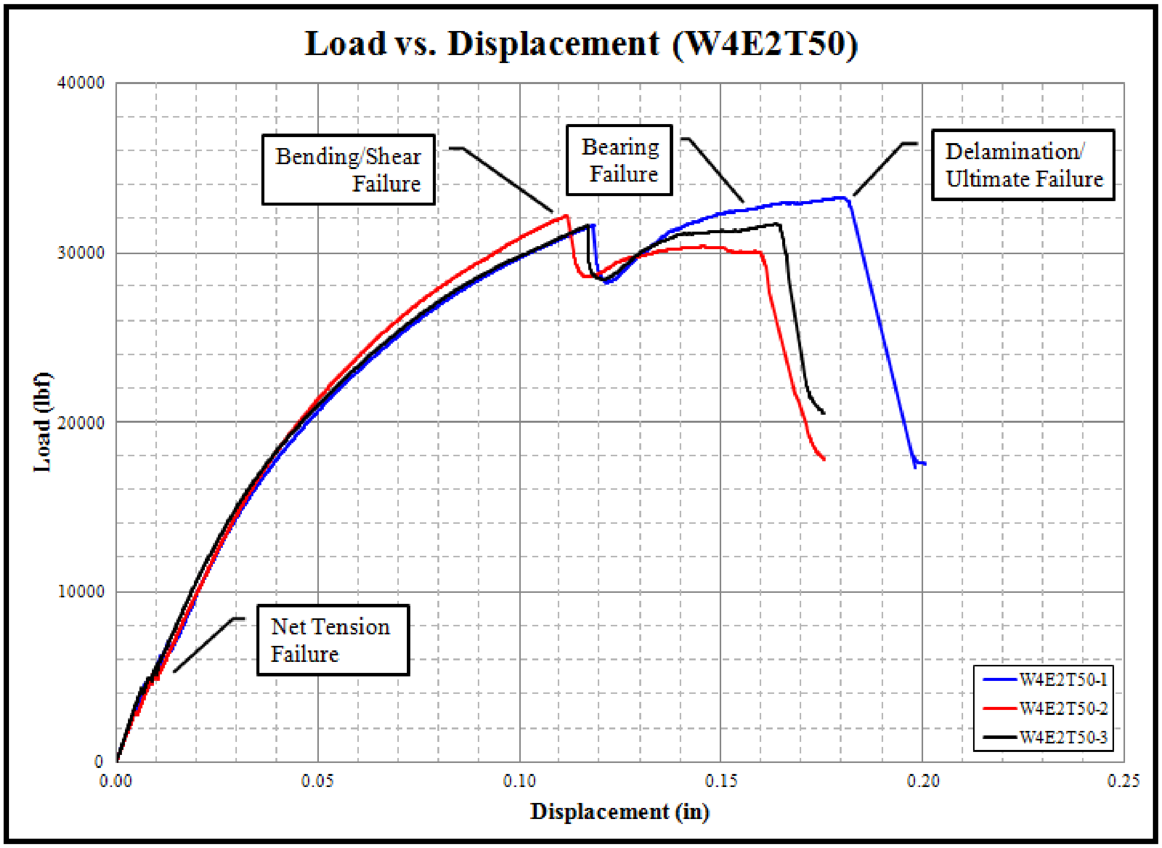

Figure E.4: Load vs. Displacement (W4E2T50)

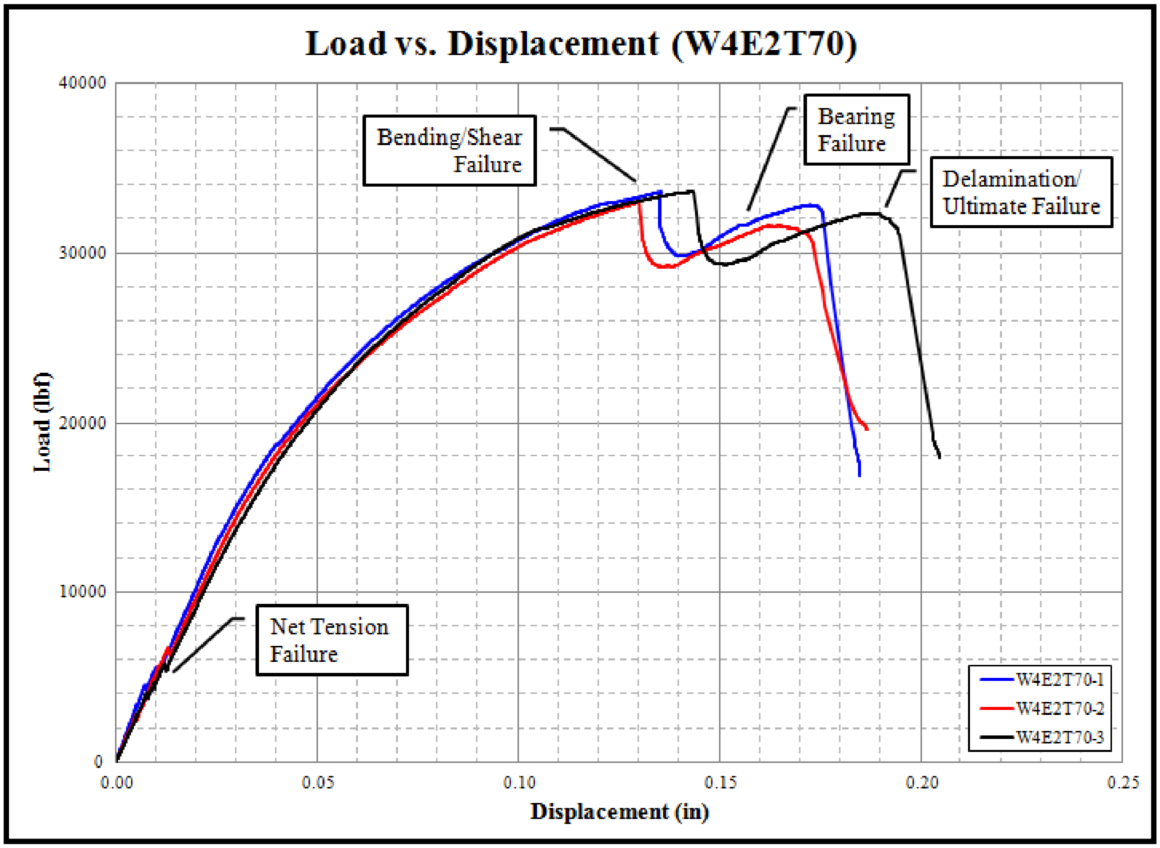

Figure E.5: Load vs. Displacement (W4E2T70)

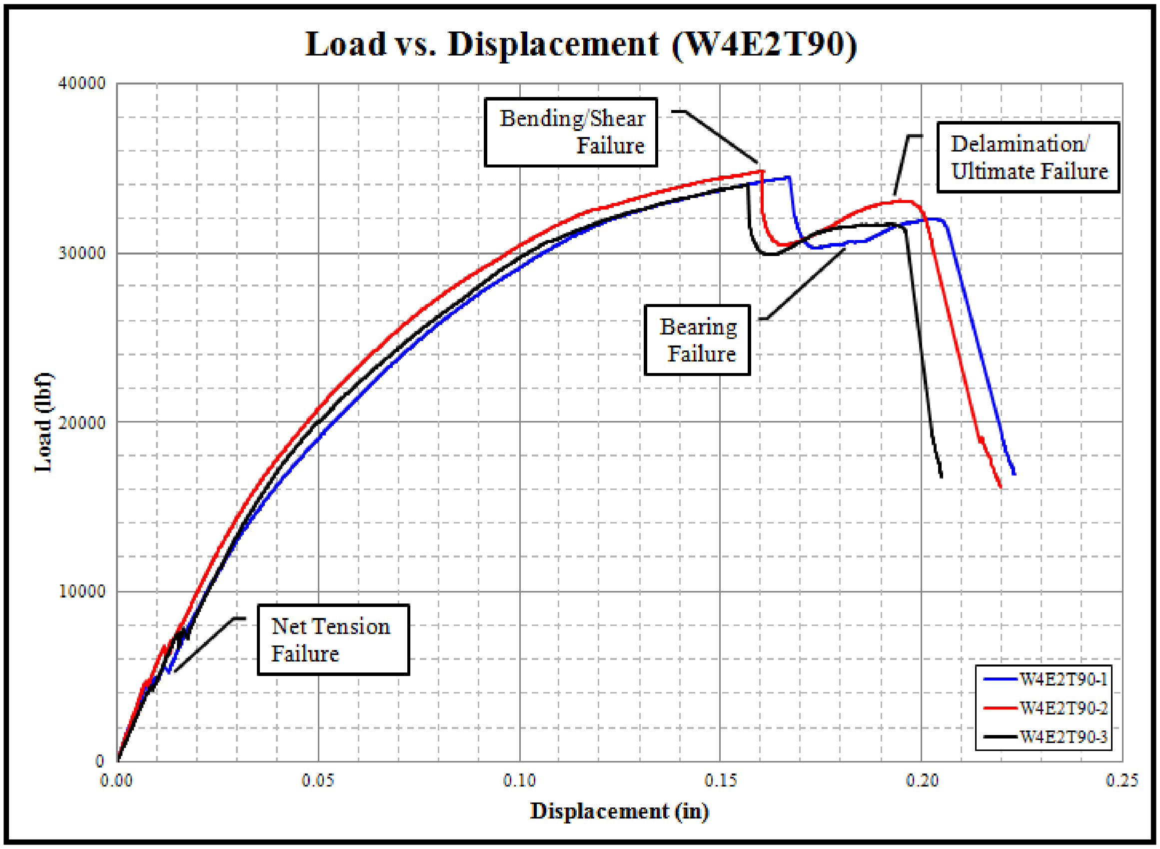

Figure E.6: Load vs. Displacement (W4E2T90)

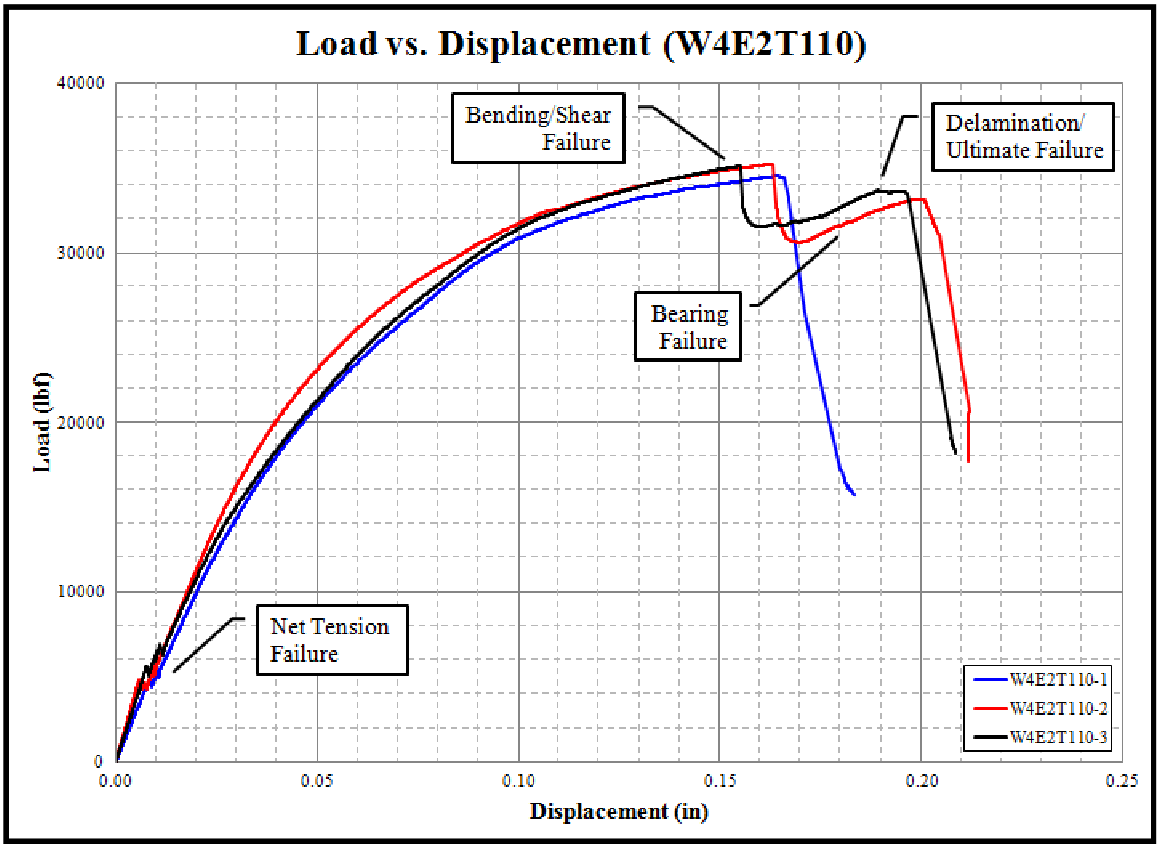

Figure E.7: Load vs. Displacement (W4E2T110)

Appendix F

DCCS STRUCTURE BASELINE FAILURE MODES

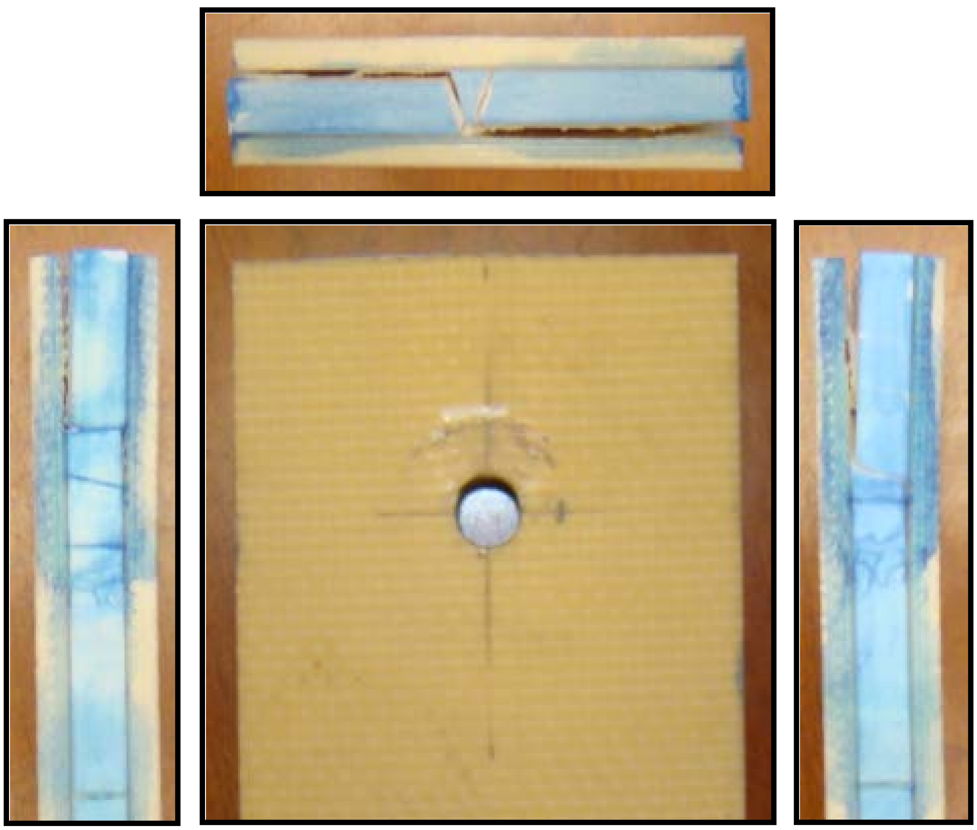

Figure F.1: Baseline Failure of DCCS Structure with Torque = 90 ft-lbs

Appendix G

DCCS STRUCTURE FATIGUE DAMAGE/FAILURE MODES

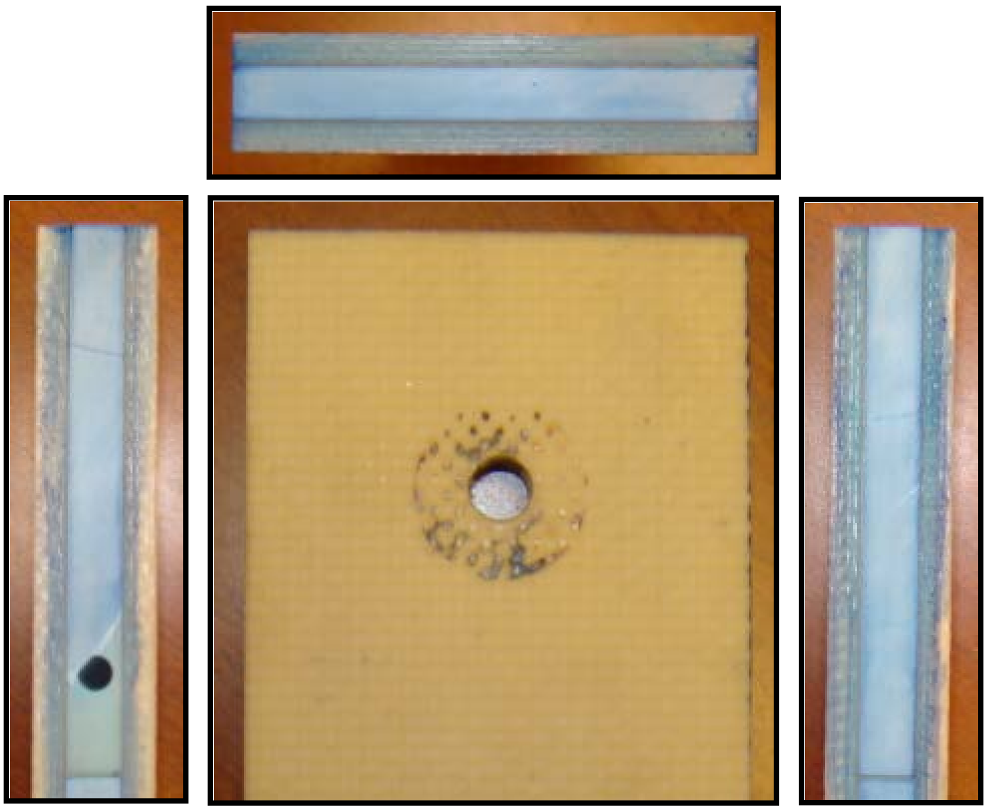

Figure G.1: Stress Level 1 High Level (5120 lbs/512 lbs) after 1 Million Cycles

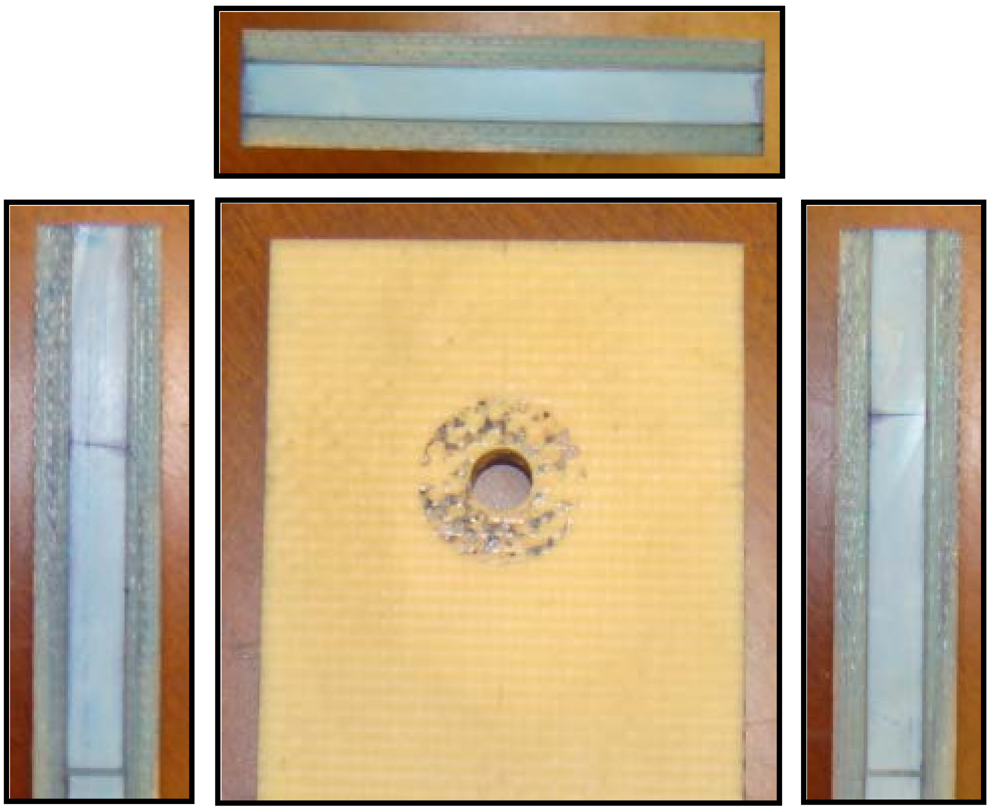

Figure G.2: Stress Level 2 High Level (10240 lbs/1024 lbs) after 1 Million Cycles

Figure G.3: Stress Level 3 High Level (15360 lbs/1536 lbs) after Bolt Failure

Figure G.4: Stress Level 4 High Level (20480 lbs/2048 lbs) after DCCS Structure Failure

Figure G.5: Stress Level 5 High Level (25600 lbs/2560 lbs) after DCCS Structure Failure

Appendix H

DCCS STRUCTURE RESIDUAL STRENGTH TEST GRAPHS

Figure H.1: Load vs. Displacement at Stress Level 2 – High Level (Pinned)

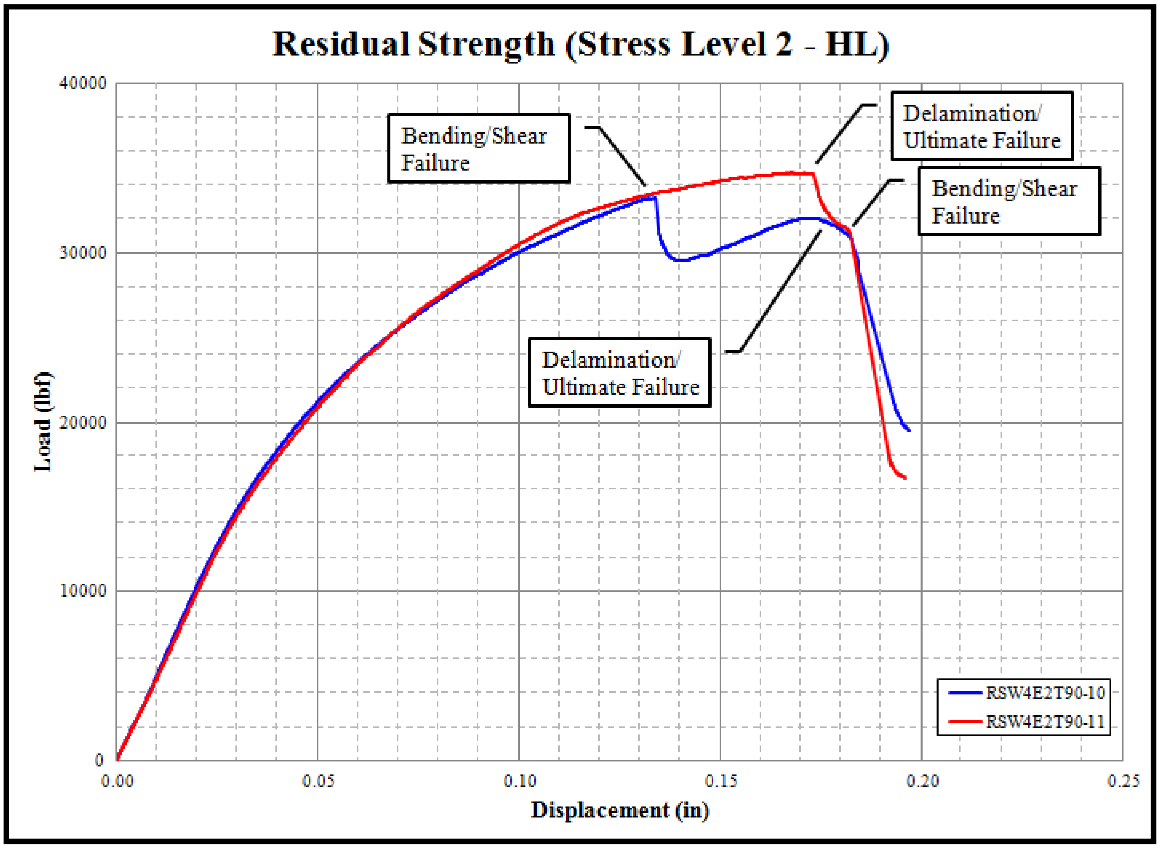

Figure H.2: Load vs. Displacement at Stress Level 2 – High Level (Clamped)

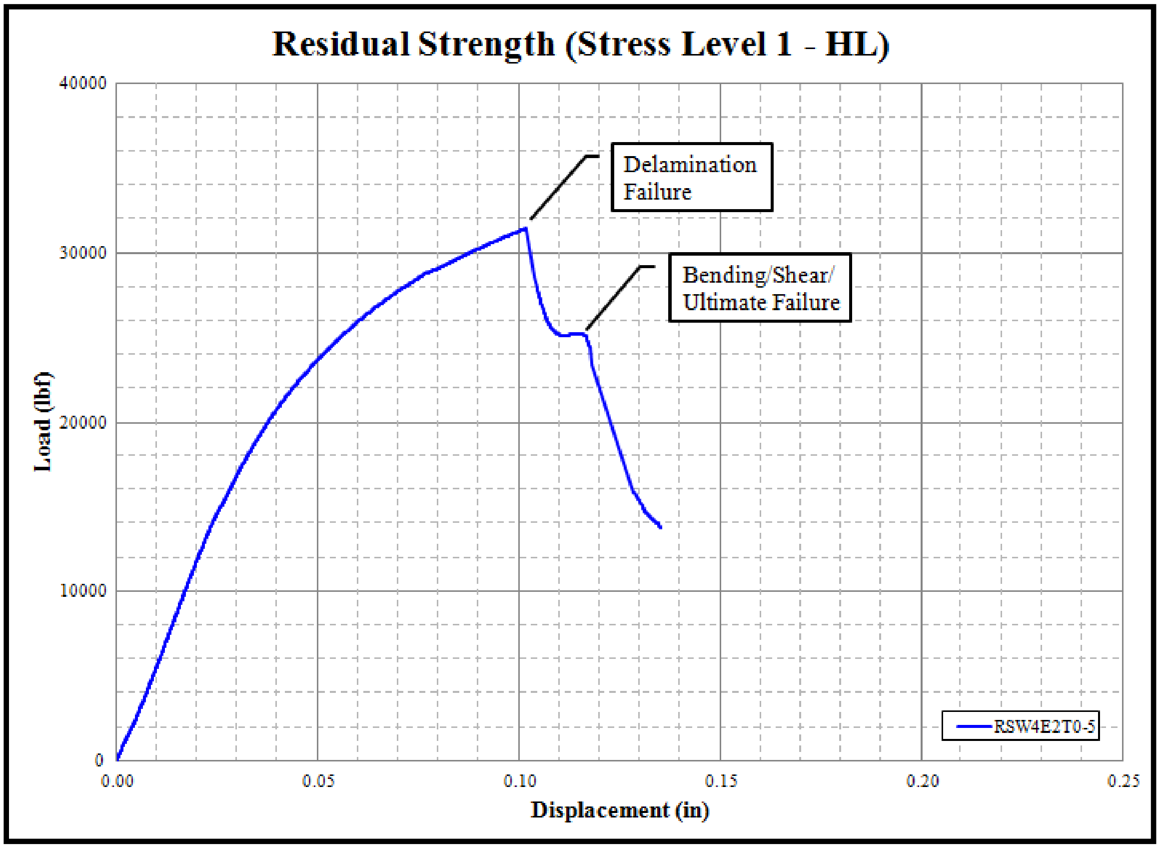

Figure H.3: Load vs. Displacement at Stress Level 1 – High Level (Pinned)

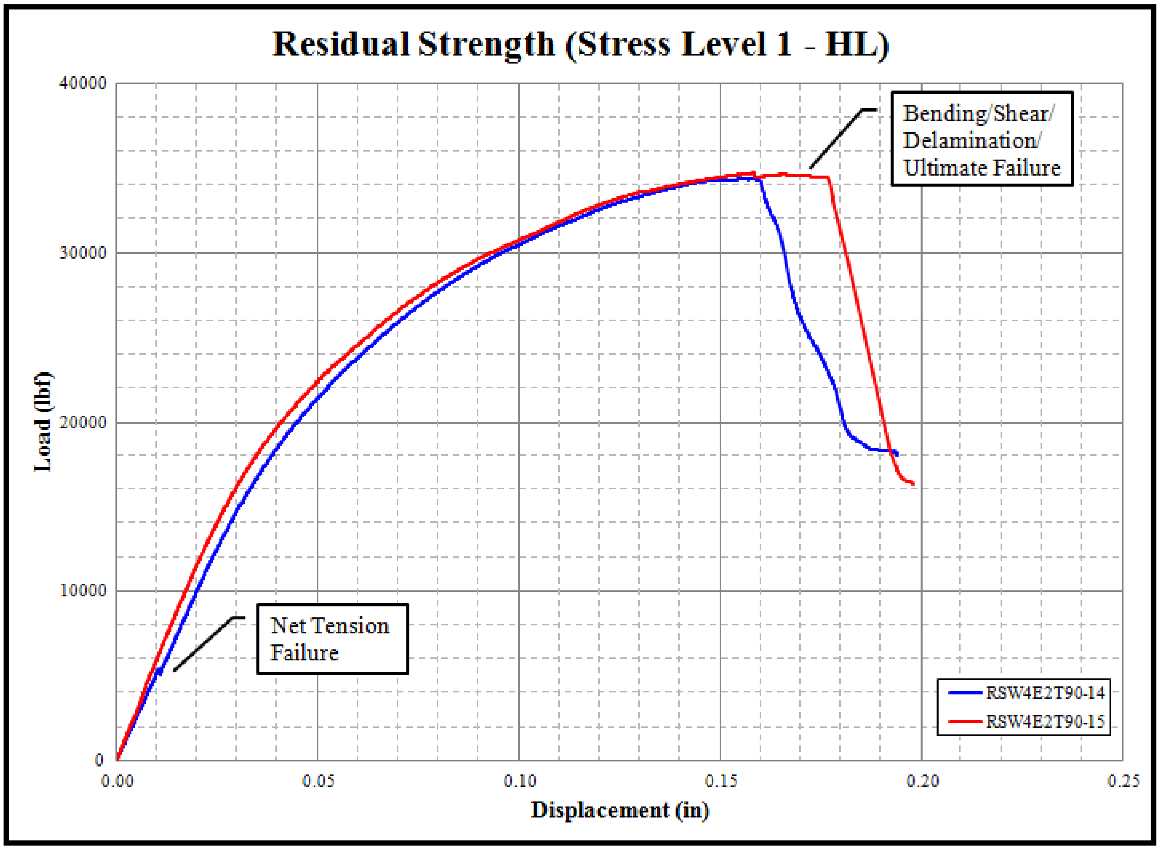

Figure H.4: Load vs. Displacement at Stress Level 1 – High Level (Clamped)

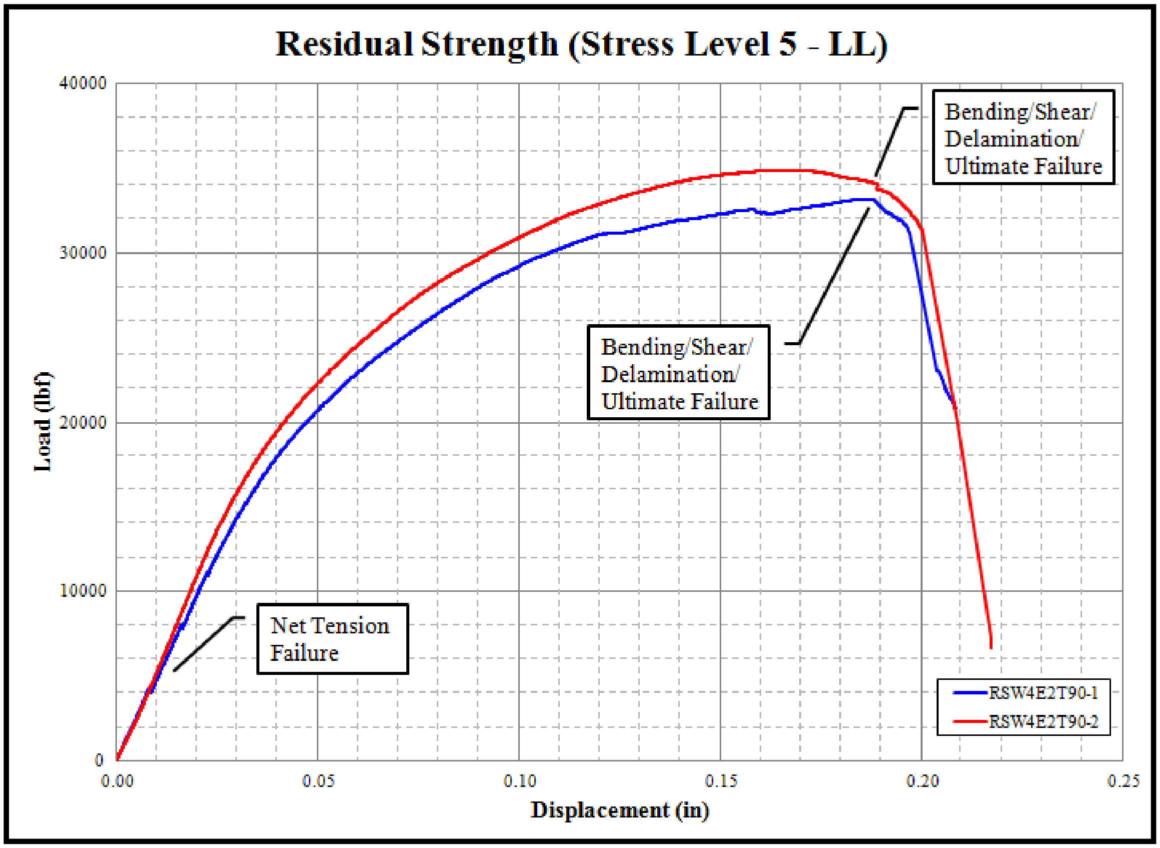

Figure H.5: Load vs. Displacement at Stress Level 5 – Low Level

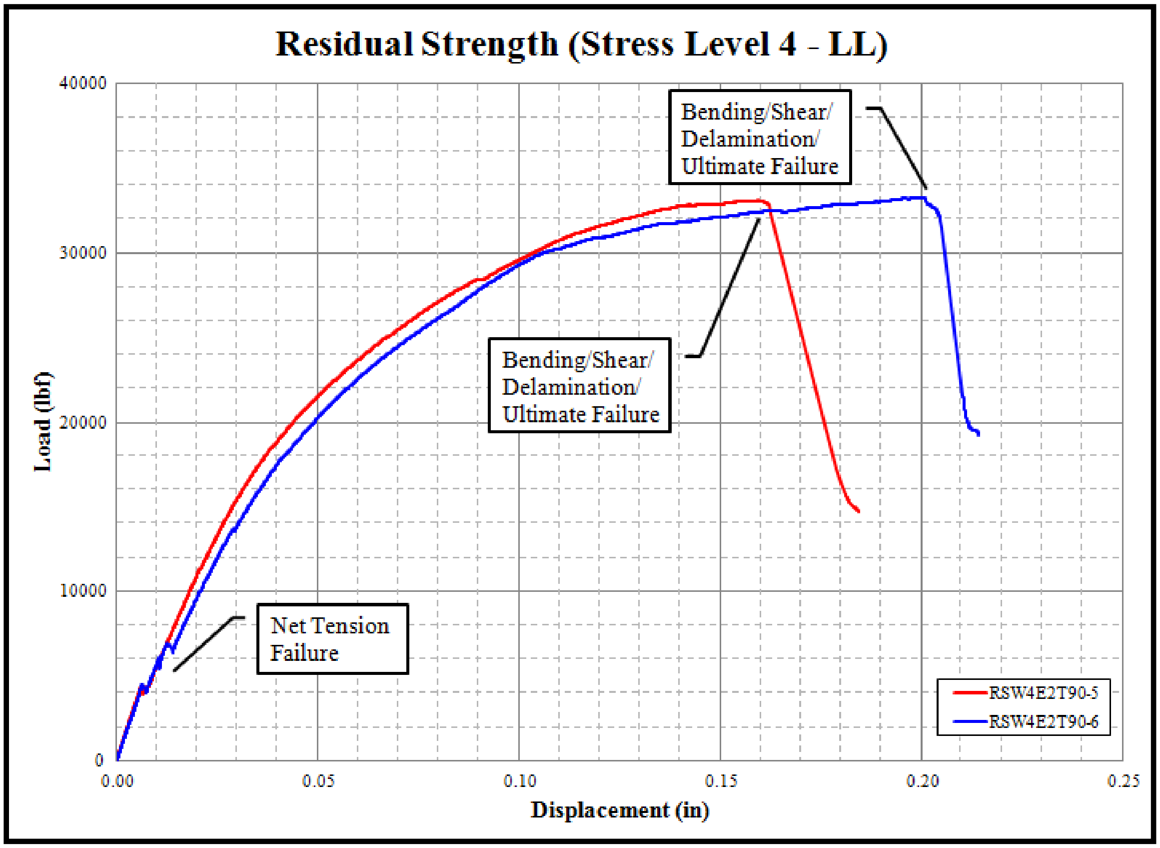

Figure H.6: Load vs. Displacement at Stress Level 4 – Low Level

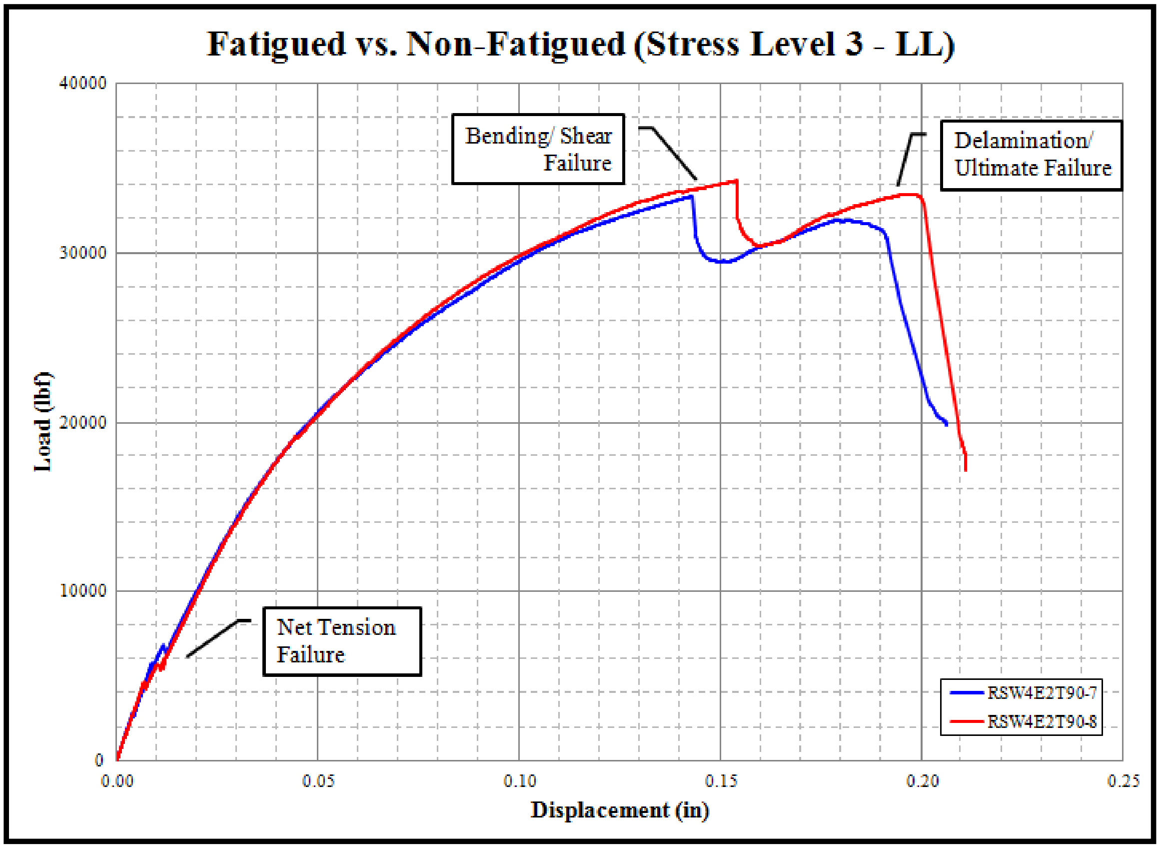

Figure H.7: Load vs. Displacement at Stress Level 3 – Low Level